Experimental and Computational Studies of Oxide Ion Conductors

Bettina Schwaighofer

Supervisors: Prof. Ivana R. Evans, Dr. Miguel A. González

A thesis submitted in partial fulfilment of the requirements for the degree of Doctor of Philosophy

Department of Chemistry
Durham University
United Kingdom
March 2023

Abstract

Experimental and Computational Studies of Oxide Ion Conductors

Bettina Schwaighofer

Solid oxide fuel cells (SOFCs) are a promising alternative to the conventional combustion engine and can be used for both energy conversion and storage. However, current SOFC electrolytes require high operating temperatures. Developing materials with excellent ionic conductivity at lower temperatures (400 - 600 °C) is a crucial step before a more widespread commercialisation of SOFCs is possible.

The work in this thesis focuses on the study of oxide ion dynamics with the aim to develop improved oxide ion conductors. As the main techniques used to achieve this were ab initio molecular dynamics (AIMD) and quasielastic neutron scattering (QENS), this combined approach is also the focus of the literature review in **Chapter 1**.

Chapter 2 introduces the methods used for synthesis, characterisation, and further study of the materials studied.

Chapter 3 investigates the effect of the dopant on the oxide ion dynamics in two doped δ-Bi_2O_3 oxide ion conductors: $Bi_{0.852}V_{0.148}O_{1.648}$ and $Bi_{0.852}P_{0.148}O_{1.648}$. QENS allowed observation of nanosecond dynamics, corresponding to the diffusion of the oxide ions in the Bi-O sublattice via vacancy-hopping, and picosecond dy-

namics, corresponding to localised motion within the dopant sublattices. AIMD gave further insight into the different oxide ion dynamics in $Bi_{0.852}V_{0.148}O_{1.648}$ and $Bi_{0.852}P_{0.148}O_{1.648}$, showing that the flexibility of the V coordination environment plays an important role, creating additional vacancies in the Bi-O sublattice, consistent with the superior conductivity of the vanadate.

Chapter 4 describes the systematic study of conductivity of the complex scheelite-type materials: $Bi_3(BO_4)(B'O_4)_2$ (B = Fe, Ga, $Fe_{0.9}Ti_{0.1}$; B' = Mo) as well as $Bi_3(B_2O_8)_{1/2}(B'O_4)_2$ (B = Sc, In; B' = Mo). Impedance measurements indicate that interstitial oxide ions are responsible for conductivity in these materials, and the conductivity of $Bi_3(Fe_{0.9}Ti_{0.1}O_{4.05})(MoO_4)_2$ was found to be 1.5×10^{-3} S cm^{-1} at 800 °C, which is comparable to the scheelite-type oxide ion conductor $LaNb_{0.92}W_{0.08}O_{4.04}$.

Chapter 5 discusses the study of two hexagonal perovskites: $Ba_3NbMoO_{8.5}$ and $Ba_7Nb_4MoO_{20}$. Using variable temperature powder X-ray diffraction, the reversibility of the phase transition in $Ba_3NbMoO_{8.5}$ was demonstrated for the first time. QENS showed that oxide ion dynamics in both compounds are too slow to be observed on a nanosecond timescale. In $Ba_7Nb_4MoO_{20}$, AIMD revealed a continuous oxide ion migration pathway in the *ab* plane, and moreover showed an important out-of-plane contribution to the long-range diffusion. This allowed suggestion of a new doping strategy to further enhance oxide ion conductivity.

Chapter 6 discusses results obtained from the first AIMD simulations on a Dion-Jacobson phase oxide ion conductor, $CsBi_2Ti_2NbO_{10-\delta}$, revealing an important contribution of the O2 site to the long-range diffusion. This suggests that oxide ion migration occurs predominantly via an O1-O2-O1 pathway, demonstrating the importance of rotationally flexible octahedra for high ionic conductivity in this new family of oxide ion conductors.

Declaration

The work submitted in this thesis is entirely my own, except where I have acknowledged help from, or collaboration with, a named person, or given reference to a published source or thesis.

The research presented was performed in the Department of Chemistry, Durham University, UK, and at the Institut Laue-Langevin, France, between October 2019 and March 2023, the results of which have not been submitted for a degree in this or any other university.

Acknowledgements

First of all, I would like to thank both my supervisors, Ivana Evans and Miguel González, for their constant support, positive feedback and constructive criticism throughout my whole PhD. I am incredibly grateful for having been their student.

My Durham supervisor, Ivana, is the main reason I am where I am now, both figuratively and literally. Doing my Masters project with her inspired me to continue with academia, and thanks to her I had both the opportunity and confidence to take on this shared PhD and move to Grenoble for half of it. Thank you for your continuous support and encouragement, and your genuinely contagious passion for science.

My PhD experience would not have been the same without my time at the ILL and my supervisor there, Miguel. A lot of what I now know about neutron scattering and simulations I learnt from him. Carrying out the experiments at the ILL was one of my highlights in the last few years, and I am very grateful to Miguel for his never-ending patience in helping me understand the details of it. Thank you for giving me the independence to try and work out problems on my own, but always being there when I needed help.

I would also like to thank some former members of my group in Durham whose guidance and friendship during my first year there I really appreciated, in particular Chloe, Josie, and Melissa.

Similarly, I am very grateful for having been part of the CS group at the ILL, the most friendly and welcoming group there in my entirely biased opinion. This also allowed me to meet my two office mates and closest friends in Grenoble, Arianna and Mo. I am so happy I met you both, my time in Grenoble would not have been the same without you. Thank you for all your science related help, but most importantly for making our office a fun and friendly place I always enjoyed being in.

Finally, I would also like to thank my friends, here in Grenoble, the UK, and anywhere else, and most importantly my family for providing excellent emotional support throughout all ups and downs of the PhD life.

Contents

Abstract **ii**

Declaration **iv**

Acknowledgements **v**

List of Abbreviations **xi**

1 Introduction **1**

1.1 Fuel Cells 1

1.1.1 SOFC Electrolytes 4

1.2 Computational Techniques for Studying Dynamics 7

1.2.1 Nudged Elastic Band (NEB) Method 8

1.2.2 Kinetic Monte Carlo (KMC) method 10

1.2.3 Molecular Dynamics 12

1.3 Combined QENS and AIMD Studies of Oxide Ion Diffusion 14

1.4 Conclusion and Project Aims 24

2 Methodology **27**

2.1 Synthetic Methods 27

2.1.1 Solid State Synthesis 27

2.1.2 Precursor and Coprecipitation Synthesis 28
2.2 Powder X-Ray Diffraction 29
2.2.1 Fundamentals of Diffraction 30
2.2.2 Rietveld and Pawley Refinements 33
2.2.3 Diffraction Instruments and Software 34
2.3 Neutron Scattering 35
2.3.1 Neutron Generation and Moderation 35
2.3.2 Fundamentals of Neutron Scattering 36
2.3.3 Quasielastic Neutron Scattering (QENS) 42
2.3.4 Neutron Scattering Instruments and Software 47
2.4 Impedance Spectroscopy 50
2.4.1 Instruments and Software 54
2.5 Molecular Dynamics (MD) Simulations 54
2.5.1 Ab initio MD 56
2.5.2 Machine learning MD 60
2.5.3 Simulation Analysis and Software 61

3 Oxide Ion Mobility in V- and P-doped Bi_2O_3-Based Solid Electrolytes 63

3.1 Summary 63
3.2 Introduction 64
3.2.1 Aims of this Work 69
3.3 Experimental Methods 69
3.3.1 Synthesis 69
3.3.2 Quasielastic Neutron Scattering (QENS) 70
3.3.3 Computational Methods 70
3.4 Results and Discussion 71
3.4.1 Structural Characterisation 71
3.4.2 Nanosecond Dynamics in BVO-148 and BPO-148 72
3.4.3 Picosecond Dynamics in BVO-148 and BPO-148 77

3.4.4 AIMD Simulations of Oxide Ion Dynamics in BVO-148 and BPO-148 . . . 81
3.5 Conclusions and Future Work . . . 91

4 Oxide Ion Conductivity in Complex Scheelite-Based Materials 94
4.1 Summary . . . 94
4.2 Introduction . . . 95
4.2.1 Aims of this Work . . . 100
4.3 Experimental Methods . . . 101
4.3.1 Synthesis . . . 101
4.3.2 Impedance Spectroscopy . . . 101
4.4 Results and Discussion . . . 102
4.4.1 Structural Characterisation . . . 102
4.4.2 Conductivity Measurements . . . 107
4.5 Conclusion and Future Work . . . 112

5 Hexagonal Perovskite Oxide Ion Conductors: $Ba_3NbMoO_{8.5}$ and $Ba_7Nb_4MoO_{20}$ 114
5.1 Summary . . . 114
5.2 Introduction . . . 115
5.2.1 $Ba_3NbMoO_{8.5}$ . . . 117
5.2.2 $Ba_7Nb_4MoO_{20}$ . . . 120
5.2.3 Aims of this Work . . . 123
5.3 Experimental Methods . . . 123
5.3.1 Synthesis . . . 123
5.3.2 Impedance Spectroscopy . . . 124
5.3.3 Quasielastic Neutron Scattering (QENS) . . . 125
5.3.4 Computational Methods . . . 126
5.4 Results and Discussion . . . 127
5.4.1 Structural Characterisation . . . 127
5.4.2 Conductivity of $Ba_3NbMoO_{8.5}$ . . . 129
5.4.3 Nanosecond Dynamics in Hexagonal Perovskites . . . 131

5.4.4 Oxide Ion Dynamics in $Ba_7Nb_4MoO_{20}$ Investigated by AIMD . 136
5.5 Conclusions and Future Work 139

6 Ionic Diffusion in $CsBi_2Ti_2NbO_{10-\delta}$: A Dion-Jacobson Type Oxide Ion Conductor 141

6.1 Summary 141
6.2 Introduction 142
6.2.1 Aims of this Work 146
6.3 Computational Methods 146
6.4 Results and Discussion 147
6.4.1 Effect of the Initial Vacancy Distribution on Oxide Ion Dynamics in $CsBi_2Ti_2NbO_{10-\delta}$ 147
6.4.2 Oxide Ion Dynamics in $CsBi_2Ti_2NbO_{10-\delta}$ Investigated by Multiple Temperature AIMD 149
6.5 Conclusion and Future Work 154

7 Overall Conclusions and Future Work 156

8 Bibliography 160

A Publications 185

List of Abbreviations

AIMD	Ab Initio Molecular Dynamics
BPO-148	$Bi_{0.852}P_{0.148}O_{1.648}$
BVO-087	$Bi_{0.913}V_{0.087}O_{1.587}$
BVO-148	$Bi_{0.852}V_{0.148}O_{1.648}$
CMD	Classical Molecular Dynamics
DFT	Density Functional Theory
EFWS	Elastic Fixed Window Scans
EISF	Elastic Incoherent Structure Factor
ESB	Er-stabilised Bi_2O_3
FWHM	Full Width Half Maximum
GDC	Gd-doped Ceria
GGA	Generalised Gradient Approximation
HWHM	Half Width Half Maximum
IFWS	Inelastic Fixed Window Scans
ILL	Institut Laue-Langevin
KMC	Kinetic Monte Carlo
LSCF	$La_{1-x}Sr_xCo_{1-y}Fe_yO_{3-\delta}$
LSGM	$La_{0.9}Sr_{0.9}Ga_{0.8}Mg_{0.2}O_{3-\delta}$
LSM	$La_{1-x}Sr_xMnO_{3-\delta}$

MD	Molecular Dynamics
MLMD	Machine Learning Molecular Dynamics
MSD	Mean Square Displacement
NEB	Nudged Elastic Band
NMR	Muclear Magnetic Resonance
PAW	Projector Augmented Wave
PBE	Perdue Burke Ernzerhof
PXRD	Powder X-Ray Diffraction
QENS	Quasielastic Neutron Scattering
SDC	Sm-doped Ceria
SOFC	Solid Oxide Fuel Cell
VASP	Vienna Ab Initio Simulation Package
YSZ	Y-stabilised zirconia

CHAPTER 1

Introduction

1.1 Fuel Cells

Fuel cells allow the conversion of chemical energy into electrical energy and heat via an electrochemical reaction between an oxidant and fuel gas. The absence of an intermediate combustion step in this conversion means that fuel cells are more environmentally friendly and efficient than conventional combustion engines. The choice of ion conducting electrolyte determines the operating temperature as well as the type of fuel gas required. The six main fuel cell types are the molten carbonate fuel cell, alkaline fuel cell, proton exchange membrane fuel cell, phosphoric acid fuel cell, direct methanol fuel cell, and the solid oxide fuel cell (SOFC).[1]

Figure 1.1 shows a schematic diagram of a SOFC in its simplest configuration, comprising of two electrodes, an anode and a cathode, separated by an electrolyte. Hydrogen, carbon monoxide and light hydrocarbons like methane are commonly used as fuel gas, which is oxidised at the anode. During this process, electrons are released, which migrate to the cathode via the external circuit and thus generate electricity. At the cathode, these electrons reduce the applied oxygen. The oxide ions then move through the ion conducting electrolyte and react with the fuel, completing

the cycle and generating heat as well as water, carbon dioxide or other emissions depending on the fuel gas used. The reaction of oxide ions with fuel results in an oxygen concentration gradient across the electrolyte that attracts oxide ions from the cathode. In SOFCs, the ceramic electrolytes traditionally are oxide ion conducting metal oxides, though in recent years proton as well as mixed oxide ion and proton conducting metal oxides have become areas of interest for use in SOFCs.[2–4]

Y-stabilised ZrO_2 (YSZ) has been the most commonly used electrolyte for high temperature oxide ion conducting fuel cells, together with $La_{1-x}Sr_xMnO_{3-\delta}$ (LSM) or $La_{1-x}Sr_xCo_{1-y}Fe_yO_{3-\delta}$ (LSCF) as cathode and Ni/YSZ as anode.[5–7] A recent review article published in 2021[8] highlighted that YSZ is still widely used as electrolyte in SOFCs commercialised for various applications.

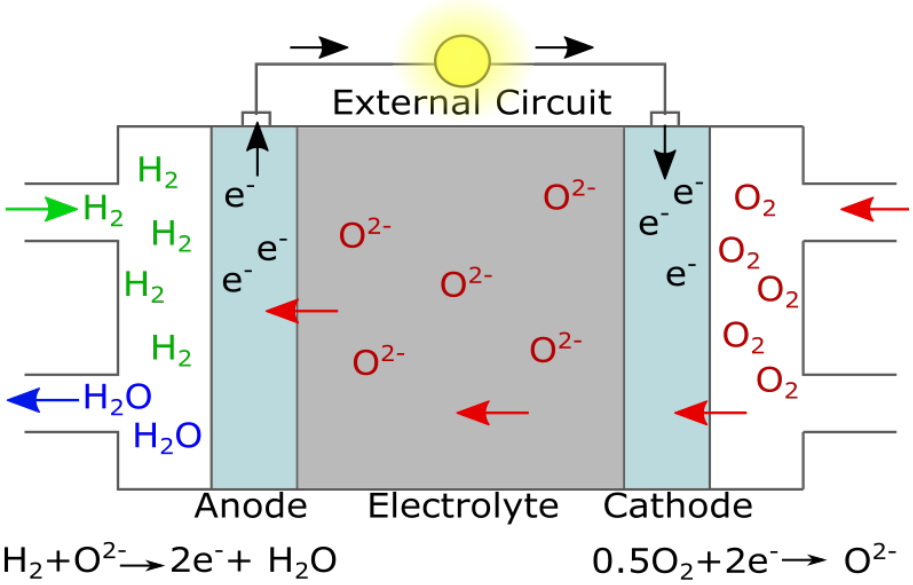

Figure 1.1: Schematic diagram of a solid oxide ion fuel cell.

Both anode and cathode need to be mixed ionic and electronic conductors (MIECs). Additionally, high catalytic activity towards the oxidation of fuel gas and fine scale porosity which creates a high number of tripel-phase boundaries are important properties of the anode. Ni-based cermets are the most commonly used anode materials in SOFCs due to the favourable catalytic activity of Ni metal for hydrogen oxidation, and the ease of production. However, the Ni/YSZ anode is prone to coking and sulfur poisoning, inherent drawbacks which have led to an interest

in finding alternative materials for SOFC anodes. Perovskite-based materials are of particular interest, and several perovskite materials like strontium-doped lanthanum chromite and lanthanum strontium titanate have been proposed as an alternative to the Ni/YSZ anode.[8] A crucial property of the cathode is a high catalytic activity for the oxygen reduction reaction. Most promising cathode materials are also based on the perovskite structure, and because the electrochemical activity of LSM decreases below 800 °C, finding alternative cathode materials is important. Perovskites containing cobalt,for example LSCF, BSCF ($Ba_{1-x}Sr_xCo_yFe_{1-y}O_{3-\delta}$) and LSC ($La_{1-x}Sr_xCoO_{3-\delta}$) are of particular interest.[8] More information on potential cathode and anode materials can be found in references.[8–10]

Solid oxide cells can operate in either a fuel cell mode, generating electricity using a fuel gas, or in electrolysis mode, which converts electricity to chemical energy through the electrolysis of water, carbon dioxide, or both. This reaction produces oxygen, hydrogen gas and/or carbon monoxide, which can be used as syngas (H_2+CO) in large scale organic synthesis, or stored and used as fuel. The same cell can operate in either mode, making it a promising concept for energy storage while also helping to manage the mismatch of electricity supply and demand from renewable energies like wind or solar energy.[11–13]

Compared to other kinds of fuel cells, SOFCs require the highest operating temperature. The commonly used electrolyte YSZ for example needs temperatures of above 700 °C so that the flow of oxide ions is not substantially restricted by the internal resistance of the electrolyte. This high operating temperature has the advantage that various different fuel gases can be utilised, which makes SOFCs the most versatile fuel cells currently used. Moreover, exploitation of the heat by-product in the form of co-generation of electricity and syn-gas and combined cycle applications increases the efficiency of a SOFC from around 40 % up to 90 %.[8,14] Furthermore, the high operating temperatures mean that any carbon monoxide produced during operation is converted to carbon dioxide, and the overall emissions of carbon dioxides and other pollutants are significantly lower than from traditional power plants or combustion engines.[14]

At present, SOFCs are mainly used in large-scale industrial and power generation

applications such as auxiliary power units due to their long start up times. However, advances in solid oxide fuel cell technology could lead to their use in vehicles where SOFCs could replace the combustion engine and also as a power source in portable and stationary applications. The stack size of SOFCs can easily be adjusted using interconnects which provide electronic contacts and gas channels between separate cells. This modularity means that the required power output can easily be achieved, making them a popular choice in various different applications.[8,15,16]

1.1.1 SOFC Electrolytes

The electrolyte is a key component in SOFCs. Aside from thermal and chemical stability and compatibility with the electrodes, a negligible electronic conductivity to avoid electronic leakage - the conduction of electrons through the electrolyte instead of the external circuit - is a key requirement of any potential electrolyte material. The most important property, however, is the ionic conductivity (σ).

For YSZ, temperatures of above 700 °C are needed to reach a conductivity of above 10^{-2} S cm^{-1}, a commonly accepted threshold determined by Steele and Heinzel[17] by assuming that the contribution of the electrolyte to the total cell area specific resistance (ASR) should not be more than 0.15 Ω cm^2 in order to ensure adequate cell performance. Considering that 15 μm is the thinnest electrolyte layer that can be produced reliably using low cost processes, and σ = thickness / ASR, 10^{-2} S cm^{-1} is the ionic conductivity needed to achieve the target ASR.

On one hand, this high operating temperature means that hydrogen, hydrocarbons and even unrefined natural gas can be used as fuel, making SOFCs a very versatile energy source. Additionally, it makes the fuel cell less prone to carbon monoxide poisoning and increases the tolerance to fuel impurities and changes in fuel composition, all of which pose problems for other types of fuel cells.[8,14] However, this high temperature also results in significant disadvantages. Firstly, it is prohibitively high for non-industrial, small scale applications, e.g. in cars, and results in long start-up times. It also means that high temperature alloys and ceramics are required, and it decreases the lifetime of the cell, further limiting the use

of SOFCs. Lowering the operating temperature to an intermediate range (400 - 600 °C) would significantly relax the requirements of the separate components, making it easier and cheaper to produce and also increasing the lifetime, while still allowing fuel flexibility. This is therefore an important area in current research.[15,16,18]

Limitations of Current Electrolyte Materials

As mentioned above, YSZ, which adopts the fluorite structure, is commonly used as an electrolyte in SOFCs. At intermediate temperatures, high ionic conductivity and hence high power output is only ensured if the thickness of the YSZ electrolyte layer is reduced, which is constrained by industrial feasibility. Therefore, if cheap, conventional manufacturing methods are used, the extent to which electrolytes based on YSZ can be enhanced is limited.[8,17]

Gd- or Sm-doped ceria (GDC, SDC) also crystallise in the fluorite structure and show a high ionic conductivity of 10^{-2} S cm^{-1} at 500 °C, significantly higher than the conductivity of YSZ at that temperature. However, they require high sintering temperatures of about 1400 °C for densification in order to avoid leakage of gas across the electrolyte which can lead to damages of the microstructure, and it is also a high cost process. Additionally, doped ceria compounds tend to be unstable in the reducing anode environment, resulting in a reduction of Ce^{4+} to Ce^{3+} and leading to unfavourable electronic conductivity.[6,8,19]

To prevent this reduction, doped-ceria based materials are often combined with more stable electrolytes like YSZ, creating a bilayer. It is important to ensure the chemical and physical compatibility of the chosen materials. Hence, interdiffusion between the layers should be minimal, while the agreement of the thermal expansion coefficient must be good to avoid cracking. Combining two compatible materials can help address disadvantages of otherwise promising ionic conductors, and many of these bilayer electrolytes have been tested.[6,20] Bilayer electrolytes are also relevant for doped Bi_2O_3 oxide ion conductors, a promising class of electrolyte which will be discussed in detail in chapter 3. As Bi^{3+} is prone to reduce to Bi metal at the low oxygen partial pressure environment at the anode side, Bi-containing electrolytes have to be separated from the electrode using a bilayer. The erbium-stabilised

Bi_2O_3 (ESB) conductor has been successfully combined with YSZ, creating a bilayer electrolyte which, combined with a Ni/YSZ anode and a LSM/ESB cathode, showed a 2.4 times increase in power density compared to SOFCs with a YSZ single electrolyte.[21] Bi_2O_3-based ionic conductors can also be combined with doped ceria, creating a bilayer consisting of two excellent low temperature ionic conductors. In this layout, the ceria compound is used near the anode, preventing the decomposition of the Bi_2O_3-based electrolyte, while the partial electronic conduction resulting from the reduction of the ceria layer is blocked by the Bi_2O_3 layer, precluding a short circuiting of the cell.[20] Various cells based on this configuration have been developed, for example using a GDC/ESB electrolyte[22] as well as a SDC/Y-Bi_2O_3 based electrolyte.[23]

The perovskite-type material $La_{0.9}Sr_{0.1}Ga_{0.8}Mg_{0.2}O_{3-\delta}$ (LSGM) has been suggested as alternative electrolyte material at intermediate temperatures due to its high ionic conductivity of 0.075 S cm^{-1} at 800 °C,[24] stability in both anode and cathode environments, low electronic conductivity, and stable performance over a long period of operation. However, inherent drawbacks like high material cost, poor sinterability, loss of Ga oxide at high temperatures and some reactivity towards common anode and cathode materials limit its use.[8,18,25]

The best oxide ion conductor currently known, δ-Bi_2O_3 and others closely related to it, are discussed in detail in the introduction to chapter 3, the oxide ion conductivity of scheelite-type materials is discussed in chapter 4, hexagonal perovskites in chapter 5, and the ionic conductivity recently discovered in the Dion-Jacobson phase in chapter 6. Other potential electrolyte materials have been reported, for example apatite-type materials,[26–28] brownmillerite materials[29–32] and melilite materials.[33–35] Comprehensive reviews of well-established and new oxide ion conductors are available elsewhere.[2,6,36–39]

Despite recent advances, the ionic conductivity of the electrolyte remains a limiting factor for commercial application. In order to develop new, improved oxide ion conductors, a detailed understanding of the relationship between structural features, ionic conductivity, and the underlying oxide ion dynamics is necessary. Impedance spectroscopy is commonly used to measure the macroscopic conductivity, and a de-

tailed analysis and fitting of the obtained results can provide insight into the specific electrochemical process taking place in SOFCs. It has for example been used to investigate the grain boundary effect in LSGM,[40] demonstrate that grain boundaries in the cathode/electrolyte interface facilitate the incorporation of oxide ions into a GDC electrolyte,[41] understand the degradation effects in supported electrolytes,[42] and compare the conductivities of GDC and YSZ in detail.[43] Comprehensive reviews covering studies of SOFC electrodes and electrolytes using impedance spectroscopy are available in the literature.[9,10,44–49] The underlying, microscopic dynamics and motions of oxide ions form the connection between the crystal structure, investigated by diffraction methods, and macroscopic ionic conductivity, and these dynamics are the focus of this thesis. Quasielastic neutron scattering and computer simulations have recently become attractive methods for the atomistic study of oxide ion dynamics.

1.2 Computational Techniques for Studying Dynamics

Computational simulations can be used to model ionic diffusion, allowing detailed, atomic-scale insights into oxide ion migration which can not be obtained from experimental methods alone. For example, it can provide valuable information on the oxide ion conduction pathways, and can help differentiate between the various mechanisms for oxide ion conduction which in general is a result of defects in the crystal structure i.e. interstitial oxide ions or oxide ion vacancies. While there are three well-established, textbook mechanisms for oxide ion diffusion (figure 1.2) new oxide ion conductors, for example $Bi_{0.852}V_{0.148}O_{1.648}$ and $Bi_{0.852}P_{0.148}O_{1.648}$ which will be discussed in detail in chapter 4, often have more complex conductivity mechanisms.

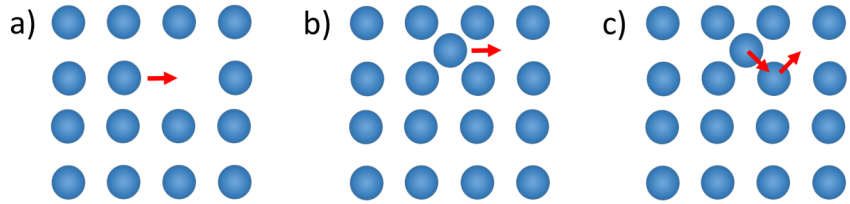

Figure 1.2: Schematic diagram of the vacancy (a), interstitial (b), and interstitialcy (c) mechanisms.

The vacancy mechanism, shown in figure 1.2a, describes the movement of an ion to an adjacent vacancy, creating a new vacancy at the original position of the ion into which a different O^{2-} can move. This mechanism is very common, and responsible for oxide ion conductivity in many currently used SOFC materials like fluorite-type structures, e.g. Y-doped zirconia (YSZ) and Gd-doped ceria (GDC). The interstitial mechanism describes the movement of an oxide ion from an interstitial site in the lattice to a neighbouring interstitial site (figure 1.2b) and is seen for example in melilite[33,34] and apatite-type[50–52] materials. A third, less common mechanism, the interstitialcy mechanism, is shown in figure 1.2c and involves the displacement of an oxide ion from its normal lattice site by an interstitial O^{2-}. The displaced oxide ion then migrates to a vacant interstitial site.[53] This mechanism has, for example, been observed in perovskite-related oxide ion conductors like the Ruddlesden-Popper phase[54,55] and hexagonal perovskites.[56,57] Technological advances in hardware as well as software have led to a more widespread use of various simulation techniques. Three techniques which are commonly used to study oxide ion dynamics are the nudged elastic band (NEB) method, the kinetic Monte Carlo (KMC) method, and molecular dynamics (MD).

1.2.1 Nudged Elastic Band (NEB) Method

One computationally inexpensive method to study transition rates as well as diffusive events is the nudged elastic band (NEB) method.[58] In ionic conductors, it can find the conduction pathway which corresponds to the most statistically relevant path between a given initial and final structure. This is done by finding the minimum energy path (MEP). Several images (i.e. crystal structures) of the system

between the initial and final structure are constructed, either prior to the simulation as user input if likely conduction pathways are know, or by interpolation. These images are then connected by an 'elastic band', a spring-like force interaction between each image. The MEP is found by minimising the entire system, i.e. relaxing the crystal structures and forces, keeping only the initial and final structures as well as the spacing between images fixed.

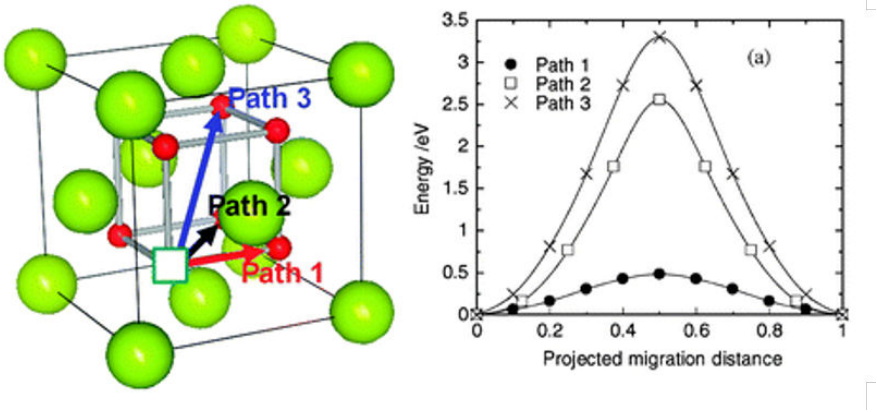

Figure 1.3: Fluorite structure of CeO_2, with Ce in green and O in red, showing the three possible oxide ion jumps (left) and their respective energy profiles determined from NEB calculations (right). (Adapted from 59).

Two different forces are considered: the 'elastic band' spring force and the potential force. The 'nudging' describes a force projection that ensures that the potential force does not change the spacing of images along the MEP, and that the spring force does not hinder convergence to the MEP. To achieve this, only the parallel component of the spring force and the perpendicular component of the potential force are considered. This method can be applied, using either empirical potentials or density functional theory (DFT) to minimise the individual images, on very big systems and slow dynamics.[58,60] An example of the output obtainable from a NEB calculation is shown on the right in figure 1.3. Each data point in figure 1.3 (right) represents an image between the initial and final structure, with the associated energy being obtained from minimising the image. This allows an energy pathway to be created, and from the maximum along that path the energy barrier for migration can be determined. The NEB method has been used to gain insight into migration pathways and energy barriers in various materials. For example, this method was

used by Nakayama et al.[59] to compare the three possible oxide ion jumps in the cubic CeO_2, shown in figure 1.3. The significantly larger activation barriers for migration obtained for path 2 and path 3 (2.5 and 3.2 eV) compared to path 1 (0.5 eV) suggest that long-range diffusion occurs predominantly via path 1. This agrees with the conduction pathway found for YSZ,[61] which also crystallises in the fluorite structure, as well as the conduction pathway suggested by neutron powder diffraction combined with the maximum entropy method.[62] Using path 1, the NEB method was further used to calculate the effect of various rare-earth dopants in CeO_2, showing that a smaller ionic radius results in a decrease in activation energy, but also increases the oxide ion vacancy trapping.[59] The NEB method has also been used to study the garnet-type oxide ion conductor $Ca_3Fe_2Ge_3O_{12}$, showing that interstitial oxide ions have a lower energy barrier for migration than oxide ion vacancies. This result indicates that ionic conductivity could potentially be improved by doping with appropriate cations to introduce more interstitial oxide ions.[63] A similar approach was used to demonstrate that the diffusion in the pyrochlore $Y_2Ti_2O_7$ is likely to be a two step cooperative mechanism due to the activation barrier for this path being low and in good agreement with experimentally determined activation energies.[64] Extensive NEB simulations were also carried out on the scheelite-type ionic conductor $LaNbO_4$, testing a total of 39 possible pathways between two adjacent interstitial sites.[65] Comparison of the obtained activation energies highlighted four possible migration pathways with similar energy barriers, and a combination of them is likely responsible for long-range ionic conduction. The activation barriers obtained from NEB in that study were used for kinetic Monte Carlo simulations.[66]

While these studies clearly demonstrate that the NEB method can provide insight into probable diffusion mechanisms, the requirement of knowing the end point biases the calculated pathway significantly.

1.2.2 Kinetic Monte Carlo (KMC) method

The kinetic Monte Carlo (KMC) method is a very fast method for simulating the dynamic evolution of a system by using a stochastic algorithm. The dynamics of a

system, for example the jump of an oxide ion to an adjacent vacancy site, is obtained by moving the entire system to the new state in which the oxide ion is in its new position. This is visualised schematically in figure 1.4 for an oxide ion or vacancy which can jump to three potential positions with different rate constants k_1, k_2, and k_3. Once this new state is reached, the path of the next jump is independent of the previous jump. Instead, it depends only on the rate constants, related to the respective activation energy E_a and simulation temperature T, of all possible paths from this state to the new state.[67,68]

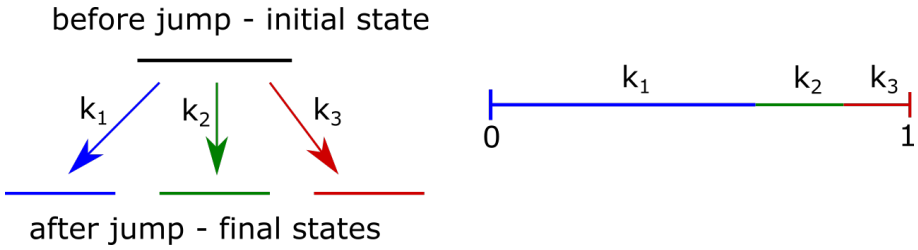

Figure 1.4: Schematic visualisation of the initial state and all paths to the possible final states (left) and selection procedure for the choice of reaction pathway (right).

To carry out a KMC simulation, a large supercell of the desired crystal structure is created, with dopants, vacancies or interstitial oxide ions randomly distributed. Then, to perform a single KMC step, a defect, e.g. a vacancy, and a direction are chosen at random. If a randomly generated number n between 0 and 1 (figure 1.4) is smaller than the Boltzmann probability ($n < e^{\frac{-E_a}{kT}}$), the jump of the chosen vacancy in the chosen direction takes place, otherwise a new combination of vacancy and direction is chosen. The result shows the statistically probable evolution of the supercell with time, and the ionic conductivity can be determined by following the motion of oxygen atoms, for example via their mean square displacement. The KMC method has been used less frequently in recent years than the NEB method to study oxide ion dynamics. Nevertheless, it has been successfully employed to understand oxide ion dynamics in various materials, for example doped CeO_2. Grope et al.[66] studied the relevance of different interactions in doped ceria to determine the origin of the conductivity dependence on the dopant concentration. The activation energies associated with each jump, which must be known prior to the calculation,

were taken from the NEB study by Nakayama et al.[59] as discussed above. By including/excluding certain interactions in the KMC simulations, it was shown that repulsive interactions between vacancies, trapping of vacancies (the dopant has different effects on the activation energies (E_a) for the forward and backward jump), and jump blocking (the dopant affects the forward and backwards jump barrier equally) through an occupied site all are needed to reproduce the experimentally observed trend, highlighting their combined effect on ionic conductivity. A more recent study on doped CeO_2[69] investigated the effect of trapping and blocking in further detail. The results agree well with the previous study by Grope et al.,[66] and further highlight that the blocking effect, which determines the dopant fraction at the maximum ionic conductivity, is generally underrated in literature.[69] KMC simulations could also accurately reproduce the experimentally determined, ideal dopant concentration in YSZ of 7-8 mol %.[70] During this study,[70] a total of 2 000 000 jumps for twelve different initial vacancy distributions at seven temperatures and ten different Y-doping levels were simulated. This emphasises the comparatively low computational power required for KMC calculations, allowing very big systems to be simulated.

Theoretically, if every single escape pathway and its associated rate constants are known exactly, KMC can accurately predict the time-evolution of a system. However, this is not usually the case, and complex or unexpected reaction pathways which are not included in the list of possible pathways cannot happen during the KMC simulation. Moreover, if a pathway is particularly complex, it is difficult to incorporate even if it is known prior to the simulation.[67]

1.2.3 Molecular Dynamics

The third and most common method for simulating the evolution of a system with time is molecular dynamics (MD). It produces a dynamic trajectory of all atoms in a simulation box using Newton's second law, and allows studying time and temperature dependent phenomena, for example phonons, free energies, molecular vibrations and, most importantly for the work presented here, diffusion. While KMC is based

on the assumption that the evolution of a system in time is caused by occasional jumps, limited by an energy barrier, from one state to another, MD is based on simulating small time steps in the order of femtoseconds, including atomic vibrations, by propagating the classical equations of motion.

Classical MD (CMD) uses empirically established force fields to determine the force acting on the atoms,[71] while ab initio MD (AIMD) uses quantum mechanical methods to calculate the forces. The theory of MD and differences between classical and ab initio MD will be described in more detail in chapter 2. While classical MD methods are generally significantly faster, they require established force fields. For many new oxide ion conductors, force fields are not readily available and AIMD is commonly used. MD requires more computational power compared to NEB and KMC methods, AIMD even more so than classical MD, limiting the system size and total time that can be simulated. However, it does not require knowledge of the end point of a jump like the NEB method, nor does it require knowledge of all possible migration pathways and rate constants like KMC, making it a very powerful tool. Very recently a new type of molecular dynamics based on machine learning (MLMD) has shown promising potential in combining the accuracy of AIMD and the efficiency of CMD.[72] In this approach, several AIMD steps are performed at the start, creating a data set of structures and associated forces, stress tensors and energy. This data is used to generate a force field. Statistical methods are then applied to compute forces, energy as well as their associated uncertainties using the generated force field. If the uncertainties are deemed to be small enough, these parameters are used to advance the MD by a time step, essentially performing a "classical" MD step. If they are too big, a new ab initio step is performed and added to the data set.[72,73] MLMD has been successfully used to calculate the melting points of various metals[73] and simulate the phase transition of a hybrid perovskite with potential application in solar cells.[74] The implementation of this machine learning MD in simulation software packages is very recent (e.g. in VASP[75] it was implemented in 2022), and at the time of writing very few articles using this novel approach to study atomic diffusion have been published. Nevertheless, MLMD has demonstrated a high potential for the study of battery materials,[76] allowing, for example, the simulation of Na^+ diffusion

in the solid electrolyte Na_3PS_4, using a supercell containing 432 atoms for up to 1 ns.[77] It also aided in a systematic screening of Li^+ diffusivity in approximately 300 potential Li^+ conductors, the structures of which were retrieved from a database, allowing diffusion coefficients from the mean square displacements to be obtained.[78] Additionally, MLMD has been used to simulate Li^+ diffusion in $Li_7P_3S_{11}$[79] and could also efficiently simulate the grain boundary effect on the Li^+ diffusivity in $Li_7La_3Zr_2O_{12}$, speeding up the the simulation by a factor of 2000 compared to pure AIMD.[80] However, to the best of my knowledge MLMD has only been used once to study proton dynamics in the perovskite Y-doped $BaZrO_3$,[81] and no papers on oxide ion dynamics studied with MLMD have been published to date.

The ability of MD to simulate properties (e.g. mean square displacements, diffusion coefficients) which are directly related to those observable in neutron scattering experiments and the comparable time scale make it an especially useful method for the analysis of complex neutron scattering data.[82]

1.3 Combined QENS and AIMD Studies of Oxide Ion Diffusion

Quasielastic neutron scattering (QENS) provides insight into the dynamics of a system, generally on a pico- to nanosecond timescale. It has been used extensively to study diffusion of protons.[2,83–86] However, due to the small and purely coherent neutron scattering cross section of oxygen, measuring oxide ion dynamics is more difficult. This will be discussed in detail in chapter 2. Computational MD studies are highly complementary to QENS, and with the increase of computational power and neutron flux, MD simulations and QENS experiments have become a crucial part in understanding oxide ion diffusion in recent years. Since the focus of this thesis is AIMD and QENS, it will also be the focus of this introduction. This subsection aims to give a comprehensive overview of studies combining QENS and AIMD to understand oxide ion diffusion.

The most studied class of oxide ion conductors is δ-Bi_2O_3 and related materials.

One of these δ-Bi_2O_3 related phases is $Bi_{26}Mo_{10}O_{69}$, a pure oxide ion conductor crystallising in a triclinic phase at room temperature. On heating above 310 °C, it undergoes a reversible phase transition to a monoclinic phase, shown in figure 1.5, which is associated with an increase in ionic conductivity. Buttrey et al.[87] first suggested the presence of an interstitial, partially occupied oxygen site O19 (circled and highlighted in yellow in figure 1.5) which is not directly bonded to any Mo site.

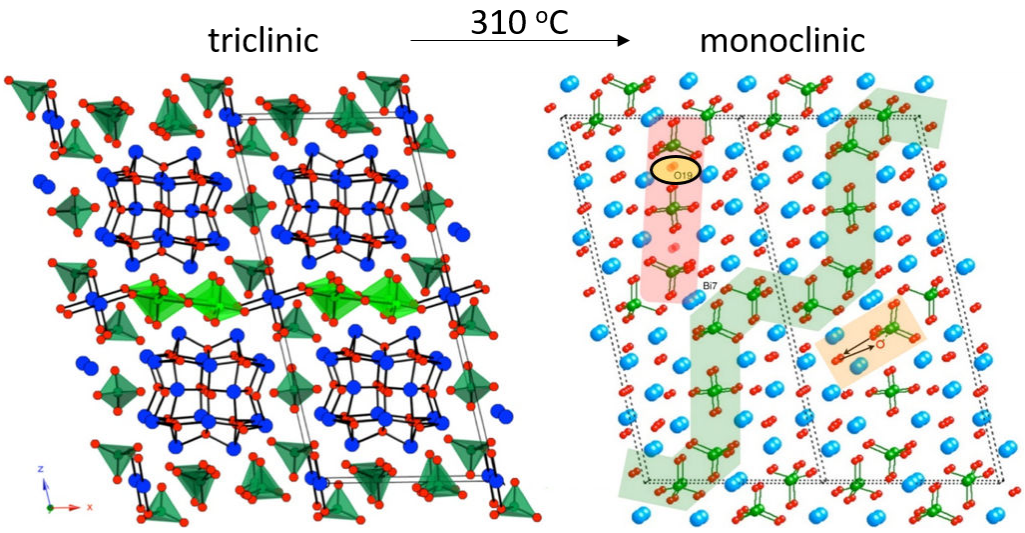

Figure 1.5: Triclinic and monoclinic structures of $Bi_{26}Mo_{10}O_{69}$, with the shaded areas highlighting three proposed diffusion pathways: red (into the page), green (in the plane of the page) and orange (into the page). Adapted from 88.

In 2012, Ling et al.[88] used a combination of QENS and AIMD to elucidate the oxide ion diffusion mechanism in this ionic conductor, considering three previously suggested pathways, highlighted in figure 1.5. AIMD simulations revealed that the interstitial oxygen atom O19, suggested to bridge between two MoO_4 tetrahedra, is unstable. Instead, this oxygen was found to move into the coordination sphere of one of the Mo atoms very rapidly, forming isolated MoO_4 and MoO_5 polyhedra, and not Mo_2O_9. Additionally, neutron scattering experiments showed the appearance of QENS at 400 °C, which is above the temperature of the triclinic to monoclinic phase transition. While the quality of the data did not allow a quantitative analysis of the QENS signal, the almost constant width of the broadening at increasing temperatures suggests low activation barriers of the observed motion, and the strong Q-dependence, so the dependence of the signal on the momentum transfer Q between

neutron and sample, of the linewidth is characteristic for a coherent scatterer like oxygen. This suggests that the QENS signal is caused by rotations of the MoO_x polyhedra, a conclusion which is supported by AIMD simulations showing the MoO_x polyhedra rotating freely on a picosecond timescale. AIMD allowed the observation of a "zig-zag"-like oxide ion conduction pathway along δ-Bi_2O_3 like slabs, highlighted by arrows in the orange shaded area in figure 1.5, facilitated by the ability of Mo^{6+} to readily adopt variable coordination environments.

A study by Mashkina et al.[89] investigated oxide ion dynamics in the perovskite $SrTi_{0.2}Fe_{0.8}O_{3-\delta}$. To overcome the small and purely coherent neutron scattering cross section of oxygen, a theory was introduced which aimed to justify an incoherent approximation of the scattering: If the defects (i.e. vacancies) in the structure are randomly distributed, they can be seen as an isotope of oxygen with a scattering length $b = 0$. The presence of these "isotopes" introduces incoherent scattering. Hence, all QENS in this study is treated as incoherent scattering, allowing observation of two different localised dynamics.

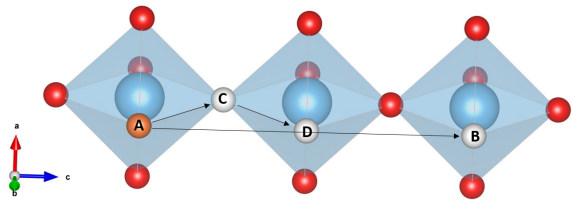

Figure 1.6: Model showing the two proposed localised motions,[89] where the substitution of Fe^{3+} for Ti^{4+} (blue atoms) introduces vacancies (white spheres), allowing an oxide ion (orange) to diffuse by performing 2-site jumps: A faster jump (A to B), and a slower jump (A to C to D to B). Other oxide ions are shown in red.

The substitution of Fe^{3+} for Ti^{4+} introduces oxide ion vacancies in the structure, and with higher doping the formation of chains of vacancies is possible, as shown in figure 1.6. The two different motions distinguished using QENS were assigned to a fast jump directly from A to B, and a series of slower jumps (A to C to D to B).[89] However, as the jump of a vacancy also means an oxide ion moves at the same time, the jumps are still strongly correlated, suggesting that an incoherent

treatment may not be justified. Therefore, further investigation into the incoherent theory of oxygen QENS developed in this paper is necessary, and AIMD simulations could potentially either refute or verify this theory.

A study combining neutron scattering with AIMD simulations investigated the difference in oxide ion mobility in $SrFeO_{2.5}$ and $CaFeO_{2.5}$, with the latter showing significantly slower oxide ion dynamics.[90] Both compounds adopt the brownmillerite structure, which can be described as an oxygen-deficient perovskite with ordered vacancies, leading to alternating layers of corner-sharing octahedra and tetrahedra, as shown in figure 1.7. The vacancies are located in the tetrahedral layers, which form one dimensional, parallel chains in the *ac* plane (figure 1.7b).

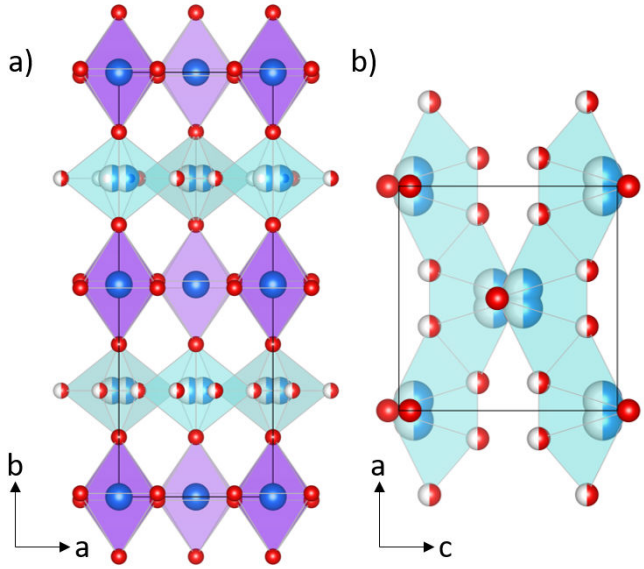

Figure 1.7: Structure of the brownmillerite $SrFeO_{2.5}$, highlighting the layers of octahedra in purple and the disordered layers of tetrahedra in blue. O and Fe atoms are shown in red and blue, respectively; Sr was omitted for clarity.

Simulations showed that, while the oxygen atoms arranged in a square in the FeO_6 octahedra are stable in both compounds, the apical oxygen atoms are readily displaced at room temperature in $SrFeO_{2.5}$, but not in $CaFeO_{2.5}$. This displacement can result in a jump of the apical oxide ion into a vacancy channel in the tetrahedral layer, and was also observed during the simulations for $SrFeO_{2.5}$. Additionally, both inelastic neutron scattering and AIMD revealed pronounced lattice dynamics of the

tetrahedral chains in $SrFeO_{2.5}$. This only appears at higher temperatures (1070 K) for $CaFeO_{2.5}$, a difference which is highlighted by the QENS data which shows fast dynamics in $SrFeO_{2.5}$, but no QENS broadening in $CaFeO_{2.5}$. This study suggests that oxide ion migration in brownmillerite-type materials is facilitated by structural flexibility of metal cations (i.e. FeO_4, FeO_5, and FeO_6 polyhedra), as well as lattice dynamics in the tetrahedral chains.[90]

The underlying, localised oxide ion dynamics in $SrFeO_{2.5}$ were further investigated by Auckett et al.[29] with the aim to better understand long-range diffusion. Neutron scattering experiments were performed at 600 and 750 °C, with QENS broadening only being apparent in the high temperature data. The linewidth of the Lorentzian used to fit this QENS signal suggests that the observed dynamics are on a timescale of approximately 4 ps. The signal was assumed to be incoherent, but no further explanation on how incoherent QENS can be the dominant contribution for a purely coherent scatterer like oxygen or whether this is based on the theory suggested by Mashkina et al.,[89] was provided. AIMD was used to simulate the incoherent neutron scattering function, the linewidth of which was in excellent agreement with the experimental data.[29] However, no information on the simulated coherent scattering function, for example the relative contributions of incoherent and coherent scattering or the linewidth obtained from the simulated coherent data, was given. Despite that, the agreement between experimental and simulated quasielastic linewidths is important to show the compatibility of these methods and highlights the potential of AIMD to aid in the analysis of experimental QENS data.

While these earlier studies were restricted to measuring localised dynamics because of instrument constraints as well as slow dynamics in the studied materials, QENS is particularly well suited for observing long-range diffusion. It can offer a unique insight into the diffusion mechanism by allowing extraction of jump lengths l, residence times τ, diffusion coefficients and activation energies. To obtain these parameters, a model is used to describe the Q-dependence of the Lorentzian linewidth, Γ, obtained from fitting, as will be discussed in detail in Chapter 2. For solid-state diffusion of incoherent scatterers, this can be described by the Chudley-Elliott model:[91]

$$\Gamma = \frac{1}{\tau} \times \left[1 - \frac{\sin(Ql)}{Ql}\right] \tag{1.1}$$

In oxide ion conductors, QENS was first used to observe long-range, translational diffusion in 2016 by Mamontov using δ-Bi_2O_3.[92] It was found that, as long as Bragg peaks were excluded from the fitted Q-range, the Chudley-Elliott model (equation 1.1), commonly used for incoherent scatterers, gave jump lengths comparable to the distance between nearest neighbour oxygen sites of 2.83 Å. This agrees well with the accepted oxide ion diffusion pathway for δ-Bi_2O_3 along $\langle 100 \rangle$, as shown in figure 1.8, with vacancies moving from one to an adjacent oxygen site via an octahedral hole.[38,93,94] Additionally, it is also consistent with the lowest energy pathway found by NEB in CeO_2 as discussed above, which also adopts a fluorite structure.

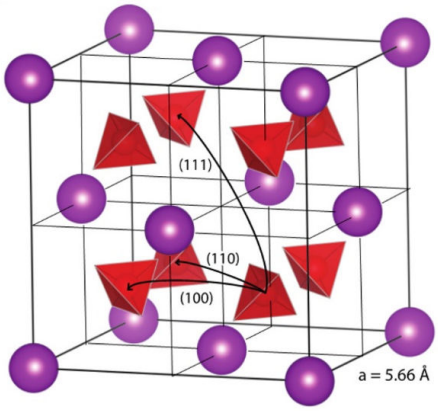

Figure 1.8: Fluorite structure of δ-Bi_2O_3, with Bi atoms shown in purple, oxygen atoms in red, and the red tetrahedra showing the disorder around oxygen position; the arrows show the three possible oxide ion jumps. Taken from 95.

The temperature dependence of the diffusion coefficient allows the activation energy of the process causing the broadening to be derived. For δ-Bi_2O_3, it was found to be approximately 0.47 eV. This is similar to the activation energy of approximately 0.4 eV found by impedance spectroscopy.[96] However, there were still some deficiencies, especially at the lowest Q values, when fitting the experimental data with the standard Chudley-Elliott model, and a study in 2017 by Wind et al.[95] further questioned whether the effects from coherent scattering are indeed negligible as assumed by Mamontov.[92] A first attempt to analyse the data using the standard,

incoherent Chudley-Elliott model did not reproduce the Q-dependence adequately, indicating that due to the coherent scattering nature of oxygen, the structure factor S(Q) needs to be taken into account.

$$\Gamma = \frac{1}{\tau S(Q)} \times \left[1 - \frac{sin(Ql)}{Ql}\right] \tag{1.2}$$

Therefore, a modified Chudley-Elliott model, given in equation 1.2, was proposed. This, however, requires knowledge of S(Q) in absolute units. Due to the fast, isotropic diffusion in δ-Bi_2O_3, S(Q) was assumed to approach 1 at the highest Q value measured, comparably to the behaviour of liquids. The jump length obtained from this coherent Chudley-Elliott model (equation 1.2) (3.33 Å) does not correspond to one specific oxygen site distance (i.e. along $\langle 100 \rangle$), but instead is the weighted average of all possible oxide ion jumps, including those in $\langle 110 \rangle$ and $\langle 111 \rangle$ directions, as shown in figure 1.8. Moreover, separation of the mean square displacements obtained from AIMD by direction shows no differences between $\langle 100 \rangle$, $\langle 110 \rangle$ and $\langle 111 \rangle$. Together with the results obtained using the coherent Chudley-Elliott model, this suggests isotropic, liquid-like diffusion of oxide ions in Bi_2O_3.[95]

To further test this coherent Chudley-Elliott model, Wind et al.[97] applied it to three cubic, transition metal doped bismuth oxides: $Bi_{22}W_5O_{48}$, $Bi_{22}Nb_5O_{48}$, and $Bi_{22}W_{2.5}Nb_{2.5}O_{48}$. These materials, while crystallising in ordered, complex superstructures, keep a δ-Bi_2O_3-like substructure. Similarly to the undoped δ-Bi_2O_3, the standard Chudley-Elliott model did not fit the oscillations of the Q-dependence of the Lorentzian linewidth well. Due to the presence of Bragg peaks, determination of the elastic structure factor in absolute units was not possible. Instead, it was again assumed to approach 1 just before the first Bragg peak, at the highest Q value measured. For all three materials, the extracted jump lengths were comparable (3.2 Å for $Bi_{22}W_5O_{48}$ and 3.0 Å for $Bi_{22}Nb_5O_{48}$ and $Bi_{22}W_{2.5}Nb_{2.5}O_{48}$) to that found for δ-Bi_2O_3. This suggests similar oxide ion diffusion mechanisms in all of these materials, which is not surprising considering the presence of a δ-Bi_2O_3-like substructure. AIMD simulations revealed little variation in the W-coordination number in $Bi_{22}W_5O_{48}$ as well as the presence of stable W_4O_{18} units which do not

contribute to long-range diffusion. The constraint of oxide ion diffusion to the δ-Bi_2O_3-like regions is the reason for the reduced average jump distance observed in the doped compounds. While the coherent Chudley-Elliott model (equation 1.2) describes long-range diffusion in three different, cubic materials well, it is important to keep in mind that they are based on the same structural motives, and with isotropic diffusion fast enough to be approximated as "liquid-like". In order to use this model to fit QENS spectra obtained from structurally more complex oxide ion conductors, knowledge of the structure factor, in absolute units, is necessary.

Another paper investigating the dynamics in δ-Bi_2O_3 as well as the Y-doped Bi_2O_3 compound $Bi_{0.7}Y_{0.3}O_3$ with QENS and AIMD was published in 2020.[98] Visualisation of separate oxide ion jumps obtained from AIMD trajectories indicate that diffusion is isotropic, in good agreement with the previous study on δ-Bi_2O_3. However, the activation energy obtained from simulated diffusion coefficients is 0.9 ± 0.1 eV, significantly higher than previously reported activation energy of 0.4 eV.[92,95,96] The activation energies for the Y-doped bismuth oxide determined in this work are 0.04 ± 0.01 eV below 900 K, and 0.6 ± 0.2 eV above that. No discussion on the large error or the disagreement with previous literature is provided. Additionally, since doping reduces the overall conductivity, it generally also results in higher activation energies compared to the undoped compound, a discrepancy which the authors did not comment on either. Fitting of the QENS data using the coherent Chudley-Elliott model (equation 1.2) was not successful. Instead, a theory similar to that proposed by Mashkina et al.[89] was introduced, suggesting that because of the high vacancy concentration in δ-Bi_2O_3 of 25 %, the oxygen atoms move independently enough to be described by the incoherent model. While the fit of data on δ-Bi_2O_3 at low Q using equation 1.1 is good, a separate model with different parameters was used to fit the high Q region.[98] However, as the Q-dependence of any particular Lorentzian linewidth is characteristic for that motion, using two sets of parameters to fit the same Q-range requires further justification.

While the observed long-range dynamics in δ-Bi_2O_3 take place on a picosecond timescale, QENS can also probe dynamics on a slower, nanosecond timescale. This was fist observed on $La_2Mo_2O_9$,[99] a material with an abrupt change in oxide ion

conductivity at about 580 °C due to an order-disorder transition to an on average cubic structure,[100] shown in figure 1.9.

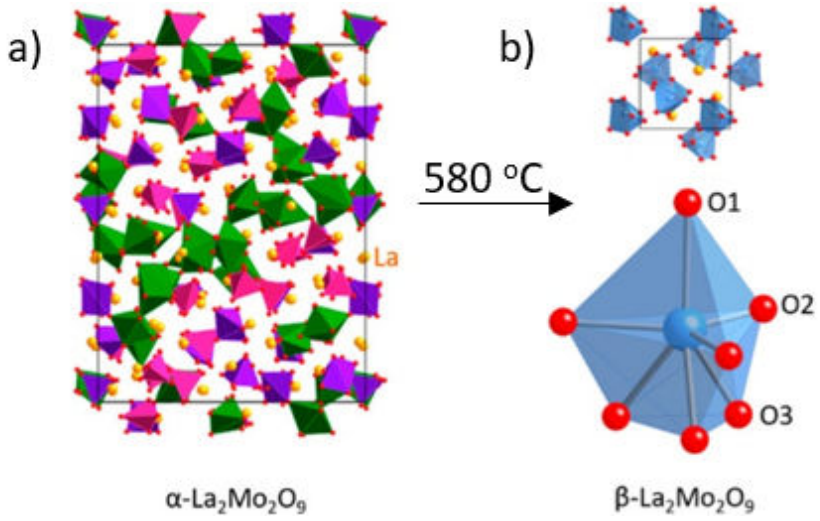

Figure 1.9: Structure of the (a) room temperature phase α-$La_2Mo_2O_9$ highlighting various MoO_x environments in pink, green, and purple polyhedra, and (b) high-temperature phase β-$La_2Mo_2O_9$ consisting of one unique Mo site (blue) and three unique O sites (red).[100,101] Taken from 99.

At temperatures above this phase transition a broadening of the elastic peak was observed,[99] and an activation energy for the long-range diffusion of 0.61 ± 0.05 eV could be extracted, which is in good agreement with previous data obtained using ^{18}O tracer diffusion,[102] but significantly lower than the activation energy of 1.2 eV obtained from impedance spectroscopy.[100] However, the good agreement between QENS and ^{18}O tracer diffusion, two methods which probe microscopic dynamics, suggests that this discrepancy can be explained by the dependence of impedance spectroscopy (measuring macroscopic diffusion) on the sample morphology, i.e. pellet density and grain boundaries. A similar effect was observed when comparing activation energies obtained using ^{17}O nuclear magnetic resonance (NMR) to impedance data on YSZ[103] and doped CeO_2,[104] as well as on other ionic conductors like Li^+.[105,106] To gain a more detailed insight into the diffusion mechanism in $La_2Mo_2O_9$, long (650 ps) AIMD simulations were performed,[99] and verified by comparing the simulated density-of-states (DOS) to that obtained from neutron scattering experiments. Mean square displacement (MSD) plots show no sign of plateauing, which is indicative of long-range oxide ion motion. This is in contrast to

a previous AIMD study on this materials[107] showing signs of saturation, but only a single unit cell and relatively short simulation times of < 30 ps were used. This contrast emphasises the importance of using big simulation boxes as well as sufficiently long simulation times to obtain reliable results from MD. Analysing the separate jumps occurring during the simulation[99] allowed for the long-range diffusion to be separated into two processes: Local movement of oxide ions to different positions on the same MoO_x polyhedra, and jumps between different MoO_x polyhedra, which are facilitated by the ability of Mo to adopt various coordination environments. Both of these processes occur on comparable time scales. Interestingly, the simulations also showed that only two out of the three distinct oxygen atoms in MoO_x polyhedra can directly move to adjacent polyhedra, while the third can only contribute to long-range diffusion by moving to a different oxygen position on the same MoO_x polyhedron first, a result which can only be obtained from simulations.

A detailed study by Peet et al.[108] used both QENS and AIMD to study oxide ion dynamics in the V-doped Bi_2O_3 compound $Bi_{0.913}V_{0.087}O_{1.587}$. QENS was successfully observed, and the Q-dependence could be fitted with the standard Chudley-Elliott model for jump diffusion (equation 1.1). Using a fixed jump length of 2.83 Å, the residence time was determined to be 1 ns. This suggests that the observed QENS signal corresponds to long-range diffusion on a nanosecond timescale. The coherent model (equation 1.2) and its potential use on this material was not discussed. The structure of $Bi_{0.913}V_{0.087}O_{1.587}$ is also δ-Bi_2O_3-like, and long-range diffusion is very fast, similar to the compounds modeled using the coherent model. However, the oscillating Q-dependence of the Lorentzian linewidth observed in δ-Bi_2O_3 and $Bi_{22}W_5O_{48}$ is not clearly apparent in $Bi_{0.913}V_{0.087}O_{1.587}$. One reason for this could be the presence of Bragg peaks across the measured Q-range. Nevertheless, the temperature dependence of the QENS broadening allowed a reasonable activation energy of 0.39 ± 0.04 eV to be obtained. This is smaller than the value found by impedance spectroscopy (0.68 eV[109]), but can be explained by QENS probing microscopic diffusion in contrast to impedance spectroscopy, as discussed above. While experimental data on a nanosecond timescale suggests the presence of a second, faster motion in $Bi_{0.913}V_{0.087}O_{1.587}$, no broadening could be observed on a picosecond timescale,

either because the rotational motions around the V-polyhedra do not occur on that timescale, or because the signal is simply too weak to be detected. Therefore, to gain insight into the picosecond dynamics, AIMD simulations were performed. The plateauing of the MSD plots of oxygen atoms in the V-O sublattice indicates that the picosecond dynamics suggested in the first data set are localised rotations of the VO_x polyhedra. Separating the oxygen atoms according to the sublattice they are part of at the start of the simulation allowed calculation of two activation energies from the MSD plots. For oxygen atoms in the Bi-O sublattice, this was found to be 0.38 ± 0.01 eV, in excellent agreement with that obtained from QENS, and for oxygen atoms in the V-O sublattice, the activation energy of 0.05 ± 0.01 eV agrees well with the small activation barrier expected for rotations.

A study by Fuller et al.[110] was the first example of observing dynamics on two different timescales in any oxide-ion conductor. QENS measurements were performed on the highly disordered perovskite-type compound $SrSc_{0.3}Zn_{0.2}Ga_{0.5}O_{2.4}$, and experimental data shows the increasing dynamics on a picosecond timescale between 800 and 1000 °C. However, the weak signal prevented quantitative analysis of the Q-dependence or the temperature dependence of the Lorentzian. Fixed window scans, which measure the elastic intensity ($\omega = 0$ μeV) and the inelastic intensity at a certain offset ($\omega = 2$ μeV), show the point at which dynamics enter the nanosecond time scale measured by the instrument (IN16b). The fixed window scans suggest the onset of oxide ion dynamics at 600 °C, but again the signal is too weak to obtain quantitative parameters from either the fixed window scans or the broadening of the elastic peak. This study highlights the possibilities QENS offers as well as the challenges in observing QENS on oxide ion conductors. No AIMD simulations were performed, which could potentially aid a more detailed analysis of the experimental data in this case.

1.4 Conclusion and Project Aims

This chapter provided a review of recent applications combining two very powerful techniques, AIMD and QENS, to study oxide ion diffusion and conduction pathways.

These techniques helped elucidate the oxide ion dynamics by highlighting the importance of certain structural motives in various oxide ion conductors. A combination of AIMD and QENS has also provided new insight into the oxide ion diffusion in the best oxide ion conductor currently known, δ-Bi_2O_3, showing that a combination of AIMD and QENS can provide key information which cannot be readily obtained using other methods. As this review shows, the combined application of QENS and AIMD is a relatively new development in the research concerning oxide ion diffusion. A detailed understanding of oxide ion dynamics can allow improvement of known oxide ion conductors, and also help identifying new structures with promising oxide ion conduction properties.

Because of that, several crystal structures with high oxide ion conductivity, a detailed literature review of which is provided in the relevant chapters, were investigated using various methods, and the obtained results are presented here:

- Chapter 2 provides an introduction to the theory behind the experimental and computational methods used throughout this work, including synthesis methods, powder X-ray diffraction, neutron scattering, impedance spectroscopy, and molecular dynamics simulations.

- Chapter 3 focuses on doped δ-Bi_2O_3 oxide ion conductors. A combination of AIMD simulations and QENS experiments on the isostructural materials $Bi_{0.852}V_{0.148}O_{1.648}$ and $Bi_{0.852}P_{0.148}O_{1.648}$ were used to study the effect of the dopant on local and long-range dynamics in these excellent oxide ion conductors.

- Chapter 4 presents a systematic investigation of the oxide ion conductivity in a series of scheelite-type conductors, $Bi_3(BO_4)(MoO_4)_2$ (B=Fe, Ga, In, Sc), for the first time. Samples were synthesised and characterised by powder X-ray diffraction and impedance spectroscopy. Structural considerations and bond valence sum calculations were used to determine the coordination environment around In^{3+}, and donor doping was used to investigate whether additional interstitial oxide ions can be introduced in these scheelite-type materials.

- Chapter 5 discusses QENS studies of a new family of oxide ion conductors. Two hexagonal perovskites, $Ba_3NbMoO_{8.5}$ and $Ba_7Nb_4MoO_{20}$, were synthesised and, after initial characterisation using powder X-ray diffraction, used for QENS experiments. For $Ba_7Nb_4MoO_{20}$, a mixed oxide ion and proton conductor, a separation of oxide ion and proton dynamics was attempted by performing experiments under vacuum as well as humid N_2, and AIMD provided a more in-depth insight into oxide ion dynamics in this material.

- Chapter 6 centres around the material $CsBi_2Ti_2NbO_{10-\delta}$, a novel oxide ion conductor which crystallises in the Dion-Jacobson phase. The oxide ion dynamics are investigated using AIMD, as no prior studies of local and long-range oxide ion dynamics using computational simulations have been reported for this structural family.

CHAPTER 2

Methodology

The following chapter provides a general introduction to the experimental methods and computational simulation techniques used during this project. Experimental details of individual compounds are outlined in the corresponding experimental sections.

2.1 Synthetic Methods

2.1.1 Solid State Synthesis

Solid state synthesis, also known as the ceramic method, is the most straightforward and therefore also the most commonly used method for synthesising ceramics. It finds application in small scale lab settings as well as in industry, and can be used to synthesise a large variety of materials.[111] Generally, in solid state synthesis, stoichiometric amounts of reagents, often metal oxides, are thoroughly mixed and heated at high temperatures for several hours.

However, a reaction between solids is only possible at the interface of grains that are in close proximity. If the wanted reaction is $AO_x + BO_y \rightarrow ABO_{x+y}$, the

initial reaction only occurs at the interfaces of touching AO_x and BO_y grains. This leads to an ABO_{x+y} phase forming and separating AO_x from BO_y: AO_x – ABO_{x+y} – BO_y. Further reaction happens by any given atom A displacing one of the A atoms in ABO_{x+y}. This leads to a hopping motion through ABO_{x+y} until the final displaced atom A reacts with BO_y. A more simplistic picture is that once the phase boundary is established, the reacting atoms A and B must diffuse through the phase ABO_{x+y} to reach the opposite phase boundary in order to react.[112] Therefore, solid state synthesis is a process limited by the diffusion of ions through a solid. High temperatures of above 500 °C and long reaction times (≈ 12-48 h) are consequently often required for a single phase to be obtained.

Since a reaction is only possible at the interface, the degree of mixing of the reagents limits the overall speed of the reaction. This is why the starting materials are ground up into a fine powder, either by hand using pestles and mortars or using a ball milling machine, in order to maximize the surface area. The contact areas between the reagents can be further increased by pressing the powder into pellets. In addition to that, it is common practice to remove the sample repeatedly during the heating process and regrind it, creating new interfaces and thereby speeding up the synthesis.[111,112]

The ceramic methods favours the thermodynamically most stable phase, which may not be the desired product. It is also important to use accurate amounts of high-purity reagents since the solid product generally cannot be purified. Additionally, the high temperatures and long sintering times make it an expensive method, and the obtained products may be inhomogeneous.

2.1.2 Precursor and Coprecipitation Synthesis

Precursor and coprecipitation methods are "wet" methods and typically use carbonates and nitrates which decompose on heating instead of oxides as reagents. This creates a fine, very homogeneous powder which is generally more reactive than the respective oxides.[111]

Coprecipitation is the process of mixing completely dissolved soluble salts of

the required metal ions in the correct stoichiometry, after which precipitation is induced. This is commonly done by changing the pH of the solution, making use of the better solubility of metal ions in acids compared to bases. The precipitate is generally a very fine powder consisting of a completely homogeneous mixture of the starting materials. The precursor method is similar to the coprecipitation method. In contrast to the latter, a homogeneous powder is obtained by mixing salts of the required metal ions in the correct stoichiometry and heating this mixture until it decomposes. The powders obtained during this process are generally finer and more reactive compared to those based on oxides.

The fine powders created using these "wet" methods have an increased number of interfaces between grains compared to the solid-state method. This decreases the temperature required for product formation significantly, and also reduces the likelihood of impurity formation.[111]

2.2 Powder X-Ray Diffraction

Powder X-ray diffraction (PXRD) is an analytical technique used for structural analysis and identification of crystalline materials. It provides information about atomic arrangements as well as the size and symmetry of the unit cell. In addition to that it can probe disorder in solids, allow a quantitative analysis of mixtures, and help obtain information about the microstructure (size and strain) of solid materials. Moreover, non-ambient PXRD can be used to investigate phase transitions, the stability of materials at different temperatures and in various environments as well as thermal expansion.[113] Advanced applications like parametric refinements and symmetry distortion modes analysis can give information ranging from kinetics and activation energies for processes to group-theoretical descriptions and enhanced understanding of phase transitions.[114–116] In this section, the theory behind PXRD is described, and the instruments and analysis software used are discussed.

2.2.1 Fundamentals of Diffraction

Diffraction describes the bending of waves around obstacles or small slits. When a wave encounters a slit with a width comparable to its wavelength, it behaves as though the gap is a single point source, as shown in figure 2.1. If two slits are present, the wave is diffracted by both, giving the impression that the wave originates at each slit. The waves propagating from different slits either interfere constructively or destructively with each other, depending on whether they are in phase or out of phase.[117]

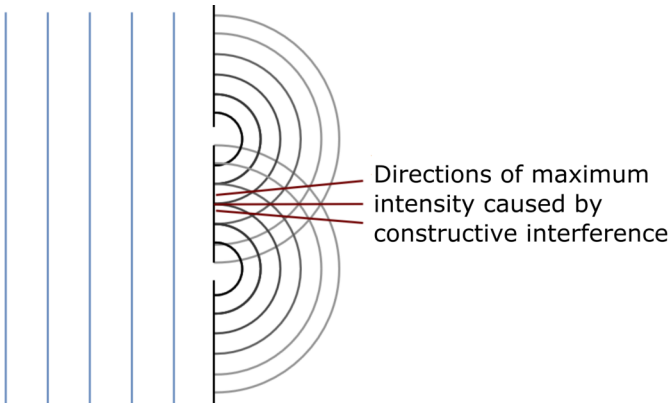

Figure 2.1: Diffraction of a wave through two slits and interference of the diffracted waves.

Incident X-rays result in the oscillation of the electron clouds of all atoms in the material, causing emission of a spherical wave from each atom. The wavelength of X-rays can range from 0.1 to 100 Å, and therefore their wavelengths can be chosen to be comparable to interatomic distances. Because of that, as well as the periodic arrangement of atoms in crystals, diffraction occurs. In certain directions, constructive interference is possible, giving rise to a diffraction pattern.[118]

To determine the conditions required for constructive interference, it is useful to treat diffraction not as scattering of X-rays by electrons, but as mirror reflections off parallel planes of atoms which are described by their Miller indices, *hkl*. The constant spacing between two planes is denoted d_{hkl}, shown in figure 2.2.

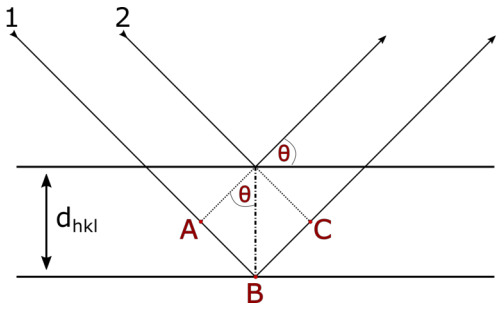

Figure 2.2: Conventional derivation of Bragg's law - a schematic diagram of two lattice plane reflecting incoming X-rays.

One can then consider two parallel rays of the same wavefront hitting two adjacent, also parallel planes of atoms. One of the rays is reflected by the first plane, while the second ray hits the adjacent plane and is reflected there. This means that the difference in path length between ray 1 and ray 2, shown in figure 2.2, is AB, and similarly the reflected rays have a path length difference of BC.[118] Therefore, if the incident angle is θ:

$$AB + BC = 2d_{hkl}sin\theta \tag{2.1}$$

Constructive interference can only occur if the path length difference (AB+BC) is an integer number of wavelength, $n\lambda$. Hence, a reflection is observed when the incident angle θ satisfies equation 2.2, Bragg's law:

$$n\lambda = 2d_{hkl}sin\theta \tag{2.2}$$

Due to the random orientations of the separate crystallites constituting a powder sample, each set of hkl planes reflect incoming X-rays in all directions on a cone of angle 2θ relative to the incident beam. A powder X-ray diffraction pattern is a one dimensional slice of this cone, and therefore the intensities of the diffracted X-rays are measured as a function of angle.

Since the incident wavelength λ and angle θ in a diffraction experiment are generally known, Bragg's law (equation 2.2) can be used to determine d_{hkl}, thereby relating the positions of peaks in a diffraction pattern to the spacing between adjacent planes of atoms. This spacing only depends on the unit cell parameters a,

b, c, α, β, and γ, which can be extracted once d_{hkl} has been determined for each reflection. For an orthorhombic system for example, equation 2.3 can be used to link the cell parameters to the Miller indices h, k, and l.[117]

$$\frac{1}{d_{hkl}^2} = \frac{h^2}{a^2} + \frac{k^2}{b^2} + \frac{l^2}{c^2} \tag{2.3}$$

While the peak position provides information about the unit cell parameters, the peak intensity I_{hkl} provides information about the electron density, and hence the atom type and its position in the unit cell. Since X-rays interact with the electron clouds of atoms, heavier atoms scatter X-rays more strongly than lighter atoms. The scattering power of individual atoms is described by the atomic scattering factor f_j, and it increases systematically with atomic number Z. However, due to interference between X-rays scattered from different electrons of one atom (e.g. valence vs. core electrons), the atomic scattering factor decreases with increasing angle 2θ. At $\theta = 0$, the scattering factor is proportional to Z.[117,118] The peak intensities, I_{hkl}, are proportional to the square of the modulus of the structure factor F_{hkl}, which describes the overall amplitude of the diffracted wave and depends on the atomic scattering factors f_j and coordinates x_j, y_j, and z_j of each atom j in the crystal structure:

$$F_{hkl} = \sum_{1}^{j} f_j \exp^{2\pi i(hx_j + ky_j + lz_j)} \tag{2.4}$$

The constant relating F_{hkl} to the peak intensities I_{hkl} contains site occupancies, effects of absorption, etc. It also accounts for thermal vibrations in the form of the Debye-Waller factor. This important factor describes the attenuation of scattering due to thermal motions, which cause atoms to oscillate about their ideal lattice site. Constructive interference of scattered X-rays is only possible when the atom sits at its nominal lattice site. Therefore, increasing temperature causes a loss of intensity of all Bragg peaks to the background as the Debye-Waller factor increases. Additionally, the Debye-Waller factor also increases at larger 2θ values.

Because of X-rays being scattered by electrons and the atomic scattering factor increasing systematically with atomic number Z, the sensitivity of X-ray diffraction

towards lighter atoms like oxygen or hydrogen in a compound consisting mainly of comparably heavy metal atoms is poor.[118]

2.2.2 Rietveld and Pawley Refinements

The Rietveld method[119] is commonly used for the analysis of PXRD data. A complete structural model (obtained from structure solution or from a database), containing unit cell parameters, space group, as well as types, fractional atomic coordinates and fractional occupancies of the atoms in the asymmetric unit is generally required. However in certain types of analyses, partial structural models can be used to locate missing atoms by difference Fourier analysis. Based on this model, a diffraction pattern is calculated. Various global and phase-specific variables (typically a zero point, pseudo-Voigt peak shape function parameters, a Chebyshev polynomial for the background, instrumental parameters, unit cell parameters, and isotropic temperature factors) are refined and adjusted using an iterative least square fit approach which minimises the sum (S) of the squared differences of observed (y_{obs}) and calculated (y_{calc}) intensities at the i^{th} point in the diffraction pattern:

$$S = \sum_i w_i (y_{i(obs)} - y_{i(calc)})^2 \tag{2.5}$$

The weighting factor w_i is equal to $\frac{1}{\sigma_i^2}$ where σ_i is the experimental uncertainty of $y_{i(obs)}$. The quality of the fit is then indicated by the weighted profile residual factor R_{wp}, which normalises S by the total measured intensity:

$$R_{wp} = \left(\frac{S}{\sum w_i (y_{i(obs)})^2} \right)^{\frac{1}{2}} \tag{2.6}$$

Rietveld refinements allow detailed analysis of a powder diffraction pattern by providing information on the unit cell parameters as well as atomic displacement parameters, fractional occupancies, and positional parameters of all individual atoms present. When no full structural model is available but the space group and unit cell parameters of a compound are known, a Pawley refinement[120] can be used instead to refine the unit cell parameters. It is also a least square minimisation

method, but in contrast to the Rietveld method, the peak intensities and therefore the contents of the unit cell are not considered, resulting in a significantly less detailed analysis. Only unit cell parameters, space group, a Chebyshev polynomial for the background, and pseudo-Voigt peak shape function parameters are adjusted to minimise the difference between the observed and calculated data.

2.2.3 Diffraction Instruments and Software

In lab diffractometers, X-ray radiation is generated in an X-ray tube. In this evacuated chamber, a tungsten filament is heated, resulting in the emission of electrons. High voltage is used to accelerate these electrons towards a metal target, usually copper, which ionises a core electron in the metal. This causes an electron in an outer shell to relax rapidly, emitting a photon at a specific wavelength. These photons are then used as a source of monochromatic radiation for X-ray diffraction experiments. The two diffractometers used during this project were both Bruker D8 Advance powder diffractometers operating at 40 kV and 40 mA, and using a Lynx-Eye detector. Copper is used as metal target, generating CuK_{α} ($2p \rightarrow 1s$) and CuK_{β} ($3p \rightarrow 1s$) radiation, and a nickel filter removes the CuK_{β} X-rays. Because of two possible spin states of the 2p electrons in Cu, the CuK_{α} radiation used to interact with the sample consists of $CuK_{\alpha 1}$ (1.54051 Å) and $CuK_{\alpha 2}$ (1.54433 Å) radiation. In-situ variable-temperature PXRD was performed using an Anton Paar HTK1200 chamber, and a previously derived temperature profile function was used to account for systematic discrepancies between the set temperature (T_{set}) and the actual temperature (T_{corr}) at the sample:

$$T_{corr} = T_{set} + (aT_{set}^3 + bT_{set}^2 + cT_{set} + d) \tag{2.7}$$

where a, b, c, and d are constants equal to 1.61×10^{-7}, -5.86×10^{-4}, 0.565, and -134, respectively. The software EVA, provided by Bruker, has a search and match function which was used to identify unknown phases in synthesised materials. This is done by comparison of the peak positions and intensities of the provided PXRD pattern to a database. For all Rietveld refinements in this work, the TOPAS Aca-

demic software was used.[121] Crystallographic information files (*.cif*) were obtained from the inorganic crystal structure database (ICSD),[122] and used as starting model for the refinements

2.3 Neutron Scattering

Neutron scattering describes a variety of experimental techniques which probe the structure and dynamics of a material using neutrons. A detailed introduction to the theory of neutron scattering can be found in books by Squires[123] and Lovesey.[124]

2.3.1 Neutron Generation and Moderation

Neutrons for scientific research are produced at central facilities, either by fission in a nuclear reactor or by spallation. The high-energy reactions required to produce neutrons are one of the biggest disadvantages of this technique.

Spallation sources make use of high-energy protons accelerated in a synchrotron. They are then fired at a heavy metal target such as tungsten or mercury. Upon collision the protons transfer energy to the target nuclei, resulting in high-energy neutrons being ejected. This results in a pulsed beam, generating neutrons every time the metal target is hit. Once these neutrons are thermalised, a wide range of energies is accessible for various types of experiments. The ISIS facility at the Rutherford Appleton Laboratory is such a spallation source.[125]

Alternatively, neutrons can be produced by fission in nuclear reactors. These reactors generally have comparatively low thermal powers (≈20 MW) and use fissile material, e.g. enriched uranium (^{235}U), as fuel.[126] Bombarding the fuel with high-energy neutrons results in the formation of the unstable isotope ^{236}U, which splits into lighter fission products, generating 2.7 fast neutrons on average per fission event. The energy of these neutrons (≈ MeV) is too high to be used in experiments, and a moderator is used to slow them down to energies in the order of meV. This also increases the likelihood of a neutron being absorbed by a new uranium atom, making a chain reaction more easily attainable. Generally, from the released 2.7 neutrons, one causes further fission. The remaining neutrons can either be absorbed, or they

can escape the reactor and be used in scattering experiments. Moderation occurs by repeated elastic collisions between the moderator atoms and neutrons, resulting in the neutron losing energy until a thermal equilibrium with the moderator is reached. Hence, the temperature of the moderator determines the final energy distribution of the neutrons. For this to be an efficient process, it is important that the moderator medium contains atoms with a similar mass to a neutron. Therefore, common moderators are ^{1}H as water, ^{2}D as heavy water, or C as graphite.[126]

The neutron source at the Institut Laue-Langevin (ILL) is a high flux reactor with a thermal power of 58.3 MW and a neutron flux of 1.5×10^{15} neutrons s^{-1} cm^{-2} at the moderator, providing the most intense continuous flux of neutrons in the world. It has a single fuel element which contains approximately 8.5 kg of highly-enriched ^{235}U.[125–127] Some of the moderators and respective achievable neutron energies at the ILL are summarised in table 2.1.

	Moderator	T (K)	E (meV)	λ (Å)
Hot Neutrons	graphite	2000	100-500	0.4-1.0
Thermal Neutrons	D_2O	300	5-100	1-4
Cold Neutrons	D_2	25	0.1-10	4-30

Table 2.1: Summary of moderators used to achieve various neutron energies and wavelengths at the ILL.

The neutron flux that can be achieved in nuclear reactors is limited by the possible cooling rate of the core, and modern research reactors are approaching this limit. Spallation sources on the other hand can be used to obtain even higher fluxes, as the target can be cooled between pulses.

2.3.2 Fundamentals of Neutron Scattering

Neutrons have no charge, and therefore interact with nuclear forces instead of the electron cloud. The short range of these forces compared to the distance between nuclei means that neutrons can penetrate matter significantly better than electromagnetic radiation like X-rays and move far through most materials without being absorbed or scattered. The wavelengths of neutrons and therefore their use de-

pend on the temperature of the moderator, as summarised in table 2.1. Table 2.2 summarises the basic properties of the neutron.

charge	0
spin	$\frac{1}{2}$
magnetic dipole moment	-1.913 μ_n
mass	1.675×10^{-27}kg

Table 2.2: Basic properties of the neutron.

Thermal neutrons have comparable wavelengths to interatomic distances and phonon excitations, making them ideal for studying solids. Hot neutrons allow the study of high-frequency dynamics like molecular vibrations, while cold neutrons are useful for investigating macromolecular structures with large d-spacings like proteins, making neutron scattering a very versatile technique. Moreover, in contrast to X-rays the scattering power of neutrons varies randomly from element to element and also between isotopes, and does not decrease with increasing 2θ, making neutrons very useful for studying lighter elements in the presence of heavy elements. This makes neutrons particularly well-suited for the study of hydrogen-containing materials. The difference between coherent scattering lengths for X-rays and neutrons is shown in figure 2.3.

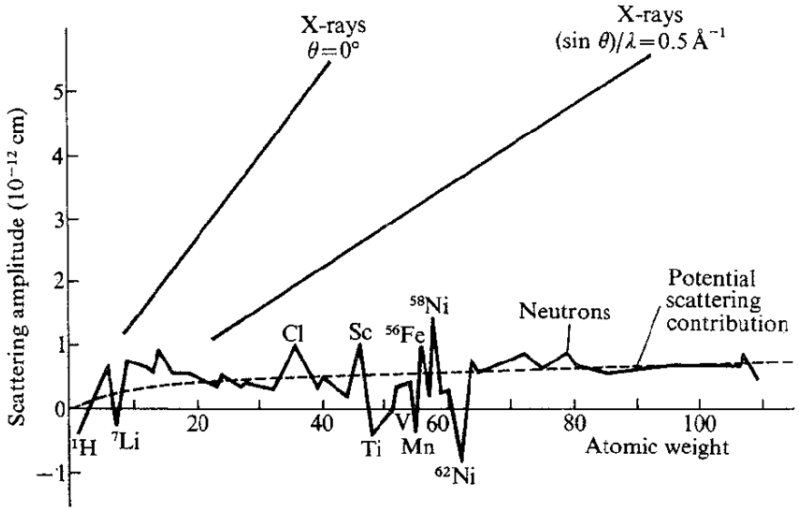

Figure 2.3: Coherent scattering lengths for X-rays and neutrons against atomic number Z. Taken from 128.

Additionally, neutrons have a magnetic dipole moment, making them excellent probes for magnetic structures and excitations. However, due to the fact that neutrons are generally scattered only weakly and that even the most powerful neutron sources provide relatively low fluxes compared to for example the X-ray flux at synchrotron sources, neutron scattering is a signal-limited technique. Despite this it is a very valuable technique that can provide information about materials which cannot be obtained by other methods.[125,126,129]

When a neutron passes in close enough proximity to a nucleus, it can either be absorbed (e.g. during the fission process) or scattered. This scattering process can either be elastic or inelastic, as visualised in figure 2.4. The special case of inelastic scattering known as quasielastic scattering (QENS) will be discussed separately in the following section.

An elastic scattering event describes the exchange of momentum between neutron and nucleus, leading to a change in direction, but with no change in energy. The initial wave vector of an incoming neutron ($\mathbf{k}_i$) and the final wave vector ($\mathbf{k}_f$) after scattering have the same modulus, but differ in their directions. Elastic neutron scattering (Bragg scattering) gives information about the equilibrium structure of a sample.

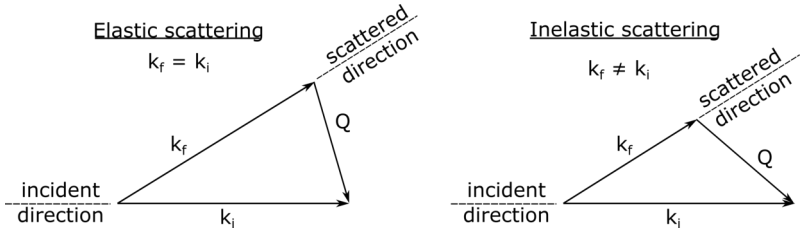

Figure 2.4: The scattering triangle, visualising elastic and inelastic scattering.

Inelastic scattering describes the exchange of both, momentum and energy between the neutron and a nucleus. An incoming neutron with initial wave vector $\mathbf{k}_i$ and energy E_i is scattered with a final wave vector $\mathbf{k}_f$ and energy E_f. Inelastic neutron scattering (INS) allows insights into the atomic scale dynamics of a sample. From this exchange of momentum and energy between neutron and nucleus, two quantities can be defined: the momentum transfer $\mathbf{Q} = \mathbf{k}_i$ - $\mathbf{k}_f$, and the energy transfer $\hbar\omega = E_i$ - E_f.

The scattering of a neutron by a single, fixed nucleus is the simplest case. The neutron-nucleus interactions are of the order of a few fm, which is several orders of magnitude smaller than the wavelength of a neutron, making the nucleus essentially a point scatterer. This means that neutrons are scattered isotropically as a spherical wave. The wavefunction of the incident neutrons can be written as $\Psi_{inc} = e^{ikz}$. After the scattering event, the wavefunction (Ψ_{sc}) at point r is

$$\Psi_{sc} = -\frac{b}{r}e^{ikr} \tag{2.8}$$

keeping in mind that the magnitude of the wave vector does not change as the scattering off a fixed nucleus is elastic. The quantity b is a constant called scattering length, which is determined experimentally and is the formal equivalent of the atomic scattering factor in X-ray diffraction. It describes the strength of the interaction between a given nucleus and the neutron and is not correlated with atomic number. The scattering length depends on the spin state of the neutron-nucleus system, and since the spin of a neutron is $\frac{1}{2}$, the possible spin states for a system with nuclei of spin I are $I \pm \frac{1}{2}$. Each of these two spin states has a different value of b. The scattering of a neutron by a single nucleus can be described by its cross section, σ, the effective area of the nucleus presented to the neutron:

$$\sigma = 4\pi b^2 \tag{2.9}$$

During a neutron scattering experiment, the number of neutrons scattered, with a certain range of energy dE, into a detector with solid angle $\Delta\Omega$ is measured. This is called the double differential cross section:

$$\frac{d^2\sigma}{d\Omega dE_f} = \frac{1}{\phi}\frac{dN_f}{d\Omega dE} \tag{2.10}$$

where ϕ is the incident neutron flux and N_f is the number of scattered neutrons. Using the two basic quantities which can be measured in a scattering experiment, the momentum transfer and energy transfer, the double differential cross section can be used to derive microscopic information about the sample, as it relates to the

atomic positions at different points in time:

$$\frac{d^2\sigma}{d\Omega dE_f} = \frac{\mathbf{k}_f}{\mathbf{k}_i}\frac{1}{2\pi\hbar}\int_{-\infty}^{\infty} dt e^{-i\omega t}\sum_{jj'}\overline{b_j b_{j'}}\langle e^{-i\mathbf{Q}.\mathbf{r}_j}e^{i\mathbf{Q}.\mathbf{r}_{j'}(t)}\rangle \tag{2.11}$$

where, at time zero, nucleus j is at position r_j , while nucleus j' is at $\mathrm{r}_{j'}$ at time t. The sum is over all nuclei positions in the sample, and the angular brackets indicate that a thermodynamic average over all possible sample configurations has to be taken. The term in the angular brackets, $\sum_{jj'}\langle e^{-i\mathbf{Q}.\mathbf{r}_j}e^{i\mathbf{Q}.\mathbf{r}_{j'}(t)}\rangle$, is commonly referred to as intermediate scattering function, I($\mathbf{Q}$, t).

Since every nucleus with non-zero spin has two values of b, and the variation of b can further increase due to the presence of isotopes, one has to consider an average value, $\overline{b_j b_{j'}}$, for systems with many nuclei. This results in two separate cases:

$$\overline{b_j b_{j'}} = (\overline{b})^2, j' \neq j \qquad \text{and} \qquad \overline{b_j b_{j'}} = \overline{b^2}, j' = j \tag{2.12}$$

Combining the two cases shown in 2.12 leads to:

$$\overline{b_j b_{j'}} = [(|\overline{b}|)^2 + \delta_{jj'}(\overline{|b|^2} - (\overline{|b|})^2)] = \frac{\sigma_c}{4\pi} + \delta_{jj'}\frac{\sigma_i}{4\pi} \tag{2.13}$$

with σ_c=$4\pi b_{coh}^2$ being the coherent cross section, and σ_i=$4\pi b_{inc}^2$ the incoherent cross section. Combining 2.11 and 2.13 gives:

$$\frac{d^2\sigma}{d\Omega dE_f} = \frac{\mathbf{k}_f}{\mathbf{k}_i}\frac{\sigma_c}{4\pi}S_c(\mathbf{Q},\omega) + \frac{\mathbf{k}_f}{\mathbf{k}_i}\frac{\sigma_i}{4\pi}S_i(\mathbf{Q},\omega) \tag{2.14}$$

The expressions

$$S_c(\mathbf{Q},\omega) = \frac{1}{2\pi\hbar}\sum_{jj'}\int_{-\infty}^{\infty}\langle e^{-i\mathbf{Q}.\mathbf{r}_j}e^{i\mathbf{Q}.\mathbf{r}_{j'}(t)}\rangle e^{-i\omega t}dt \tag{2.15}$$

and

$$S_i(\mathbf{Q},\omega) = \frac{1}{2\pi\hbar}\sum_{j}\int_{-\infty}^{\infty}\langle e^{-i\mathbf{Q}.\mathbf{r}_j}e^{i\mathbf{Q}.\mathbf{r}_{j}(t)}\rangle e^{-i\omega t}dt \tag{2.16}$$

are called coherent and incoherent dynamic structure factor, respectively, and are correlation functions related to the sample properties only. The difference in con-

tribution of coherent and incoherent scattering is visualised schematically in figure 2.5.

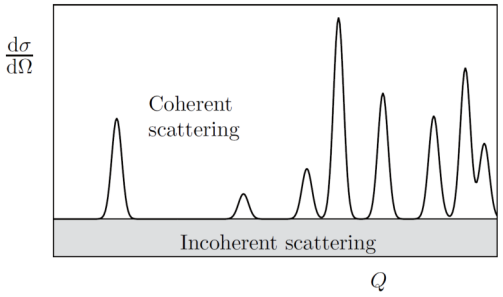

Figure 2.5: Schematic figure showing the incoherent and coherent scattering parts of the differential cross section. Taken from 130.

One can therefore differentiate between coherent and incoherent scattering:[123,130]

- Coherent scattering depends on both the correlation between positions of the same nucleus at different times, and the correlation between the positions of different nuclei at different times. These are interference effects, depending on the distances between nuclei, thereby reflecting their correlation of positions. It generally describes collective properties like the atomic structure. Figure 2.5 shows how, due to being caused by interference effects, the coherent scattering intensity varies with $\mathbf{Q}$.

- Incoherent scattering on the other hand depends only on the correlation between the positions of the same nucleus at different times. It appears because of the random variation of scattering lengths of the atoms in a sample caused by non-zero nuclear spins or different isotopes. Intensities scattered from individual nuclei add up independently, and incoherent scattering is characteristic of diffusion, i.e. the movement of individual atoms. As visualised in figure 2.5, the incoherent scattering intensity does not depend on $\mathbf{Q}$ (once the Debye-Waller factor has been accounted for).

The difference between coherent and incoherent scattering becomes more obvious when looking at the space-time Fourier transforms of the structure factor, a link first found by Van Hove.[131] The time-dependent pair correlation function can be simplified in its classical form:

$$G(\mathbf{r},t) = \sum_{j,j'} \delta(\mathbf{r} - [\mathbf{r}_j(0) - \mathbf{r}_{j'}(t)]) \tag{2.17}$$

This shows clearly that G(**r**, t) is only non-zero when the distance between nucleus j at time = 0 and nucleus j' at time = t is equal the vector **r**. Therefore, in the coherent case, G(**r**, t) describes the probability that there is a nucleus at the origin of the system and any nucleus at point **r** at time t, whereas in the incoherent case (j = j'), it describes the probability that there is a nucleus at the origin of the system at t = 0, and the same nucleus is at point **r** at time t.

2.3.3 Quasielastic Neutron Scattering (QENS)

Figure 2.6 shows a schematic example of a spectrum obtained from neutron scattering. Theoretically, the elastic peak should be at $\omega = 0$. Because of the finite resolution of all instruments, this line broadens into a Gaussian peak.

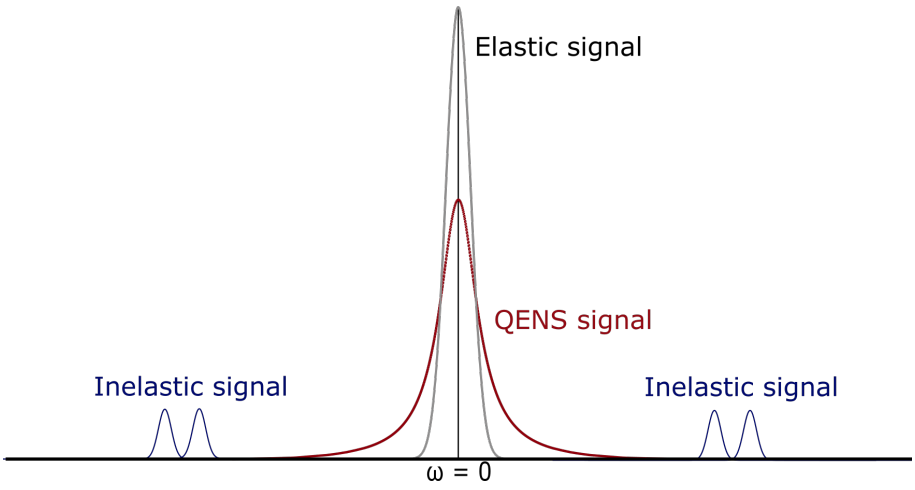

Figure 2.6: Schematic diagram of a neutron scattering spectrum, showing the elastic peak, a QENS broadening, as well as inelastic peaks at higher energy transfers.

The resolution of a particular instrument determines the timescales of dynamics which can be probed. If the timescale of diffusion in a material is approximately the same as the timescale probed by the instrument, a Lorentzian appears, leading to a further broadening of the elastic line. This is caused by thermally activated processes (translational motions or random jumps), which lead to a change of the system between configurations of the same energy. In principle, this is inelastic

scattering centred at $\omega = 0$ due to the rapid dissipation of the transferred energy, leaving the system in a final state of the same energy as the initial state. Therefore it is referred to as quasielastic neutron scattering, or QENS.[130,132]

QENS can give information about the geometry of dynamics as well as timescales. However, as the possible resolution of neutron scattering instruments is limited, the diffusion has to occur at a certain rate to be observable. Generally speaking, a diffusion coefficient of D $> 10^{-7}$ cm^2 s^{-1} is required, and dynamics on a time scale of 10^{-7} - 10^{-13} s can be studied. In order to obtain useful information from QENS experiments, a model must be fitted to the measured data.

Diffusion can be described as a relaxation process, during which a system changes from one state to another. Therefore, an important function in QENS is the intermediate scattering function, I($\mathbf{Q}, t$), which is the time Fourier transform of the structure factor and describes the correlation of a system at two different times. Equation 2.18 describes the coherent intermediate scattering function, and if j = j$'$, it describes the incoherent equivalent.

$$I(\mathbf{Q}, t) = \sum_{jj'} \langle e^{-i\mathbf{Q}.\mathbf{r}_j} e^{i\mathbf{Q}.\mathbf{r}_{j'}(t)} \rangle \tag{2.18}$$

Here, $\mathbf{Q}$ refers to the momentum transfer vector, which is direction dependent and relevant for single crystals. In this work all samples used are polycrystalline powders, causing an averaging over all directions in space and hence the modulus of $\mathbf{Q}$ is measured instead. Therefore, instead of $\mathbf{Q}$, only Q will be used in the following text.

As I(Q, t) is related to S(Q, ω), both contain the same information. This means that, if there is one type of diffusive motion present in a system i.e. one relaxation process in the form of an exponential decay, this diffusion appears as a Lorentzian function in S(ω). Neutron spin echo allows a direct observation of the intermediate scattering function, but as this method was not used in this work, this section will focus on the Lorentzian observable in S(Q, ω) data. Generally, the full width half maximum (FWHM, Γ) of this Lorentzian is the most important quantity obtained from QENS measurements, as its Q-dependence provides information about the type

of diffusion, and even further details in the case of long-range diffusion.

In the following, some models valid for the incoherent $I(Q,t)$ which are commonly used for the analysis of incoherent QENS will be discussed. Brownian diffusion is the most well-known form of diffusion in general. It describes a continuous process caused by random collisions of particles, and transforms into Fick's law in the macroscopic limit. In the intermediate scattering function, this can be described as:[132]

$$I(Q,t) = e^{-Q^2 D_s |t|} \tag{2.19}$$

and a Fourier transform gives the equivalent in S(Q,ω):

$$S(Q,\omega) = \frac{1}{\pi} \frac{\hbar D_s Q^2}{(\hbar D_s Q^2)^2 + (\hbar\omega)^2} \tag{2.20}$$

where D_s is the self-diffusion coefficient. Thus, the Q-dependence of the Lorentzian linewidth Γ is described as $\Gamma = \hbar D_s Q^2$. At low Q values, this dependence is valid regardless of the details of the diffusive process, and it is therefore referred to as the Q^2-law. At higher momentum transfer values (typically $Q > 1$ Å^{-1}), different diffusion mechanisms result in differences in the Q dependence. In solid state diffusion, these can generally be described by jump diffusion on a lattice. The simplest as well as most relevant model for this work is the one developed by Chudley and Elliott.[91] It generally assumes that successive jumps are uncorrelated and only nearest-neighbour jumps on a Bravais lattice are allowed. Moreover, in this model all possible jumps (z) have the same jump length l and moving atoms remain at a lattice site for a residence time τ, resulting in the following law:

$$I(Q,t) = exp\left(-\frac{t}{z\tau}\sum_{j=1}^{z} 1 - e^{-iQl_j}\right) \tag{2.21}$$

Again, a Fourier transform gives:

$$S(Q,\omega) = \frac{1}{\pi} \frac{\Gamma(Q)}{\Gamma^2(Q) + (\hbar\omega)^2} \tag{2.22}$$

and the HWHM of the Lorentzian is described by:

$$\Gamma(Q) = \frac{\hbar}{\tau}\left(1 - \frac{sin(Ql)}{Ql}\right) \tag{2.23}$$

For small values, the Q^2-law is obeyed, linking the linewidth directly to the diffusion coefficient. At high Q, the linewidth mirrors the jump rate (Γ=$\frac{\hbar}{\tau}$).

The models discussed so far are used to fit and analyse long-range diffusion, and allow extraction of diffusion coefficients, jump length and residence times. In addition to that, QENS can also be used to study confined, localised motions.

Local motions like rotations (continuous motions of atoms in a restricted spatial region and around some centre) are generally characterised using the elastic incoherent structure factor (EISF) - the long-time limit of the incoherent $I(Q,t)$. The EISF is defined as the integrated elastic intensity (I_{el}) divided by the sum of the integrated elastic intensity and integrated quasielastic intensity (I_{el}+I_{qel}) and gives direct information about the space accessible to the scattering nucleus.

$$\text{EISF} = \frac{I_{el}}{I_{el} + I_{qel}} \tag{2.24}$$

Hence the EISF represents the probability that, after a time t_{max} which is set by the resolution of an instrument, a particular atom is still in the same volume of space. It therefore does not provide information about the long-range dynamics of a system, but instead about the geometry of the present motion. Once the EISF from experimental data is extracted, it can be fitted with various models, e.g. the uniform diffusion over the surface of a sphere of radius R[132] or the reorientation on the four vertices (length = d) of a regular tetrahedron:[133]

$$\text{EISF}_{sphere} = \left(\frac{\sin(QR)}{QR}\right)^2 \tag{2.25}$$

and

$$\text{EISF}_{tetrahedron} = \frac{1}{4}\left(1 + 3 \times \frac{\sin(Qd)}{Qd}\right) \tag{2.26}$$

As was mentioned briefly for equation 2.18 and similarly to inelastic scattering, QENS can be coherent or incoherent. Incoherent QENS describes the condition that, if a particle is at position **r**=0 at time t=0, the same particle is found at position **r** at time t. Hydrogen is the most prominent example of a scatterer causing incoherent QENS due to its large incoherent cross section (table 2.3). Coherent QENS on the other hand describes the correlated motions of atoms and interference effects. Because this many body problem is very complex, the coherent QENS theory is difficult to treat and not very well developed. An additional complication is the fact that coherent scattering describes the structure of a system. This is particularly relevant near Bragg peaks. A change of quasielastic linewidth near maxima of the structure factor S(Q) was first suggested by de Gennes.[134] Since a system is most correlated when constructive interference is greatest, the accommodation of rearrangements is more difficult, leading to a slower relaxation and hence a narrower broadening.

Element	Natural abundance (%)	σ_{coh}	σ_{inc}
O	100	4.232	0.0008
^{16}O	99.762	4.232	0
^{17}O	0.038	4.2	0.004
^{18}O	0.2	4.29	0
H	100	1.756	80.26
^{1}H	99.985	1.758	80.27
^{2}H (D)	0.015	5.592	2.05

Table 2.3: Natural abundance and scattering cross sections of O and H.[135]

Oxygen has a small and almost purely coherent neutron scattering cross section (table 2.3). This makes the detection and analysis of QENS difficult. Additionally, oxide ion dynamics are generally slower than e.g. proton dynamics, and access to longer timescales is needed to observe long-range diffusion. In recent years, the availability of higher fluxes and better detectors as well as better instrumental resolutions has made it a more accessible technique for studying oxide ion diffusion.

As mentioned at the start of this discussion about QENS, the broadening is caused by thermally activated processes. Generally, the Lorentzian linewidth Γ is proportional to the diffusion coefficient D, which therefore has an Arrhenius type relationship with temperature:

$$D = D_0 \times e^{-\frac{E_a}{k_b T}} \tag{2.27}$$

where D_0 is the preexponential factor. This can be used to obtain the activation energy E_a of the process causing the broadening.

2.3.4 Neutron Scattering Instruments and Software

During this work, two different types of neutron spectrometers were used: a backscattering spectrometer and a time-of-flight spectrometer, which will be introduced here. All data reduction and analysis was performed using the Mantid software,[136] with data reduction scripts, written in Python, provided by the instrument scientists. The data were fitted using the fitting interface implemented in Mantid.

Backscattering Spectrometer - IN16b

IN16b is a backscattering spectrometer at the ILL in Grenoble. It uses cold neutrons with a wavelength of 6.271 Å, giving rise to a momentum transfer range of $Q = 0.1$ - 1.8 Å and an energy transfer range of $\hbar\omega = \pm 31$ μeV. Its high energy resolution of ≈ 0.75 μeV means slow dynamics on a nanosecond timescale can be observed.

The backscattering method allows observation of dynamics on long timescales due to the very high resolution it provides. The differential of Bragg's law (equation 2.2) shows how this high resolution can be achieved:

$$\frac{\Delta E}{2E} = \frac{\Delta \lambda}{\lambda} = \frac{\Delta d}{d} + \cot\theta \Delta\theta \tag{2.28}$$

Equation 2.28 shows how choosing a Bragg angle of $\theta = 90\,^\circ$ leads to $\frac{\Delta d}{d}$ being the only contribution to the energy resolution of an instrument. Since this depends only on the properties of the monochromator and analyser crystals used for backscatter-

ing, and not the beam divergence, it can be optimised by using high-quality crystals, thereby minimising the width of the wavelength distribution $\Delta\lambda$.

IN16b uses backscattering off Si(111) crystals in both, the monochromator before the sample (in the primary spectrometer) and the analysers after scattering off the sample (in the secondary spectrometer). This allows the incident and final neutron energy to be determined very accurately, giving rise to the high resolution.[129,137] While polished Si(111) crystals result in an excellent energy resolution of ≈ 0.3 μeV, they also significantly reduce the neutron flux. Therefore, the standard setting of IN16b uses strained Si(111) crystals, resulting in a slightly worse resolution ($\approx$ 0.75 μeV) but significantly higher intensity. The standard, high-flux mode of IN16b was used for all experiments reported in this thesis, and the setup in this mode is shown in figure 2.7.

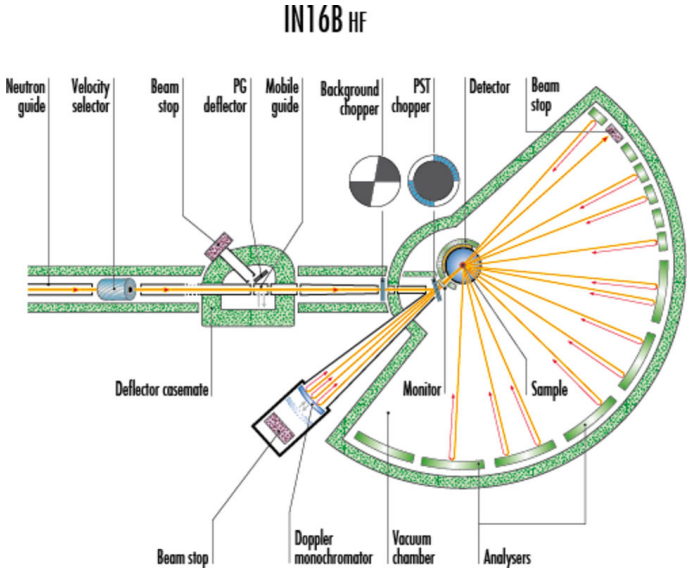

Figure 2.7: IN16b layout.[138]

Neutron energies are selected using a first velocity selector, and the background chopper then pulses the incoming beam and helps reduce the background. A phase space transformation (PST) chopper increases the flux by modifying the momentum distribution of incoming neutrons and directs the pulses towards the monochromator Si(111) crystal, which is mounted on a Doppler drive that can move the crystal perpendicular to the lattice plane. The Doppler effect shifts the d-spacing which the neutron beam encounters, varying the initial energy of the pulse to provide an energy

transfer range while keeping the high resolution by maintaining the backscattering geometry. The range of initial energies of the neutrons is defined by the velocity profile of the Doppler drive. The pulse is then directed at the sample and scattered, but only neutrons with a wavelength of 6.271 Å are backscattered by the analysers towards the detectors. The time at which they hit the detector depends only on their initial energy which is well-defined by the velocity profile of the Doppler drive. Therefore $\hbar\omega$ can be determined, and the scattering angle allows Q to be calculated.[129]

Time-of-flight Spectrometer - IN5

IN5 is a direct geometry time-of-flight (ToF) spectrometer at the ILL used to study low energy transfer processes as a function of momentum transfer. Its layout is shown in figure 2.8.

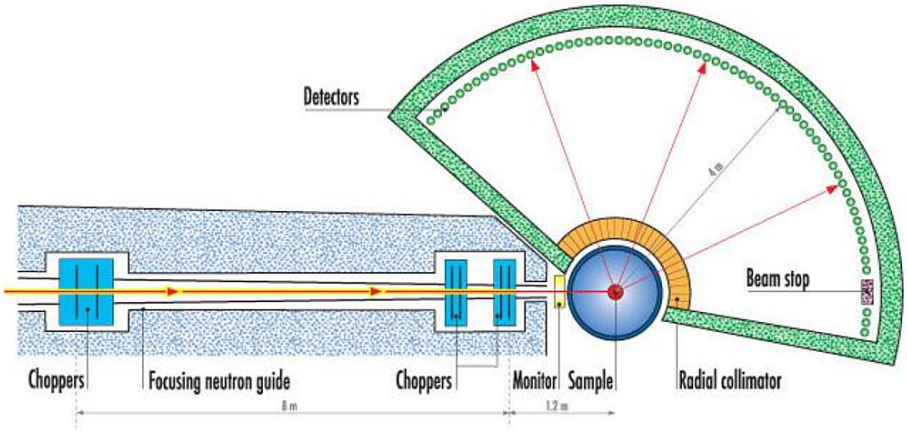

Figure 2.8: IN5 layout.[139]

It uses cold neutrons and allows complete flexibility of incident wavelengths (1.8 - 20 Å) and chopper speeds. For the experiments described in this report, two wavelengths (4.8 Å and 10 Å) were used, giving energy resolutions of 11 μeV and 89 μeV and hence measuring dynamics on a picosecond timescale. In the primary spectrometer, three pairs of choppers are used to chop the continuous, cold neutron beam, and select the desired incident energy by varying the phase and speed of the choppers. This creates a monochromatic, pulsed beam. These pulses are scattered by the sample in the secondary spectrometer at a known time, and fly to the po-

sition sensitive detector (PSD) array. The time-of-flight is measured, which allows determination of the final energy. The obtained raw data are a three dimensional spectrum of detector position (2θ) and ToF, which can then be converted to the more meaningful S(Q, ω).[140]

2.4 Impedance Spectroscopy

Resistance, R, is the opposition of a circuit to the flow of electric current, and can be defined by Ohm′s law as R = V/I, where V and I are the voltage and current, respectively. However, this only fully describes the opposition of current under a direct current and in ideal conductors. For real materials exposed to alternating currents, the resistance alone is not enough, as it does not take other processes resulting in a decrease in conduction into account. Instead, impedance, Z, is used. It represents the decrease in conductivity caused by any opposition of a circuit to the flow of a sinusoidal current, and consists of three components: resistance, capacitance and inductance. Capacitance describes the storage of small amounts of charge in a material, and inductance is the process of an induced current, caused by induction of a magnetic field in a material by the alternating current, opposing the applied current, thereby decreasing the conductivity. Inductance and capacitance can be summarised as reactance.[141,142]

Impedance spectroscopy measures the response of a sample to a small sinusoidal current or potential of a fixed frequency. The frequency-dependent impedance, Z_ω, can then be determined by repeating this process for a range of frequencies, and is defined as:

$$Z_\omega = \frac{E_\omega}{I_\omega} \tag{2.29}$$

where I_ω is the frequency-dependent current and E_ω the frequency-dependent potential. Capacitance and inductance cause a phase shift, ϕ, in the generated current in response to the applied, alternating potential:

$$Z_\omega = \frac{E_0 sin(\omega t)}{I_0 sin(\omega t - \phi)} \tag{2.30}$$

where ω is the angular frequency of the oscillation, E_0 the amplitude of the potential difference, I_0 the amplitude of the current oscillation, and t is the time. This equation can be rearranged using Eulers relationship. This gives impedance in the form of a complex function:

$$Z_\omega = Z^{'} cos\phi + Z^{"} isin\phi \tag{2.31}$$

where $Z^{'}$, the real part, resembles the resistance, and $Z^{"}$, the imaginary part, corresponds to the reactance. Impedance data is commonly visualised by plotting $Z^{"}$ against $Z^{'}$, a so-called Nyquist plot, a schematic example of which is shown in 2.9.

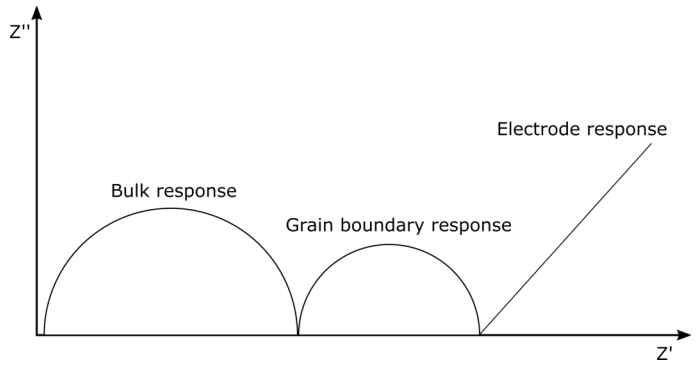

Figure 2.9: Schematic drawing of an ideal Nyquist plot where the grain boundary and bulk contribution can be separated.

Grain boundaries in a material provide more resistance to ionic movement than the bulk, leading to a variation of impedance in the sample. Because of differences in relaxation times in the different parts of the material, the grain boundary and bulk contributions to the impedance can be separated in the frequency domain. For ceramics, in an ideal Nyquist plot distinct semicircles are apparent, which can be attributed to the grain boundary regions or the bulk of the sample, as shown in figure 2.9.[141,143] However, this separation is not always possible, and often a single semicircle which combines the bulk and grain boundary responses is observed instead. Because of that it is important to use dense samples in order to max-

imise the contribution of the bulk, and at the same time minimise the number of grain boundaries to the measured impedance. Therefore, samples are pressed into pellets using high pressures, and subsequently heated at high temperatures which encourages grain growth and reduces the total grain boundary area.

Experimental impedance data is commonly analysed by fitting an equivalent electrical circuit. However, these empirical models are not unique,[144] and especially in cases where the grain boundary and bulk contributions cannot be clearly separated, fitting of an equivalent circuit can be very challenging. While such in-depth analysis of impedance data can provide valuable information on the microstructure, separate processes and electrochemical reactions occurring in a material, its purpose in this work was solely to allow a direct comparison of the total conductivity in a series of similar electrolytes. Because of this, no equivalent circuit fits will be discussed.

The resistance of either the grain boundary, bulk, or combined response can be obtained from the second intercept of the respective semicircle with the $Z^{'}$ axis. The conductivity of a material, σ, is then defined as:

$$\sigma = \frac{l}{RA} \tag{2.32}$$

where l is the sampe length and A the sample area. The activation energy of oxide ion migration can then be obtained from the gradient of an Arrhenius plot of $\ln(\sigma T)$ vs $\frac{1}{T}$.

Impedance measurements are used to separate the contribution of distinct processes to the total impedance, but do not separate ionic and electronic contributions to the conductivity. The transport number, also called transference number, is the fraction of the total current carried by a given ionic species. The ionic transport number, t_i, is given by

$$t_i = \frac{\sigma_i}{(\sigma_i + \sigma_e)} \tag{2.33}$$

where σ_i and σ_e are the ionic and electronic conductivity, respectively. Measurements of the oxide ion transport number can therefore be used to determine the ionic and electronic contribution to the total conductivity. There are three commonly used

techniques for determining the ionic transport number of solid materials.

One relatively simple technique to determine whether conduction is ionic or electronic involves conductivity measurements under different oxygen partial pressures over a wide range of temperatures. If the material has negligible electronic conductivity, the measured conductivity will be constant as a function of oxygen partial pressure. In most oxide ion conductors, it is the dopant concentration which controls the concentration of defects. The ionic conductivity is therefore mostly independent of the oxygen partial pressure over a certain range. The concentration of electronic defects however is influenced by small changes in the composition of the material with respect to oxygen, and electronic conductivity therefore varies as a function of oxygen partial pressures.[145] This method is mainly used to determine the range of oxygen partial pressures in which ionic conduction is dominant.

Electromotive force (EMF) measurements are commonly used to determine the ionic contribution to the total conductivity in ionic conductors with a transport number close to unity. If the electronic contribution to the conductivity becomes appreciable, this method is problematic due to internal current flow and short circuiting leading to material transport, which can result in a change of oxygen concentration near the interface. To determine the ionic transport number, the oxide ion conductor is placed between two reversible electrodes at different chemical potentials, and the EMF is measured across the cell.

$$E = (\frac{t_i RT}{4F}) \ln(\frac{p'O_2}{p''O_2}) \tag{2.34}$$

where t_i is assumed to be constant and close to unity and p'_{O2} and p''_{O2} are the oxygen partial pressures at the electrodes.[145,146]

Another extensively used method for determining the electronic contribution to the total conductivity is the ion blocking method (sometimes also called DC polarisation cell method or Hebb-Wagner technique). Like the name suggests, a small direct current (DC) voltage is applied to the material, which is sandwiched between an ion blocking electrode and a reversible electrode with a known chemical potential. Under steady state conditions a chemical potential gradient is generated by the DC

voltage across the conducting material, but the ion blocking electrode prevents the flow of ionic current. Therefore, the current measured is only carried by electrons and holes. An electron blocking electrode can be used to measure ionic current. This method also allows the separation of electron and hole conductivities. It is important that the solid material used is very dense, since the presence of pores could allow oxide ions to move through the material, affecting the measured current. Additionally, electrode reactions at the blocking electrode/conductor interface cannot be fully eliminated and may cause errors. Two or more of these methods are therefore often combined to ensure reliable and reproducible results.[145,147]

2.4.1 Instruments and Software

Impedance measurements were performed using a Solartron 1260A analyser. A frequency range of 0.1 - 10^7 Hz was used. The voltage used for separate measurements are specified in the respective experimental chapters. The measurements were carried out on pelletised samples to ensure a high density. Both sides of the pellets were coated with Pt-paste and attached to the Pt-electrodes on a Probostat cell. To remove the organic components of the paste, the samples were dried at 850 °C for 25 mins.

2.5 Molecular Dynamics (MD) Simulations

Depending on the method used to treat interatomic forces, Molecular Dynamics Simulations can be divided into three categories: classical MD (CMD), ab initio MD (AIMD), and, thanks to very recent advances in the field, machine learning MD (MLMD). Since the main technique used in this work is AIMD, this will also be the focus of this section.

All three types of MD simulations are based on the same underlying principles. First of all, the initial positions and velocities of all atoms in the simulation box must be given. For crystalline materials, diffraction data provides atomic coordinates of the unit cell. Several unit cells can be combined to obtain a supercell, here also called simulation box, in order to increase the accuracy of the simulation. A Maxwell-

Boltzmann distribution at the desired temperature is used to randomly attribute the initial velocities.[71,82] This initial information can then be used to solve the classical equation of motion:

$$-\frac{dU}{d\mathbf{r}} = m\frac{d\mathbf{v}}{dt} = m\frac{d^2\mathbf{r}}{dt^2} \tag{2.35}$$

where U is the potential energy, t is the time, and $\mathbf{r}$ and $\mathbf{v}$ are the positions and velocities of atoms, respectively. Using equation 2.35, the trajectory of all atoms can be derived from the initial coordinates and potential energies. This equation cannot, however, be solved exactly. Instead, a numerical solution must be found, solving the equation of motion in discrete steps and using integration algorithms such as the leap-frog[148] or Verlet[149] algorithm to obtain atomic positions and velocities at each time step.

When solving the equation of motion 2.35, an appropriate ensemble has to be chosen. If the number of atoms N, volume of the simulation box V and total energy E are kept constant, this ensemble is called the microcanonical or NVE ensemble. To allow comparison to experimental results, simulations at a constant temperature T can be more favourable. The NVT (or canonical) ensemble keeps the temperature of the simulation box constant by allowing energy exchange with a thermostatic bath. Alternatively, a thermostat and barostat can be combined to keep both temperature and pressure p constant, allowing the volume of the simulation box to vary. This is called NpT (or isothermal-isobaric) ensemble.

In order to accurately simulate the bulk of a material, it is important to impose boundary conditions to account for surface effects caused by atoms close to the edge of the simulation box. Therefore, periodic boundary conditions are commonly used, which means that the simulation box is surrounded in all three directions by infinite copies of itself. The movement of the atoms in the original simulation box are replicated in all its copies, meaning that if an atom leaves the box, the corresponding copy enters from the opposite side.

In classical MD, force fields are used to model intra- and intermolecular forces, with bonds being described as harmonic oscillators. These force fields are either

derived from experimental data or calculated using quantum mechanics. Once the accuracy of a force field for a particular system has been tested, it allows the simulation of thousands of atoms for long simulation times of several nanoseconds. A big variety of force fields, each with its particular strengths, has been developed. Systems of general interest, for example water and hydrocarbons, have a big selection of well-established force fields available for study. However, the loss of accuracy for systems that deviate from the one used to derive the force field, as well as the inability of CMD to simulate bond forming and breaking limits its applicability significantly.[71,82]

For these reasons, CMD was not used for the simulation of oxide ion dynamics in this work. Instead, the movement of oxide ions was simulated using quantum mechanical methods.

2.5.1 Ab initio MD

Ab initio means "from first principles" and describes the use of fundamental laws, i.e. quantum mechanics, instead of empirical fits to continuously calculate the forces during a simulation. This allows precise control of the system under study and can help interpret experimental data as well as predict new properties. However, in order to obtain the forces and potential energies which are required to solve the equation of motion (2.35) using quantum mechanics, the Schrödinger equation of the system of interest must be solved. This cannot be done analytically for many-atom systems, and therefore several approximations have to be made.

The Born-Oppenheimer approximation allows a separation of the motions of electrons and nuclei by assuming that, due to the much higher mass of the latter, electrons react instantaneously to nuclear motions. Therefore, the quantum-mechanical effort can be focused on solving the electronic wavefunction, keeping all nuclei fixed, which reduces their kinetic energy to zero and the nucleus-nucleus interaction energy to a constant. This significantly simplifies the Schrödinger equation of a system to the electronic Schrödinger equation:[150,151]

$$\hat{H}_e \psi_e = E_e \psi_e \tag{2.36}$$

and

$$\hat{H}_e = \hat{T} + \hat{V}_{en} + \hat{V}_{ee} = -\frac{\hbar^2}{2m} \sum_i^N \nabla_i^2 + \sum_i^N v(\mathbf{r}_i) + \sum_{i<j}^N \frac{1}{r_{ij}} \tag{2.37}$$

where ψ_e is the electronic wavefunction, E_e the electronic ground-state energy, m the electron mass, $\hat{T}$ the kinetic energy of the electrons, $\hat{V}_{ee}$ the interaction energy between different electrons, and $\hat{V}_{en}$ the interaction energy between electrons and nuclei. Since the nuclei are fixed, this can be seen as the interaction of electrons with an external potential $v(\mathbf{r}_i)$, defined by the nuclei.

The Hartree-Fock method can be used to solve the Schrödinger equation by approximating the total electronic wavefunction of a system into a product of separate, one-electron wavefunctions. However, this is still a very computationally expensive task, and impractical for big systems containing many electrons.

Density Functional Theory (DFT) offers an alternative way of determining the ground-state energy. It simplifies quantum mechanics by rewriting the underlying theory in terms of the electronic charge density $\rho(\mathbf{r})$, a quantity which, in contrast to ψ, can be experimentally observed. It was developed by Hohenberg and Kohn[152] who established two key theorems, the first of which proves that the external potential $v(\mathbf{r}_i)$, which determines $\hat{H}$, is a unique functional of the electronic density. It follows that a system's ground-state energy and all ground-state properties depend only on the electronic density, and can hence be determined using a universal energy functional. The second theorem states that the density which gives the lowest energy of the functional will always be the ground state density. We can therefore define the ground-state energy in terms of electron density:

$$E_e[\rho] = V_{en}[\rho] + T[\rho] + V_{ee}[\rho] \tag{2.38}$$

with

$$V_{en}[\rho] = \int \rho(\mathbf{r}) v(\mathbf{r}) d\mathbf{r} \quad \text{and} \quad T[\rho] + V_{ee}[\rho] = F[\rho] \tag{2.39}$$

where $F[\rho]$ is called the universal functional and does not depend on individual electron coordinates, but instead the electron density of the system.

While these two theorems prove that using the electron density as a variable is physically sound, they provide no information on how the functionals in equation 2.38 can be obtained. In particular, the determination of the kinetic energy of a density is problematic, and since the kinetic energy is very large compared to the other contributions in equation 2.38, small errors in this expression will have a detrimental effect on the overall result. This was changed by the second ground-breaking paper concerning modern DFT, published by Kohn and Sham,[153] who introduced orbitals as a non-interacting reference system, allowing a significant part of the kinetic energy to be determined with good accuracy. The residual kinetic energy is small and can be approximated together with the other unknown contributions.

Kohn and Sham defined the universal functional as:

$$F[\rho] = T_s[\rho] + J[\rho] + E_{XC}[\rho] \tag{2.40}$$

where $T_s[\rho]$ is the kinetic energy of a system of non-interacting electrons with density ρ, and J[ρ] the classical Coulomb repulsion interaction within the density ρ. Combining equations 2.39 and 2.40 shows that the exchange-correlation energy E_{XC} can be defined as:

$$E_{XC}[\rho] = (T[\rho] - T_s[\rho]) + (V_{ee}[\rho] - J[\rho]) \tag{2.41}$$

It includes and combines the residual part of the real kinetic energy which is not covered by the non-interacting reference system, and the residual electrostatic contributions not covered by the classical Coulomb potential. Hence, E_{XC} contains all contributions of the kinetic and potential energy which cannot be handled exactly.

The exact electronic energy of a system can therefore be written in the Kohn-

Sham formalism as:

$$E = \int \rho(\mathbf{r}) v(\mathbf{r}) d\mathbf{r} + T_s[\rho] + J[\rho] + E_{XC}[\rho] \tag{2.42}$$

Kohn and Sham showed that the ground state energy and density of a real system are exactly the same as those of a non-interacting system ($V_{ee} = 0, T = T_s$) if an extra potential $v_{eff}(\mathbf{r})$ is included. The Kohn-Sham equation of a system of non-interacting electrons moving in an external potential $v_{eff}(\mathbf{r})$ can be written as:

$$\left[-\frac{\hbar^2}{2m} \nabla^2 + v_{eff}(\mathbf{r}) \right] \psi_i(\mathbf{r}) = \epsilon_i \psi_i(\mathbf{r}) \tag{2.43}$$

The density of this reference system and hence also the density of the real system $\rho(\mathbf{r})$ can be obtained by summing the Kohn-Sham orbitals:

$$\rho(\mathbf{r}) = \sum_{i}^{N} \psi_i^2(\mathbf{r}) \tag{2.44}$$

and the non-interacting part of the kinetic energy T_s is:

$$T_s[\rho] = \sum_{1}^{N} \langle \psi_i | - \frac{\hbar^2}{2m} \nabla^2 | \psi_i \rangle \tag{2.45}$$

Therefore, the total energy of a real system, given by 2.42, can be evaluated with only the small $E_{XC}[\rho]$ needing to be approximated.

The local density approximation (LDA) is one method used to approximate E_{XC} in real systems. It is centered around an infinite, uniform electron gas moving on a positive background, a system for which exact results can be obtained. This result, obtained at a certain density, is then used as E_{XC} of a real system. LDA works well for some molecular structures and metals, but tends to underestimate bond lengths.[150]

LDA assumes a constant electron density, which is not physical. The generalised gradient approximation (GGA) is built on that idea by adding information about the gradient of the charge density at a certain point. This is done by using the LDA

as the first term of a Taylor expansion.

2.5.2 Machine learning MD

While AIMD can very accurately predict the properties of systems, it is severely limited by the required computational power. This means that only small systems consisting of a few hundred atoms can be simulated, and the feasible time is restricted to several hundred picoseconds. Machine learning MD is a very new technique and attempts to combine the speed of CMD with the accuracy of AIMD by creating a reliable potential energy surface (PES). In simple terms, this can be achieved by:[72]

1. Creating a database using AIMD
2. Choosing a descriptor to represent the local environment
3. Fitting the data using a regressor

The first step can either be done at the start, in which case a certain number of AIMD steps are performed and then used as the fixed database, or 'on-the-fly'. During 'on-the-fly' machine learning, the PES and uncertainties are predicted using the created database. If the uncertainties exceed a predefined threshold (which can be updated during the simulation), an AIMD step is performed and added to the database.

In step two, a descriptor is calculated from the density distribution of all atoms around a central atom using pair and angular correlation functions. This step requires one assumption to be made, namely that the local energy is a function of the local environment. This constitutes a key difference between AIMD and MLMD, as in pure AIMD the energy is not separated into its local contributions. In simple cases, the descriptor is a function of coordinates and atom types, but more complex functions have been developed.

Step three requires the use of a regressor to construct a PES from all descriptors. The two main choices for regressors are neural networks or Kernel based methods. The force field created in this step is then used for further MD steps.

A summary of some ML methods including the descriptor and regressor used is given in,[71] and a detailed description of the theory behind MLMD as well as the difference between regressors can be found in.[72]

2.5.3 Simulation Analysis and Software

For all AIMD simulations performed in this thesis the Vienna ab initio simulation package (VASP) code[75] was used in the NVT ensemble. To integrate the equation of motion 2.35, VASP utilises the Verlet algorithm. Since generally only the outer valence electrons are active, the core electrons can be combined with the nucleus into a pseudo ion. This is accounted for by replacing the Coloumb potential of the nucleus with a weaker pseudopotential. This reduction of electrons helps increase the performance of simulations, and VASP uses projector augmented wave (PAW) pseudopotentials.[154] To approximate the exchange functional, the GGA approximation[155] was used, and due to the very large simulation boxes necessary, only the gamma point was sampled. The parameters used for each simulation are detailed in the relevant chapters.

The AIMD data were analysed using the MDANSE code,[156] as well as Python scripts. The space visited by particular atoms was visualised in the form of cloud plots using LAMP.[157] For all simulations, MDANSE was used to calculate the mean square displacement (MSD). For a particle, the MSD $\langle r^2 \rangle$ is given by:

$$\langle r^2(m) \rangle = \frac{1}{N_t - m} \sum_{k=0}^{N_t - m - 1} [\mathbf{r}(k+m) - \mathbf{r}(k)]^2, m = 0 ... N_t - 1 \tag{2.46}$$

where N_t is the total number of frames in the trajectory, and $\mathbf{r}(k)$ is the trajectory. Equation 2.46 shows how, towards the end of a trajectory, $N_t - m$ becomes smaller, meaning that a smaller number of datapoints can be used for the average. Therefore, towards the end of a simulation, the error on the MSD curves increases significantly. As diffusion can be approximated well by a random walk, the MSD is proportional to the elapsed time and can be related to the self-diffusion coefficient D:

$$\langle r^2 \rangle = 6Dt + C \tag{2.47}$$

where C is a constant. Since diffusion is a thermally activated process, the activation energy for diffusion can be extracted from the temperature dependence of the diffusion coefficent, using the Arrhenius relationship (equation 2.27).

CHAPTER 3

Oxide Ion Mobility in V- and P-doped Bi_2O_3-Based Solid Electrolytes

3.1 Summary

This chapter reports the observation of oxide ion dynamics on both nano- and picosecond timescales in isostructural Bi_2O_3-derived solid electrolytes $Bi_{0.852}V_{0.148}O_{1.648}$ and $Bi_{0.852}P_{0.148}O_{1.648}$ using quasielastic neutron scattering. Comprehensive ab initio molecular dynamics simulations allowed reproduction of the experimental picosecond timescale data by directly simulating the scattering function at various temperatures. Our analysis of the experimental data in conjunction with the simulations revealed the origin of the picosecond dynamics to be localised motions within the V-O and P-O sublattices, while nanosecond dynamics correspond to the diffusion of the oxide ions in the Bi-O sublattice via vacancy-hopping. This combined approach provides insight into the different oxide ion migration pathways and mechanisms in $Bi_{0.852}V_{0.148}O_{1.648}$ and $Bi_{0.852}P_{0.148}O_{1.648}$, with the flexibility of the V coordination environment playing an important role, consistent with the superior conductivity of the vanadate.

3.2 Introduction

The fluorite structure and its derivatives are ubiquitous in solid state chemistry, and one of the most widely studied families of ionic conductors. The ideal fluorite structure is shown in figure 3.1.

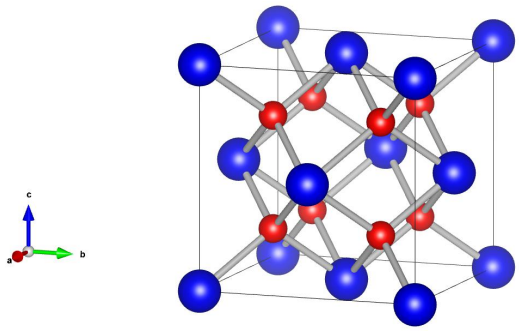

Figure 3.1: Ideal, cubic fluorite structure AO_2. Blue and red spheres represent the A site cations and O^{2-}, respectively.

It is cubic, in space group Fm-3m, and has the general formula AO_2, with the eight-coordinated A-site cations forming a face centred cubic array. The four coordinated oxide ions occupy the tetrahedral holes. Many oxide ion conductors adopt the fluorite structure, for example Y-doped zirconia (YSZ) and Gd-doped ceria (GDC) compounds, which were discussed in Chapter 1.

The high-temperature (> 730 °C) phase of bismuth oxide, δ-Bi_2O_3, also adopts a fluorite-related structure. However, unlike in YSZ or GDC, only $\frac{3}{4}$ of the tetrahedral holes are occupied by oxide ions in a random fashion, resulting in intrinsic oxygen vacancies. Neutron diffraction has shown displacements of nearly half of the oxide ions towards one of the faces of the OA_4 tetrahedra, in the direction of the octahedral holes. Additionally, the lone pair of Bi^{3+} is very polarisable, which further lowers the ionic potential at the octahedral hole.[38,93] Therefore, oxide ion conduction was suggested to consist of vacancies moving from one oxygen site via an octahedral hole to an adjacent oxygen site.[38,92,94] However, as discussed in Chapter 1, a recent combined QENS and AIMD study suggests that diffusion in δ-Bi_2O_3 is more isotropic and liquid-like than previously thought.[95]

The large number of intrinsic oxide ion vacancies leads to the high oxide ion conductivity of 1 S cm^{-1} at 750 °C, making it the best oxide ion conductor known

so far.[93,158] Despite that, pure δ-Bi_2O_3 is unsuitable as electrolyte material in SOFCs because of two main issues. First, Bi^{3+} is prone to reduce to Bi metal at the anode side of the cell, due to the low partial oxygen pressure of $\approx 10^{-13}$ atm.[159] This can be readily overcome by the use of bilayer electrolytes, as discussed in Chapter 1. Second is the issue that δ-Bi_2O_3 is only stable in the narrow temperature range between 730 °C and its melting point at 824 °C. The low temperature α-phase and intermediate β-and γ-phases crystallise in structures which do not possess intrinsic vacancies, reducing the conductivity by several orders of magnitude.[160] Additionally, the phase transition at 730 °C results in a volume change which creates strain, weakening the structural integrity of the material, which would ultimately damage the fuel cell. Therefore, stabilising the cubic, highly conductive phase at lower temperatures by iso- or aliovalent doping is a crucial step in the development of electrolytes based on bismuth oxide. Many viable dopants have been found, including Sr^{2+}, Nb^{5+}, Mo^{6+}, Er^{3+}, Dy^{3+}, W^{6+}, Re^{7+}, Tm^{3+}, and V^{5+}.[38,88,158,161–167]

Substituting Bi^{3+} for different cations, however, lowers the conductivity. Erbium has been found to stabilise the δ-Bi_2O_3 phase at a doping concentration of 20 %, and $Bi_{0.8}Er_{0.2}O_{1.5}$ (ESB) has a high conductivity of 4.1×10^{-1} and 2.1×10^{-2} S cm^{-1} at 800 °C and 500 °C, respectively.[38,163] Double cation substitution can result in even higher conductivities. $Bi_{0.76}Lu_{0.16}Ti_{0.08}O_{1.5+\delta}$ has recently been reported to have a conductivity of 0.37 S cm^{-1} at 700 °C and 0.1 S cm^{-1} at 300 °C,[168] and $Bi_{12.5}La_{1.5}ReO_{24.5}$ has a conductivity of 1.1×10^{-3} S cm^{-1} at 300 °C.[165] However, the conductivity of $Bi_{0.76}Lu_{0.16}Ti_{0.08}O_{1.5+\delta}$ starts to decrease after approximately 10 h of heating, and $Bi_{12.5}La_{1.5}ReO_{24.5}$ undergoes a phase transition to a less conductive, stable tetragonal phase after one heating cycle, reducing the conductivity by two orders of magnitude.[167]

Kuang et al.[109] reported the remarkably high oxide ion conductivities of two V-doped Bi_2O_3 materials, $Bi_{0.913}V_{0.087}O_{1.587}$ (BVO-087) and $Bi_{0.905}V_{0.095}O_{1.595}$ to be 3.9×10^{-2} S cm^{-1} and 2.6×10^{-2} S cm^{-1} at 500 °C, respectively, which is even higher than that of ESB . These pseudo-cubic $3 \times 3 \times 3$ δ-Bi_2O_3 ordered superstructures are stable below 450 °C and above 825 °C.[109] Prolonged heating within this temperature range results in slow, partial decomposition of the samples to $Bi_{16}V_2O_{29}$ and V-

doped γ-Bi_2O_3, leading to a decrease in conductivity. The original phases reform fully at 825 °C. Takahashi et al.[159] reported the conductivity of the closely related composition $Bi_{0.91}Vi_{0.09}Oi_{1.59}$ to be lower (10^{-3} S cm^{-1} at 500 °C), which Kuang et al. ascribed to partial decomposition of their sample to $Bi_{16}V_2O_{29}$ and V-doped -Bi_2O_3 caused by data collection through the instability region.[109] EMF measurements gave an oxide ion transport number of 0.96 for $Bi_{0.91}V_{0.09}O_{1.59}$,[159] showing negligible electronic contribution to the conductivity in these materials. The structure of BVO-087 consists of corner- and edgesharing Bi-O tetrahedra which form a network of fluorite-like slabs. Isolated V-O groups are distributed between these slabs. Similar to δ-Bi_2O_3, only $\frac{3}{4}$ of oxygen sites in the Bi-O sublattice are occupied, resulting in intrinsic oxygen vacancies. Ab initio molecular dynamics (AIMD) calculations (20 ps) showed an exchange of oxide ions between the Bi-O sublattice and the V-O sublattice at 200 °C and 600 °C.[109] The high conductivity is a result of oxide ion diffusion through the Bi-O sublattice via vacancy hopping which was observed at 600 °C, analogous to the mechanism seen in δ-Bi_2O_3. The average coordination number of the V sites was found to vary between 4 and 4.33 due to O^{2-} moving from Bi-O to V-O groups, which creates additional vacancies in the Bi-O sublattice.[109] This is facilitated by the ease of rotation of VO_x polyhedra in this structure as well as the ability of V^{5+} to support a variety of coordination environments. Overall, the high, isotropic ionic conductivity of BVO-087 can be attributed to the extended, δ-Bi_2O_3-like sublattice, the variable V coordination environment, and the ability of the VO_x coordination polyhedra to rotate and thereby support localised motion of oxide ions and oxide ion jumps between the Bi-O and the V-O sublattices, which in turn facilitates long-range diffusion.[109]

The long-range oxide ion dynamics in BVO-087 have been directly observed using quasielastic neutron scattering (QENS).[108] Mean-square displacements (MSD) for oxide ions starting in the Bi-O or the V-O sublattice obtained from further AIMD simulations on a longer timescale (200 ps) suggest that long-range diffusion occurs through the Bi-O sublattice, whereas faster, localised motions arise from oxide ion mobility within individual VO_x groups. The activation energy obtained from MSDs for the Bi-O sublattice (0.38 ± 0.01 eV) agrees with the one obtained

from QENS (0.39 ± 0.04 eV), indicating that it is this long-range diffusion that was directly observed. An attempt to observe the dynamics in the V-O sublattice using QENS was unsuccessful, but MSD curves from AIMD trajectories allowed the determination of the activation energy for this fast process to be 0.05 ± 0.01 eV.[108]

β-$Bi_{46}V_8O_{89}$ ($Bi_{0.852}V_{0.148}O_{1.648}$, BVO-148) has an oxide ion conductivity of 1×10^{-2} S cm^{-1} at 600 °C,[169] and oxide ion transport numbers reported by Watanabe et al. (0.9 - 0.95 above 600 °C)[170] suggest negligible electronic contribution to the total conductivity. Both the α polymorph in space group $P2_1/c$ and the β polymorph in space group $C2/m$ have groups of isolated V-O tetrahedra and a Bi-O sublattice. They also both consist of stacks of two ($Bi_{14}V_4O_{31}$) layers followed by one ($Bi_{18}O_{27}$) layer, and to emphasise this the formula can be written as [($Bi_{14}V_4O_{31}$)$_2$($Bi_{18}O_{27}$)].[169] These building blocks, however, are arranged differently in the two polymorphs due to different cation distributions, and the structure of the β polymorph is shown in figure 3.2.

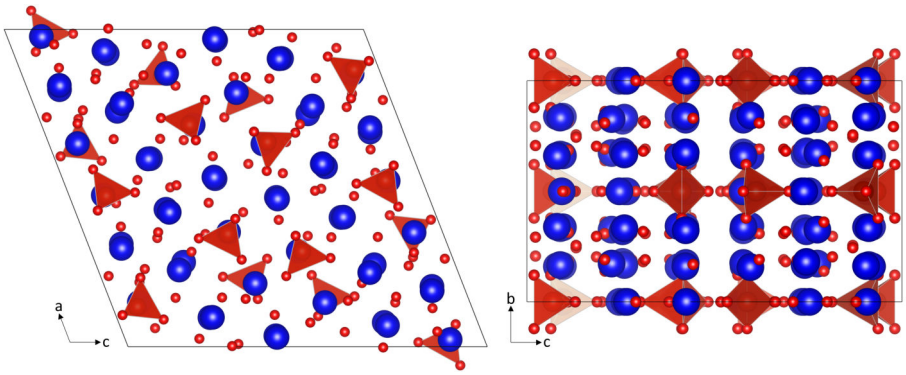

Figure 3.2: Structural models of the isostructural materials BVO-148 and BPO-148, both in space group $C2/m$, with blue and red spheres representing Bi and O atoms, respectively, and red tetrahedra showing VO_4 or PO_4 groups. Disorder is omitted for clarity.

Previous, short (20 ps) AIMD calculations revealed an increase in the average coordination number of V^{5+} in BVO-148 from 4 to 4.31 caused by O^{2-} diffusing from the Bi-O sublattice to V-O tetrahedra as well as similar oxide ion exchange and migration mechanisms as observed in BVO-087. Despite that and the fact that BVO-148 is an excellent ionic conductor, its conductivity is lower than that of BVO-087. This is attributed to the higher V-doping resulting in shorter distances between

separate VO_x polyhedra. Therefore, the three dimensional, δ-Bi_2O_3-like sublattice, which is one of the factors contributing to the remarkably high conductivity of BVO-087, is strongly disrupted in BVO-148.[108,169]

Despite having the same structural motifs, BVO-087 and BVO-148 adopt different superstructures. While $Bi_{0.913}V_{0.087}O_{1.587}$ has a pseudo-cubic $3 \times 3 \times 3$ δ-Bi_2O_3 ordered superstructure, the higher-doped $Bi_{0.852}V_{0.148}O_{1.648}$ adopts a monoclinic, ordered fluorite superstructure with layers of Bi and O being interspersed with V-O containing layers,[169] as shown in figure 3.2. A similar structure has been reported for $Bi_{0.852}P_{0.148}O_{1.648}$ (BPO-148), with P-O layers instead of V-O layers.[171] These structures can be described as containing a Bi-O sublattice and a dopant sublattice. The Bi-O sublattice contains OBi_4 as well as OBi_3 groups. These tetrahedral and trigonal groups are connected by edge- and corner sharing, which provides oxide ion diffusion pathways.[169] The VO_4 and PO_4 tetrahedra are all isolated.

An extensive multinuclear (^{17}O, ^{51}V, ^{31}P) variable-temperature solid-state NMR study[172] on BVO-087, BVO-148, and BPO-148 supports the exchange of oxide ions between the Bi-O and V-O sublattice suggested by AIMD simulations, highlighting the contribution of the VO_x polyhedra to the high conductivities. ^{17}O NMR reveals that oxygen atoms in BVO-148 and BVO-087 behave comparably with increasing temperatures, with resonances assigned to O^V (oxygen atoms in the V-O sublattice) and O^{Bi} (oxygen atoms in the Bi-O sublattice) first narrowing and then reappearing as a single signal at 825 K.[172] In contrast, the O^P and O^{Bi} resonances in BPO-148 do not merge at high temperatures, which is consistent with a lack of oxide ion exchange in the phosphate due to the strong preference of P^{5+} for tetrahedral coordination. From the ^{17}O spin-lattice relaxation times, activation energies of the probed motions can be extracted. For the motion of O^{Bi} atoms, the activation energies are 0.16 ± 0.02 eV for BVO-148 and BVO-087, and 0.11 ± 0.02 eV for BPO-148. These are assigned to local nearest-neighbour jumps of oxide ion vacancies in the Bi-O sublattice. From the temperature dependence of the central transitions, the activation energies for motions in the dopant sublattices were determined, and the small values of 0.06 ± 0.02 eV, 0.07 ± 0.02 eV, and 0.04 ± 0.02 eV for BVO-148, BVO-087, and BPO-148[172] respectively, are consistent with the small energy barrier

expected for rotations of polyhedra.[173,174]

3.2.1 Aims of this Work

The aim of the work presented in this chapter is to study the effect of the dopant on localised and long-range dynamics in the isostructural δ-Bi_2O_3-based materials BVO-148 and BPO-148. Direct observation of the pico- and nanosecond dynamics will be attempted by performing QENS experiments at various temperatures as well as on two different instruments. This should allow a separation of the nanosecond dynamics in the Bi-O sublattice and the picosecond dynamics in the dopant sublattices. AIMD simulations will be used to aid analysis of the QENS data, and the potential of AIMD to simulate the neutron scattering function S(Q, ω) directly will be tested. The results shown in this chapter have been published in Chemistry of Materials.[175]

3.3 Experimental Methods

3.3.1 Synthesis

Large (10 g) polycrystalline samples of BVO-148 and BPO-148 were prepared according to previous literature,[109,169,170] using stoichiometric amounts of Bi_2O_3 (Aldrich, 99.9 % pure), V_2O_5 (Aldrich, > 99.6 % pure) and $(NH_4)H_2PO_4$ (Aldrich, > 99.5 % pure). The reagents were ground under isopropanol using an agate mortar and pestle and heated in open alumina crucibles at 700 °C, 750 °C, 800 °C, and either 825 °C for $Bi_{0.852}V_{0.148}O_{1.648}$ or 850 °C for $Bi_{0.852}P_{0.148}O_{1.648}$ for 12 h at each temperature, with intermittent grinding under isopropanol after each heating. To confirm sample purity, powder X-ray diffraction (PXRD) patterns were collected on a Bruker D8 ADVANCE diffractometer using Cu Kα radiation. The patterns were analysed using the Rietveld method[119] implemented in Topas Academic.[121]

3.3.2 Quasielastic Neutron Scattering (QENS)

Neutron scattering data were collected on the time-of-flight spectrometer IN5 and the backscattering spectrometer IN16b at the Institut Laue-Langevin (ILL) in Grenoble.[176] The sample holder used was a cylindrical Nb can (diameter ≈ 8 mm, sample height ≈ 5 cm), which was placed in a furnace.[177]

For the IN5 experiment, an incident neutron wavelength of 4.8 Å giving a resolution of ≈ 86 μeV (FWHM) was used, providing insight into the fast (picosecond) dynamics. Data on BVO-148 were recorded for 2h each at RT, 400, 500, 600 °C, and on BPO-148 at 100 °C for 2 h, at 200 and 400 °C for 1 h each and at 500 and 600 °C for 4 h each. Data were also recorded on the empty Nb cell for 3.5 h and a vanadium sample for 30 min for data reduction. For the analysis, the room temperature data were used as resolution.

On IN16b, the incident neutron wavelength was 6.271 Å and the instrument resolution was ≈ 0.8 μeV (FWHM), giving access to dynamics on the nanosecond timescale. On heating from room temperature to 600 °C for the vanadate, and to 800 °C for the phosphate, elastic (E = 0 μeV) and inelastic (E = 2 μeV) scattered intensities were measured, so called elastic and inelastic fixed window scans[178] (EFWS, IFWS), in steps of 25 K, for 5 min and 30 min, respectively. During this heating ramp, QENS measurements were performed at 25, 200, 400, 500, and 600 °C with collection times between 10 h and 12 h per temperature, and an energy transfer window of 7 μeV. Using the same energy transfer window, measurements were also performed on the empty Nb sample holder (2.5 h) for data reduction and analysis.

The data from both IN5 and IN16b were reduced and analysed using the Mantid[136] software.

3.3.3 Computational Methods

Ab initio molecular dynamics calculations were performed using the density functional theory (DFT) method implemented in the Vienna ab initio simulation package (VASP) code.[75] As starting point, the structural models previously reported

for $Bi_{0.852}V_{0.148}O_{1.648}$ and $Bi_{0.852}P_{0.148}O_{1.648}$, transformed into P1 symmetry, were used. To preserve the nominal compositions while also ensuring full occupancy of all crystallographic sites in the simulation boxes, V and O atoms were removed from BVO-148 using a random number generator, and likewise Bi and O atoms from BPO-148, while maintaining a tetrahedral environment around the dopant cations. The atomic contents of the simulation boxes generated in this way were $Bi_{92}V_{16}O_{178}$ and $Bi_{92}P_{16}O_{178}$, in agreement with the nominal compositions. For all simulations, projector augmented wave (PAW) pseudopotentials[154] with the GGA-PBE (Perdew-Burke-Ernzerhof generalized-gradient-approximation) functional[155] were used. The electronic structure was sampled at the gamma-point only due to the large number of atoms in the simulation box. For both materials, AIMD calculations were performed at 500, 800, 950, 1100, 1250, and 1400 °C in the NVT ensemble, using a time step of 2 fs and a cutoff energy of 400 eV to simulate a total of 400 ps per temperature for each material. The data analysis was carried out using the MDANSE code.[156]

3.4 Results and Discussion

3.4.1 Structural Characterisation

The PXRD patterns of large samples of $Bi_{0.852}V_{0.148}O_{1.648}$ and $Bi_{0.852}P_{0.148}O_{1.648}$ used for neutron scattering experiments are shown in figure 3.3.

Rietveld refinements[119] were performed using the structural data reported by Darriet et al.[171] for the phosphate and Kuang et al.[169] for the vanadate as initial model. Aside from the unit cell parameters, the zero point, scale factor, one global isotropic temperature factor and pseudo-Voigt peak shape function parameters were refined. The background was modelled using a 9 parameter Chebyshev polynomial. The lattice parameters obtained for $Bi_{0.852}V_{0.148}O_{1.648}$ (a = 19.9977(3) Å, b = 11.5919(2) Å, c = 21.1539(4) Å, β = 111.342(1) °) and $Bi_{0.852}P_{0.148}O_{1.648}$ (a = 19.6524(2) Å, b = 11.4466(1) Å, c = 21.1502(3) Å, β = 112.378(8) °) are in good agreement with previously reported data.[169,171] This, combined with the

good fits of the Rietveld refinements, indicates that BVO-148 and BPO-148 were synthesised successfully as pure samples, and these samples were therefore used for further study.

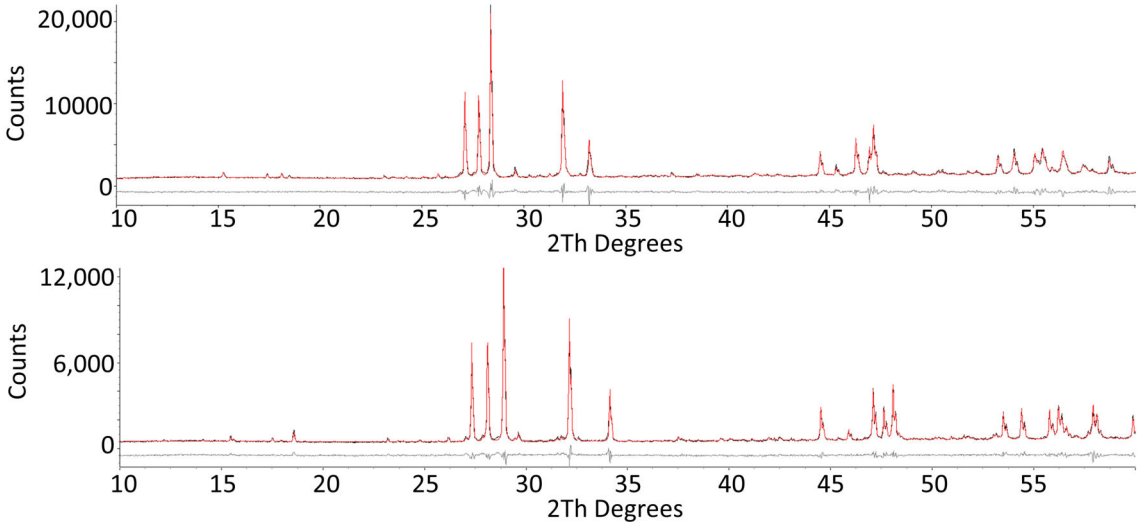

Figure 3.3: PXRD patterns of BVO-148 (top) and BPO-148 (bottom) samples used for neutron scattering experiments. The black curve shows the observed data, red the calculated Rietveld fit and grey the difference between them.

3.4.2 Nanosecond Dynamics in BVO-148 and BPO-148

Figure 3.4 shows the elastic and inelastic fixed window scans (EFWS, IFWS) for BVO-148 and BPO-148 collected on IN16b.[178] Both EFWS and IFWS were corrected for the sample can contributions. In addition to that, the IFWS were corrected for a residual elastic contribution which was apparent below 200 °C, by rescaling the EFWS and subtracting the slope obtained from EFWS below 200 °C from the IFWS. The small decrease of inelastic intensity below 200 °C for BVO-148 seen in figure 3.4 is caused by elastic leakage which could not be fully corrected for with this procedure.

These scans measure the inelastic intensity at a defined energy offset close to the elastic peak (± 2 μeV) as a function of temperature. The onset of dynamics in a system causes a broadening of the elastic peak (QENS signal), resulting in an increase in inelastic intensity at the chosen energy offset. Therefore, IFWS can be used to estimate in which temperature range the systems dynamics can be observed

as the wing of the quasielastic signal reaches the fixed observation energy, or becomes too broad with respect to that energy. There is a clear increase in inelastic intensity at 200 °C as the dynamics enter the measured energy transfer window. This results in a broad maximum at around 420 °C for BVO-148 and 500 °C for BPO-148 (figure 3.4). At higher temperatures, faster dynamics lead to a decrease in the IFWS intensity as the QENS broadening becomes larger than the observed energy transfer window. Assuming an Arrhenius process, the IFWS intensity has the following temperature dependence:[178]

$$I_{\omega_{\text{off}}}^{\text{IFWS}}(T) \propto \frac{B}{\pi}[1 - A(Q)]\frac{\tau(T)}{1 + \omega_{\text{off}}^2\tau(T)^2} \tag{3.1}$$

where $I_{\omega_{\text{off}}}^{\text{IFWS}}$ is the intensity of the IFWS at the chosen energy offset ω_{off}, B a constant taking into account the instrument resolution, $A(Q)$ the elastic incoherent structure factor, and the relaxation time $\tau(T)$, the inverse of the measured linewidth, is given by:

$$\tau(T) = \tau_0 \times e^{\frac{E_a}{k_B T}} \tag{3.2}$$

where E_a is the activation energy, k_B the Boltzmann constant and τ_0, the Arrhenius prefactor, the relaxation time at infinite T. Since, in this work, the IFWS intensity was summed over all detectors, the Q-dependence in equation 3.1 is ignored, and the prefactor $\frac{B[1-A(Q)]}{\pi}$ becomes a single fitting constant.

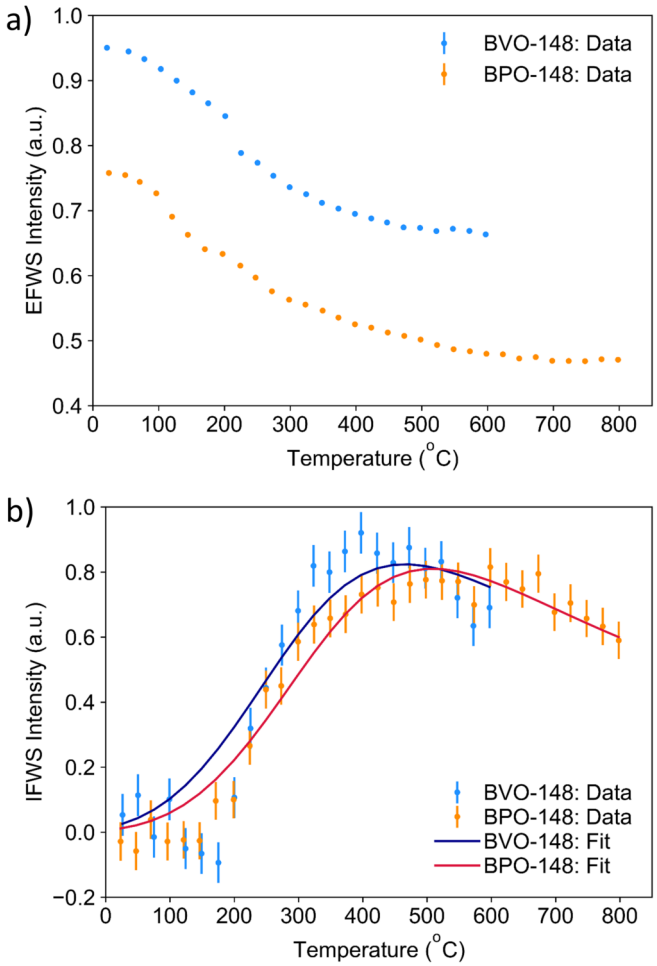

Figure 3.4: Plots of the elastic intensity (a) and the inelastic intensity (b) for BVO-148 and BPO-148 measured at 2 μeV and summed over all measured Q as a function of temperature. The fits (using equation 3.1) of the IFWS are shown as solid lines (b) and indicate a maxima at 420 °C for BVO-148 and 500 °C for BPO-148. For BVO-148, the activation energy obtained from QENS (0.18 eV, see below) was used for fitting.

Using equation 3.1 to fit the IFWS allows for the activation energy of the observed dynamic process to be determined, giving a value of 0.20 ± 0.01 eV for BPO-148, as shown in the red fit in figure 3.4. For BVO-148, the activation energy obtained from QENS (0.18 eV, see below) was used, and the good fit shown in figure 3.4 confirms that both the IFWS and QENS probe the same process. The isostructural nature of BVO-148 and BPO-148 as well as the good agreement of the onset temperatures and activation energies of the dynamics, suggests that the same type of dynamics is measured in both compounds.

The Q-dependence of the Arrhenius prefactor obtained from the fits of the IFWS at individual Q values, using the activation energy as a global parameter, is shown in figure 3.5 and provides additional information on the diffusive process. This prefactor describes the linewidth at infinite temperature of both materials and appears constant within the accessed Q-range, indicating that the observed dynamics are primarily localised.[178]

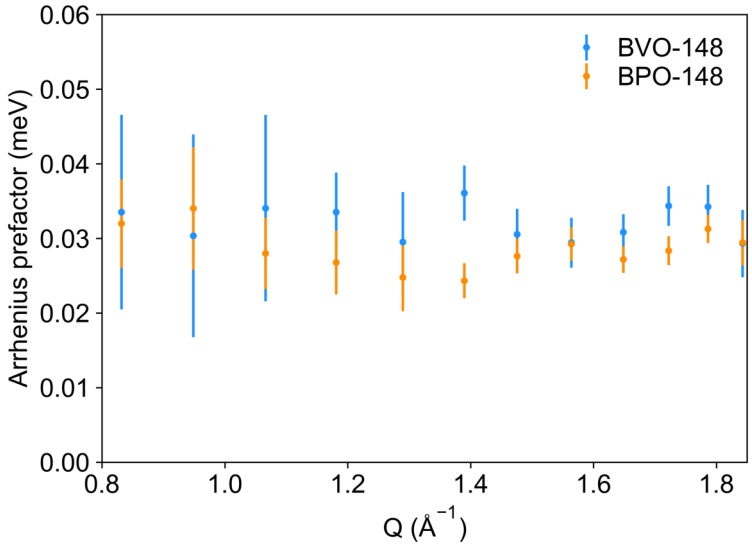

Figure 3.5: The Arrhenius prefactor obtained from fitting the IFWS collected on IN16b. It is related to the relaxation time, and the lack of Q-dependence suggests localised motions observed on the nanosecond timescale.

Plots of the scattering function S(ω) at room temperature and at 400 °C for BVO-148 and BPO-148 are shown in figure 3.6. The neutron scattering cross section of oxygen is moderate and fully coherent, which generally means that the observed QENS broadening is small, making the analysis of experimental results challenging. Therefore, data were summed over selected detectors in which the broadening was most apparent, covering a Q-range of 1.39 to 1.74 Å^{-1}. The QENS signal is significantly weaker than that reported for the pseudo-cubic BVO-087[108] which is consistent with impedance data showing the lower conductivity of the monoclinic materials BVO-148 and BPO-148.[169,170]

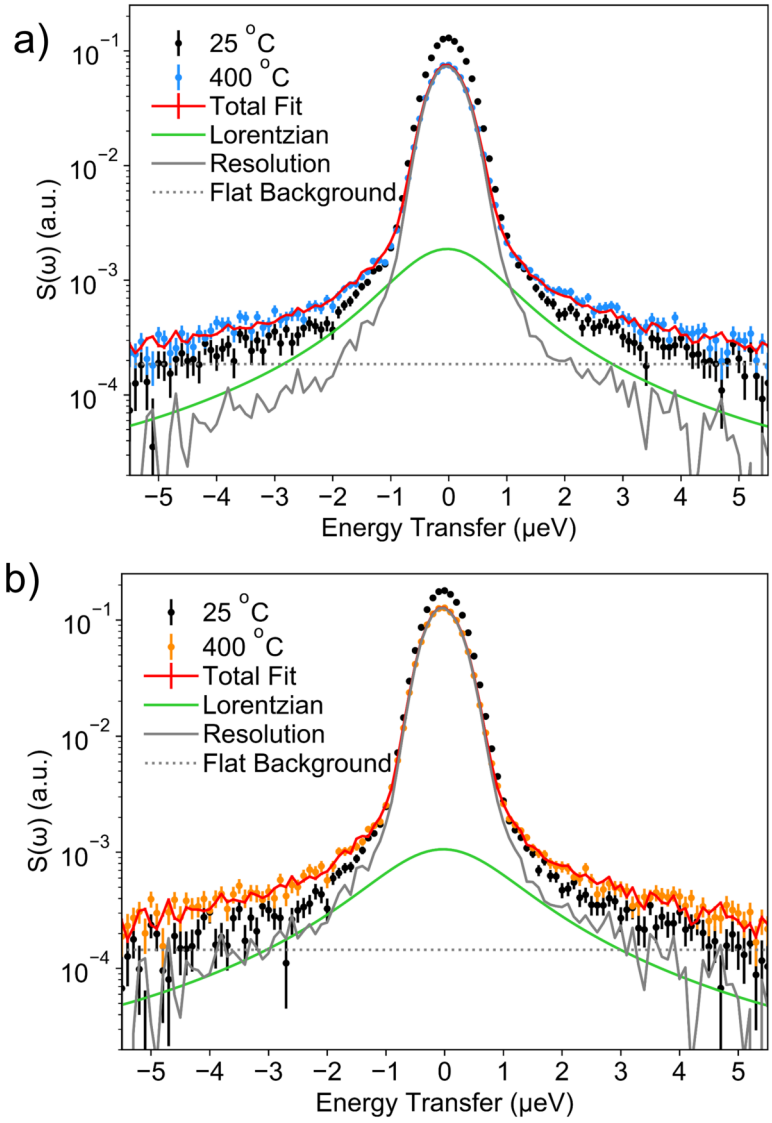

Figure 3.6: Total scattering function S(ω) of BVO-148 (a) and BPO-148 (b) measured on IN16b at room temperature and at 400 °C. Fits of the 400 °C data using equation 3.3, showing the different contributions. The data were summed over the detectors where the broadening was clearest, covering a Q-range from 1.39 to 1.74 Å^{-1}.

The Q-integrated scattering function S(ω) was fitted as shown in equation 3.3, using a single Lorentzian function L of full width at half maximum (FWHM) Γ and amplitude A, and a delta function $\delta(\omega)$ of height h, whose sum was then convoluted with the resolution function $R(\omega)$. A flat background B was also added.

$$S(\omega) = R(\omega) \otimes [h\delta(\omega) + AL(\Gamma, \omega)] + B \tag{3.3}$$

The FWHM of the Lorentzian has an Arrhenius type relationship to the activation energy of the process causing the broadening,[91] and could be extracted at three temperatures for the vanadate (figure 3.7), giving an activation energy of 0.18 ± 0.04 eV. For BPO-148, some broadening at 400 °C could also be observed as shown in figure 3.4, but due to the weak temperature dependence of the dynamics above 400 °C, no activation energy from the QENS data could be extracted.

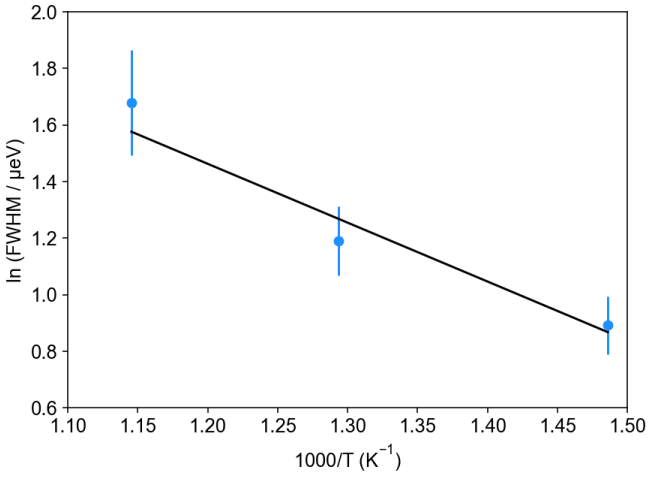

Figure 3.7: Arrhenius-type plot of the FWHM (μeV) obtained from fitting the IN16b data at various temperatures for BVO-148.

The activation energy found for BVO-148 is in good agreement with that of 0.16 ± 0.02 eV found by ^{17}O T_1 relaxation measurements from solid state NMR for dynamics in the Bi-O sublattice, which the authors ascribed to nearest neighbour vacancy jumps.[172] Despite impedance data showing significant ionic conductivity for BVO-148 in the measured temperature range,[169] this long-range diffusion is likely too slow to fall completely within the timescale probed by IN16b, meaning that the nanosecond dynamics observed in this study on BVO-148 and BPO-148 are predominantly local nearest neighbour jumps.

3.4.3 Picosecond Dynamics in BVO-148 and BPO-148

To obtain a more complete insight into the dynamics, and one which can be directly compared to the AIMD calculations which will be discussed in the following section, measurements probing the picosecond timescale on IN5 were performed.

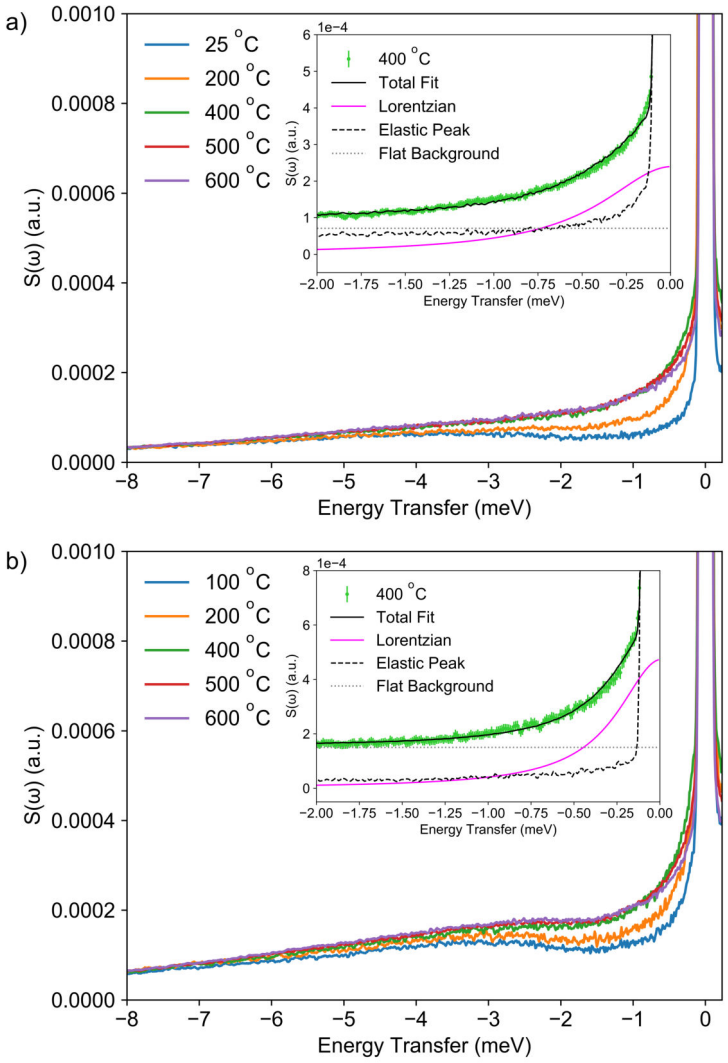

Figure 3.8: S(ω) of (a) BVO-148 and (b) BPO-148 collected on IN5 at various temperatures and summed over Q = 1.6 - 1.8 Å^{-1}. The insets show the fit of the data at 400 °C using a convolution of the resolution with a delta function for the elastic peak and a Lorentzian function for the QENS signal.

Simple temperature effects were taken into account by scaling the experimental spectra to room temperature using the Debye-Waller (f_{DW}) and Bose population factors (f_{BP}):

$$f_{BP} = \frac{\exp(\frac{-\omega}{k_b \times T}) - 1}{\exp(\frac{-\omega}{25.9}) - 1} \quad \text{and} \quad f_{DW} = \frac{\exp(-Q^2 \times (B \times 300))}{\exp(-Q^2 \times (B \times T))} \tag{3.4}$$

where ω is the energy transfer, k_B the Boltzmann constant (in meV K^{-1}), Q the

momentum transfer, and B a factor which, multiplied by the temperature, gives the mean-square displacement $\langle u^2 \rangle_T$. The factor 25.9 is $k_B \times T$ at 300 K. The resulting curves, exhibiting a clear quasielastic broadening with increasing temperature, are shown in figure 3.8.

This observation is in contrast with the results previously obtained for BVO-087, where measurements performed on the IN6 spectrometer did not show any observable dynamics on the picosecond timescale.[108] In that case, the authors hypothesised that either the local dynamics take place on a different timescale to that of IN6 or that the signal was too weak to be observed.

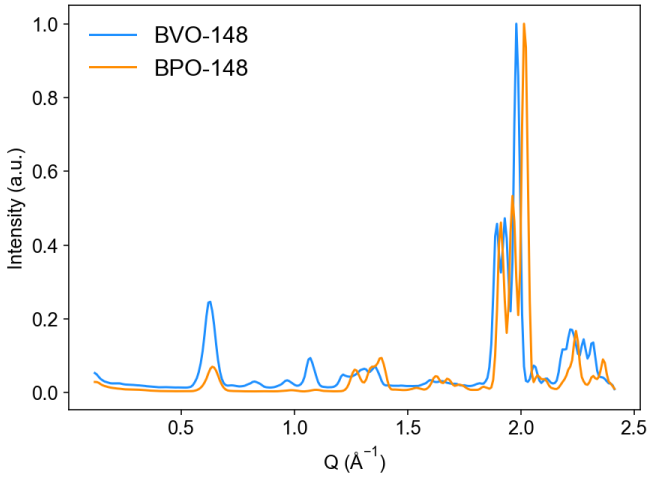

Figure 3.9: Diffraction patterns of BVO-148 and BPO-148 from neutron scattering experiments on IN5 at 500 °C.

In our present study, the higher V-doping results in a larger number of oxide ions moving in the V-O sublattice, causing a larger signal. Additionally, the experimental setup (better resolution of purely Gaussian shape) in our current investigation compared to the one used previously on BVO-087[108] facilitates the observation of a small QENS signal in the meV range (figure 3.8).

The complex fluorite superstructures in which BVO-148 and BPO-148 crystallise lead to Bragg peaks in large parts of the measured Q-range, as shown in figure 3.9. In addition to that, below 0.8 Å^{-1} the signal was too weak to be fitted. Therefore, to analyse the temperature dependence of the elastic broadening, only data in the Q-range of 1.6 - 1.8 Å^{-1} were summed and used for fitting with the model described

by equation 3.3. A plot of Lorentzian linewidth against temperature for BVO-148 and BPO-148 is shown in figure 3.10.

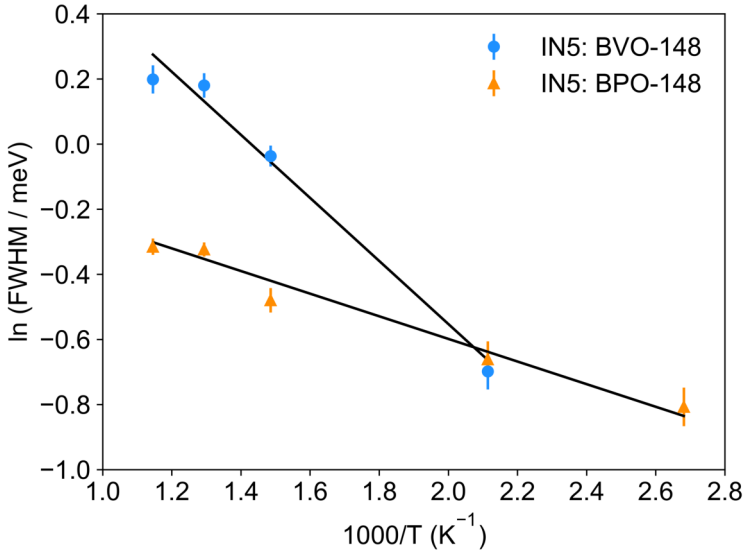

Figure 3.10: Arrhenius-type plot of the FWHM (meV) obtained from fitting experimental IN5 S(Q, ω) data summed over a Q-range of 1.6-1.8 Å^{-1}, giving the activation energy of the picosecond dynamics observed on IN5.

The extracted activation energies are 0.083 ± 0.009 and 0.030 ± 0.004 eV for the vanadate and phosphate, respectively. These values are in excellent agreement with NMR data for motions in the V-O (0.06 ± 0.02 eV) and P-O (0.04 ± 0.02 eV) sublattices,[172] as well as with the small activation barriers of 0.05 - 0.07 eV previously reported for other tetrahedral species like MnO_4 and SO_4^{2-}.[173,174] This suggests that the dynamics observed here on IN5 are localised motions of O atoms within the VO_x and PO_4 polyhedra. A similar flexibility of VO_x polyhedra has also been reported for Sr-doped $BiVO_4$.[179] The activation energy of rotation of VO_x polyhedra determined from IN5 data is higher than that for rotation of PO_4. One explanation for this could be the on average shorter P-O bond length compared to V-O. Typical bond lengths in VO_4 and VO_5 polyhedra are 1.72 and 1.82 Å respectively,[180] and the typical bond length in PO_4 is 1.53 Å.[180] This leads to PO_4 tetrahedra being smaller compared to VO_x polyhedra, resulting in shorter O-O distances and therefore a lower activation energy for jumps between oxygen sites on the apices of the coordination polyhedra.

3.4.4 AIMD Simulations of Oxide Ion Dynamics in BVO-148 and BPO-148

While direct observation of dynamics with QENS generally allows for a very detailed analysis of different motions in ionic conductors, this is severely limited for oxide ion conductors due to the relatively small and fully coherent character of the neutron scattering cross section of oxygen.[135] Additionally, in structurally complex materials like the ones investigated here, the presence of Bragg peaks makes the analysis of the Q-dependence of the QENS signal extremely difficult or even impossible. AIMD calculations have previously been used to gain a better understanding of the observed dynamics and show good compatibility with QENS.[29,95,99,108,169]

Preliminary AIMD simulations[169] suggested that the average coordination number of V in BVO-148 increases during the simulation at elevated temperatures as a result of oxide ions diffusing from the Bi-O sublattice into the V-O sublattice. A recent solid state NMR study[172] suggested an increase in oxide ion exchange between the Bi-O and V-O sublattices with increasing temperatures for BVO-087 and BVO-148, but only very limited exchange in BPO-148. This structural aspect was addressed by our AIMD simulations. Figure 3.11 depicts the average coordination number of all V and P atoms in the simulation boxes at 500 and 1100 °C during the first 100 ps of the simulation. At 500 °C, there is some variation in the coordination number of V, but the average value of 4.02 corresponds to all V being tetrahedral. At 1100 °C, the average coordination environment of V varies significantly. The average coordination number at 1100 °C is 4.12, corresponding to 2 out of 16 V being 5-coordinate, and reaches a maximum of 4.37, where 6 out of 16 V are 5-coordinate. In contrast to that, the average coordination number of P at both, 500 and 1100 °C is 4.00, showing that P essentially remains tetrahedral.

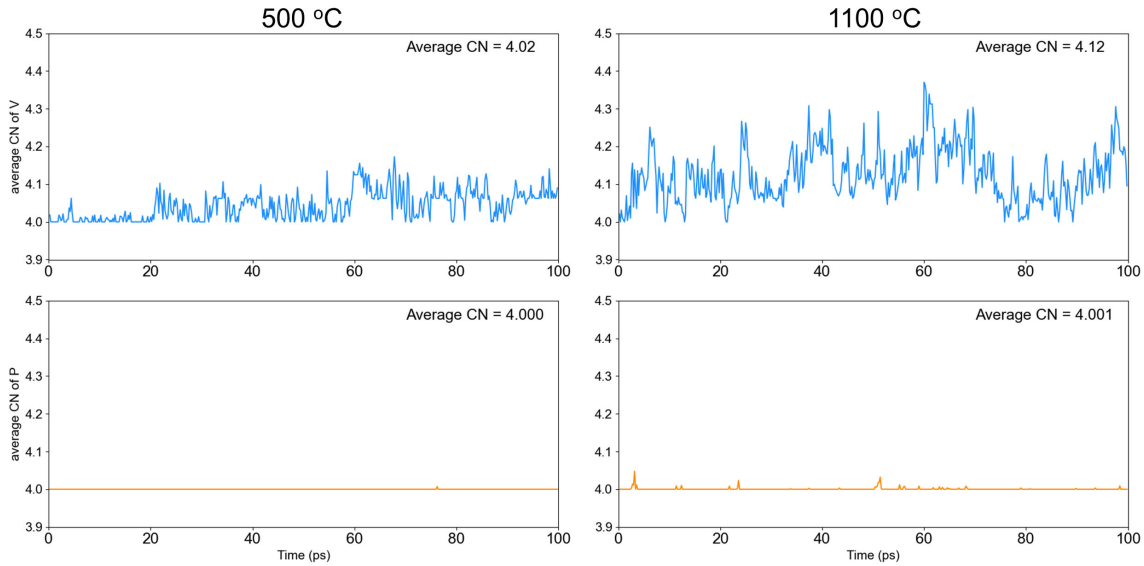

Figure 3.11: Average coordination number (CN) of V in BVO-148 (top) and P in BPO-148 (bottom) derived from AIMD simulations at 500 and 1100 °C.

Counting the number of jumps helps quantify the coordination number plot (figure 3.11). A jump was defined as an oxide ion moving more than 1.5 Å over 1 ps during the entire simulation at both 500 °C and 1100 °C, and the results of this analysis are summarised in table 3.1. To gain more detailed insight into the dynamics, oxygen atoms were separated into two groups, depending on the sublattice in which they originated at the start of the simulation, i.e. V/P-O and Bi-O. Comparing the results for BVO-148 and BPO-148 shows that, at both temperatures, the number of total jumps are comparable between the two materials. The distribution of jumps, however, differs. At 500 °C, significant dynamics in the Bi-O sublattice are apparent in BVO-148, while in BPO-148 the number of jumps is only approximately $\frac{1}{3}$ of that. At 1100 °C, in BVO-148, the jumps of oxide ions in both sublattices contribute almost equally to the total number of jumps, while in BPO-148 dynamics in the P-O sublattice are still clearly dominant.

The analysis also shows that, while some inter-sublattice jumps in BVO-148 are apparent even at 500 °C, the sublattice exchange increases significantly at 1100 °C. In contrast, very few such jumps are observed in BPO-148. The number of jumps from the Bi-O sublattice into the V-O sublattice in BVO-148 is larger than vice versa, which is in good agreement with the observed increase in average V-O

coordination number.

Jump type	500 °C		1100 °C	
V-O	2934	88 %	5831	46 %
Bi-O	301	9 %	6235	49 %
V-Bi	39	1 %	260	2 %
Bi-V	53	1.5 %	319	2.5 %
Total	3327		12664	

Jump type	500 °C		1100 °C	
P-O	3722	97 %	10534	85 %
Bi-O	96	3 %	1795	14 %
P-Bi	0	0 %	0	0 %
Bi-P	0	0 %	2	0.02 %
Total	3818		12331	

Table 3.1: Number of oxide ion jumps counted over the entire simulation at two different temperatures for BVO-148 (top) and BPO-148 (bottom). V/P-O describes jumps around one V/PO_x polyhedra, Bi-O describes jumps in the Bi-O sublattice, V/P-Bi and Bi-V/P describes jumps from one sublattice into the other.

In doped bismuth oxides, migration of oxide ions into the dopant sublattice creates additional vacancies in the Bi-O sublattice.[108,109] An increase in this hopping rate with temperature therefore results in faster dynamics in the Bi-O sublattice, In contrast to that, there is only limited oxide ion exchange in BPO-148 as shown by our simulations. This directly shows the importance of a dopant that readily adopts various coordination environments to achieve faster dynamics and therefore a high conductivity.[34,99,108,161,169]

To allow direct comparison of AIMD to experimental data, S(ω) was simulated for both BVO-148 and BPO-148 using the resolution of IN5 at 4.8 Å and the various simulated temperatures. To allow comparison to IN5 data, the same scaling using equation 3.4 was applied to the simulated data. The variation of the corrected S(ω), summed over a Q-range of 1.6 - 1.8 $Å^{-1}$, with increasing temperature is shown for BPO-148 in figure 3.12.

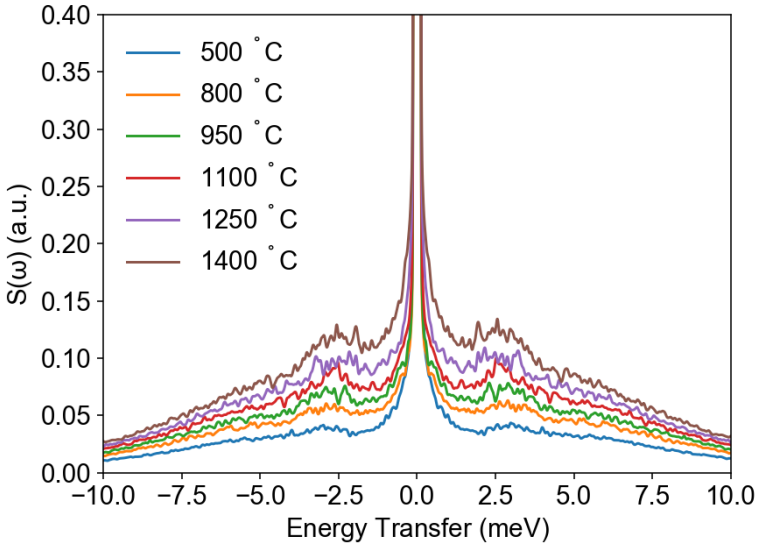

Figure 3.12: Simulated S(ω) of BPO-148 obtained from AIMD trajectories at various temperatures and summed over Q = 1.6 - 1.8 Å^{-1}.

The small fluctuations of the simulated data at all temperature are artifacts of the Fourier transform of the AIMD trajectory. The presence of an inelastic peak in the simulated S(ω) data between -2 and -3 meV agrees well with that observed on IN5. While, in the experimental data, this feature limited the energy range over which the data could be fitted, it can be accounted for in the simulated data and therefore fitting was possible over a larger energy range. To achieve this and at the same time minimise the effect of the data fluctuation on the final fit, both, S(ω) of the whole system, as well as S(ω) of Bi and V/P, excluding all oxygen atoms, were simulated separately. During the fitting, S(ω) of BiV or BiP was used as resolution and, similarly to the IN5 data, convoluted with a delta function, Lorentzian function and flat background. A representative fit at 1100 °C is shown in figure 3.13.

From the temperature dependence of the FWHM obtained from the fits of S(ω) for BVO-148 and BPO-148, activation energies of 0.069 ± 0.008 eV and 0.028 ± 0.004 eV, respectively, could be determined. A comparison of the experimental and simulated FWHM is shown in figure 3.14. The difference in experimental and simulated FWHM, which is apparent in figure 3.14, can be explained by the larger energy range over which the simulated data was fitted in order to improve the quality of the fit, compared to the energy range over which the experimental data could be

fitted. Nevertheless, the temperature dependence of the QENS signal is reproduced well, and the excellent agreement of experimental and simulated activation energies confirms that the same dynamics are observed by both methods. This validates the simulations, warranting their further, in-depth analysis.

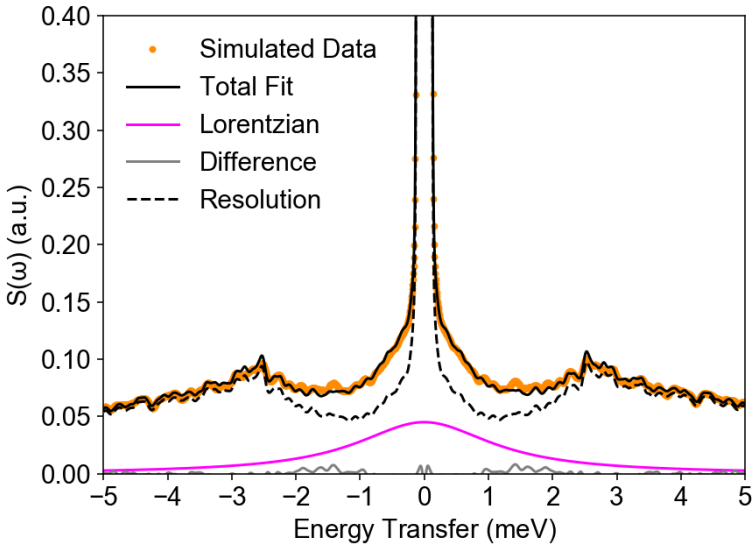

Figure 3.13: Representative fit of the simulated S(ω), summed over a Q-range of 1.6 - 1.8 Å^{-1}, data obtained from AIMD trajectories at 1100 °C of BPO-148.

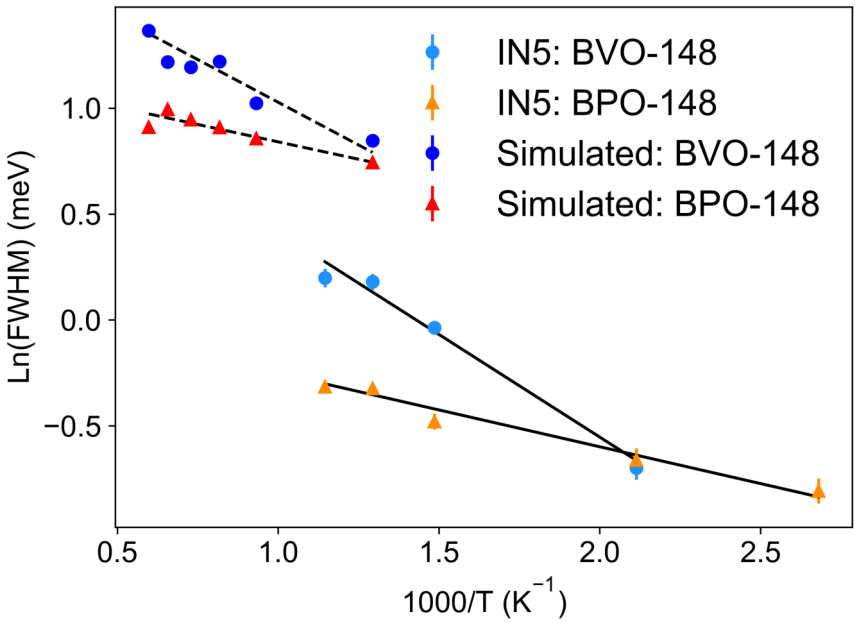

Figure 3.14: Arrhenius-type plot of the FWHM (meV) obtained from simulated S(ω) data, compared to experimental S(ω) data, both summed over the same Q-range.

Firstly, it allows extraction of the elastic incoherent structure factor (EISF), a parameter which, due to the essentially purely coherent scattering nature of oxygen, is not generally obtainable from experiments. It can be related to the space accessible to scattering atoms for localised motions, thereby providing information about the geometry of the dynamics.[132] The EISF was extracted from the value of the simulated self-intermediate scattering function for oxygen at 500 °C and 300 ps. For this purpose, oxygen atoms were again grouped into two categories depending on the sublattice in which they start the simulation.

Figure 3.15 shows the EISF of the oxygen atoms in the V-O and P-O sublattices corrected by the Debye-Waller factor, using the mean-square displacement obtained from the EISF of Bi. Fitting of the EISF shows that the dynamics on the picosecond timescale can be reasonably approximated by a model of diffusion on the surface of a sphere[132] in both BVO-148 and BPO-148.

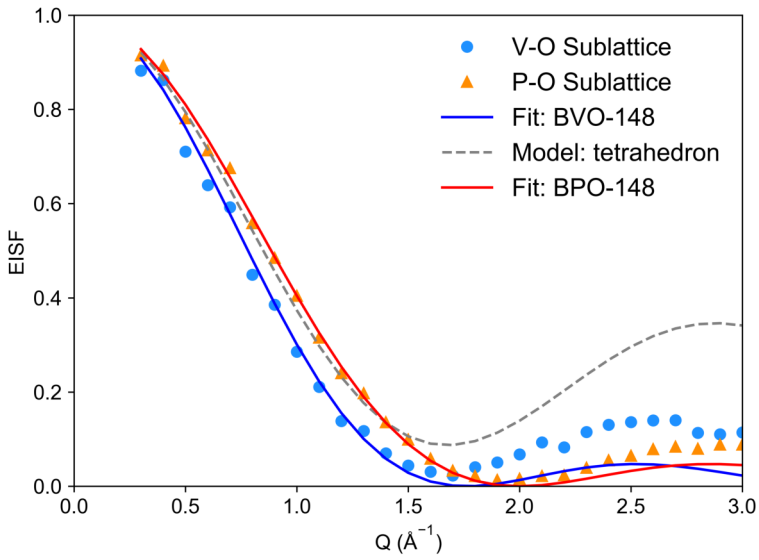

Figure 3.15: Simulated EISF, showing localised motion in the V-O and P-O sublattices in BVO-148 and BPO-148 which can be fitted with the diffusion on the surface of a sphere model; a fit of the EISF of BPO-148 using a jump diffusion over the four vertices of a regular tetrahedron is shown for comparison (grey dotted line).

As shown in figure 3.15, a model describing the jump diffusion over the four vertices of a regular tetrahedron (equation 2.26) is a worse fit to the data. For a uniform diffusion over a sphere, the EISF is given by equation 2.25. The fit of

this simple model to the AIMD-derived EISF for BVO-148 and BPO-148 is shown in figure 3.15. The model reproduces the data below the minimum very well, while some deviations at larger Q values are observed. This is not surprising, as the VO_x/PO_4 polyhedra cannot be expected to define a perfectly spherical surface. In addition to that, preferential orientations in some particular crystallographic directions will also result in deviations from the ideal isotropic spherical model. Nevertheless, the fit of a model describing diffusion on the surface of a sphere (equation 2.25) to the simulated EISF gives an estimate of the average rotational radii of 1.78 ± 0.04 and 1.57 ± 0.02 Å for the vanadate and phosphate, respectively, which are in very good agreement with known V-O and P-O distances.

The simulation time of 400 ps was not long enough to simulate IN16b data which probes a timescale of several nanoseconds. The mean-square displacements (MSDs) can nevertheless give reliable information about the long-range dynamics. The MSD curves for all oxygen atoms at all simulated temperatures for both materials are shown in figure 3.16. In both materials, the MSD curves increase without plateauing, showing long-range diffusion at elevated temperatures above 800 °C. The average MSD at all temperatures is higher in the vanadate than the phosphate, consistent with higher conductivity in BVO-148.[169,170] At 500 °C, the MSD curves corresponding to the oxide ions in both materials reach a constant value after a few ps. There are no signs of long-range diffusion, therefore the dynamics observed at this temperature are localised motions within the VO_x/PO_4 polyhedra. These relatively fast local motions are the origin of the simulated EISF shown in figure 3.15, as well as the QENS broadening observed in the meV regime in both, the experimental and simulated spectra.

Again, to gain a better understanding of the effect of the dopant on long-range diffusion, oxygen atoms were separated into V/P-O and Bi-O oxygen atoms depending on their original sublattice. A direct comparison of the MSD curves of oxygen atoms in each sublattice for both BVO-148 and BPO-148 can be seen in figure 3.17.

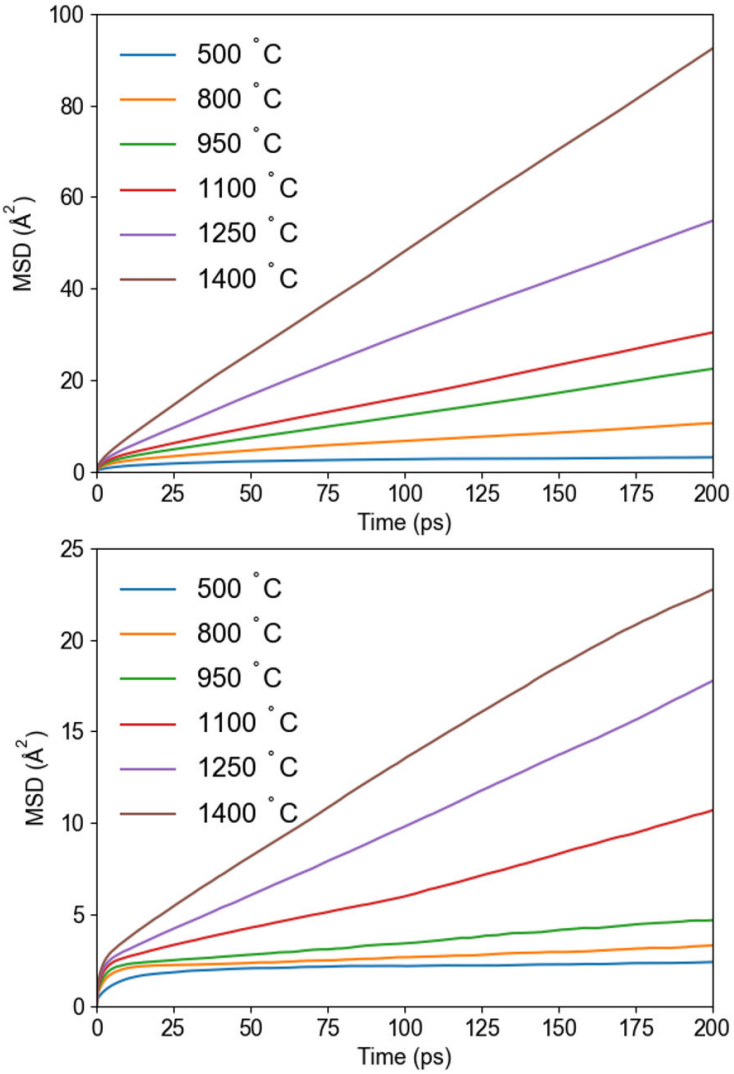

Figure 3.16: MSD curves of all oxygen atoms in BVO-148 (top) and BPO-148 (bottom) at all simulated temperatures.

At 500 °C, the plots for the dopant sublattice of both compounds show a clear plateau, indicating predominantly localised diffusion at this temperature as discussed previously, and while there is a small slope in the MSD of oxygen atoms starting in the Bi-O sublattice in both compounds, this indicates that long-range dynamics are very slow. As the temperature increases, the difference in the dynamics in the two materials becomes more pronounced, highlighting the difference in conduction mechanism in BVO-148 and BPO-148. The MSDs of oxygen atoms in the P-O sublattice suggest largely localised motions even at 1100 °C, and it is evi-

dent from figure 3.17 that ionic conductivity is dominated by the diffusion of Bi-O oxygen atoms, with little contribution of the P-O sublattice.

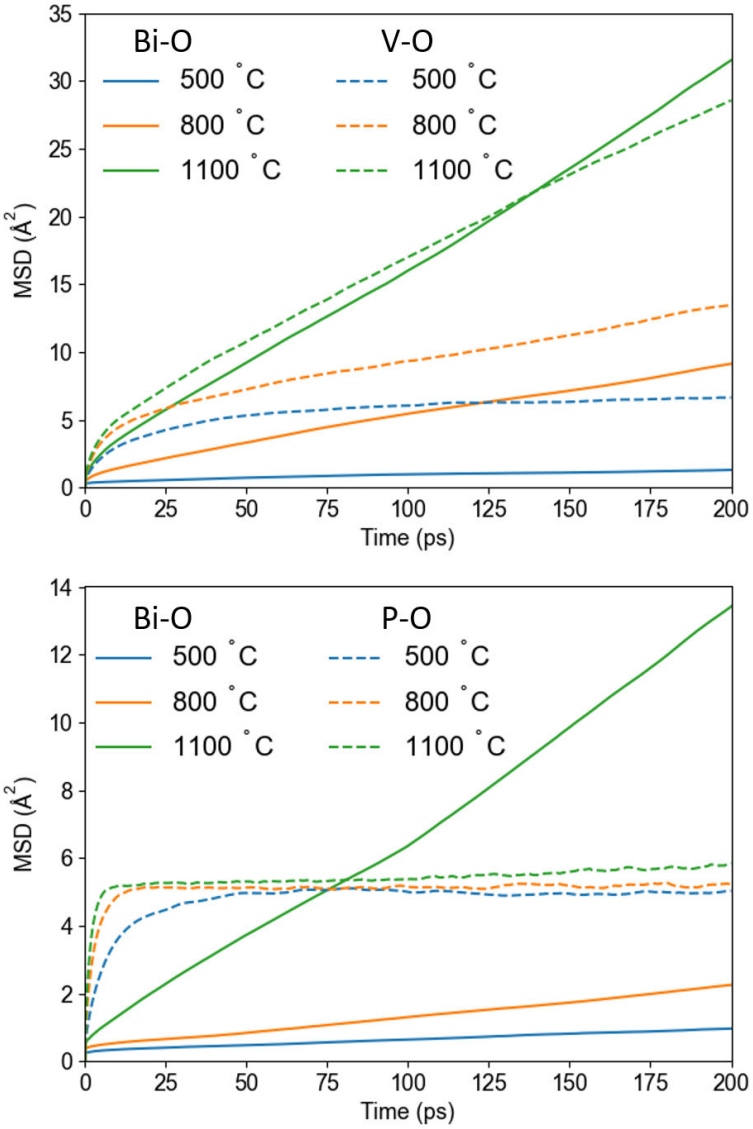

Figure 3.17: MSD curves for oxygen atoms initially in the V-O (top) or P-O (bottom) sublattice at 500, 800, and 1100 °C compared to MSD curves of oxygen atoms initially in the Bi-O sublattices.

In contrast to that, the MSD curves of oxygen atoms initially within the V-O sublattice show no sign of saturation at 800 °C and above due to the rapid exchange between sublattices at increased temperatures in BVO-148. The large number of jumps from one sublattice to another, as shown in table 3.1, makes a separation of oxygen atoms into their original sublattice difficult, which leads to the correlation

between Bi-O and V-O oxygen MSD curves for BVO-148.

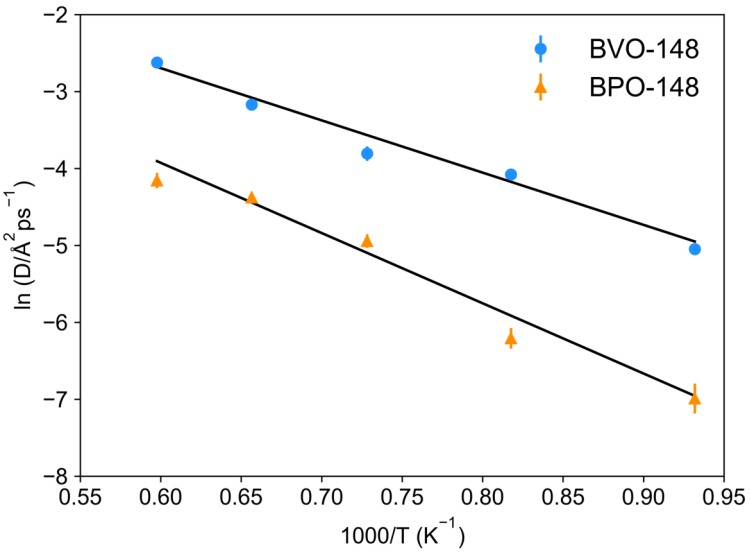

Figure 3.18: Arrhenius-type plot of the diffusion coefficients against inverse temperature for BVO-148 and BPO-148.

The slope of the MSD curves can be used to determine the diffusion coefficients, D, as described in the previous chapter by equation 2.47, which can then be used to calculate the activation energy for the long-range diffusion. Figure 3.18 shows the diffusion coefficients determined from the behavior of the MSD curves of all oxygen atoms, which are also summarised in table 3.2. The obtained activation energies are 0.60 ± 0.05 and 0.77 ± 0.07 eV for the vanadate and phosphate, respectively. These are slightly lower than values determined from impedance data (0.73 eV for BVO-148[169] and 0.85 eV for BPO-148[170]), a type of discrepancy which has often been found when comparing data from microscopic methods like AIMD simulations or NMR to impedance spectroscopy.[99,103,105,108,181,182] However, the higher activation energy of BPO-148 compared to BVO-148 is reproduced well, further validating the AIMD simulations. Examining the diffusion coefficients at 800 °C directly gives further insights into the long-range dynamics. The determined values are 9.5×10^{-7} cm^2 s^{-1} for BVO-148 and 0.6×10^{-7} cm^2 s^{-1} for BPO-148, i.e. about 15 times smaller in the latter, reflecting the inferior conductivity of the phosphate.

	D (cm^2 s^{-1})	
Temperature (°C)	BVO-148	BPO-148
800	1.0×10^{-6}	0.1×10^{-6}
950	1.7×10^{-6}	0.2×10^{-6}
1100	2.2×10^{-6}	0.7×10^{-6}
1250	4.2×10^{-6}	1.3×10^{-6}
1400	7.3×10^{-6}	1.6×10^{-6}

Table 3.2: Summary of the diffusion coefficients (D) obtained from MSD curves for BVO-148 and BPO-148.

Comparison to the value of pure δ-Bi_2O_3 at the same temperature,[95] 1.7×10^{-5} cm^2 s^{-1}, is consistent with the disruption of the Bi-O sublattice and the change from a cubic to a monoclinic structure decreasing conductivity. For BVO-087, the highest simulation temperature, 600 °C,[108] gives a diffusion coefficient of around 5×10^{-7} cm^2 s^{-1}, comparable to that of BVO-148 at 800 °C, showing that long-range dynamics are significantly faster in the former. This faster diffusion in BVO-087 supports the conclusions drawn from IN16b data, explaining why long-range motion could be observed in the previous study of BVO-087[108] but was outside the timescale covered by IN16b for BVO-148.

3.5 Conclusions and Future Work

In this chapter, a combination of QENS and AIMD was used to advance our understanding of the oxide ion dynamics in two good ionic conductors, $Bi_{0.852}V_{0.148}O_{1.648}$ and $Bi_{0.852}P_{0.148}O_{1.648}$, and the effect of the dopant on the dynamics and overall diffusion mechanism. Quantitative analysis of QENS data on two different timescales was possible for the first time in any oxide ion conductor, showing that, with new advances in neutron flux and instruments, QENS has become a very powerful probe for oxide ion dynamics.[175] Long-range dynamics are present in the Bi-O sublattice, resulting in motions on a nanosecond timescale. While relatively low activation energy and lack of Q-dependence observed for BVO-148 on IN16b suggests that

these dynamics are primarily short-range on the nanosecond timescale covered by this instrument, these local nearest neighbour jumps can be expected to directly influence bulk ionic conductivity. However, longer timescales are needed to observe long-range diffusion in BVO-148 and BPO-148 directly. The dominant oxide ion motion in the dopant sublattice is of localised nature and caused by rotations of PO_4 and VO_x polyhedra. This was observed on the picosecond timescale covered by IN5, and activation energies of 0.083 ± 0.009 eV and 0.030 ± 0.004 eV could be obtained.

AIMD simulations were used to help analyse the QENS data and gain further insight into the dynamics. Thanks to the long simulation times of 400 ps at six different temperatures, the scattering functions $S(\omega)$ could be simulated, which allowed a direct comparison to the IN5 QENS data. The activation energies of 0.069 ± 0.008 eV for the vanadate and 0.028 ± 0.004 eV for the phosphate are in excellent agreement with experimental data, further highlighting the compatibility of QENS and AIMD, and also warranting a more in-depth analysis of the simulations. The EISF demonstrated that the origin of the picosecond dynamics are fast rotational motions of the oxygen atoms in the dopant sublattice, a result which could not be obtained from QENS alone. Activation energies for the long-range diffusion obtained from MSD curves at various simulation temperatures agree well with previously reported impedance data.

The simulations reveal a distinct difference in dynamics in BVO-148 and BPO-148 caused by the choice of dopant. In BVO-148, the ability of V^{5+} to adopt variable coordination environments allows more oxide ions to move from the Bi-O sublattice into the V-O sublattice than vice versa, as is apparent in the increase of average coordination number as well as in the jump analysis. This introduces additional oxide ion vacancies in the Bi-O sublattice, facilitating faster long-range dynamics. In BPO-148, on the other hand, this exchange is severely limited due to the strong preference of P^{5+} to remain tetrahedrally coordinated. Because of that, no additional vacancies are introduced in the Bi-O sublattice, leading to slower long-range diffusion. This lack of exchange is also apparent when comparing the MSD curves of the Bi-O and P-O sublattice, which show that oxygen atoms in the dopant

sublattice in BPO-148 cannot contribute to long-range diffusion.

In the future, the onset of machine learning molecular dynamics (MLMD) methods could allow simulations on much longer timescales, up to several nanoseconds. This would allow comparison to QENS on a nanosecond timescale, providing an even more in-depth comprehension of dynamic processes occurring in various oxide ion conductors. With regards to the future design of potential oxide ion conductors based on δ-Bi_2O_3, the work presented in this chapter highlights the importance of using dopants which readily adopt various coordination environments, creating additional vacancies in the Bi-O sublattice and thereby enhancing the conductivity.

CHAPTER 4

Oxide Ion Conductivity in Complex Scheelite-Based Materials

4.1 Summary

This chapter presents a systematic study of the total conductivity of a series of complex scheelite-type oxide ion conductors with the general formulae $Bi_3(BO_4)(B'O_4)_2$ (B = Fe, Ga, $Fe_{0.9}Ti_{0.1}$; B' = Mo) and $Bi_3(B_2O_8)_{1/2}(B'O_4)_2$ (B = Sc, In; B' = Mo). Ti-doping was found to increase the conductivity of $Bi_3(FeO_4)(MoO_4)_2$, with $Bi_3(Fe_{0.9}Ti_{0.1}O_{4.05})(MoO_4)_2$ having the highest conductivity (1.5×10^{-3} S cm^{-1} at 800 °C) in this series. This suggests that interstitial oxide ion can be readily introduced.

4.2 Introduction

The tetragonal scheelite structure (space group $I4_1/a$) is named after the calcium tungstate mineral $CaWO_4$, the structure of which is shown in figure 4.1.

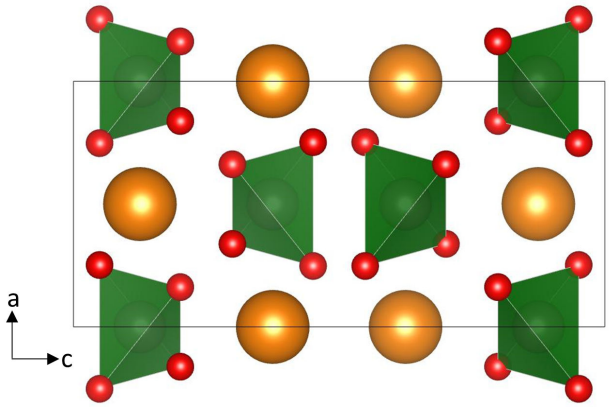

Figure 4.1: Unit cell of the scheelite structure ABO_4 using $CaWO_4$ as example. The eight-coordinate A cations (Ca-atoms) are shown in orange and the tetrahedrally coordinated B-site atoms (W) are shown as green polyhedra. Oxygen atoms are shown in red.

The general formula of this structure family is ABO_4, with the cations occupying the A site being eight-coordinated and the B-site cations being tetrahedrally coordinated. Materials crystallising in the scheelite structure have interesting properties like luminescence[183–185] and photocatalysis[186–188] and have also attracted attention due to their oxide ion, electronic and proton conducting properties.[179,182,189–194]

Both interstitial oxide ions as well as oxide ion vacancies have been reported to facilitate ionic conductivity in materials adopting the scheelite structure.[179,190,195,196] Oxide ion defects can be stabilised by tetrahedral units which can deform and rotate, and oxide ion conductivity has been reported in several materials which crystallise in structures consisting of isolated tetrahedra.[26,34,51,99,179] If the central cations of these tetrahedra can adopt various coordination geometries, interstitial oxide ions can be incorporated and stabilised. Oxide ion vacancies in these structures are less common compared to interstitial defects, as this would result in unstable, three-fold coordination of the cation at the centre of the tetrahedral units. However, if the tetrahedra have enough rotational flexibility to permit oxide ions to bridge between them, this can be avoided, and thereby oxide ion vacancies can be stabilised.[179]

One important example of an interstitial-driven oxide ion conductor adopting the scheelite structure is $CeNbO_{4+x}$, which has been shown to form linked polyhedral networks through incorporation of interstitial O^{2-} into the tetrahedra.[195,197] The additional charge is compensated by oxidation of some Ce^{3+} to Ce^{4+}, which results in electronic conductivity. The significant electronic contribution to the conductivity is reflected in the low oxide ion transfer number of 0.42 at 800 °C, making it a mixed ionic and electronic conductor with a total conductivity of 2.6×10^{-2} S cm^{-1} at 800 °C.[198] $LaNbO_4$ has also been explored as an oxide ion conductor, and interstitial oxide ions can be readily introduced via doping.[65,199] The conductivity of $LaNb_{0.84}W_{0.16}O_{4.08}$, for example, has been reported to be 2.0×10^{-2} S cm^{-1} at 900 °C, and that of $LaNb_{0.84}Mo_{0.16}O_{4.08}$ is 1.7×10^{-2} S cm^{-1} at 900 °C.[193,200,201]

$BiVO_4$ is an example of a scheelite oxide ion conductor in which oxide ion vacancies have been successfully introduced. The vacancy-driven total conductivity below 400 °C of $BiVO_4$ and a Ca-doped $BiVO_4$ material was first reported by Lu and Steele in 1986.[196] More recently, Sr-doping was found to also stabilise vacancies in $BiVO_4$, leading to the formation of corner-sharing V_2O_7 units. Oxide ion diffusion is then possible via breaking and reforming of these flexible dimers.[179,202] Acceptor-doping increased the conductivity of $BiVO_4$ (2.0×10^{-4} S cm^{-1} at 600 °C)[179] by about one order of magnitude for $Bi_{0.75}Ca_{0.25}VO_{3.875}$ (1.6×10^{-3} S cm^{-1})[202] and $Bi_{0.95}Sr_{0.05}VO_{3.975}$ (1.8×10^{-3} S cm^{-1})[179] at 600 °C.[203] While electromotive force measurements on $BiVO_4$ give an ion transport number of 0.12 at 700 °C,[179] showing that this material is a mixed ionic and electronic conductor, the transport number of $Bi_{0.95}Sr_{0.05}VO_{3.975}$ is significantly higher (0.71 - 0.88 between 500 - 700 °C).[179] The promising properties of these scheelite-type materials suggest that other complex scheelite-type compounds could also show good oxide ion conductivities.

The synthesis and scheelite-related structure of $Bi_3FeMo_2O_{12}$ and $Bi_3GaMo_2O_{12}$ was first reported by Sleight and Jeitschko in 1974.[204] These compounds were the first examples of trivalent cations on the tetrahedral B-site of the scheelite structure, and to emphasise the tetrahedral arrangement of the Fe^{3+}, Ga^{3+} and Mo^{6+} ions, the alternative formulae $Bi_3(FeO_4)(MoO_4)_2$ and $Bi_3(GaO_4)(MoO_4)_2$ are used. A closer investigation of the structure of $Bi_3(FeO_4)(MoO_4)_2$ as a function of temperature

revealed an irreversible first-order phase transition at around 500 °C.[205,206]

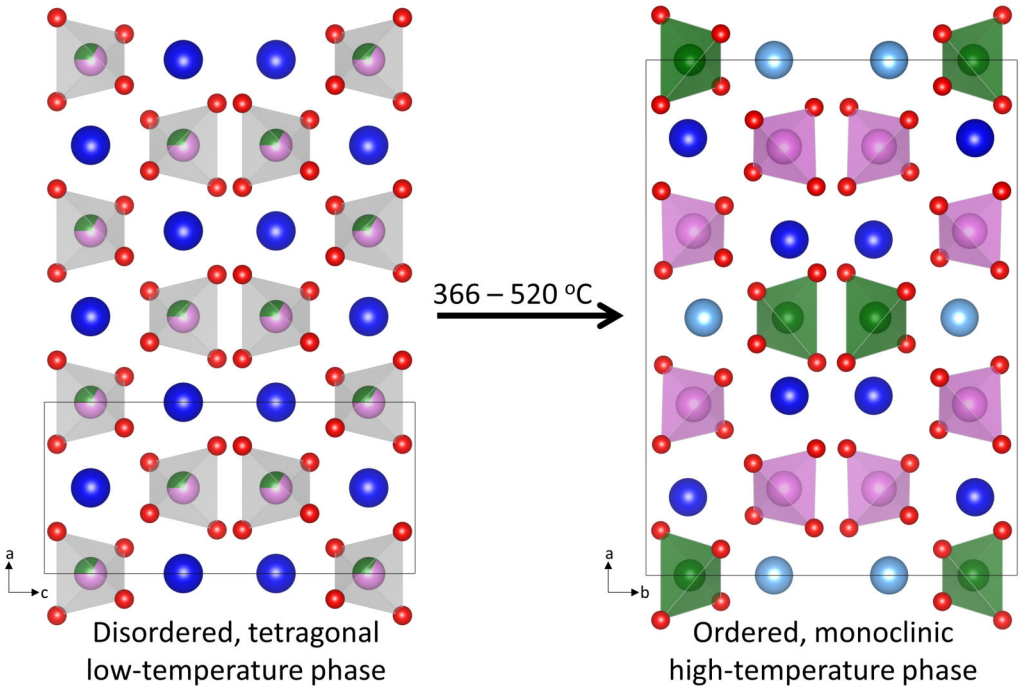

Figure 4.2: Crystal structures of $Bi_3(FeO_4)(MoO_4)_2$ in its low-temperature (LT), disordered phase (left) and high-temperature (HT) phase where cation ordering results in a tripling of the unit cell (right). The grey tetrahedra show Fe/MoO_4 tetrahedra, and pink and green tetrahedra show MoO_4 and FeO_4, respectively. Bi atoms are shown in blue (with the two different Bi sites in the HT phase being distinguished by light and dark blue) and oxygen atoms in red.

The low temperature phase has a $I4_1/a$ scheelite-type structure, with Fe and Mo cations randomly distributed on the tetrahedral B-site (figure 4.2). Therefore, this phase is called disordered $Bi_3(FeO_4)(MoO_4)_2$. Heating above 520 °C results in the irreversible transformation to a monoclinic, ordered scheelite superstructure in space group $C2/c$.[205,206] The phase transition is caused by the ordering of Fe and Mo cations on the tetrahedral site resulting in a tripling of the unit cell along the a-axis, as shown in figure 4.2. Furthermore, the phase transition results in a splitting of the Bi site, leading to two distinct Bi^{3+} environments in the monoclinic structure.[206] Neutron powder diffraction showed that, while the $6s^2$ lone pairs of Bi^{3+} ions on the Bi(1) sites are oriented towards a corner of the BiO_8 cubes, displacing one oxygen significantly further than the others, the lone pairs of Bi^{3+} atoms on the Bi(2) sites point towards a face of the cube, displacing four oxygen atoms. This

causes significant distortions of the original BiO_8 cubes, leading to variations in Bi-O bond lengths.[206] Consequently, Bi(1) has three close O^{2-} neighbours, with bond lengths between 2.205(6) and 2.278(7) Å, and five longer bonds between 2.530(6) and 2.799(7) Å, with the longest bond (2.799(7) Å) being affected by the lone pair. This results in an average Bi(1)-O distance of 2.484(2) Å.[206] Bi(2), on the other hand, has four close O^{2-} neighbours, with distances between 2.199(6) and 2.318(6) Å, as well as four longer bonds due to the $6s^2$ lone pair between 2.744(6) and 2.860(7) Å. The average Bi(2)-O bond length is therefore 2.529(2) Å.[206]

Several analogous compounds to $Bi_3(FeO_4)(MoO_4)_2$ have been reported. The Ga-analogue $Bi_3(GaO_4)(MoO_4)_2$ shows the same disorder-order phase transition as $Bi_3(FeO_4)(MoO_4)_2$.[205] The unit cell parameters of $Bi_3(GaO_4)(MoO_4)_2$ are comparable to those reported for $Bi_3(FeO_4)(MoO_4)_2$ (table 4.1), and due to the smaller ionic radius of $^{IV}Ga^{3+}$ (0.47 Å)[180] in comparison to $^{IV}Fe^{3+}$ (0.49 Å),[180] the unit cell volume is slightly smaller. The compound $Bi_3(ScO_4)(MoO_4)_2$ was reported by Kolitsch et al.[207] and its structure, refined from single crystal data, is shown in figure 4.3. In contrast to Fe and Ga atoms in $Bi_3(FeO_4)(MoO_4)_2$ and $Bi_3(GaO_4)(MoO_4)_2$, the Sc atoms in this scheelite-type compound were found to have a distorted octahedral coordination.

B-cation		a (Å)	b (Å)	c (Å)	β (°)	V (Å^3)
Fe^{3+}	[206]	16.8796(2)	11.6108(1)	5.25017(5)	107.1931(6)	982.97(2)
Ga^{3+}	[205]	16.863(2)	11.665(1)	5.227(1)	107.23(1)	980.4(1)
Sc^{3+}	[207]	16.996(3)	11.601(2)	5.319(1)	104.67(3)	1014.6(3)
In^{3+}	[208]	16.9043(3)	11.6535(3)	5.2547(8)	107.15(1)	988.93(1)

Table 4.1: Summary of the unit cell parameters reported for $Bi_3(BO_4)(B'O_4)_2$ (B = Fe, Ga, In, Sc; B' = Mo).

The unit cell parameters of $Bi_3(ScO_4)(MoO_4)_2$ are shown in table 4.1. They are similar to those reported for $Bi_3(FeO_4)(MoO_4)_2$ and the increase in volume is expected due to the bigger ionic radius of octahedrally coordinated Sc^{3+} (0.745 Å) compared to tetrahedral Fe^{3+} (0.49 Å).[180] The ScO_6 octahedra are edge-sharing and form zig-zag chains along the c-axis (figure 4.3). To reflect the octahedral

coordination of Sc^{3+} and the edge-sharing nature of these octahedra, the formula can be written as $Bi_3(Sc_2O_8)_{1/2}(MoO_4)_2$. Bond valence analysis and occupancy refinements of the Sc site indicate that approximately 4 % of Sc is substituted by Bi atoms, resulting in the nominal composition $Bi_3(Bi_{0.04}Sc_{0.96}O_4)(MoO_4)_2$. Impedance spectroscopy measurements on $Bi_3(Sc_2O_8)_{1/2}(MoO_4)_2$ have been reported by Zhou et al.[209] The total conductivity at 500 °C was found to be 2×10^{-6} S cm^{-1} and the activation energy 0.97 eV. Due to the absence of a grain boundary response, the authors suggested that grain boundaries might be electrically conducting, but no information on the ionic and electronic contribution to the total conductivity was given.[209]

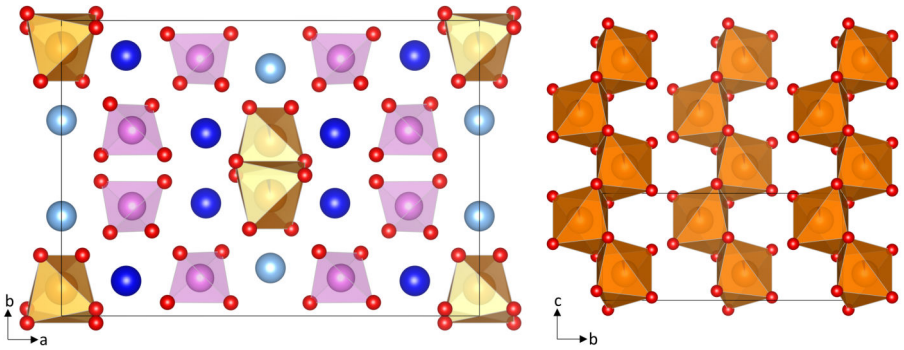

Figure 4.3: Monoclinic, ordered crystal structures of $Bi_3(Sc_2O_8)_{1/2}(MoO_4)_2$. The pink and orange polyhedra show MoO_4 and ScO_6, respectively. The two different Bi sites are shown in light and dark blue, and oxygen atoms in red. The zig-zag chains formed by Sc_2O_8 units along the *c*-axis are shown on the right, and for clarity Mo and Bi atoms are omitted.

$Bi_3(InO_4)(MoO_4)_2$ and its powder X-ray diffraction data were reported in 1987. Kolitsch et al.[207] suggest that, despite the original analysis suggesting tetrahedral coordination of In^{3+} in $Bi_3(InO_4)(MoO_4)_2$, it is more likely to be a structural analogue to $Bi_3(Sc_2O_8)_{1/2}(MoO_4)_2$ with octahedrally coordinated In^{3+}, due to the average In-O bond length (2.141 Å) being similar to those found for Sc-O bond lengths (2.162 Å). However, the original paper reporting the structure of $Bi_3(InO_4)(MoO_4)_2$ is in Russian and not available online, and no further study of bond lengths has been reported. Nie et al.[208] investigated the structure and optical properties of $Bi_3(InO_4)(MoO_4)_2$. However, the reported unit cell parameters are very close to those published for $Bi_3(FeO_4)(MoO_4)_2$ by Jeitschko et al.[205] and the volume is only

slightly larger. This is unlikely to be correct, because the ionic radius of tetrahedral Fe^{3+} (0.49 Å)[180] is significantly smaller than that of tetrahedral or octahedral In^{3+} (0.62 and 0.80 Å, respectively),[180] and the unit cell of $Bi_3(InO_4)(MoO_4)_2$ can therefore be expected to be considerably larger than that of $Bi_3(FeO_4)(MoO_4)_2$.

The high ionic conductivities of several complex, scheelite-related materials which contain relatively isolated tetrahedral units with central atoms that can adopt a variety of coordiantion environments suggests that $Bi_3(FeO_4)(MoO_4)_2$-related compounds could be promising candidates for intermediate temperature oxide ion conductors. Additionally, $Bi_3(FeO_4)(MoO_4)_2$ has been reported to be a good and selective catalyst for olefin oxidation reactions,[210] a property which is advantageous for a potential intermediate temperature SOFC electrolyte material.

4.2.1 Aims of this Work

To date, the conductivities in the $Bi_3(BO_4)(B'O_4)_2$ (B = Fe, Ga, In, Sc; B' = Mo) series have not been systematically studied and compared. Previous work[211] has shown that the total conductivity of $Bi_3(FeO_4)(MoO_4)_2$ at 600 °C is 5×10^{-5} S cm^{-1}. Sr-doping on the Bi site resulted in the conductivity decreasing by about one order of magnitude, indicating that vacancies are not readily introduced in the structure. This suggests that interstitial oxide ions are more likely to cause ionic conduction in these materials. The work presented in this chapter describes the synthesis and characterisation of this series of complex scheelite-type materials and reports the dependence of conductivity on the ionic radius of B for the first time. Since both vacancy- and interstitial driven ionic conductivity in scheelite structures have been reported and the attempt to increase conductivity by introducing vacancies has previously been unsuccessful,[211] donor-doping of the best conductor in the series is carried out to investigate if interstitial oxide ions can be introduced to further enhance oxide ion conductivity.

4.3 Experimental Methods

4.3.1 Synthesis

A solution precursor approach was used to synthesise 2 g polycrystalline samples of the high temperature, monoclinic forms of $Bi_3(FeO_4)(MoO_4)_2$, $Bi_3(GaO_4)(MoO_4)_2$, $Bi_3(Sc_2O_8)_{1/2}(MoO_4)_2$, $Bi_3(InO_4)(MoO_4)_2$ and $Bi_3(Fe_{0.9}Ti_{0.1}O_{4.05})(MoO_4)_2$. Stoichiometric amounts of reagents ($Bi(NO_3)_3.5H_2O$ Aldrich, 98 %; $(NH_4)_6Mo_7O_{24}.4H_2O$, Aldrich, $\geq$ 99.98 %; $Fe(NO_3)_3.9H_2O$, Aldrich, $\geq$ 99.95 %; Ga_2O_3, Aldrich, $\geq$ 99.99 %; Sc_2O_3, Aldrich, 99.9 %; In_2O_3, Fisher Sci, 99.9 % and TiO_2, Aldrich, $\geq$ 99.8 %) were mixed with 20 ml of water and stirred thoroughly. The solutions were dried overnight at 250 °C and then heated at 850 °C. The heating times are summarised in table 4.2. PXRD patterns of the obtained products (shown in figure 4.4) were typically recorded for 25 min using a 2θ range of 10 - 70° and a step size of 0.02° to check and confirm phase purity.

Nominal Composition	Heating time (hours)	Purity (%)
$Bi_3(FeO_4)(MoO_4)_2$	48	98.0(3)
$Bi_3(GaO_4)(MoO_4)_2$	60	98.8(2)
$Bi_3(Sc_2O_8)_{0.5}(MoO_4)_2$	48	100
$Bi_3(InO_4)(MoO_4)_2$	62	100
$Bi_3(Fe_{0.9}Ti_{0.1}O_{4.05})(MoO_4)_2$	182	98.6(2)

Table 4.2: Summary of compounds synthesised, heating times and percentage purities as determined by PXRD.

4.3.2 Impedance Spectroscopy

The compounds listed in table 4.2 were uniaxially pressed into 10 mm pellets using approximately 4000 kg cm^{-2} and sintered at 850 °C for 12 h. Before each measurement, the pellets were weighed, and their diameters and thickness measured. This allowed for the density to be calculated and compared to the theoretical density obtained during the Rietveld analysis of the appropriate PXRD pattern, giving percentage densities of all pellets between 80 and 90 %. Platinum paste was used to

attach the electrodes to both sides of the pellet. The organic component of the dye was removed by firing the pellet at 850 °C for 30 min. The furnace was programmed to cool from 800 °C to 300 °C using a heating rate of 2 °C min^{-1}. The impedance was measured using a Solartron 1260 impedance analyser, and measurements of average duration of 48 s were carried out approximately every 20 °C. The temperature in the furnace was recorded every 10 s and the average temperature at which each measurement was performed was extracted. A frequency range of 0.1 - 1 × 10^7 Hz and voltages of 100 - 1000 mV were used.

4.4 Results and Discussion

4.4.1 Structural Characterisation

An attempt to synthesise $Bi_3(FeO_4)(MoO_4)_2$ and $Bi_3(GaO_4)(MoO_4)_2$ using a solid-state approach resulted in the formation of impure products. Synthesis using a solution of aqueous nitrates as described in the literature[205] led to the desired products when heated at 850 °C. This approach was therefore used for the synthesis of all compounds in this series, and the PXRD patterns of $Bi_3(BO_4)(B'O_4)_2$ (B = Fe, Ga, In, Sc; B' = Mo) as well as that of $Bi_3(Fe_{0.9}Ti_{0.1}O_{4.05})(MoO_4)_2$ are shown in figure 4.4. The patterns were analysed using the Rietveld method[119] implemented in Topas Academic.[121] The $C12/c1$ structural model published by Jeitschko et al.[205] was used for $Bi_3(FeO_4)(MoO_4)_2$, $Bi_3(GaO_4)(MoO_4)_2$ and $Bi_3(Fe_{0.9}Ti_{0.1}O_{4.05})(MoO_4)_2$ and a model reported by Kolitsch et al.,[207] also in space group $C12/c1$, was used for $Bi_3(Sc_2O_8)_{1/2}(MoO_4)_2$ and $Bi_3(InO_4)(MoO_4)_2$. A small $Mo_3Bi_{10}O_{24}$[212] impurity was identified in $Bi_3(FeO_4)(MoO_4)_2$, $Bi_3(GaO_4)(MoO_4)_2$ and $Bi_3(Fe_{0.9}Ti_{0.1}O_{4.05})(MoO_4)_2$, but because of its very low weight percentages it is unlikely to influence the results from conductivity measurements presented here. In all refinements, a zero point, cell parameters, isotropic temperature factors and pseudo-Voigt peak shape function parameters were refined. The background was modelled using a 9 parameter Chebyshev polynomial.

	$Bi_3(FeO_4)(MoO_4)_2$	$Bi_3(GaO_4)(MoO4)_2$	$Bi_3(Fe_{0.9}Ti_{0.1}O_{4.05})(MoO_4)_2$	$Bi_3(Sc_2O_8)_{1/2}(MoO_4)_2$	$Bi_3(InO_4)(MoO_4)_2$	
Model	Jeitschko[205]	Jeitschko[205]	Jeitschko[205]	Kolitsch[207]	Jeitschko[205]	Kolitsch[207]
a (Å)	16.906(2)	16.874(1)	16.902(2)	16.984(1)	17.004(3)	17.004(2)
b (Å)	11.645(2)	11.665(1)	11.645(1)	11.600(1)	11.612(2)	11.612(1)
c (Å)	5.2544(7)	5.2317(4)	5.2548(6)	5.3118(7)	5.3471(8)	5.3469(7)
β (°)	107.134(9)	107.433(6)	107.146(8)	104.647(8)	105.08(1)	105.085(8)
Volume ($Å^3$)	988.5(2)	982.5(2)	988.3(2)	1012.5(2)	1019.4(3)	1019.4(2)
Bi1-O (Å)	2.49(8)	2.48(8)	2.49(8)	2.48(7)	2.50(9)	2.49(7)
Bi2-O (Å)	2.5(1)	2.5(1)	2.5(1)	2.6(1)	2.6(1)	2.6(1)
B-O (Å)	1.91(1)	1.90(1)	1.91(1)	2.16(3)	1.95(4)	2.17(4)
B'-O (Å)	1.77(2)	1.77(2)	1.77(2)	1.77(2)	1.81(5)	1.78(2)

Table 4.3: Summary of lattice parameters, volumes and average bond lengths obtained from PXRD data of $Bi_3(BO_4)(B'O_4)_2$ (B = Fe, Ga, In, Sc,$Fe_{0.9}Ti_{0.1}$; B' = Mo) as well as the structural model used for each refinement.

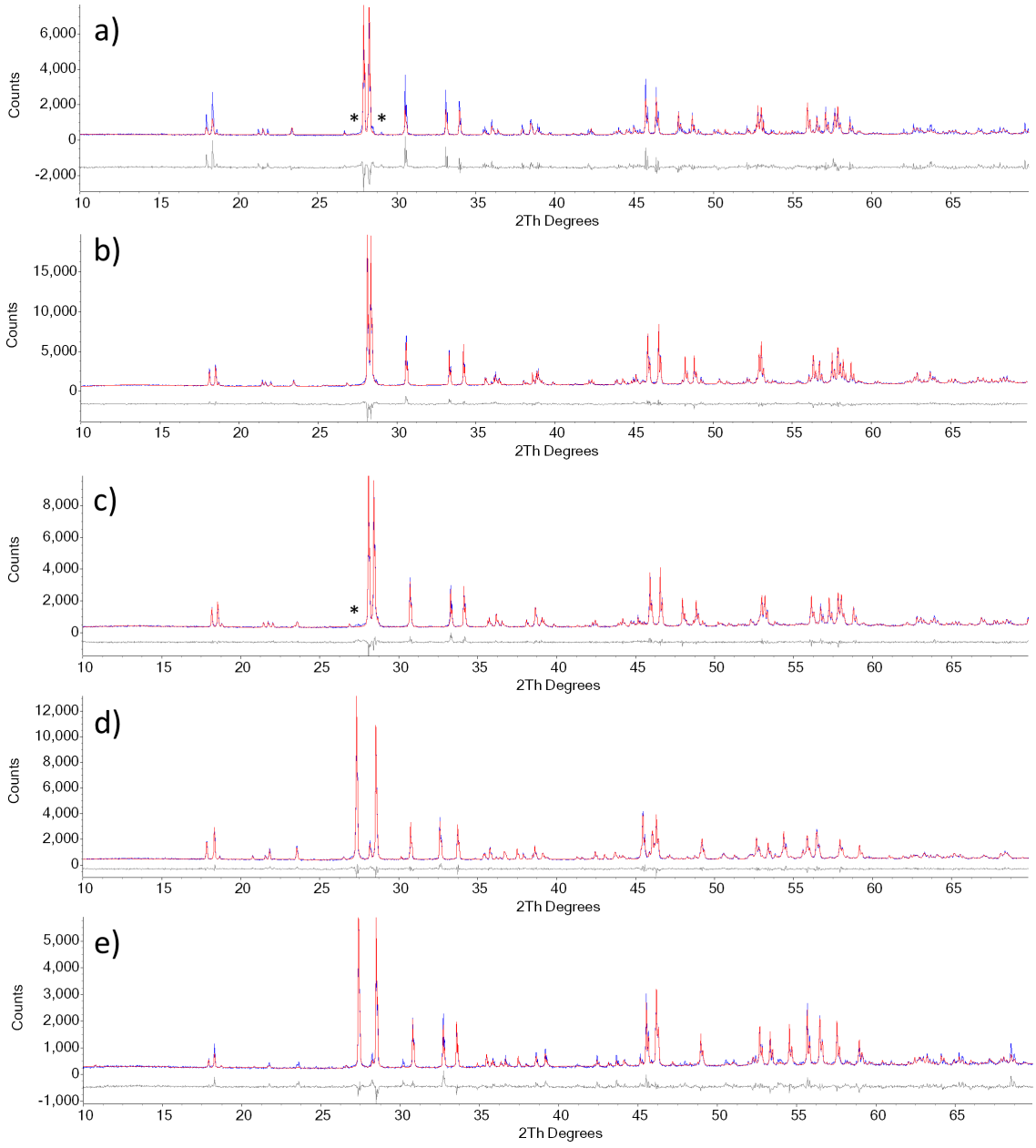

Figure 4.4: PXRD patterns of $Bi_3(FeO_4)(MoO_4)_2$ (a), $Bi_3(Fe_{0.9}Ti_{0.1}O_{4.05})(MoO_4)_2$ (b), $Bi_3(GaO_4)(MoO_4)_2$ (c), $Bi_3(InO_4)(MoO_4)_2$ (d) and $Bi_3(Sc_2O_8)_{1/2}(MoO_4)_2$ (e). The observed patterns are shown in blue and the calculated Rietveld fits in red. The difference curve is shown in grey. Impurity peaks are marked by a *.

Because of the ability of Mo to adopt a variety of coordination environments, the presence of isolated tetrahedra and the previously observed decrease in conductivity of $Bi_3(FeO_4)(MoO_4)_2$ on Sr-doping,[211] any oxide ion conductivity observed in these scheelite-type structures is likely caused by the presence of interstitial oxide ions. This suggests that donor-doping could, in principle, increase the ionic conductivity

by introducing interstitial defects into the structure. Ti^{4+} was chosen as a dopant due to its ionic radius (CN = 4, 0.42 Å) being very close to that of tetrahedral Fe^{3+} (0.49 Å).[180] The weight percentage of TiO_2 corresponding to 0.1 Ti per unit formula is below 1 %, therefore any Ti-containing impurities would not be observable in the PXRD pattern of $Bi_3(Fe_{0.9}Ti_{0.1}O_{4.05})(MoO_4)_2$. However, the change in conductivity, discussed in section 4.4.2, indicates that doping was successful.

The unit cell parameters, volumes and average bond distances obtained from Rietveld refinements of the PXRD data of $Bi_3(BO_4)(B'O_4)_2$ (B = Fe, Ga, In, Sc, $Fe_{0.9}Ti_{0.1}$; B' = Mo) are summarised in table 4.3, and plots of unit cell parameters and volumes against the ionic radius are shown in figure 4.5. For $Bi_3(FeO_4)(MoO_4)_2$, $Bi_3(GaO_4)(MoO_4)_2$ and $Bi_3(Sc_2O_8)_{1/2}(MoO_4)_2$ the unit cell values are similar to those reported in the literature (summarised in table 4.1). As expected due to the smaller ionic radius of tetrahedral Ga^{3+}, the volume of $Bi_3(GaO_4)(MoO_4)_2$ is smaller than that of $Bi_3(FeO_4)(MoO_4)_2$. Sc^{3+} strongly favours octahedral coordination,[213] and the ionic radius of $^{VI}Sc^{3+}$ is 0.745 Å,[180] significantly larger than that of tetrahedral Fe^{3+}, explaining the larger unit cell volume of $Bi_3(Sc_2O_8)_{1/2}(MoO_4)_2$.

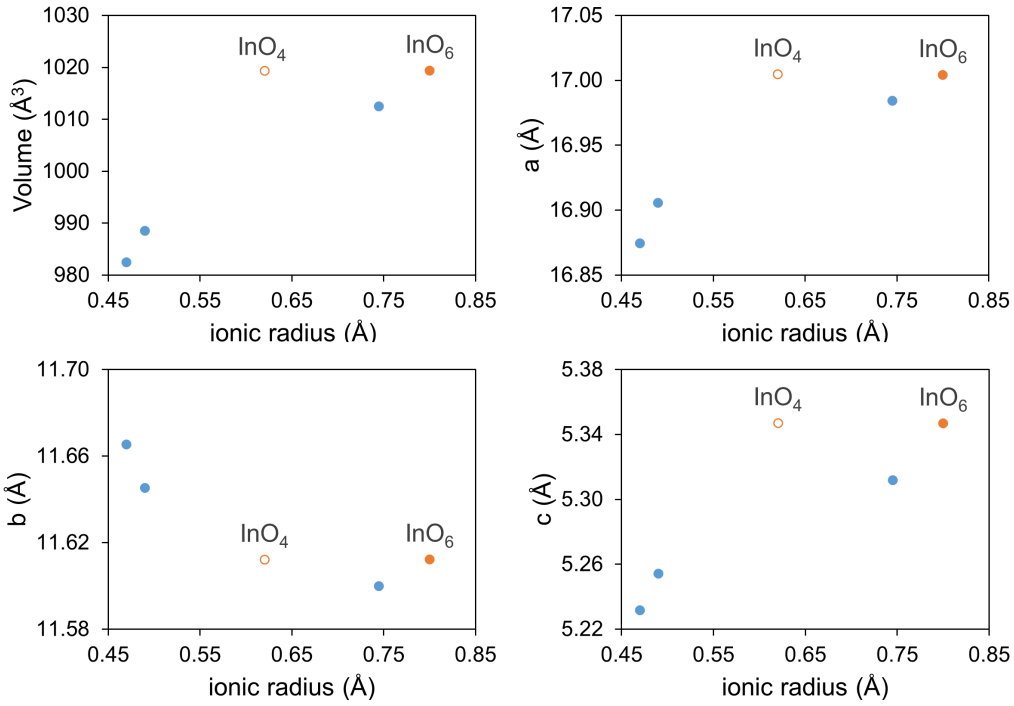

Figure 4.5: Cell parameters and volumes of $Bi_3(BO_4)(B'O_4)_2$ (B = Ga, Fe, In, Sc; B' = Mo). The data for B = Ga, Fe, Sc is shown in blue, and for B = In in orange.

The unit cell parameters and volume of $Bi_3(InO_4)(MoO_4)_2$ differ significantly from the reported literature values. In^{3+} can be tetrahedrally or octahedrally coordinated,[213] with ionic radii of 0.62 Å and 0.80 Å respectively.[180] Figure 4.5 shows a clear increase in unit cell volume with increasing ionic radius. The determined volume of $Bi_3(InO_4)(MoO_4)_2$ is larger than that of $Bi_3(Sc_2O_8)_{1/2}(MoO_4)_2$. If In^{3+} was tetrahedrally coordinated, the unit cell volume would be expected to decrease compared to that of $Bi_3(Sc_2O_8)_{1/2}(MoO_4)_2$. This suggests that $Bi_3(In_2O_8)_{1/2}(MoO_4)_2$ is a more accurate representation of the compound and In^{3+} is indeed octahedrally coordinated as suggested by Kolitsch et al.,[207] and a structural analogue of $Bi_3(Sc_2O_8)_{1/2}(MoO_4)_2$.

Unit cell parameters a and c, shown in figure 4.5, increase with increasing ionic radius similar to the volume. This trend also supports an octahedral coordination environment of In^{3+}. Only unit cell parameter b, which decreases on increasing ionic radius, suggests a tetrahedral In^{3+} environment.

Bond valence sum calculations can be used to validate chemical structures. The model is based on the concept that the sum of bond valences (v_{ij}) around an ion i is equal to the formal oxidation state V_i of the ion. The bond valence is related to the strength of the bond, which is inversely proportional to the bond length.[214,215] Using

$$V_i = \sum_j \exp\left(\frac{R_o - R_{ij}}{B}\right) \tag{4.1}$$

where R_o and B are empirically determined constants and R_{ij} is the bond length between atoms i and j, the bond valence sum can be calculated.[216] Values for R_o and B published by Brown and Altermatt[217] were used to calculate the bond valence sum for In^{3+} based on both structural models. The obtained oxidation states assuming a tetrahedral and octahedral environment are 3.55 and 3.00 respectively, thereby supporting an octahedral coordination environment. Additionally, using the structure of $Bi_3(Sc_2O_8)_{1/2}(MoO_4)_2$ as starting point for the refinement resulted in a visibly better fit compared to $Bi_3(FeO_4)(MoO_4)_2$, and decreased the R_{wp} from 9.8 to 7.6 %. Because of that, the model reported for $Bi_3(Sc_2O_8)_{1/2}(MoO_4)_2$ was also used for $Bi_3(In_2O_8)_{1/2}(MoO_4)_2$.

4.4.2 Conductivity Measurements

The total conductivity of the synthesised materials was measured using impedance spectroscopy. Figure 4.6 shows a selection of characteristic Nyquist plots observed for this series of compounds.

$Bi_3(Fe_{0.9}Ti_{0.1}O_{4.05})(MoO_4)_2$, $Bi_3(GaO_4)(MoO_4)_2$ and $Bi_3(Sc_2O_8)_{1/2}(MoO_4)_2$ are used as examples as they are the best, medium and worst conductors, respectively. The plots of $Bi_3(In_2O_8)_{1/2}(MoO_4)_2$ look similar to those of $Bi_3(Sc_2O_8)_{1/2}(MoO_4)_2$ and the plots of $Bi_3(FeO_4)(MoO_4)_2$ similar to those of $Bi_3(GaO_4)(MoO_4)_2$. Figure 4.6 shows that most Nyquist plots are semicircular which is the desired shape and indicates that the samples are conductive. $Bi_3(Fe_{0.9}Ti_{0.1}O_{4.05})(MoO_4)_2$ displays depressed semicircles, indicative of a spread of relaxation times. This is generally caused by inhomogeneities and imperfections in the sample, for example surface roughness, non-uniform current distribution or porosity.[142,218] The jump in signal at 1 MHz is present in all plots and clearly visible in figures 4.6 e and f, as indicated by the red circles. It has no physical meaning and is a known instrument artefact caused by the switching of internal circuits for measurements above/below 1 MHz.

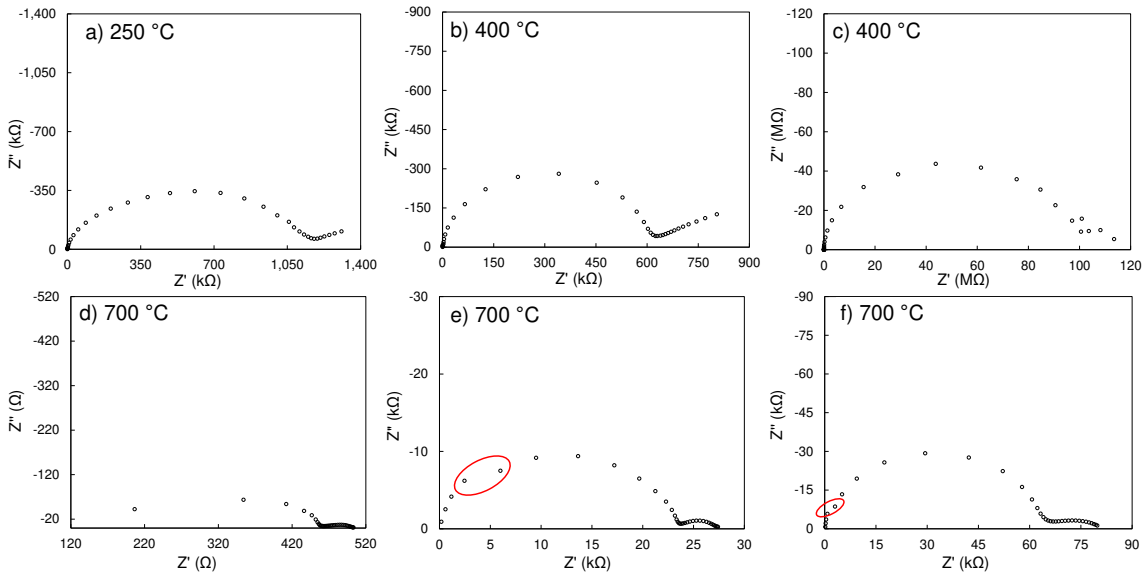

Figure 4.6: Nyquist plots of $Bi_3(Fe_{0.9}Ti_{0.1}O_{4.05})(MoO_4)_2$ (a, d) $Bi_3(GaO_4)(MoO_4)_2$ (b, e) and $Bi_3(Sc_2O_8)_{1/2}(MoO_4)_2$ (c, f) at low and high temperatures. The dip observed at 1 MHz (indicated by the red rings in (e) and (f)) is a known instrument artefact with no physical meaning.

The capacitance was calculated using the relationship $\omega_{max}RC = 1$, where R is the intercept of a semicircle with the Z' axis and $\omega_{max} = 2\pi f_{max}$ where f_{max} is the frequency at the maximum value of Z" for a semicircle. Obtained capacitances and resistances are summarised in table 4.4.

Nominal composition	Temperature (°C)	R (Ω)	C (F)
$Bi_3(Fe_{0.9}Ti_{0.1}O_{4.05})(MoO_4)_2$	250	1235967	5×10^{-11}
$Bi_3(Fe_{0.9}Ti_{0.1}O_{4.05})(MoO_4)_2$	700	459	9×10^{-11}
$Bi_3(GaO_4)(MoO_4)_2$	400	641106	2×10^{-11}
$Bi_3(GaO_4)(MoO_4)_2$	700	23736	2×10^{-11}
$Bi_3(Sc_2O_8)_{1/2}(MoO_4)_2$	400	117318198	1×10^{-11}
$Bi_3(Sc_2O_8)_{1/2}(MoO_4)_2$	700	66693	2×10^{-11}

Table 4.4: Summary of the capacitances and resistances obtained from the high frequency semicircles of the Nyquist plots shown in figure 4.6.

The capacitance of a semicircle can help determine the phenomenon responsible for the signal. At 700 °C, two distinct semicircles are observed in all three plots (figure 4.6d, e, f). The high frequency semicircles in all plots (a-f) have capacitances of 10^{-10} - 10^{-11} F (table 4.4). This is higher than the expected typical bulk capacitance values of $\approx 10^{-12}$ F, but lower than the capacitance of $\approx 10^{-9}$ F expected for grain boundaries.[141] It therefore suggests that both bulk and grain boundary responses contribute to this signal. All resistance values used for further analysis are therefore the combined response of bulk and grain boundary.

Nominal composition	Temperature (°C)	R (Ω)	C (F)
$Bi_3(Fe_{0.9}Ti_{0.1}O_{4.05})(MoO_4)_2$	700	504	5×10^{-6}
$Bi_3(GaO_4)(MoO_4)_2$	700	27843	9×10^{-8}
$Bi_3(Sc_2O_8)_{1/2}(MoO_4)_2$	700	82515	1×10^{-7}

Table 4.5: Summary of the capacitances and resistances obtained from the low frequency semicircles of the Nyquist plots shown in figure 4.6 d, e, f.

The resistances and capacitances of the low frequency semicircles observed at high temperatures (figure 4.6d-f) are summarised in table 4.5. An increase in capac-

itance upon decreasing frequency is commonly seen in oxide ion conductors, and is indicative of charge transfer at the sample-electrode interface.[141] At lower temperatures and low frequencies, the Warburg electrode response is frequently observed in oxide ion conductors and associated with the diffusion of oxide ions through the electrode, however it does not exclude the presence of electronic conductivity. This Warburg electrode response is, ideally, a 45° line, but several factors such as varying numbers of diffusing particles or particles waiting a long time between jumps can cause anomalous diffusion and therefore deviations from this value. The Nyquist plot for $Bi_3(GaO_4)(MoO_4)_2$ at 400 °C (figure 4.6b) shows a linear electrode response, however, the angle deviates from the ideal 45°. The data obtained for $Bi_3(Sc_2O_8)_{1/2}(MoO_4)_2$ (figure 4.6c) becomes noisy at low temperatures and frequencies which is a consequence of its low conductivity, lowering the signal to noise ratio. Therefore, no electrode response is observed. $Bi_3(Fe_{0.9}Ti_{0.1}O_{4.05})(MoO_4)_2$, on the other hand, has a significantly higher conductivity, and consequently the charge transfer component is still visible at 400 °C in the form of a partial semicircle. Upon lowering the temperature further to 250 °C as seen in figure 4.6a, a clear electrode response at a similar angle to that in $Bi_3(GaO_4)(MoO_4)_2$ becomes apparent.

		σ (S cm^{-1})	
Nominal Composition	E_a (eV)	600 °C	800 °C
$Bi_3(FeO_4)(MoO_4)_2$	1.06 ± 0.02	5.40×10^{-5}	7.30×10^{-4}
$Bi_3(Fe_{0.9}Ti_{0.1}O_{4.05})(MoO_4)_2$	0.687 ± 0.003	8.50×10^{-5}	15.0×10^{-4}
$Bi_{2.7}Sr_{0.3}(FeO_{4-x})(MoO_{4-x})_2$	1.39 ± 0.03	0.45×10^{-5}	1.10×10^{-4}
$Bi_3(GaO_4)(MoO_4)_2$	0.646 ± 0.003	0.34×10^{-5}	0.33×10^{-4}
$Bi_3(Sc_2O_8)_{1/2}(MoO_4)_2$	1.46 ± 0.02	0.20×10^{-5}	0.27×10^{-4}
$Bi_3(InO_4)(MoO_4)_2$	1.18 ± 0.01	0.22×10^{-5}	0.34×10^{-4}

Table 4.6: Summary of conductivities at 600 °C and 800 °C and activation energies calculated for for $Bi_3(BO_4)(B'O_4)_2$ (B = Fe, Ga, In, Sc, $Fe_{0.9}Ti_{0.1}$; B' = Mo). $Bi_{2.7}Sr_{0.3}(FeO_{4-x})(MoO_{4-x})_2$[211] was added for comparison.

Further investigations are necessary to determine the nature of the conductivity in these materials, and while the presence of a charge-transfer component indicates

that oxide ion conductivity is a dominant effect, an electronic contribution to the conductivity cannot be excluded. The temperature dependence of the total conductivity of the series $Bi_3(BO_4)(B'O_4)_2$ (B = Fe, Ga, In, Sc, $Fe_{0.9}Ti_{0.1}$; B' = Mo) is shown in figure 4.7, and conductivities at 600 °C and 800 °C are summarised in table 4.6. The % densities of all compounds discussed here were between 80 - 90 %, and while a lower density decreases the measured conductivity, this narrow range means that the obtained values are comparable.

Ti-doping resulted in an increase in conductivity from 7.3×10^{-4} S cm^{-1} to 1.5×10^{-3} S cm^{-1} at 800 °C. This increase is consistent with successful doping, and $Bi_3(Fe_{0.9}Ti_{0.1}O_{4.05})(MoO_4)_2$ shows the highest total conductivity in the series measured here. Its conductivity is one order of magnitude higher than that of $Bi_{2.7}Sr_{0.3}(FeO_{4-x})(MoO_{4-x})_2$.[211] This change in conductivity suggests that interstitial oxide ions were successfully introduced into the structure. However, the small effect of 10 % doping on the total conductivity indicates that the number of additional defects that can be introduced may be very limited. Additionally, Ti-doping could also lead to charge compensation by reduction of either Fe^{3+} or Mo^{6+}, which could result in an increase of electronic conductivity. Therefore, further investigations into the potential electronic contribution to the total conductivity are necessary. Despite the increase on Ti-doping, the total conductivity of $Bi_3(Fe_{0.9}Ti_{0.1}O_{4.05})(MoO_4)_2$ is about one order of magnitude lower than that of other scheelite-type conductors like $CeNbO_{4+x}$ (2.6×10^{-2} S cm^{-1} at 800 °C)[198] and $Bi_{0.95}Sr_{0.05}VO_{3.975}$ (1.8×10^{-3} S cm^{-1} at 600 °C).[179] These are, however, mixed conductors with a significant electronic contribution.

The conductivity of $Bi_3(Fe_{0.9}Ti_{0.1}O_{4.05})(MoO_4)_2$ is also lower than that of YSZ (0.5×10^{-2} S cm^{-1} and 4.4×10^{-2} S cm^{-1} at 600 and 800 °C respectively),[219] but it is comparable to the oxide ion conductor $LaNb_{0.84}W_{0.16}O_{4.08}$, which has a conductivity of 7.0×10^{-3} S cm^{-1} at 800 °C.[193] Compared to other conductors with similarly isolated tetrahedra like $La_{1.54}Sr_{0.46}Ga_3O_{2.27}$ which adopts a melilite-type structure[34] and the apatite material[220] $La_{10}Si_{4.5}Cu_{1.5}O_{27-x}$ (7.1×10^{-2} and 4.8×10^{-2} S cm^{-1}, respectively),[34,220] the total conductivity of $Bi_3(Fe_{0.9}Ti_{0.1}O_{4.05})(MoO_4)_2$ is lower at the same temperature.

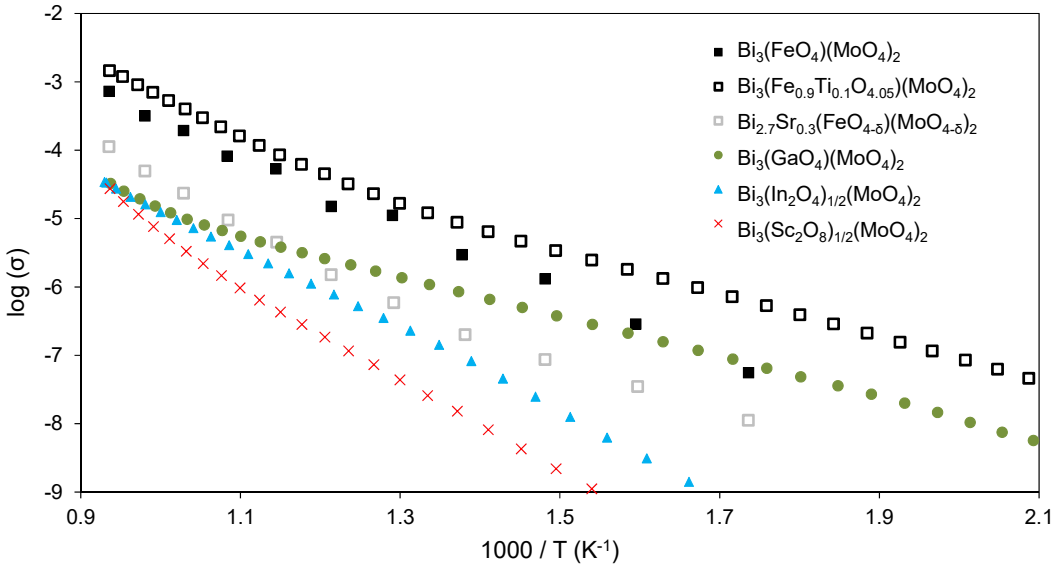

Figure 4.7: Arrhenius plots showing the temperature dependence of conductivity for $Bi_3(BO_4)(B'O_4)_2$ (B = Fe, Ga, In, Sc, $Fe_{0.9}Ti_{0.1}$; B' = Mo) compounds. The conductivity data of $Bi_{2.7}Sr_{0.3}(FeO_{4-x})(MoO_{4-x})_2$ is shown for comparison.[211]

The conductivity curve of $Bi_3(GaO_4)(MoO_4)_2$ shown in figure 4.7 has a significantly lower slope than those of the other compounds, owing to a lower activation energy, as can be seen in table 4.6. It has a higher conductivity than $Bi_3(FeO_4)(MoO_4)_2$ at temperatures below 350 °C, but its conductivity is over one order of magnitude lower than that of $Bi_3(Fe_{0.9}Ti_{0.1}O_{4.05})(MoO_4)_2$ at all temperatures measured. Table 4.6 shows that at 600 and 800 °C, the conductivities of $Bi_3(GaO_4)(MoO_4)_2$, $Bi_3(In_2O_8)_{1/2}(MoO_4)_2$ and $Bi_3(Sc_2O_8)_{1/2}(MoO_4)_2$ are comparable. Lowering the temperature further results in a substantial decrease of the conductivities of $Bi_3(Sc_2O_8)_{1/2}(MoO_4)_2$ and $Bi_3(In_2O_8)_{1/2}(MoO_4)_2$. $Bi_3(Sc_2O_8)_{1/2}(MoO_4)_2$ has the lowest conductivity in this series. One reason for this could be the reported distorted octahedral coordination of Sc in this compound, which has a significantly higher ionic radius than tetrahedrally coordinated Fe^{3+}, and therefore results in less available space for oxide ion migration. Furthermore, Fe^{3+} and Ga^{3+} can both readily adapt to a four-, five-, or six-coordination environment similar to Mo^{6+}, whereas Sc^{3+} is either octahedrally or eight-coordinated.[213] Fe^{3+} and Ga^{3+} can therefore be expected to support oxide ion migration by changing between coordination numbers four and five. In $Bi_3(Sc_2O_8)_{1/2}(MoO_4)_2$ on the other hand, the ScO_6 octahedra are

less flexible, and oxide ion migration is likely to only be supported by the MoO_4 tetrahedra. A similar argument can be made for In^{3+}, which can either be tetrahedrally, octahedrally, or eight-coordinate, and does not have the flexibility of Fe^{3+} and Ga^{3+} to change between a four coordinate and five-coordinate environment. The conductivity of $Bi_3(Sc_2O_8)_{1/2}(MoO_4)_2$ reported by Zhou et al.[209] (1.2×10^{-5} S cm^{-1} at 600 °C) is over one order of magnitude higher than that measured in this work. Additionally, the reported activation energy of 0.97 eV is significantly lower than the activation energy determined here. This difference can be explained by the very high density of the pellet of 96.7 % used in the previously reported measurements[209] and therefore very low grain boundary contributions.

4.5 Conclusion and Future Work

A systematic study of the total conductivity of $Bi_3(BO_4)(B'O_4)_2$ (B = Fe, Ga, $Fe_{0.9}Ti_{0.1}$; B' = Mo) and $Bi_3(B_2O_8)_{1/2}(B'O_4)_2$ (B = Sc, In; B' = Mo) was reported for the first time. An increase in conductivity upon Ti-doping suggests that interstitial oxide ions are responsible for ionic conduction in these scheelite-type materials. The best conductor in this series, $Bi_3(Fe_{0.9}Ti_{0.1}O_{4.05})(MoO_4)_2$, has a conductivity of 1.5×10^{-3} S cm^{-1} at 800 °C. This is comparable to the scheelite-type oxide ion conductor $LaNb_{0.84}W_{0.16}O_{4.08}$. Moreover, structural considerations suggest that In^{3+} is octahedrally coordinated and a structural analogue to $Bi_3(Sc_2O_8)_{1/2}(MoO_4)_2$.

Further work is required to determine if the series $Bi_3(BO_4)(B'O_4)_2$ (B = Fe, Ga, $Fe_{0.9}Ti_{0.1}$; B' = Mo) could lead to promising intermediate temperature oxide ion conductors and to confirm conduction via the interstitial mechanism. Firstly, the synthesis and characterisation of $Bi_3(Fe_{1-x}Ti_xO_{4+})(MoO_4)_2$ with various different doping concentrations could help clarify to what extent interstitial oxide ions can be introduced into the structure and hence if the conductivity of this material could be further enhanced. Further to that, the oxide ion transport number of this material should be measured and impedance measurements in different atmospheres carried out to determine the electronic contribution to the total conductivity. Moreover, a detailed diffraction study of $Bi_3(In_2O_8)_{1/2}(MoO_4)_2$ could help confirm the coordina-

tion environment of In^{3+}. While neutrons are generally better suited for detecting oxygen atoms in the presence of heavy metal atoms, the high neutron absorption cross-section of In means neutron diffraction would be difficult, and single crystal XRD is therefore preferable. This would also be useful to confirm whether the low conductivities of $Bi_3(Sc_2O_8)_{1/2}(MoO_4)_2$ and $Bi_3(In_2O_8)_{1/2}(MoO_4)_2$ are a result of the octahedral coordination of the B cations in these materials. Finally, the successful synthesis of the low temperature phases and impedance measurements on the disordered compounds are needed to show what effect the cation disorder has on the conductivity of the compounds in this series.

CHAPTER 5

Hexagonal Perovskite Oxide Ion Conductors: $Ba_3NbMoO_{8.5}$ and $Ba_7Nb_4MoO_{20}$

5.1 Summary

In this chapter, the reversibility of the phase transition in $Ba_3NbMoO_{8.5}$ was demonstrated for the first time using variable temperature X-ray diffraction. Quasielastic neutron scattering on $Ba_3NbMoO_{8.5}$ and $Ba_7Nb_4MoO_{20}$ showed that dynamics are too slow to be observable on a nanosecond timescale. Furthermore, a detailed ab initio molecular dynamics study on $Ba_7Nb_4MoO_{20}$ revealed a continuous oxide ion migration pathway in the *ab* plane, as well as an important out-of-plane contribution to the dynamics, highlighting the importance of facile (Nb/Mo)O_x polyhedral rotation for long-range oxide ion diffusion.

5.2 Introduction

The perovskite structure and its derivatives are prevalent in solid state chemistry due to their versatility and large range of useful properties,[221,222] and find applications for example in solar cells[223,224] and as ionic and mixed conductors. Oxide ion as well as mixed ionic and electronic conductivity have been reported for various materials crystallising in the perovskite structure, many of which have been explored as potential candidates for SOFC electrolytes (eg. Mg-doped $LaGaO_3$, $Na_{0.5}Bi_{0.5}TiO_3$),[24,225] anodes (eg. La-doped $SrTiO_3$, Sr- and Cr-doped $LaMnO_{3\delta}$)[226,227] and cathode materials (eg. Sr-doped $LaMnO_3$, $LaNiO_3$).[228–233]

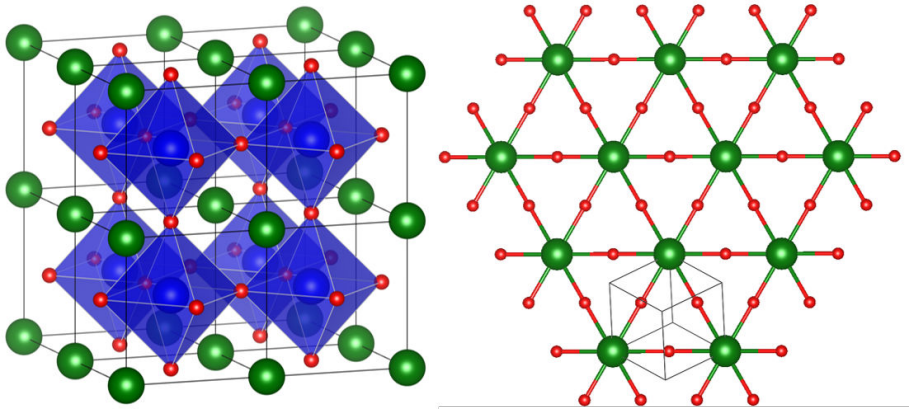

Figure 5.1: Ideal, cubic perovskite structure ABO_3. Green, blue and red spheres represent A and B site cations and O^{2-} respectively. Blue polyhedra (left) show the octahedral environment of the B-site. The hexagonal AO_3 layer is shown on the right, stacking of which results in corner- or face sharing BO_6 octahedra. The cubic perovskite unit cell is shown for reference.

The ideal, cubic perovskite structure has the general formula ABO_3 (A = rare earth, group 2, B = transition metals). It can be described in two different ways, as shown in figure 5.1. The left structure shows the more typical image of a perovskite, consisting of two interlocked primitive lattices of corner-sharing BO_6 octahedra and A-site cations. This description is useful for illustrating the distortions of the structure resulting from tilting and rotating of the BO_6 octahedra. The right structure (figure 5.1) shows an alternative description which is based on close-packed hexagonal AO_3 layers. Cubic stacking (abc-abc) of these AO_3 layers results in corner-sharing octahedra, whereas hexagonal stacking (ab-ab) leads to the BO_6

octahedra sharing faces.[234,235] This description is useful for understanding more complex, hexagonal perovskite structures, which are discussed in more detail here.

The B-O sublattice is both chemically and structurally very flexible. It can accommodate a wide range of different elements, which, depending on the ionic radii of the elements, can lead to rotation, tilting or distortion of the octahedra. Another consequence of this flexibility is that the perovskite structure supports a high degree of non-stoichiometry and defects.

The relationship between the ionic radii of the A- and B-site cations and structural distortions in perovskite materials was first studied by Goldschmidt[236] and can be described by the tolerance factor, t:

$$t = \frac{(r_A + r_O)}{\sqrt{2}(r_B + r_O)} \tag{5.1}$$

where r_A, r_B, and r_O are the ionic radii of the cations A and B and the oxide ion, respectively. The ideal perovskite structure forms for t = 0.9 - 1.0. If the cation occupying the A site is smaller relative to B, then $t < 0.9$ and the empty space created by the smaller A-site cation results in tilting of the BO_6 octahedra in order to fill the vacant space. This generates structures with tetragonal, rhombohedral, orthorhombic and monoclinic symmetries. If the A-site cation is significantly bigger than the cation occupying the B site, however, then $t > 1.0$. This generally leads to the formation of hexagonal perovskites by some of the corner-sharing BO_6 octahedra (formed by cubic stacking of AO_3 layers) becoming face-sharing in order to release strain, resulting in a structure of one dimensional, octahedral chains.[236,237] Hexagonal perovskite derivatives are formed either purely by hexagonal stacking of AO_3 layers, or via stacking of hexagonal and cubic AO_3 layers in sequence. Different combinations of face- and corner-sharing octahedra give rise to a variety of hexagonal perovskites, which readily support cation and anion vacancies.

Hexagonal perovskite derivatives have only recently become an area of interest in the field of oxide ion conductors. Many of these materials are mixed conductors, showing both ionic (proton and/or oxide ion) and electronic contributions to the total conductivity.[238–240] Two hexagonal perovskites with significant ionic conduc-

tivity and a negligible electronic contribution to the conductivity are $Ba_3NbMoO_{8.5}$ and $Ba_7Nb_4MoO_{20}$.[241,242]

5.2.1 $Ba_3NbMoO_{8.5}$

The high bulk oxide ion conductivity of $Ba_3NbMoO_{8.5}$ was reported by Fop et al.[241] to be 2.2×10^{-3} S cm^{-1} at 600 °C, which is comparable to that of YSZ (5×10^{-3} S cm^{-1} at 600 °C), making it the first purely oxide ion conducting, hexagonal perovskite-related compound to be reported. Measurements under different partial oxygen pressures showed negligible electronic conductivity between 10^{-20} and 10^{-4} atm. A reduction of conductivity is observed under wet air flow, suggesting that there is no proton conductivity. Additionally, $Ba_3NbMoO_{8.5}$ is stable under reducing atmospheres, making this material a promising candidate as electrolyte for intermediate-temperature SOFCs.[241]

The trigonal $R\bar{3}m$ structure of $Ba_3NbMoO_{8.5}$ was first described in 1998.[243] It is an oxygen deficient derivative of the hexagonal 9R (i.e. a rhombohedral system with a periodicity of 9 layers) perovskite structure $A_3B_3O_9$ (A = Ba, B = Nb, Mo), with $\frac{1}{3}$ of the B sites being vacant, as shown in figure 5.2, resulting in significant cationic and anionic disorder.[244,245] The ideal 9R perovskite consists of triplets of face-sharing MO_6 octahedra. These stacks are connected via corner-sharing of the terminal octahedra to three other stacks. In $Ba_3NbMoO_{8.5}$, however, the position on the middle site (M2) of the trimers is split[245] and only two cations are distributed over the three polyhedra, with occupancy of the terminal site (M1) being favoured over M2. The distance of ≈ 1.5 Å between neighbouring M1 and M2 sites means that simultaneous occupancy is unfavourable, and figure 5.2b shows the resulting three possible cation distributions in the trimers. The lower oxygen content compared to the ideal 9R perovskite structure results in mixed coordination environments of the M1-centred polyhedra, and in anionic vacancies being distributed over O2 and O3 sites.

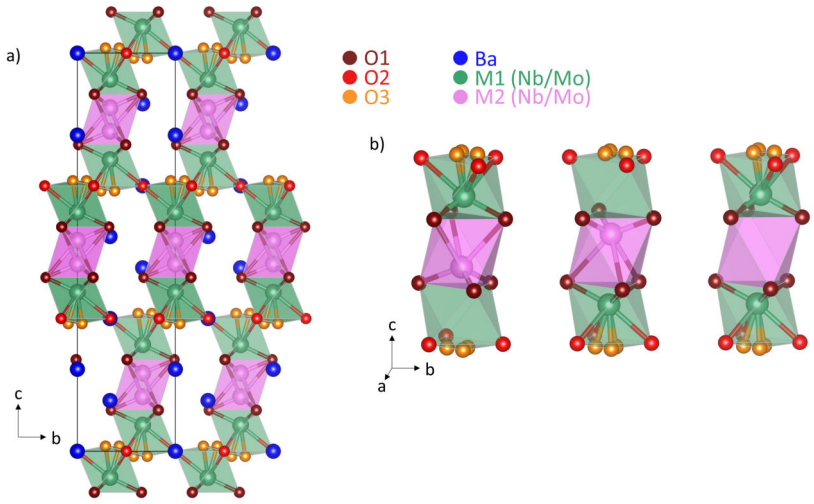

Figure 5.2: The structure of $Ba_3NbMoO_{8.5}$ obtained from single crystal X-ray diffraction data reported by Auckett et al.[245] Oxygen sites O1 and O2, and metal sites M1 and M2 are partially occupied (left). Three possible configurations of the trimers (right).

A previously proposed model[246] suggested that O2 and O3 oxygen sites, located on the faces of the terminal polyhedra in the trimers, cannot be simultaneously occupied. This in turn would result in exclusively tetrahedrally or octahedrally coordinated M1 cations, while M2 cations would always be octahedrally coordinated.[246,247] Using this model, it was argued that the conductivity of several $Ba_3M_2O_{8.5\pm\delta}$ (M = Nb, V, Mo, W) compounds depends on the ratio of $M1O_4$ and $M1O_6$ units present in the structure, with a higher percentage of tetrahedra leading to a higher occupancy of the O3 sites and an increase of the ionic conductivity.[248–251]

However, this model relies on the assumption that occupancy of an O3 site causes all adjacent O2 sites to be unoccupied, and that occupancy of one O2 site means all neighbouring O2 sites are occupied. Therefore, it implies that five coordinate M1 environments do not exist. Chambers et al.[244] investigated the local structure of $Ba_3NbMoO_{8.5}$ using neutron total scattering and pair distribution function (PDF) analysis. This revealed that Nb^{5+} and Mo^{6+} are predominantly five-coordinated at all temperatures, despite a small increase of tetrahedral environments on increasing temperature. M2 sites are found to be mostly octahedrally coordinated as would be expected from the crystallographic models showing a full O1 occupancy.[244]

Single crystal neutron diffraction on $Ba_3NbWO_{8.5}$ suggested a correlation be-

tween oxygen site distributions and ionic conductivity in $Ba_3M_2O_{8.5\pm\delta}$ (M = Nb, V, Mo, W).[252] However, instead of higher O3 occupancy leading to low-energy conduction pathways as previously suggested,[250] it was shown that the presence of cations which favour occupancy of the O3 site results in a lower energy barrier for oxide ion diffusion, while simultaneously increasing the occupancy of the O3 sites.[252]

Synchrotron PXRD revealed a first-order phase transition between 150 °C and 370 °C.[244] This was attributed to a shift in the distribution of cations from M2 to M1, with M2 sites being essentially unoccupied at 600 °C.[244] The high temperature (HT) phase has a smaller lattice parameter a (5.936 Å compared to 5.955 Å at 200 °C) and larger lattice parameter c (21.157 Å compared to 21.112 Å at 200 °C) with an overall decrease in unit cell volume to 645.81 $Å^3$ compared to 648.53 $Å^3$ of the low temperature (LT) form at 200 °C. Above 370 °C, only the high temperature form is present, and between 150 °C and 370 °C, both phases exist. A combined thermogravimetric analysis with mass spectrometry (TGA-MS) experiment performed in that study[244] also suggests that the observed loss of mass ($\approx$ 0.4 %) up to 600 °C is primarily caused by water, and unlikely to be a loss of oxygen, as was proposed by Yashima et al.[253]

The ability of Nb^{5+} and Mo^{6+} to adopt a variety of coordination environments is likely to provide a low-energy oxide ion migration pathway, resulting in oxide ion conductivity. While the dominant contribution to the ionic conductivity has been proposed to be in the ab plane,[241,244,253,254] three-dimensional diffusion has been suggested to contribute to the total conductivity.[245,255]

Various compounds with the general formula $Ba_3M_2O_{8.5\pm\delta}$ (M = Nb, V, Mo, W) have been reported.[248–251,255] $Ba_3Nb_{0.9}V_{0.1}MoO_{8.5}$ exhibits the highest bulk ionic conductivity of this family of compounds so far, reaching 0.01 S cm^{-1} at 600 °C.[250] This shows that there is significant potential for further improvement of the oxide ion conductivity, and a more in-depth understanding of oxide ion dynamics in these materials is necessary to achieve this.

5.2.2 $Ba_7Nb_4MoO_{20}$

The structure of $Ba_7Nb_4MoO_{20}$ was first reported in 1999.[256] It is shown in figure 5.3 and can be described as an ordered intergrowth of palmierite $Ba_3M_2O_8$ units and 12R perovskite $Ba_4M_3O_{12}$ units (where M = Nb or Mo), forming a 7H hexagonal perovskite with empty cationic sites.[242,256] It consists of stacked cubic (c), hexagonal (h), and oxygen deficient pseudo-cubic (c′) layers in the sequence [c′hhcchh].[256]

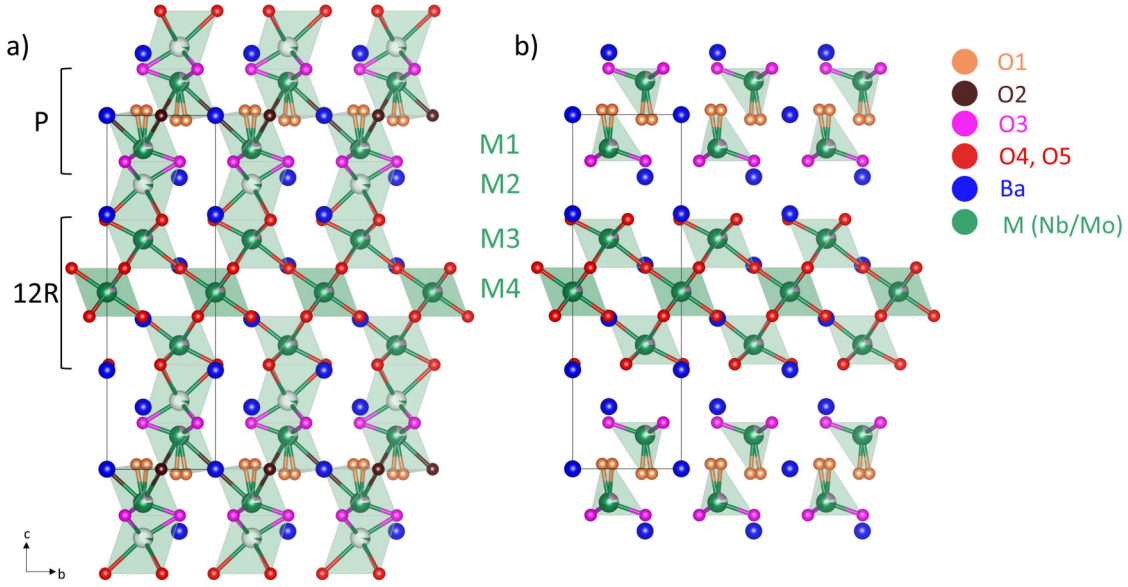

Figure 5.3: Crystal structure of $Ba_7Nb_4MoO_{20}$ obtained from neutron diffraction data highlighting the unique O and M crystallographic sites: (a) at 50 °C and (b) at 530 °C.[242]

At 50 °C (figure 5.3a), there are four crystallographically independent M sites modelled as jointly occupied by Mo and Nb. The intrinsic cation vacancies are located on M1 and M2 sites, with fractional occupancies of 0.899(3) and 0.101(3), respectively.[242] At increasing temperature, the occupancy of the M1 site increases further, while that of M2 decreases, resulting in occupancies of 0.931(3) and 0.069(3) at 530 °C.[242] The distribution of cationic vacancies over M1 and M2 introduces various possible stacking configurations, causing a disruption of the average, ordered intergrowth structure. M3 and M4 sites, located in the 12R perovskite layers, as well as the four unique Ba sites are fully occupied at all temperatures. Due to the very similar neutron scattering cross sections of Mo and Nb, no refinement of the fractional occupancy was possible, and these cations were therefore assumed

to be statistically distributed over all M sites. However, on the related compound $Ba_7Ta_{3.7}Mo_{1.3}O_{20.15}$, synchrotron X-ray diffraction data as well as first-principle calculations suggest a strong preference of Mo for the M1 sites in the palmierite layers.[56] This suggests that a cation site preference could also play a role in $Ba_7Nb_4MoO_{20}$. Additionally, the previously reported,[242] partially occupied M2 site was found to be unoccupied in $Ba_7Ta_{3.7}Mo_{1.3}O_{20.15}$.[56]

At low temperature there are five unique oxygen sites. Neutron diffraction data collected at 50 °C revealed large atomic displacement parameter values for the O1 site located in the *ab* plane in the palmierite layer, suggesting the presence of significant oxygen disorder.[242,256] To account for this, the O1 site was split from Wyckoff position 2d to 6i, and an additional oxygen site, O2, was introduced in the *ab* plane to account for missing nuclear scattering density apparent in difference Fourier maps.[242] The small distance between O1 and O2 means that simultaneous occupancy is very unfavourable. At 50 °C, the occupancy of O2 is 0.138(5), and at temperatures above 530 °C it is, on average, unoccupied,[242] resulting in four distinct oxygen sites in the high-temperature structure and tetrahedral coordination environments for the M1 Nb/Mo site (figure 5.3b). While O1 and O2 located in the *ab* plane of the palmierite $Ba_3M_2O_8$ units are partially occupied below 530 °C, the O3 site, also located in the palmierite layer, as well as O4 and O5 sites in the 12R perovskite $Ba_4M_3O_{12}$ units, are fully occupied at all temperatures.[242]

$Ba_7Nb_4MoO_{20}$ is an excellent mixed proton and oxide ion conductor, with negligible electronic conductivity.[242] The thermal reorganisation of the vacancies on O1 and O2 sites, resulting in full occupancy of O1, has been found to influence conductivity by lowering the activation energy of oxide ion conduction from 0.56 ± 0.01 eV (< 300 °C) to 0.30 ± 0.02 eV (300 - 655 °C).[242] This leads to the high bulk conductivity of 4×10^{-3} S cm^{-1} at 525 °C, and the proton transport number reaches 0.81.[242] Comparing the measured total conductivity at 600 °C in dry air (0.3×10^{-3} S cm^{-1}) to that in humidified air (2×10^{-3} S cm^{-1}) highlights the large contribution of protons to the conductivity. Thermogravimetric analysis showed a hydration of ≈ 0.8 H_2O molecules per formula unit. Chemical modification of $Ba_7Nb_4MoO_{20}$ has been found to increase oxide ion conductivity while decreasing proton conduction.

Several doped $Ba_7Nb_4MoO_{20}$ materials have been reported, and are summarised in table 5.1 with their conductivities and proton transport numbers (if given).

		σ_{tot} at 525 °C (S cm^{-1})	t_H
$Ba_7Nb_4MoO_{20}$	[242]	0.3×10^{-3}	0.81
$Ba_7Nb_{3.9}Mo_{1.1}O_{20.05}$	[257]	1.4×10^{-3}	0.04
$Ba_7Nb_{3.8}Cr_{0.2}MoO_{20.1}$	[258]	2.0×10^{-3}	< 0.1
$Ba_7Nb_{3.85}W_{0.15}MoO_{20.075}$	[57]	2.5×10^{-3}	≈ 0
$Ba_7Ta_{3.7}Mo_{1.3}O_{20.15}$	[56]	3.6×10^{-3}	-

Table 5.1: Comparison of the total conductivity (σ_{tot}) of various $Ba_7Nb_4MoO_{20}$-type materials at 525 °C and their reported proton transport number (t_H).

The oxide ion conduction pathway in three doped $Ba_7Nb_4MoO_{20}$ compounds, $Ba_7Nb_{3.9}Mo_{1.1}O_{20.05}$, $Ba_7Nb_{3.8}Cr_{0.2}MoO_{20.1}$, and $Ba_7Nb_{3.85}W_{0.15}MoO_{20.075}$ was investigated using the maximum entropy method.[57,257,258] This showed that in all three materials, the additional oxygen atoms are located primarily on the O2 sites, suggesting that diffusion is two-dimensional and occurring via O1 and O2 sites. A similar pathway was found in $Ba_7Ta_{3.7}Mo_{1.3}O_{20.15}$ using bond-valence-based energy calculations.[56]

Additionally, Fop et al.[259] investigated the proton and oxide ion diffusion in $Ba_7Nb_4MoO_{20}$ using neutron diffraction and short ab initio molecular dynamics (AIMD) simulations. This revealed that, in dry air, the M2 site of $Ba_7Nb_4MoO_{20}$ is, on average, unoccupied at all temperatures, while it is partially occupied in humid conditions, suggesting that water absorption causes disorder in the cationic vacancy layer. AIMD was used to investigate the proton and oxide ion diffusion mechanism. Proton conduction was found to be comprised of hopping of protons from one M1 centre to another, as well as rotations around the O1 and O2 positions. Oxide ion diffusion was also suggested to be two dimensional and restricted to the palmierite layer, but the simulation on a sample without water was very short (20 ps) and only carried out at one temperature, allowing only one jump to be observed. Bond-valence energy landscape calculations were then used to extrapolate a likely pathway, which is in agreement with that postulated for several doped compounds.[259]

5.2.3 Aims of this Work

Hexagonal perovskites constitute a new class of potential solid electrolytes, as they exhibit promising oxide ion conductivities which could be further improved by doping. $Ba_3NbMoO_{8.5}$ is a promising candidate for use in practical applications, and the first hexagonal perovskite to show predominantly oxide ion conduction. No attempt to directly observe oxide ion dynamics in this new, complex structure family has been reported previously. This could provide further insight into the details of oxide ion diffusion, and was therefore the main objective of the study of this material. Additionally, as the reversibility of the phase transition on cooling has not yet been demonstrated, this will be attempted using laboratory PXRD. $Ba_7Nb_4MoO_{20}$ also crystallises in a hexagonal perovskite structure, and exhibits both, proton and oxide ion conductivity. Doping of $Ba_7Nb_4MoO_{20}$ has shown to result in even higher oxide ion conductivity and suppresses proton conduction, allowing a compositional tuning of the material's properties. To do this, atomistic understanding of the oxide ion diffusion in this new oxide ion conductor is important. Extensive AIMD simulations at multiple temperatures were therefore carried out, giving a significantly more detailed insight into the oxide ion diffusion mechanism than was previously possible.[259] Furthermore, direct observation of both oxide ion and proton dynamics in $Ba_7Nb_4MoO_{20}$ was attempted using quasielastic neutron scattering and different atmospheres to separate the contributions of the different charge carriers.

5.3 Experimental Methods

5.3.1 Synthesis

A 6 g sample of $Ba_3NbMoO_{8.5}$ was prepared using stoichiometric amounts of $BaCO_3$ (Fisher Sci 99 %), MoO_3 (Fisher Sci 99.97 %) and Nb_2O_5 (Fisher Sci 99.99 %). The reagents were ground for 15 min using a pestle and mortar and pressed into 3 × 2 g pellets with a diameter of 10 mm. The pellets were heated at 1100 °C. After 48 h the pellets were reground, pelletised and heated again at 1100 °C. This process was repeated until a pure product was obtained after a total heating time of 192

h. Following the success of this synthesis, a second 6 g sample was made using the same heating pattern. After the purity was confirmed to be comparable to the first batch using PXRD, the samples were combined and mixed thoroughly to create a large sample of 12 g for neutron scattering experiments.

For neutron scattering experiments on $Ba_7Nb_4MoO_{20}$, two large (7 g) polycrystalline samples were prepared using stoichiometric amounts of $BaCO_3$ (Merck 99 %), Nb_2O_5 (Fisher Sci 99.5 %) and MoO_3 (Fisher Sci 99.5 %).[260] The reagents were ball-milled under ethanol for 30 min at 300 rpm. The samples were left to dry and then heated at 900 °C for 12 h. The powder was ground thoroughly using an agate mortar and pestle, pressed into a rod using a hydraulic press and approximately 70 MPa, and heated at 1100 °C for 24 h.

5.3.2 Impedance Spectroscopy

Approximately 1 g of $Ba_3NbMoO_{8.5}$ was uniaxially pressed into two pellets with a diameter of 10 mm which were sintered at 1100 °C for 12 h. One of the pellets was ground up for PXRD in order to confirm that the purity of the sample did not change during the sintering process. The mass, diameter, and thickness of the second pellet were measured, which, by comparing to the theoretical density obtained during the Rietveld analysis, allowed the determination of the percentage density to be 91 %. Pt-paste was used to attach the electrodes to the pellet, and the organic component of the dye was removed by heating at 850 °C for 30 min. Measurements were performed in air, wet N_2 and dry N_2 over a temperature range of 250 - 800 °C. The furnace was programmed to heat and cool using a rate of 2 °C min^{-1}. The impedance was measured using a Solartron 1260 impedance analyser, and measurements of an average duration of 48 s were taken approximately every 20 °C. The temperature in the furnace was recorded every 10 s and the average temperature at which each measurement was performed was extracted. Two heating/cooling cycles were performed in each atmosphere. A voltage of 100 mV and a frequency range of 0.1 - 1 $\times$ 10^7 Hz were used.

5.3.3 Quasielastic Neutron Scattering (QENS)

Neutron scattering data were collected on the backscattering spectrometer IN16b at the Institut Laue-Langevin (ILL) in Grenoble, using an incident neutron wavelength of 6.271 Å and instrument resolution of ≈ 0.8 μeV (FWHM). This gives access to dynamics on a nanosecond timescale.

Measurements on $Ba_3NbMoO_{8.5}$ were performed in a stainless-steel sample holder due to the potential loss of oxygen upon heating in vacuum.[253] This allowed the sample to stay in contact with air during the measurements. 7.3 g of sample were placed inside the tube. Initial elastic intensity measurements were made from 150 - 800 °C using a heating rate of 10 K min^{-1}, and data points were collected every 30 s. Following that, elastic (E = 0 μeV, 1 min) and inelastic (E = 2 μeV, 3 min) scattered intensities, so called elastic and inelastic fixed window scans (EFWS, IFWS),[178] were measured on cooling to 150 °C and again on heating to 800 °C, with a heating rate of 1.8 K min^{-1}. QENS measurements were performed at 800 °C and 400 °C with an energy transfer window of ± 15 μeV and a data collection time of 4 h at each temperature.

Measurements on $Ba_7Nb_4MoO_{20}$ were performed using a furnace[177] in humidified N_2 and under vacuum. The energy transfer window used for all QENS measurements on $Ba_7Nb_4MoO_{20}$ was ± 7 μeV. For the measurements performed under vacuum, 5.3 g of sample were placed in a Nb sample holder (diameter ≈ 8 mm, sample height ≈ 4 cm). During heating to 950 °C, EFWS (2 min) and IFWS (E = 2 μeV, 10 min) were collected, and at 950 °C a QENS measurement was performed with a total data collection time of 5 h. The sample was then cooled to 50 °C while again collecting EFWS (1 min) and IFWS (5 min). At 50 °C, QENS data were collected for 3 h. For the measurement in humid atmosphere, approximately 8 g of sample were placed in a stainless-steel sample holder (diameter ≈ 10 mm). N_2 was bubbled through distilled water and blown on the sample via a thin metal capillary in the steel tube. A first QENS spectrum (5 h) was measured at room temperature. The sample was then heated to 500 °C during which EFWS (2 min) and IFWS (10 min) were collected. During heating, QENS measurements were also performed at 350

°C, 425 °C and 500 °C for 6 h per temperature. The sample was then cooled to 225 °C, measuring EFWS (2 min) and IFWS (10 min), to collect QENS data at 225 °C for 6 h, and after further cooling at 175 °C for 4 h.

Data were also collected at room temperature on the empty tube (QENS: 4 h; EFWS: 2 min; IFWS 10 min) and on a vanadium standard (QENS: 30 min) for data reduction and analysis, which was carried out using the Mantid[136] software.

5.3.4 Computational Methods

Density Functional Theory (DFT) simulations were performed on $Ba_7Nb_4MoO_{20}$ with the Vienna ab initio simulation package (VASP).[75] The projector augmented wave (PAW) method[154] with the GGA-PBE (Perdew-Burke-Ernzerhof generalized-gradient-approximation) exchange-correlation functional[155] were used for all simulations. Before any AIMD simulations were performed, a geometry optimisation of the supercell, keeping the cell parameters fixed, was carried out, allowing ions to relax until the residual forces on them were less than 0.01 eV $Å^{-1}$. A structural model in space group $P1$, containing 288 atoms, and consisting of a 3 × 3 × 1 supercell of the high-temperature (530 °C) structure of $Ba_7Nb_4MoO_{20}$ determined from neutron diffraction[242] was used as a starting point for the simulations. As the occupancy of the M2 site at this temperature is very low (0.069), it was assumed to be empty, resulting in full occupancy of the M1 site. Distribution of Mo atoms and choosing one out of three partially occupied symmetry-equivalent O1 positions for each $M1O_4$ tetrahedron were done using a random number generator. The atomic content of the final simulation box was $Ba_{63}Nb_{36}Mo_9O_{180}$, consistent with the formula $Ba_7Nb_4MoO_{20}$. Ab initio molecular dynamics (AIMD) simulations were carried out with a cut-off energy of 300 eV and the k-space was sampled at the gamma-point only. AIMD simulations of 180 ps (1000 °C), 100 ps (1500 °C), and 200 ps (2000 °C) using the NVT ensemble and a time step of 2 fs were performed. The data analysis was carried out using the MDANSE code,[156] and the space visited by oxide ions was visualised in cloud plots using LAMP.[157]

5.4 Results and Discussion

5.4.1 Structural Characterisation

The phase purity of the samples of $Ba_3NbMoO_{8.5}$ and $Ba_7Nb_4MoO_{20}$ was checked using PXRD. Patterns were collected on a Bruker D8 ADVANCE diffractometer using Cu Kα radiation, and analysed using the Rietveld method[119] implemented in Topas Academic.[121] The refinement parameters included cell parameters, zero-point, one global temperature factor, and pseudo-Voigt peak shape parameters. The background was modelled using a 9 parameter Chebyshev polynomial.

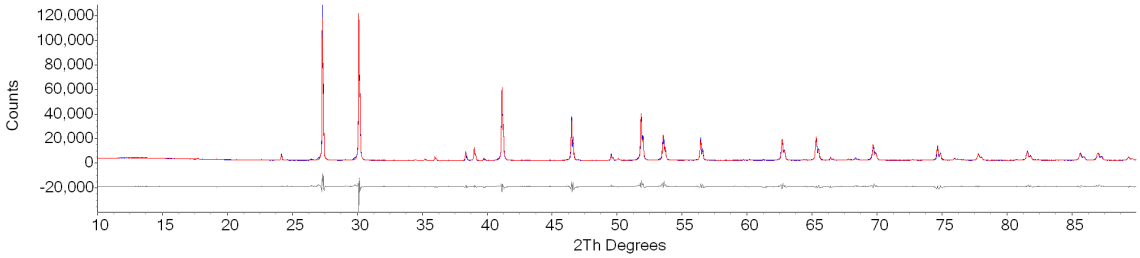

Figure 5.4: PXRD pattern of the $Ba_3NbMoO_{8.5}$ sample used for all further characterisation. The blue curve shows the observed data, red the calculated Rietveld fit and grey the difference between them.

The PXRD pattern collected on a large 12 g batch of $Ba_3NbMoO_{8.5}$ is shown in figure 5.4. The $R\bar{3}m$ structure model of $Ba_3NbMoO_{8.5}$ obtained from single crystal XRD by Auckett et al.[245] was used as a starting point for the refinement. The good fit of the Rietveld refinement suggests that the synthesis of $Ba_3NbMoO_{8.5}$ was successful, and this sample was therefore used for further characterisations.

Previously published unit cell parameters[241,244,245] of $Ba_3NbMoO_{8.5}$ show some unusual variation, as shown in table 5.2. Chambers et al.[244] ascribed this to the hysteresis of the first order phase transition, which was observed on heating between 150 °C and 370 °C, resulting in a dependence of the unit cell parameters on the thermal history of a sample. However, the reversibility of this phase transition on cooling to room temperature has not been demonstrated previously. Therefore, variable temperature PXRD experiments were performed in an attempt to investigate this.

		a (Å)	c (Å)	Volume (Å^3)
Fop et al.	241	5.921(1)	21.0908(2)	640.34(5)
Auckett et al.	245	5.9509(4)	20.9258(2)	641.76(1)
Chambers et al.	244	5.92805(5)	21.0910(3)	641.875(1)

Table 5.2: Previously reported unit cell parameter of $Ba_3NbMoO_{8.5}$.

Attempts to directly observe the peak splitting caused by this phase transition[244] using laboratory variable-temperature PXRD data were unsuccessful, due to a lower instrumental resolution compared to the synchrotron XRD study in which this was first observed. However, examination of the changes of the cell parameters and unit cell volume shown in figure 5.5 shows the expected trends on heating to 600 °C.

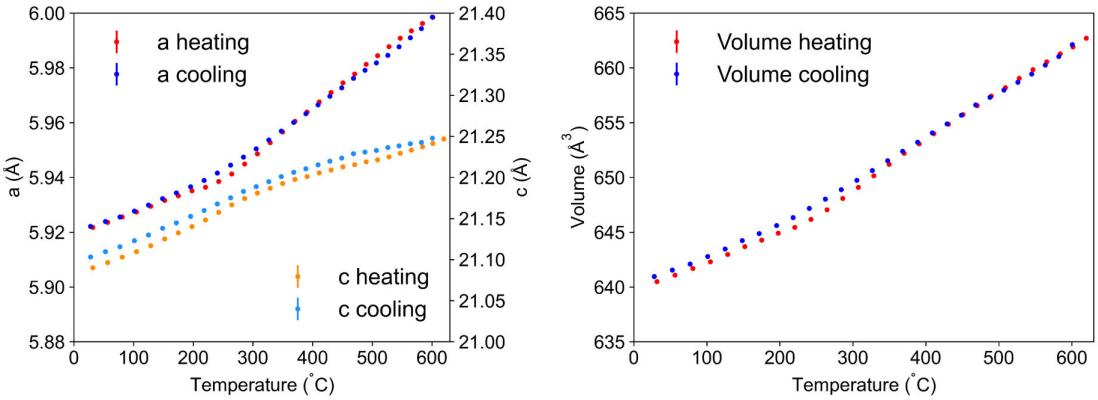

Figure 5.5: Variable-temperature PXRD experiment on a powdered sample of $Ba_3NbMoO_{8.5}$ on heating from room temperature to 600 °C (red, orange) and cooling back to room temperature (blue). The unit cell parameters a and c are shown on the left, and the volume is shown on the right.

At 300 °C, the majority of the sample has the structure of the high temperature phase, with a smaller cell parameter a and a bigger cell parameter c, resulting in an overall decrease in cell volume. The phase transition therefore leads to an increase in the rate of change of the unit cell parameter a and the unit cell volume with temperature, and a decrease in slope of cell parameter c, as is apparent in figure 5.5. On cooling to room temperature, the sample appears to have reverted back almost completely to the low temperature phase, with cell parameter a being the same before and after heating (5.922(1) Å), and c and the volume having increased

only marginally from 21.090(4) Å to 21.103(3) Å and 640.5(2) Å^3 to 641.0(2) Å^3, respectively. These data demonstrate the reversibility of the phase transition in $Ba_3NbMoO_{8.5}$ on cooling for the first time, and also confirm the existence of some hysteresis,[244] which can explain small discrepancies in reported unit cell parameters of $Ba_3NbMoO_{8.5}$.[241,244,245]

The PXRD pattern of the large sample of $Ba_7NB_4MoO_{20}$ used for neutron scattering experiments is shown in figure 5.6.

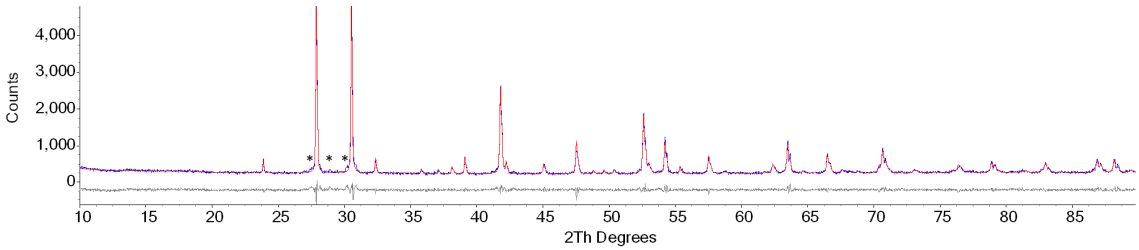

Figure 5.6: PXRD pattern of $Ba_7NB_4MoO_{20}$ used for QENS experiments, showing observed data in blue, calculated pattern in red, and the difference in grey. Peaks caused by the presence of $Ba_5Nb_4O_{15}$ and $Ba_3NbMoO_{8.5}$ impurities are marked by *.

The structural information of $Ba_7Nb_4MoO_{20}$ obtained from neutron diffraction data reported by Fop et al.[242] was used as a starting model for refinements. The final product was found to be 92 ± 1 % pure, and $Ba_5Nb_4O_{15}$ (2.3 ± 0.3 %) and $Ba_3NbMoO_{8.5}$ (5.0 ± 1 %) were identified as the impurities present. Due to time constraints, the synthesis of a more pure sample was not possible.

5.4.2 Conductivity of $Ba_3NbMoO_{8.5}$

Impedance spectroscopy was used to measure the total conductivity of $Ba_3NbMoO_{8.5}$. The Nyquist plots obtained at 400 °C and 700 °C in air are illustrated in figure 5.7. At 400 °C the plot shows a depressed semicircle caused by inhomogeneities in the sample like porosity or surface roughness, and an electrode response at low frequencies, which, in materials with partially blocking electrodes like Pt, is indicative of ionic conduction.[141]

At 700 °C the electrode response is the main component and becomes semicircular, a behaviour which is commonly seen in oxide ion conductors and indicates that diffusion occurs through a layer of finite thickness.[141] The jump in conductiv-

ity at 1 MHz, marked by the red circle in figure 5.7 and caused by the instrument, makes it impossible to separate potential bulk and grain boundary responses at low temperatures.

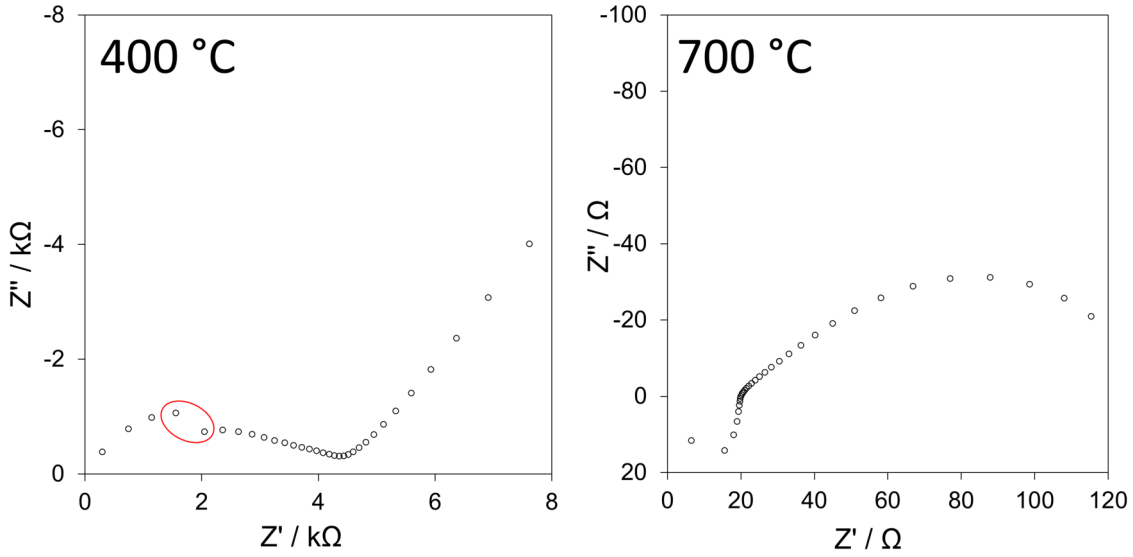

Figure 5.7: Nyquist plot of $Ba_3NbMoO_{8.5}$ at 400 °C (left) and 700 °C (right). The dip observed at 1 MHz (indicated by the red circle) is a known instrument artefact with no physical meaning.

Therefore, the combined response was measured by taking R as the intercept of the linear electrode response with the Z′ axis. The capacitance, summarised in table 5.3 was calculated using the relationship $\omega_{max}RC = 1$, where R is the intercept of a semicircle with the Z′ axis and $\omega_{max} = 2\pi f_{max}$ where f_{max} is the frequency at the maximum value of Z″ for a semi-circle.[141]

Nominal composition	Temperature (°C)	R (Ω)	C (F)
$Ba_3NbMoO_{8.5}$	400	4366	2×10^{-11}
$Ba_3NbMoO_{8.5}$	700	20	2×10^{-9}

Table 5.3: Summary of the capacitances and resistances obtained from the Nyquist plots shown in figure 5.7.

The temperature dependence of the total conductivity of $Ba_3NbMoO_{8.5}$ in three different atmospheres is shown in figure 5.8. To ensure complete equilibration of the sample, the data obtained during the second cooling cycle were used, at which point the sample had spent over 12 h in any given atmosphere. The conductivity of

$Ba_3NbMoO_{8.5}$ in air is comparable to that reported by Fop et al.[241] No significant change in conductivity on changing the atmosphere to dry N_2 was observed, which indicates that the electronic contribution to the conductivity is negligible. However, a small decrease of conductivity at increased temperatures is evident, which could indicate some electronic contribution to the total conductivity at high temperatures. A decrease in conductivity, especially at lower temperatures, was observed in wet N_2. This suggests that protons do not contribute to the ionic conductivity, and that water uptake might even hinder oxide ion diffusion, resulting in the observed decrease. These results are in good agreement with previous reports of the nature of conductivity in $Ba_3NbMoO_{8.5}$.[241]

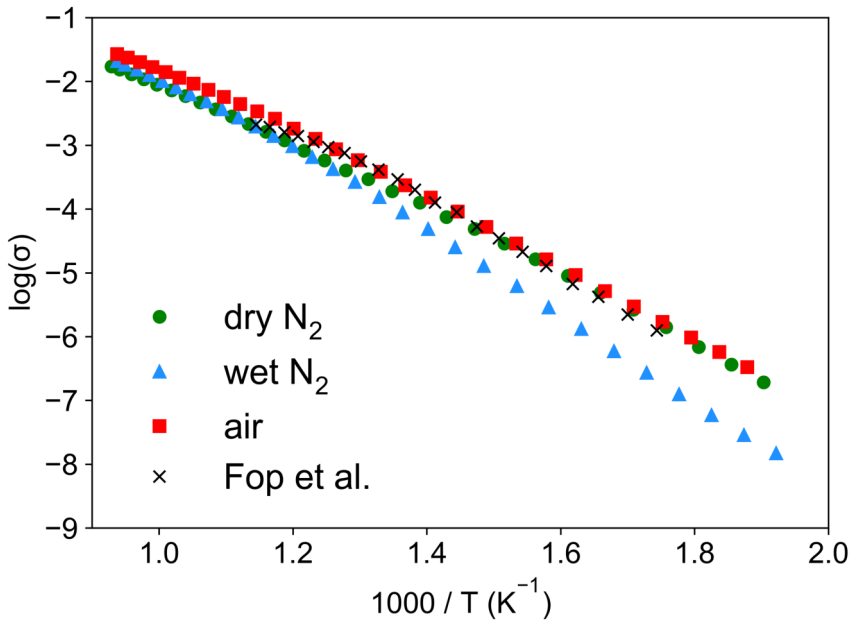

Figure 5.8: Arrhenius plot showing the temperature dependence of conductivity for $Ba_3NbMoO_{8.5}$ in various environments. The conductivity reported by Fop et al.[241] in air is shown for comparison.

5.4.3 Nanosecond Dynamics in Hexagonal Perovskites

In an attempt to directly observe nanosecond dynamics on both, $Ba_3NbMoO_{8.5}$ and $Ba_7Nb_4MoO_{20}$, elastic (EFWS) and inelastic (IFWS) fixed window scans were collected while heating and cooling the samples, and corrected for the sample can contributions. The IFWS were also corrected for residual elastic contribution. Gen-

erally, a gradual decrease of elastic intensity on heating is expected due to the Debye-Waller factor, which describes the loss of elastic intensity caused by an increase of thermal motions of atoms at higher temperatures. Any decrease of elastic intensity in addition to that is indicative of other effects, for example diffusion or dehydration. If the elastic intensity decreases due to diffusion processes, the IFWS is expected to increase at the same temperature. Dehydration, on the other hand, results in a loss of intensity in EFWS and no increase in IFWS intensity, due to the decrease of the total number of scattering atoms in the system, and because hydrogen is a particularly strong neutron scatterer, this effect is very pronounced.

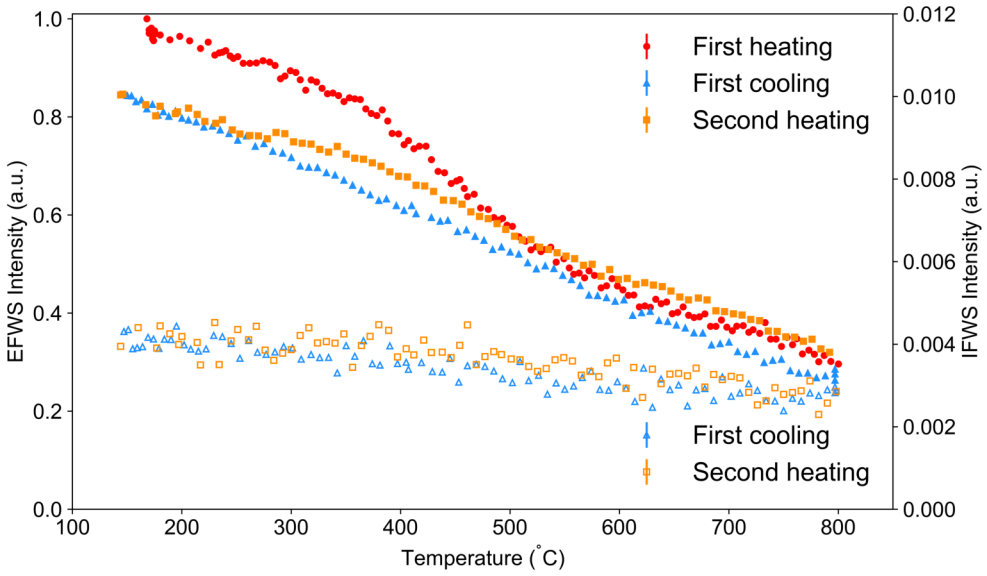

Figure 5.9: Elastic (full markers, left axis) and inelastic (empty markers, right axis) fixed window scans collected on $Ba_3NbMoO_{8.5}$.

The EFWS and IFWS measured for $Ba_3NbMoO_{8.5}$ are shown in figure 5.9. The total loss of elastic intensity during the first heating to 800 °C is ≈ 70 %. A noticeable change of slope was observed at approximately 390 °C, as shown in figure 5.9. This is similar to the temperature range in which the sample loses water, as indicated by TGA.[244] Because of this as well as the lack of increase observed in the IFWS at the same temperature, water loss is likely to be the main reason for the decrease in intensity. In addition to that, enhanced oxide ion dynamics could contribute to the intensity loss. On cooling to room temperature, the intensity increased linearly,

but stays ≈ 15 % lower than before the first heating. This could be caused by some water being readsorbed, but a partial decomposition of the sample makes the analysis difficult. QENS data were recorded at 800 °C and 400 °C, but the sample decomposed (< 50 % pure) while held at 800 °C, making a further analysis of the data impossible. Moreover, the IFWS show no sign of increasing intensity at higher temperatures, and therefore no QENS signal is expected.

Figure 5.10 shows the EFWS and IFWS measured for $Ba_7Nb_4MoO_{20}$. To separate the dynamics occurring due to two different charge carriers, measurements in vacuum, investigating oxide ion diffusion, and in humid N_2, investigating proton diffusion, were performed

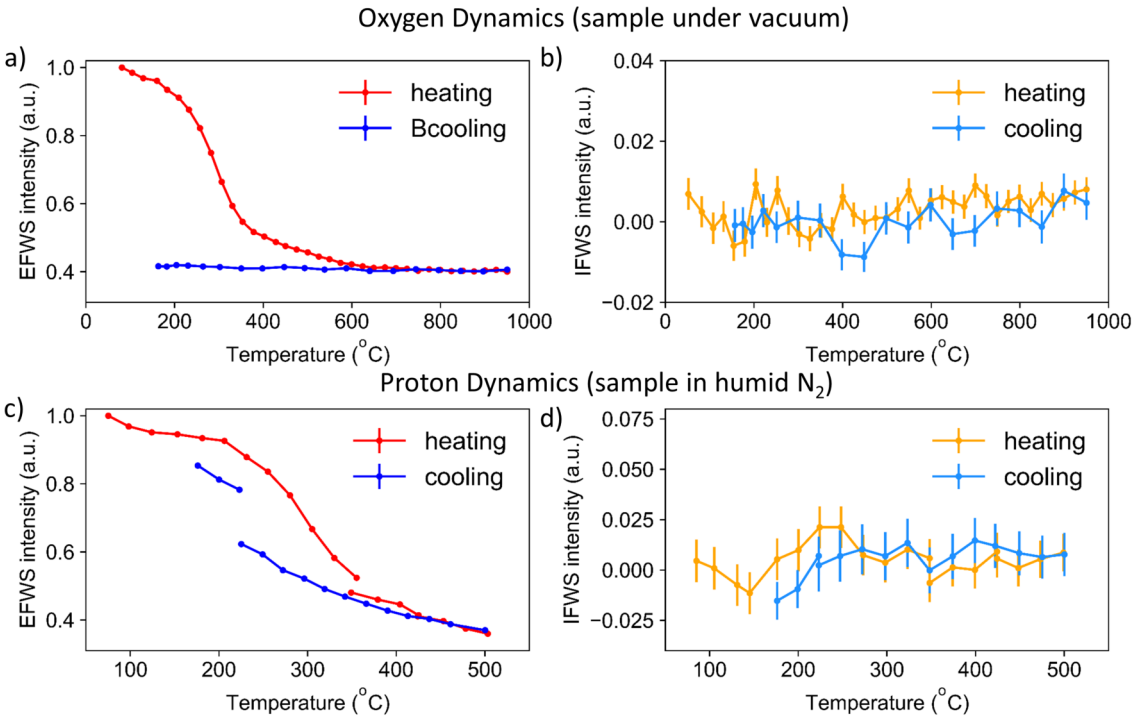

Figure 5.10: Elastic (a, c) and inelastic (b, d) fixed window scans in vacuum (top) and in humid N_2 (bottom). Gaps in curves are caused by QENS measurements performed for several hours between the fixed window scans during which some intensity is gained (if water is reabsorbed on cooling) or lost (if water is lost on heating).

A large (≈ 50 %) decrease in elastic intensity occurs between 210 °C and 360 °C on heating under vacuum (figure 5.10a). The lack of increase in inelastic intensity in the same temperature range (figure 5.10b) suggests that this is caused by

dehydration, i.e. the loss of protons from the sample, and not an onset of dynamics. The data collected on cooling further support this, as under vacuum the lost elastic intensity is not regained, suggesting an irreversible process under these conditions. This agrees well with TGA data reported by Fop et al.[242] (figure 5.11) showing the dehydration of the sample between approximately 200 and 400 °C. While the IFWS collected on cooling in vacuum (figure 5.10b) appears to suggest a very slight gradual increase in intensity above 650 °C, this is too small to be analysed. Furthermore, no broadening could be observed in the QENS data collected at 950 °C (figure 5.12), indicating that, even at such a relatively high temperature, the dynamics of the oxide ions are too slow or the number of oxide ions diffusing through the sample is too small to give a measurable contribution to the signal in the nanosecond timescale accessible with IN16b.

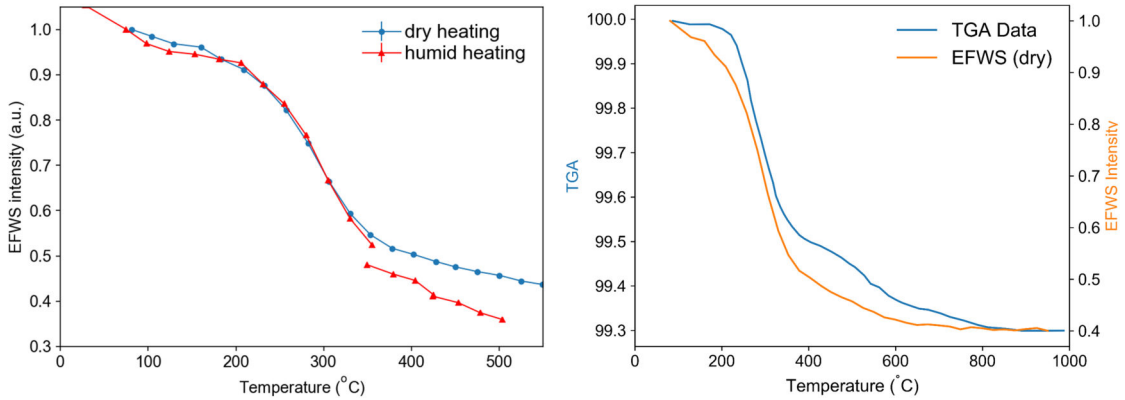

Figure 5.11: Comparison of EFWS in dry and humid atmosphere (left) and EFWS intensity of the dry sample collected on heating to TGA data (right).[259]

In the data collected on a separate sample under humid N_2, the decrease in elastic intensity on heating (figure 5.10c) is comparable to that observed under vacuum (figure 5.11). The corresponding inelastic intensity (figure 5.10d) shows the appearance of a small peak starting at 150 °C and reaching a maximum at 225 °C. While this peak is indicative of increased proton dynamics in this temperature range, no QENS broadening was observed in QENS data collected at 225 °C and 175 °C on cooling (figure 5.12). This is likely due to the slow reabsorption of water, consistent with the IFWS not regaining all intensity on cooling.

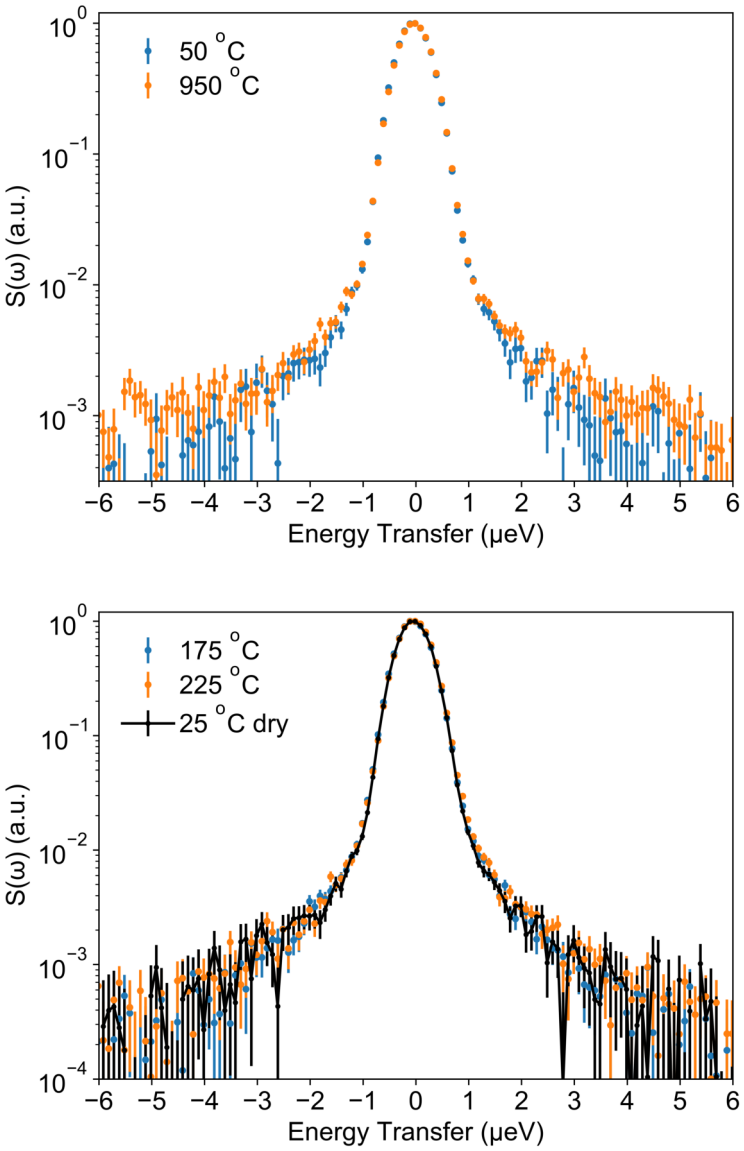

Figure 5.12: Data measured on IN16b and summed over all detectors, collected on $Ba_7Nb_4MoO_{20}$ under vacuum at 50 and 950 °C (top) and in humid N_2 at 175 and 225 °C (bottom), showing no sign of QENS broadening in either atmosphere.

Overall, the data collected on IN16b suggests that longer counting times would be required to determine quantitative parameters of proton dynamics in $Ba_7Nb_4MoO_{20}$, while observation of oxide ion dynamics would require significantly higher temperatures.

While QENS is a powerful tool for the study of oxide ion diffusion,[92,95,97,99,108] the small and predominantly coherent neutron scattering cross section of oxygen makes both observation and analysis of QENS difficult in many cases. Ab initio

molecular dynamics (AIMD) are very compatible with QENS,[29,95,99,175] and this complementarity is therefore frequently used to investigate oxide ion diffusion.

5.4.4 Oxide Ion Dynamics in $Ba_7Nb_4MoO_{20}$ Investigated by AIMD

Mean square displacement (MSD) plots of all oxygen atoms at 1000, 1500, and 2000 °C are shown in figure 5.13.

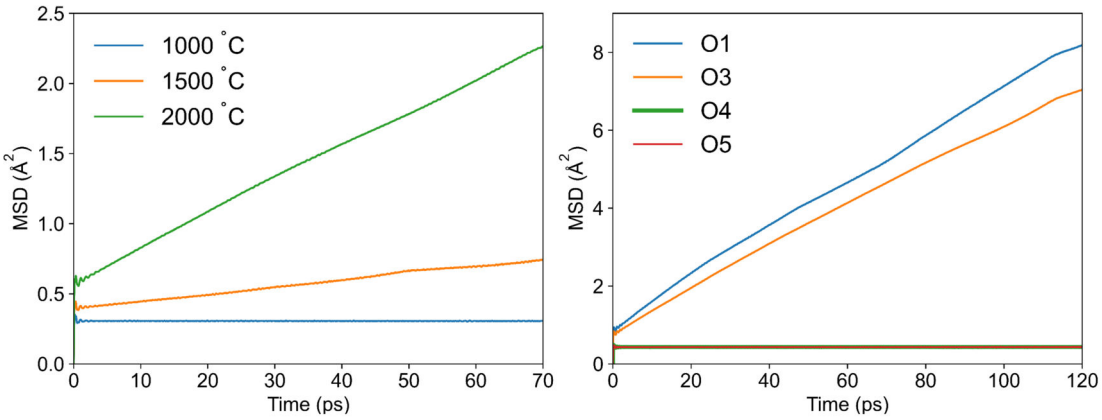

Figure 5.13: MSD curves of all oxygen atoms at three temperatures (left) and contribution of the individual oxygen sites to the MSD at 2000 °C (right).

The flat MSD plot at 1000 °C is indicative of the absence of significant oxide ion dynamics, showing that higher temperatures are required to simulate diffusion of oxide ions. At 1500 °C, a slope in the MSD curve is apparent, suggesting the onset of long-range diffusion. This allows a diffusion coefficient of 0.8×10^{-7} cm^2 s^{-1} to be calculated, showing that diffusion is slow. This is consistent with the absence of the QENS signal in the neutron scattering data collected on IN16b at 950 °C in $Ba_7Nb_4MoO_{20}$. For comparison, the diffusion coefficient determined from AIMD for the excellent oxide ion conductor $Bi_{0.931}V_{0.087}O_{1.587}$, on which dynamics were clearly observed on IN16b,[108] was approximately 5×10^{-7} cm^2 s^{-1} at 600 °C.[108] Further increase of the simulated temperature to 2000 °C leads to a more pronounced slope in the MSD curve caused by significant dynamics, with the diffusion coefficient increasing to 3.3×10^{-7} cm^2 s^{-1}. While this simulation temperature is very high, AIMD often requires higher temperatures than needed in experiments to observe

long-range diffusion due to the constraints of small simulation cells and relatively short simulation lengths.[261–264] This is also evident from the previous AIMD simulation on $Ba_7Nb_4MoO_{20}$ at 1100 K,[259] where only one jump was observed, despite the high, experimentally determined oxide ion conductivity of $Ba_7Nb_4MoO_{20}$ at this temperature. Consistent with this, the simulation at 2000 °C was analysed in detail to gain insights on the present dynamics.

The individual MSD curves for the different occupied oxygen sites (O1, O3, O4, O5) indicate that only oxygen atoms originally at O1 and O3 crystallographic sites contribute to oxide ion dynamics in $Ba_7Nb_4MoO_{20}$, while O4 and O5 oxygen atoms do not contribute to the dynamics (figure 5.13).

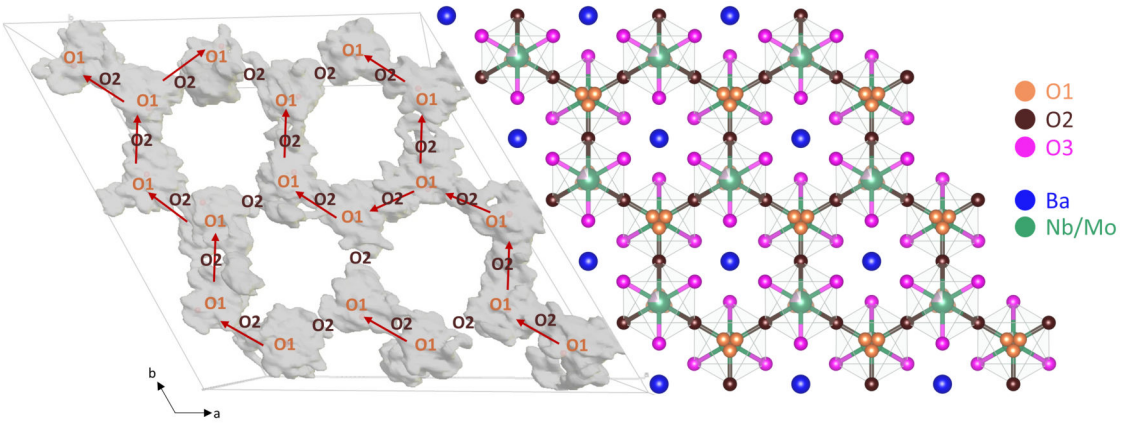

Figure 5.14: Visualisation of the 200 ps trajectory obtained from AIMD simulations at 2000 °C. The red arrows highlight the continuous pathway observed in the *ab* plane caused by O1 jumps. The grey clouds show the space visited by all O1 oxygen atoms.

Cloud plots can be used to visualise the simulated trajectories by highlighting the space visited by certain oxygen atoms over the course of the simulation. Figure 5.14 shows the trajectories of all O1 atoms in the simulation box at 2000 °C, demonstrating for the first time a continuous pathway for oxide ion diffusion in the *ab* plane. This in-plane diffusion occurs by hopping of O1 oxygen atoms to neighbouring O1 sites via the empty O2 sites, consistent with facile 2D migration pathways suggested by bond valence consideration.[57,257,258] In addition to this, these simulations reveal significant contribution to the overall diffusion by O3 oxygen atoms, as shown in the MSD curves (figure 5.13). No direct O3-O3 jump was observed, despite the average

distance of 2.9 Å between O3 sites being comparable to the O1-O1 distance (2.8-3.8 Å due to the split nature of the O1 site), highlighting the importance of the O2 position, acting as a transition site, for the long-range conductivity.

Rotational flexibility of the (Nb/Mo)O_x polyhedra allows O3 oxygen atoms to jump to the nearest O1 site. This is the first observation of oxide ion dynamics perpendicular to the *ab* plane in $Ba_7Nb_4MoO_{20}$. Once an O3-O1 jump has occurred, these atoms can diffuse via the O1-O2-O1 two-dimensional pathway. The significant delocalisation of O1 and O3 atoms is shown in figure 5.15. This is facilitated by the ability of both Mo and Nb to adopt various coordination environments, which has been shown to support fast dynamics in several other oxide ion conductors.[88,162,181,241,265–268]

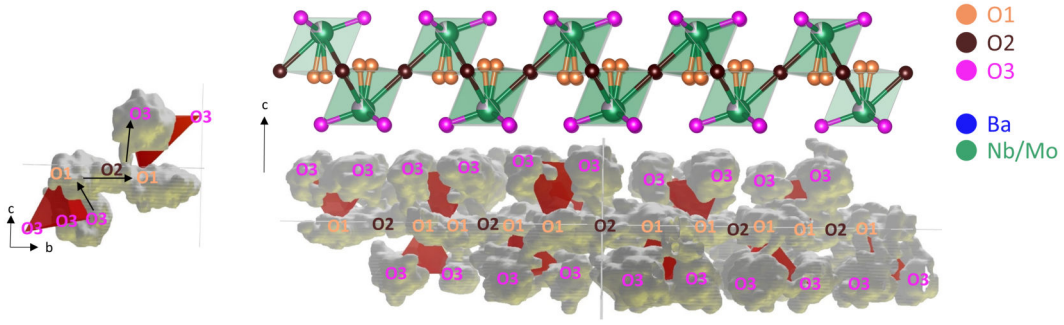

Figure 5.15: Visualisation of the O3 dynamics during 200 ps AIMD simulations at 2000 °C. The black arrows (left) highlight the jump of an O3 oxygen atom to an adjacent Nb/Mo_x via two O1 sites. The grey clouds (right) show the space visited by all O3 oxygen atoms, revealing strong delocalisation.

	1500 °C (50 ps)		1500 °C (100 ps)		2000 °C (100 ps)		2000 °C (200 ps)	
	O1	O3	O1	O3	O1	O3	O1	O3
total jumps	2	4	3	6	11	28	25	60
% of total jumps	33	67	33	67	28	72	29	71

Table 5.4: Summary of all jumps occurring during the simulations at 1500 and 2000 °C.

An analysis of all occurring jumps at 1500 °C and 2000 °C provides further insight into the oxide ion dynamics (table 5.4), highlighting the significant mobility

of O3 oxygen atoms. To ensure statistical accuracy of the comparison, the first 100 ps of the 1500 °C simulation and all 200 ps of the 2000 °C simulation were split in half, resulting in excellent agreement between the obtained percentage of total jumps of each site, O1 and O3, at both temperatures. Comparing the number of jumps occurring at 1500 °C and 2000 °C shows that O3 dynamics become more significant with increasing temperatures, which can be explained by the activation energy for localised motions being generally lower than for long-range diffusion, as has been observed in other oxide ion conductors.[108,172]

5.5 Conclusions and Future Work

This chapter focused on the study of two hexagonal perovskite materials, a new family of oxide ion conductors, $Ba_3NbMoO_{8.5}$ and $Ba_7Nb_4MoO_{20}$. The phasetransition which was observed in synchrotron PXRD data[244] was successfully measured using variable-temperature laboratory PXRD, and the reversibility of this transition was clearly demonstrated for the first time. QENS measurements on $Ba_3NbMoO_{8.5}$ and $Ba_7Nb_4MoO_{20}$ were unsuccessful, suggesting that higher temperatures are required to observe oxide ion dynamics on a nanosecond timescale in both materials. While an onset of proton dynamics in $Ba_7Nb_4MoO_{20}$ was apparent, longer measuring times are required to allow a quantitative analysis.

AIMD simulations on $Ba_7Nb_4MoO_{20}$ were performed at various temperatures and for significantly longer times than previously reported,[259] showing a continuous oxide ion diffusion pathway in the *ab* plane. This highlights the importance of the O2 site for long-range diffusion. Moreover, the simulations revealed a significant contribution of out-of-plane O3 dynamics to the conductivity mechanism, through a process which essentially amounts to the rotation of the $M1O_4$ tetrahedra followed by injection of O3 atoms into the *ab* plane. This is the first time out-of-plane dynamics have been reported in $Ba_7Nb_4MoO_{20}$. The contribution of this process to the long-range diffusion is very significant, and suggests that enhancing the ease of rotation of these $M1O_4$ tetrahedra could be a viable method to further increase oxide ion conductivity in $Ba_7Nb_4MoO_{20}$, for example by substituting some Mo^{6+} with V^{5+},

as VO_4 groups are known to be rotationally flexible, and La^+ to charge-compensate, creating a $Ba_{7-x}La_xNb_4Mo_{1-y}V_yO_{20}$ series.

Future work on $Ba_3NbMoO_{8.5}$ is needed to fully understand oxide ion diffusion. Single crystal impedance spectroscopy could help determine whether the ionic conductivity is predominantly two dimensional. This could also be achieved with AIMD simulations, which would generally allow a more detailed insight into oxide ion dynamics in this complex material.

Regarding $Ba_7Nb_4MoO_{20}$, the exploratory synthesis and characterisation of a series of $Ba_{7-x}La_xNb_4Mo_{1-y}V_yO_{20}$-compounds would be important, as it could lead to an increase in oxide ion conductivity. This would further validate the conclusions of this work regarding the importance of rotational flexibility of the M1-centred polyhedra to long-range oxide ion dynamics in $Ba_7Nb_4MoO_{20}$. Further substitution, e.g. V- and La- co-doping, should increase dynamics perpendicular to the *ab* plane, and AIMD simulations of a $Ba_{7-x}La_xNb_4Mo_{1-y}V_yO_{20}$ compound could be used to probe this out-of-plane dynamics.

CHAPTER 6

Ionic Diffusion in $CsBi_2Ti_2NbO_{10-\delta}$: A Dion-Jacobson Type Oxide Ion Conductor

6.1 Summary

This chapter presents the first ab initio molecular dynamics simulations performed to investigate oxide ion dynamics in the new Dion-Jacobson phase oxide ion conductor $CsBi_2Ti_2NbO_{10-\delta}$. Simulations show high mobility of oxygen atoms in and adjacent to the conducting *ab* plane, while the contribution of other oxygen atoms is significantly lower. Additionally, analysis of the total number of jumps indicates that long-range oxide ion migration predominantly occurs via jumps out of and back into the conducting plane, giving crucial insight into which structural features are important to achieve a high ionic conductivity in these materials.

6.2 Introduction

The Dion-Jacobson phases belong to the structure family of layered perovskites, several of which have been found to be oxide ion conductors, for example the brownmillerites,[29,269–271] and Ruddlesden-Popper phases.[272–275]

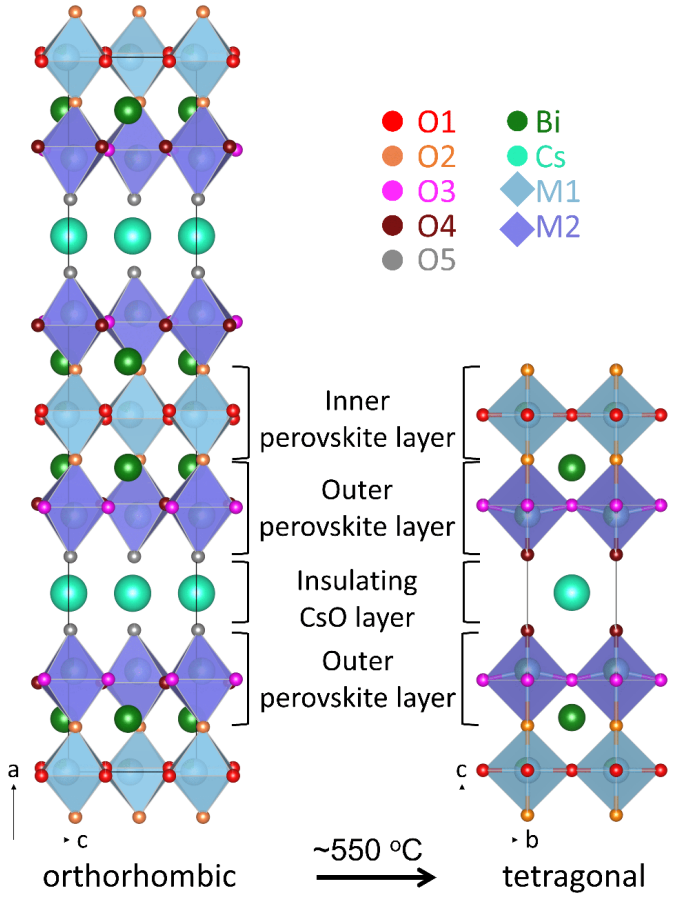

Figure 6.1: $CsBi_2Ti_2NbO_{10-\delta}$ in its low-temperature, orthorhombic structure (left) and high-temperature, tetragonal structure (right) obtained from neutron diffraction.[276]

Dion-Jacobson layered perovskite-type compounds[277,278] have the general formula $M_m[A_{n-1}B_nO_{3n+1}]$, where M is an interlayer cation (e.g. Cs, Rb, Li, H, Ag). The inner and outer perovskite layers consist of cubically arranged BO_6 octahedra, with A being a large cation occupying the central 12-coordinated sites of each cube.[277] The interlayer cation, located in the insulating layer, limits this $[A_{n-1}B_nO_{3n+1}]$ block in the c-direction, creating separate, perovskite-like layers. The number of BO_6 octahedra is given by n, which also determines the thickness of the

perovskite layers. The size of the A cation influences the stacking of the layers, with larger cations (e.g. Cs^+) resulting in an eclipsed conformation, and smaller ones (e.g. K^+) in a staggered conformation.[279] The ideal, tetragonal structure of the Dion-Jacobson phases is shown in figure 6.1 (right), with $CsBi_2Ti_2NbO_{10-\delta}$ being used as example. Here, Cs^+ is the interlayer cation (M), Bi^{3+} the central, 12-coordinated cation (A), and Ti^{4+}/Nb^{5+} are the cations at the centre of the BO_6 octahedra.

Oxide ion conductivity in a material adopting the Dion-Jacobson phase was first reported in 2020.[276] Using bond-valence site energy (BVSE) calculations, the activation energy for oxide ion migration was calculated for 69 Dion-Jacobson phases, fourteen of which were found to have an energy barrier of < 0.51 eV. The composition $CsBi_2Ti_2NbO_{9.80}$ was chosen for further investigation. Its high bulk oxide ion conductivity of 8.9×10^{-2} S cm^{-1} at 800 °C and 1.5×10^{-2} S cm^{-1} at 600 °C shows the high potential of discovering excellent oxide ion conductors in this new structure family.

$CsBi_2Ti_2NbO_{10-\delta}$ was found to undergo a reversible, first-order phase transition between 540 and 560 °C from an orthorhombic $Ima2$ structure to a tetragonal $P4/mmm$ structure[276,279] as shown in figure 6.1. The orthorhombic distortion of the low-temperature structure compared to the high-temperature structure results in a doubling of the unit cell (figure 6.1), and is caused by rotations of the octahedra centered on the M1 and M2 sites.[279] Oxide ion conductivity was found to increase abruptly by approximately one order of magnitude at the transition temperature. Additionally, both TGA data and neutron diffraction data suggest a decrease in oxygen concentration from $CsBi_2Ti_2NbO_{10}$ in the low-temperature phase to $CsBi_2Ti_2NbO_{9.80}$ in the high-temperature phase. This increase in oxygen vacancies, represented by δ in $CsBi_2Ti_2NbO_{10-\delta}$, contributes to its high oxide ion conductivity.[276] No proton conductivity was observed, and while a low oxygen partial pressure of $< 2.0 \times 10^{-22}$ atm resulted in a small electronic contribution to the total conductivity, oxygen concentration cell measurements at temperatures between 600 and 900 °C showed that oxide ions are the dominant charge carriers, making it a pure oxide ion conductor.[276]

The structure of the high-temperature, tetragonal phase consists of two outer

$Bi(Ti_{0.598}Nb_{0.402})O_{3-3\delta/10}$ and one inner $Bi(Ti_{0.804}Nb_{0.196})O_{3-3\delta/10}$ perovskite layer, as well as an insulating $CsO_{1-\delta/10}$ rock salt layer (figure 6.1).[276] BVSE calculations[276] suggest potential oxide ion diffusion pathways between O1-O2, O1-O1, and also O2-O3 sites, in good agreement with the large, anisotropic displacement parameters found for O1 and O2 sites. This indicates that diffusion is two-dimensional.[276] However, neutron scattering length density analysed using the maximum entropy method (MEM) did not show clear pathways.[276] It was suggested[276] that the large size of Cs^+ and Bi^{3+} cations (1.74 Å and 1.17 Å for 8-coordinated Cs^{3+} and Bi^{3+}, respectively[180]) causes a displacement of the Bi^{3+} cations along the *b* and *c* directions in the high-temperature phase, resulting in increased distances between Bi sites, thereby creating favourable, large bottlenecks. Here, a bottleneck describes the limiting point for oxide ion migration along a certain migration pathway, with a smaller bottleneck constraining diffusion more. These large bottlenecks, in addition to the intrinsic oxide ion vacancies, was proposed to facilitate diffusion of O1 and O2 oxygen atoms in $CsBi_2Ti_2NbO_{10-\delta}$.[276]

Despite its good ionic conductivity, the phase transition of $CsBi_2Ti_2NbO_{10-\delta}$ would pose a problem in potential practical applications. To overcome this, a series of $CsA_2Ti_2NbO_{10-\delta}$ with A = La^{3+}, Pr^{3+}, Nd^{3+}, Sm^{3+}, which adopt the tetragonal $P4/mmm$ structure at room temperature, was synthesised.[280] The total conductivity was found to increase with increasing ionic radius of the A cation. $CsLa_2Ti_2NbO_{10-\delta}$ exhibits the highest conductivity and was therefore investigated further.[280] No phase transition was observed on heating to 800 °C. The distribution of Ti and Nb over the inner and outer perovskite layers was found to differ from that observed in $CsBi_2Ti_2NbO_{10-\delta}$. The M1 cation site of the inner perovskite layer is predominantly occupied by Ti ($Ti_{0.985}Nb_{0.015}$), while the M2 cation site of the outer layer has a statistical distribution of cations ($Ti_{0.508}Nb_{0.492}$). This was further confirmed by density functional theory (DFT) geometry optimisation calculations, indicating that M1 is exclusively occupied by Ti.[280] The bulk conductivity of $CsLa_2Ti_2NbO_{10-\delta}$ at 800 °C is 2.2×10^{-4} S cm^{-1}, more than two orders of magnitude lower than that of $CsBi_2Ti_2NbO_{10-\delta}$. While no proton conduction was observed, the oxide ion transport number reduces from 0.99 at 600 °C, to 0.71 at 800

°C. At even higher temperatures as well as in a reducing atmosphere it decreases to 0.32 - 0.13, showing significant electronic conductivity.[280]

The significantly lower conductivity was attributed to the smaller ionic radii of La^{3+} compared to Bi^{3+} causing smaller bottlenecks for diffusion, as well as a lower vacancy concentration in the La compound. However, comparing the ionic radii of, for example, 8-coordinate Bi^{3+} (1.17 Å)[180] and 8-coordinate La^{3+} (1.16 Å)[180] shows that the sizes of these two cations are very comparable. This suggests that the decrease in conductivity of $CsLa_2Ti_2NbO_{9.92}$ compared to $CsBi_2Ti_2NbO_{9.80}$ is either predominantly caused by the lower vacancy concentration, or that the $6s^2$ lone pairs of Bi^{3+} play a significant role in increasing the bottleneck. BVSE calculations suggest O1-O1 (0.74 eV), O1-O2 (1.24 eV), O2-O3 (1.35 eV) and O3-O3 (1.32 eV) migration paths, with estimated activation barriers for each given in parentheses.[280] This implies that oxide ion diffusion in $CsLa_2Ti_2NbO_{10-\delta}$ occurs predominantly via O1-O1 jumps.

Further improvement of the oxide ion conductivity of $CsBi_2Ti_2NbO_{10-\delta}$ was attempted by acceptor doping of Bi with alkaline earth metals.[281] While an unknown impurity is present in all samples of this $CsBi_{2-x}M_xTi_2NbO_{10-x/2}$ (M = Mg^{2+}, Ca^{2+}, Sr^{2+}, Ba^{2+}) series, compositions with M = Ca^{2+}, Sr^{2+}, Ba^{2+} show a majority orthorhombic Dion-Jacobson phase. Out of this series, only $CsBi_{1.9}Sr_{0.1}Ti_2NbO_{9.95}$ has a higher total conductivity than the parent compound (6×10^{-3} S cm^{-1} compared to 3×10^{-3} S cm^{-1} at 800 °C, and 0.7×10^{-3} S cm^{-1} compared to 0.4×10^{-3} S cm^{-1} at 600 °C). At 600 °C, the conductivity is independent of partial oxygen pressure over a wide range of 1 to 10^{-25} atm, indicating oxide ion conductivity.[281] The increase of conductivity can be attributed to an increase in oxide ion vacancies, and the better size match of Sr^{2+} and Bi^{3+} compared to the other dopants.[281] Moreover, variation of the Ti^{4+}/Nb^{5+} ratio in a $CsBi_2Ti_{2-x}Nb_{1+x}O_{10+x/2}$ (x = 0.1, 0.2, -0.1, -0.2) series resulted in an increased total conductivity compared to $CsBi_2Ti_2NbO_{10-\delta}$ for all studied compounds. $CsBi_2Ti_{1.8}Nb_{1.2}O_{10.10}$ showed the highest conductivity in this series, with an increase of approximately half an order of magnitude compared to the parent compound $CsBi_2Ti_2NbO_{10-\delta}$.[282]

6.2.1 Aims of this Work

The discovery of high ionic conductivity in new classes of materials provides significant opportunities for improving their properties by chemical modifications. This could give rise to the discovery of new, better-performing oxide ion conductors, making it an area of considerable scientific interest. $CsBi_2Ti_2NbO_{10-\delta}$ shows high oxide ion conductivity, and doping has been shown to increase it further. However, no ab initio molecular dynamics simulations investigating oxide ion diffusion in Dion-Jacobson phase oxide ion conductors have been published to date. Therefore, the aim of the work presented in this chapter is to gain a detailed insight into the local and long-range oxide ion diffusion mechanism using AIMD simulations.

6.3 Computational Methods

Ab initio molecular dynamics simulations were performed using the density functional theory (DFT) method implemented in the Vienna ab initio simulation package (VASP) code.[75] The electronic structure was obtained using the GW approximation.[283] The projector augmented wave (PAW) method[154] with GGA-PBE (Perdew-Burke-Ernzerhof generalized-gradient-approximation) exchange-correlation functional were used for all simulations.[155]

As significant conductivity is expected in the high-temperature phase, the data reported by Zhang et al.[276] at 700 °C in space group $P4/mmm$ was used to create a $4 \times 4 \times 1$ supercell of $CsBi_2Ti_2NbO_{10-\delta}$. Ti and Nb atoms were distributed over M1 and M2 sites according to their relative occupancies obtained from neutron diffraction data using a random number generator. To account for the oxygen deficiency, four vacancies were introduced, resulting in an atomic content of the final simulation box of $Cs_{16}Bi_{32}Ti_{32}Nb_{16}O_{156}$, giving a formula of $CsBi_2Ti_2NbO_{9.75}$, which is close to the atomic formula of $CsBi_2Ti_2NbO_{9.80}$ determined from neutron diffraction data at 700 °C. Three different models, varying in the initial, random distribution of vacancies, were generated. In model 1, O1 sites were fully occupied, one vacancy was introduced on each O2 and O3 sites, and two vacancies were distributed over O4

sites. In model 2, each O1, O2, O3, and O4 site contained one vacancy. In model 3, two vacancies were distributed on each O1 and O2 sites, and O3 and O4 sites were fully occupied.

Simulations were performed first for 100 ps at 1000 °C for the three different models, and for all further simulations model 2 was used. In total, simulations were performed at 600, 800, 1000, 1200, 1400 °C for 300 ps each, using a time step of 2 fs and a cutoff energy of 300 eV. Data analysis was carried out using the MDANSE code[156] and cloud plots were generated in LAMP.[157]

6.4 Results and Discussion

6.4.1 Effect of the Initial Vacancy Distribution on Oxide Ion Dynamics in $CsBi_2Ti_2NbO_{10-\delta}$

The intrinsic oxygen deficiency in the high-temperature phase of $CsBi_2Ti_2NbO_{10-\delta}$ has been suggested to play an important role in the high oxide ion conductivity of this material.[276]

To investigate the influence of the initial distribution of vacancies in the simulation box on the results, three different models were considered and the root mean square fluctuation (RMSF) during the simulations compared (figure 6.2). The RMSF shows how much a particular atoms moves during the simulation, and hence allows distinguishing of particularly mobile atoms. It is calculated using:

$$RMSF = \sqrt{\langle (x_i - \langle x_i \rangle)^2 \rangle} \tag{6.1}$$

where x_i is the position of atom i, and $\langle x_i \rangle$ the ensemble average position of i.

Model 1 took into account the occupancy factors of the four oxygen sites refined from neutron diffraction data,[276] according to which $\frac{2}{4}$ of vacancies are located on O4 sites, and $\frac{1}{4}$ each on O2 and O3 sites. However, previous investigation suggests predominantly two-dimensional diffusion involving O1 and O2 sites, which would imply that the vacancies on the O4 site do not contribute to long-range dynamics. This is in agreement with the RMSF of oxygen atoms located on the O4 site being

low, as shown in figure 6.2a. Despite the two vacancies present on the O4 site, the RMSF indicates that oxygen atoms on O1 and O2 sites are the most mobile.

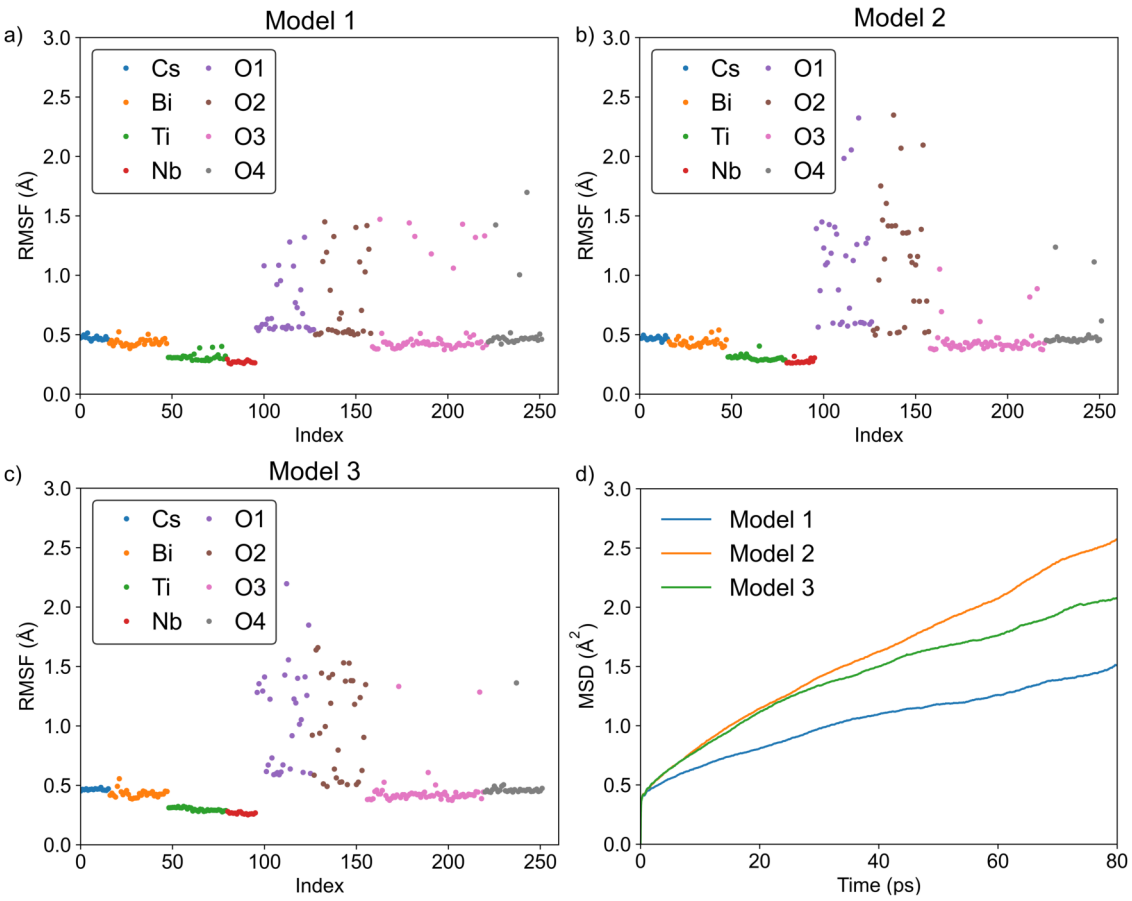

Figure 6.2: Root mean square fluctuation (RMSF) of all atoms during the simulation of 100 ps at 1000 °C for the three different initial vacancy distributions: model 1 (a), model 2 (b), and model 3 (c); Mean square displacement curves of all oxygen atoms for each model (d).

In model 2, the four vacancies were distributed evenly across all four crystallographic oxygen sites. This model emphasises the increased dynamics on O1 and O2 sites located in the inner perovskite layer, compared to O3 and O4 which are located in the outer perovskite layer.

Model 3 was created to investigate whether additional vacancies on the O1 and O2 sites would change the behaviour substantially, and therefore two vacancies were distributed over each, O1 and O2 sites. No significant change of the RMSF of O1 and O2 oxygen atoms was observed compared to model 2 (figure 6.2b), and the mean square displacement (MSD) curves of all oxygen atoms in the three distinct

models even shows a slightly lower MSD. The diffusion coefficients (D) obtained from the slopes of the MSD curves are 2.1 ± 0.5 × 10^{-7}, 4.4 ± 0.4 × 10^{-7}, and 3.3 ± 0.9 × 10^{-7} cm^2 s^{-1} for models 1, 2, and 3, respectively. As the error on the slope of the MSD curves becomes larger towards the end of the simulation, as discussed in chapter 2, it is difficult to obtain an error on these diffusion coefficients. To approximate it, the MSD curves were halved and the slope of the first and second half were compared. The diffusion coefficient calculated for model 2 and model 3 lie within the error of each other, suggesting that additional vacancies on O1 and O2 sites do not increase ionic diffusion significantly. The order of magnitude of D for all three models suggests that a potential observation of QENS on the nanosecond timescale could be possible.[92,108,175]

The three different models show that, regardless of the initial distribution of vacancies, oxygen atoms on the O1 and O2 sites are the most mobile. As model 2 shows the highest MSD while also representing the most even distribution of vacancies on all sites, enhancing the likelihood that a potential jump can be observed, this model was used for all further simulations.

6.4.2 Oxide Ion Dynamics in $CsBi_2Ti_2NbO_{10-\delta}$ Investigated by Multiple Temperature AIMD

Simulations were carried out at five temperatures (600, 800, 1000, 1200, 1400 °C), and the mean square displacement (MSD) curves for all oxygen atoms at each temperature were determined, as shown in figure 6.3. An increase in MSD at higher temperatures is consistent with increased oxide ion dynamics.

Comparison of the MSD curves obtained for the four crystallographically distinct oxygen sites provides more in-depth information about the dynamics. Figure 6.4 shows that oxygen atoms originally at the O1 and O2 sites move significantly further during 200 ps than those on O3 and O4 sites. The MSD of O1 and O2 oxygen atoms at 1200 °C is 22 $Å^2$, giving an average displacement of 4.7 Å. The maximum distance between oxygen sites on the same Ti/NbO_6 unit is ≈ 3.9 Å, significantly smaller than the average displacement, which indicates long-range diffusion of oxygen atoms

on these sites. Additionally, the strong correlation between the MSD curves of O1 and O2 oxygen atoms (figure 6.4) suggests that the oxygen atoms on these sites cannot be readily separated as a result of fast motions between these sites.

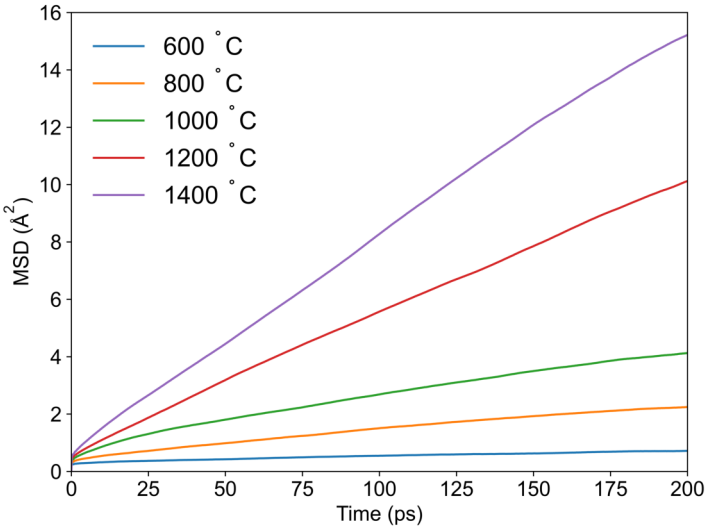

Figure 6.3: Mean square displacement curves of all oxygen atoms from simulations at 600, 800, 1000, 1200, and 1400 °C.

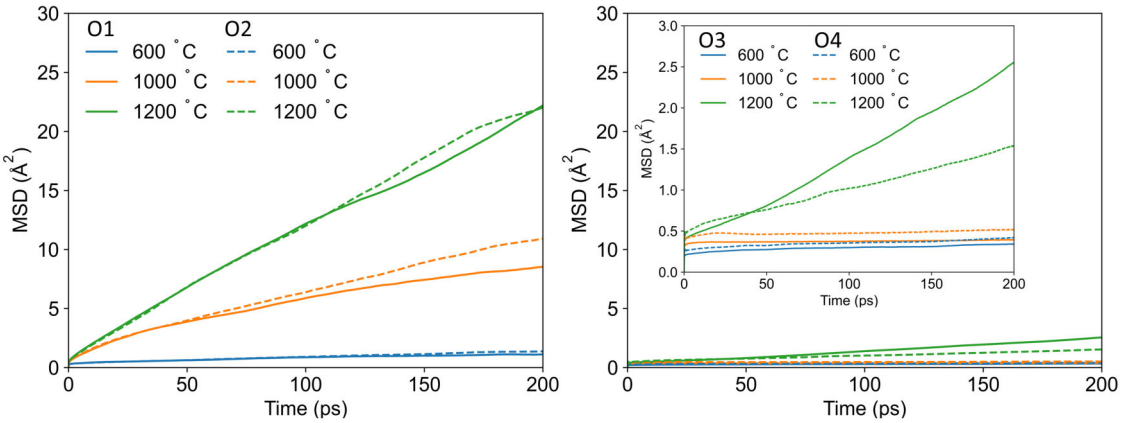

Figure 6.4: Comparison of mean square displacement curves of O1 and O2 oxygen atoms (left) and O3 and O4 oxygen atoms (right) at 600, 1000, 1200 °C.

In contrast to that, MSD curves of O3 and O4 oxygen atoms are flat, indicating no significant dynamics, even at 1000 °C. The small MSD of 0.5 Å^2 at 1000 °C suggests that oxide ion dynamics are very slow, and jumps between adjacent sites on the same polyhedron are very limited at this temperature. At 1200 °C, a difference

in behaviour of O3 and O4 oxygen atoms becomes apparent, with atoms on the O3 site moving considerably further. However, the average displacement of 1.6 Å is not enough to determine whether jumps between adjacent polyhedra take place.

From the slope of the MSD curves, the diffusion coefficient (D) was obtained. From this, the activation energy for diffusion can be obtained through an Arrhenius type relationship with temperature. Figure 6.5 shows the temperature dependence of D for $CsBi_2Ti_2NbO_{10-\delta}$. The calculated activation energy is 0.55 ± 0.03 eV. This is on the same order of magnitude though slightly smaller than the value of 0.846 ± 0.005 eV reported from impedance data.[276] However, discrepancies between microscopic measurements like AIMD and NMR and macroscopic measurements like impedance spectroscopy are common[99,103,105,108] and were also discussed in Chapter 3. The energy barrier for oxide ion migration from bond-valence-based energy calculations in $CsBi_2Ti_2NbO_{10-\delta}$ is 0.50 eV,[276] in excellent agreement with the activation energy for diffusion determined here.

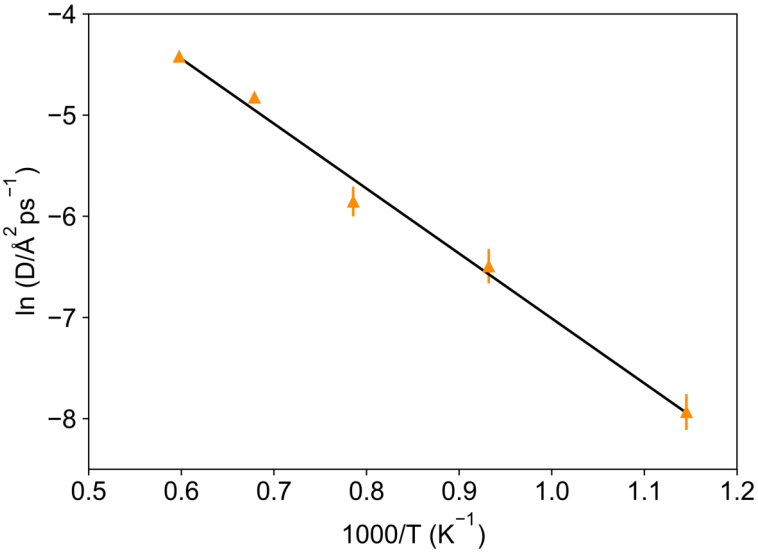

Figure 6.5: Arrhenius-type plot of diffusion coefficients (D) obtained from simulated MSD against inverse temperature.

Visualisation of the trajectories at 1000 °C, where significant dynamics are observed in the MSD curves, are shown in figure 6.6 in the form of cloud plots. It is apparent that there are no continuous oxide ion migration pathways through the simulation box along the *c* axis, as expected due to the large Cs^{3+} cation separating

the layers of $CsBi_2Ti_2NbO_{10-\delta}$. However, significant dynamics are apparent within the perovsike-type layers, and oxygen jumps can be observed for all of the four distinct oxygen sites. The considerable delocalisation of the O1 and O2 oxygen atoms can be seen in figure 6.6 b, but due to the large number of jumps, separate pathways cannot be easily distinguished.

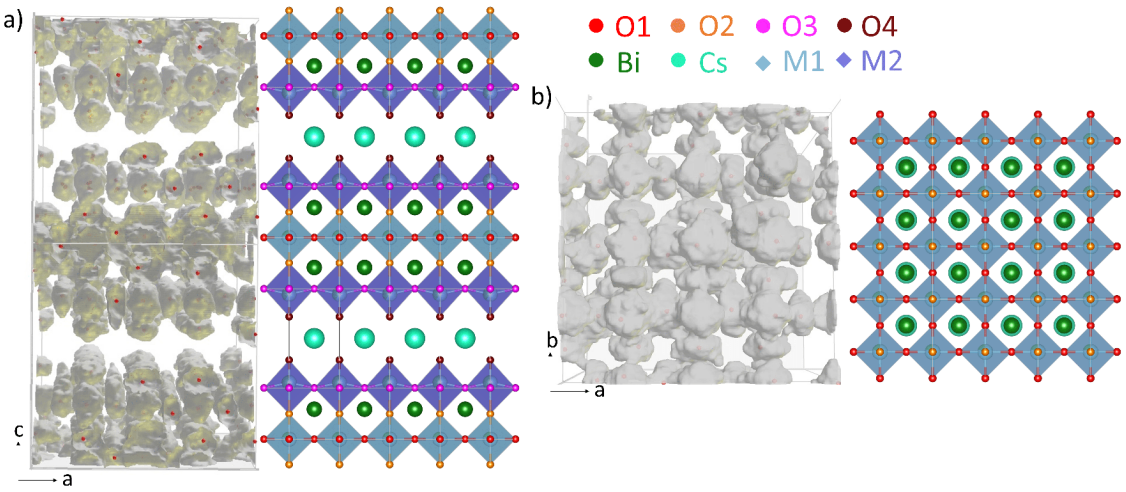

Figure 6.6: Visualisation of the 300 ps trajectory obtained from AIMD simulations at 1000 °C. The grey clouds show the space visited by all oxygen (a) and all O1 and O2 oxygen atoms (b).

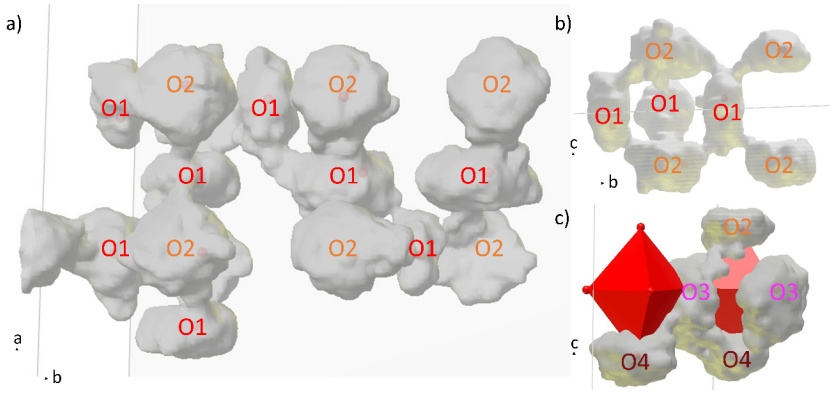

Figure 6.7: Visualisation of the 300 ps trajectory obtained from AIMD simulations at 1000 °C, showing a continuous O1-O2-O1 pathway (a, b) as well as a jump between O2-O3, and O3-O4 (c). The grey clouds show the space visited by certain oxygen atoms.

Selection of only a few specific oxygen atoms allows several oxygen jumps to be observed, as shown in figure 6.7. The O2 site appears to play an important role

in long-range diffusion, creating an O1-O2-O1 diffusion pathway (figure 6.7a, b), with jumps directly between O1 sites being less frequently observed (figure 6.7b). Additionally, continuous O2-O3-O4 and O3-O4-O3-O4 pathways indicate that jumps occur from all four crystallographically distinct oxygen sites.

To obtain a more in-depth view of the oxide ion dynamics as well as to gain insight into the contribution of each oxygen site to long-range diffusion, the total jumps per oxygen atom were analysed. Table 6.1 summarises all oxygen jumps observed at the five different simulation temperatures. Oxygen atoms were separated depending on the site at which they are located at the start of the simulation. Additionally, jumps in the *ab* plane and jumps out of the *ab* plane along the *c* axis were distinguished. This allowed separation of O1-O1 and O3-O3 jumps, i.e movement in the *ab* plane, from O1-O2, O2-O3, and O3-O4 jumps, along the *c* axis.

Table 6.1 shows that for all oxygen sites, jumps along *c* are dominant over jumps in the *ab* plane. These jumps are restricted to the separate perovskite layers and do not cause continuous pathways along the *c* axis of the unit cell. At increasing temperature, jumps in the *ab* plane are observed for all oxygen atoms except those located at O4 sites. However, it is important to note that the jump analysis shows that all O2 oxygen atoms first jump along *c* to an O1 site, and only after that can *ab* in-plane diffusion of an O2 oxygen atom take place. As expected due to the large distance of 3.9 Å between adjacent O2 sites, no direct O2-O2 jump is observed.

	600 °C		800 °C		1000 °C		1200 °C		1400 °C	
along	*ab*	*c*	*ab*	*c*	*ab*	*c*	*ab*	*c*	*ab*	*c*
O1	1	4	7	29	23	80	49	91	59	133
O2	0	9	5	38	11	124	17	137	33	199
O3	0	3	0	9	0	7	1	22	4	68
O4	0	3	0	2	0	5	0	13	0	30

Table 6.1: Number of all jumps per oxygen site occurring during the simulations.

It is evident from the simulations that O1 and O2 oxygen atoms are very mobile, while jumps of O3 and O4 oxygen atoms are significantly less frequent at all temper-

atures. This is consistent with the initially refined, high isotropic atomic displacement parameters of the O1 and O2 sites, suggesting increased mobility of oxygen atoms on these sites compared to O3 and O4 oxygen atoms,[276] and is therefore in good agreement with previously suggested O1-O1, O1-O2, and O2-O3 migrations pathways obtained using bond-valence-based energy landscape calculations.[276]

Additionally, the jump analysis shows that oxygen atoms on an O1 site are more likely to move out-of-plane to an O2 site than to an adjacent O1 site. It has been suggested[276] that the large size of Cs^{+} displaces Bi^{+3} cations along the c axis as well as along the a ($= b$) axis, resulting in larger bottlenecks for O1-O1 and O1-O2 oxide ion diffusion.[276] The larger number of out-of-plane jumps of O1 oxygen atoms observed in the AIMD results presented here suggests that this displacement favourably affects O1-O2 jumps more than O1-O1 jumps. Consideration of the subsequently refined anisotropic atomic displacement parameters for the O1 site further supports this explanation, as it is largest along the c axis (U_{33} = 0.157(3) Å^2, U_{22} = 0.017(1) Å^2, U_{11} = 0.090(2) Å^2).[276] The simulations also suggest some diffusion along O3-O4-O3 sites, as shown in figure 6.6 c. However, the low MSD of O3 and O4 oxygen atoms (figure 6.4) suggests that the contribution of these jumps to the long-range diffusion is small.

The strong correlation of simulated MSD curves for oxygen atoms on O1 and O2 sites (figure 6.4) as well as the significantly larger number of out-of-plane jumps observed during the simulations at all temperatures therefore indicates that a dominating contribution to the long-range oxide ion diffusion is via the O1-O2-O1 pathway.

6.5 Conclusion and Future Work

In this chapter, AIMD was used to investigate oxide ion dynamics of a Dion-Jacobson material for the first time. The results show that, regardless of the initial distribution of oxide ion vacancies, O1 and O2 oxygen atoms are the most mobile. This is in good agreement with the two-dimensional diffusion pathway proposed based on BVSE calculations. Additionally, the diffusion coefficient obtained from MSD suggests that

observation of QENS might be possible in this new type of oxide ion conductor.

One important aspect of future work are further experimental studies on these materials, which are required to fully validate the results obtained from simulations. Furthermore, QENS measurements should be attempted on a nanosecond timescale. While the presence of Bragg peaks and low neutron scattering signal of oxygen would make extraction of jump lengths and residence times from the Q-dependence difficult, this could allow determination of an activation energy which could further verify the simulations. Additionally, more doping studies should be undertaken to explore to what extent the oxide ion conductivity can be increased. It has been previously suggested that substitution of Cs^{+} by other alkali cations of different ionic radii should be attempted,[282] as it would provide further insight into the effect of the size of this cation on the oxide ion diffusion. Furthermore, a study on the effect of the Bi^{3+} cation and more specifically its lone pair on the structure and oxide ion diffusion is important. The results obtained from AIMD simulations presented here suggest that ionic conductivity in $CsBi_2Ti_2NbO_{10-\delta}$ could be further improved by promoting jumps between O1 and O2 sites by increasing the rotational flexibility of the octahedral units, i.e. via vanadium doping. VO_x groups are known to facilitate polyhedral rotation, and V^{5+} can support 4, 5, and 6 coordinate environments.[213] This could also increase diffusion along O3-O2-O3 sites. On top of that, as an increase in Nb^{5+} resulted in an increase in conductivity,[282] Mo^{6+} doping should be attempted.

Moreover, out of the 69 Dion-Jacobson phases screened in the original study by Zhang et al.,[276] 14 were suggested to have energy barriers below 0.51 eV, and 34 between 0.51 and 0.75 eV. Therefore, further investigation into different members of the Dion-Jacobson family should be carried out. For example, $CsCa_2Ta_3O_{10}$ and $CsCa_2Nb_3O_{10}$ were estimated to have energy barriers of 0.44 and 0.55 eV, respectively, and also do not contain expensive rare-earths, making them potential candidates for practical applications.

CHAPTER 7

Overall Conclusions and Future Work

The overall aim of this project was to advance our understanding of dynamics in oxide ion conductors using a combined experimental (impedance spectroscopy and QENS) and computational (AIMD) approach. Knowledge of structural features important for fast oxide ion dynamics allows tailoring of the ionic conductivity, creating better oxide ion conductors, and moreover helps in identifying new materials with this exploitable property. In this work, several promising oxide ion conductors in four different structural families were studied to gain detailed insight into the localised and long-range oxide ion dynamics present. This allowed determination of ionic diffusion mechanisms and pathways, and revealed structural features which are important for high oxide ion conductivity in these materials.

Impedance spectroscopy was used to investigate a series of scheelite-type oxide ion conductors with general formulae $Bi_3(BO_4)(B'O_4)_2$ (B = Fe, Ga, $Fe_{0.9}Ti_{0.1}$; B' = Mo) as well as $Bi_3(B_2O_8)_{1/2}(B'O_4)_2$ (B = Sc, In; B' = Mo). An increase in conductivity on donor doping of $Bi_3(FeO_4)(MoO_4)_2$ to obtain $Bi_3(Fe_{0.9}Ti_{0.1}O_{4.05})(MoO_4)_2$ suggests that interstitial oxide ions cause ionic conductivity in these materials. While this is an important result for further improvement of the ionic conductivity, it does not provide insight into the specific oxide ion migration pathway. AIMD simula-

tions could help elucidate oxide ion dynamics in this series further, providing more information on important structural features for long-range diffusion.

A comprehensive study of fluorite-type $Bi_{0.852}V_{0.148}O_{1.648}$ and $Bi_{0.852}P_{0.148}O_{1.648}$ using both QENS and AIMD highlighted the importance of using dopants which readily adopt various coordination environments in Bi_2O_3-based oxide ion conductors. The presence of V^{5+} in $Bi_{0.852}V_{0.148}O_{1.648}$ allows oxide ions to move from the Bi-O sublattice into the V-O sublattice, introducing additional vacancies in the former, thereby increasing the ionic conductivity. Additionally, this work provided the first direct observation and quantitative analysis of oxide ion dynamics on two different timescales using QENS in any material. As the use of QENS to study oxide ion diffusion has been historically limited due to the weak, purely coherent signal and slow oxide ion diffusion, the results presented here highlight the potential of QENS for future studies on oxide ion conductors.

Furthermore, from a methodology point of view, this study shows the good compatibility of QENS and AIMD, especially for the study of oxide ion dynamics where weak signals and the presence of Bragg peaks often make data analysis difficult. It demonstrates how the use of simulations for both analysis and interpretation of QENS data can offer crucial insight which cannot be readily obtained from experimental data alone. Here, AIMD was used for the first time to directly simulate the temperature dependence of the quasielastic broadening for oxide ion conductors, and from the simulations the geometry of the picosecond dynamics in $Bi_{0.852}V_{0.148}O_{1.648}$ and $Bi_{0.852}P_{0.148}O_{1.648}$ could be determined, which was not possible from experimental data alone.

With machine learning molecular dynamics (MLMD) becoming more prevalent, and having been successfully used to study some Li^+ conductors, this is an important area of further research. As detailed experimental data as well as pure AIMD simulations on $Bi_{0.852}V_{0.148}O_{1.648}$ and $Bi_{0.852}P_{0.148}O_{1.648}$ are available, future MLMD simulations and derived force fields on these materials could be easily verified using the data presented in this thesis.

A study on two hexagonal perovskites, $Ba_3NbMoO_{8.5}$ and $Ba_7Nb_4MoO_{20}$, showed that oxide ion dynamics in these compounds are too slow to be observable using

QENS on a nanosecond timescale, and higher temperatures as well as longer measuring times are required. While the QENS experiments on the excellent ionic conductors $Bi_{0.852}V_{0.148}O_{1.648}$ and $Bi_{0.852}P_{0.148}O_{1.648}$ demonstrate the potential of this method, the study of these hexagonal perovskites emphasises one of the main complications of QENS when studying oxide ion dynamics, caused by the low neutron scattering cross-section of oxygen and the generally slow oxide ion dynamics. Although the ILL reactor currently provides one of the best neutron fluxes in the world (1.5×10^{15} neutrons s^{-1} cm^{-2} at the moderator[127]), there is a strong drive to further increase the available neutron flux. A higher flux, for example at the European spallation source (ESS) which is currently under construction and predicted to have a flux of approximately 1×10^{18} neutrons s^{-1} cm^{-2} at the source,[284] along with improvement of neutron scattering instruments to obtain a better resolution will significantly facilitate QENS measurements on oxide ion conductors in the future.

Regarding the outlook on the European neutron science landscape with respect to the observation of oxide ion dynamics, the backscattering spectrometer MIRACLES and the cold neutron, chopper spectrometer CSPEC, both in development at the ESS, are of particular interest.[285] MIRACLES is expected to provide an high energy resolution, giving access to nanosecond dynamics, and an increase in flux at the sample of two orders of magnitude compared to IN16b, which will significantly reduce the required measurement time. CSPEC on the other hand should allow observation of picosecond dynamics. It is estimated to provide a flux at the sample one order of magnitude higher than IN5.[285]

While no further analysis of the QENS data collected on these hexagonal perovskites was possible, AIMD provided valuable insight into details of oxide ion dynamics in $Ba_7Nb_4MoO_{20}$, and showed significant contribution of oxygen atoms perpendicular to the *ab* plane to the long-range dynamics for the first time. The presence of this out-of-plane dynamics suggests that V-doping could further increase oxide ion conductivity in this compound. Based on these results, a promising doping strategy could be proposed, and synthesis of the here suggested $Ba_{7-x}La_xNb_4Mo_{1-y}V_yO_{20}$-series is an important possible area of future work.

AIMD simulations on $CsBi_2Ti_2NbO_{10-\delta}$, a new Dion-Jacobson structure type

oxide ion conductor, allowed for the first time elucidation of the oxide-ion conduction mechanism, suggesting that the main oxide ion migration pathway is not dominated by in-plane jumps of oxide ions in the *ab* plane. Instead, out-of-plane jumps of these oxide ions are significantly more favourable, resulting in a reapeated jumps out and back into the *ab* plane, with the out-of-plane oxygen site playing an important role. While extensive further experimental studies on this new type of oxide ion conductor are necessary, for example an attempt to observe either long-range or localised diffusion directly using QENS, this work provides insight into structural features important for a high ionic conductivity and can therefore help to determine strategies for further improvement.

CHAPTER 8

Bibliography

[1] A. Olabi, T. Wilberforce, and M. A. Abdelkareem, "Fuel cell application in the automotive industry and future perspective," *Energy*, vol. 214, p. 118955, 2021.

[2] M. Coduri, M. Karlsson, and L. Malavasi, "Structure-property correlation in oxide-ion and proton conductors for clean energy applications: recent experimental and computational advancements," *Journal of Materials Chemistry A*, vol. 10, no. 10, pp. 5082–5110, 2022.

[3] N. L. R. M. Rashid, A. A. Samat, A. A. Jais, M. R. Somalu, A. Muchtar, N. A. Baharuddin, and W. N. R. W. Isahak, "Review on zirconate-cerate-based electrolytes for proton-conducting solid oxide fuel cell," *Ceramics International*, vol. 45, no. 6, pp. 6605–6615, 2019.

[4] C. Zhou, J. Sunarso, Y. Song, J. Dai, J. Zhang, B. Gu, W. Zhou, and Z. Shao, "New reduced-temperature ceramic fuel cells with dual-ion conducting electrolyte and triple-conducting double perovskite cathode," *Journal of Materials Chemistry A*, vol. 7, no. 21, pp. 13265–13274, 2019.

[5] W. H. Kan, A. J. Samson, and V. Thangadurai, "Trends in electrode development for next generation solid oxide fuel cells," *Journal of Materials Chemistry A*, vol. 4, no. 46, pp. 17913–17932, 2016.

[6] B. Singh, S. Ghosh, S. Aich, and B. Roy, "Low temperature solid oxide electrolytes (LT-SOE): a review," *Journal of Power Sources*, vol. 339, pp. 103–135, 2017.

[7] M. Singh, D. Zappa, and E. Comini, "Solid oxide fuel cell: decade of progress, future perspectives and challenges," *International Journal of Hydrogen Energy*, vol. 46, pp. 27643–27674, 8 2021.

[8] C. Mendonça, A. Ferreira, and D. M. F. Santos, "Towards the commercialization of solid oxide fuel cells: Recent advances in materials and integration strategies," *Fuels*, vol. 2, pp. 393–419, 10 2021.

[9] Z. Gao, L. V. Mogni, E. C. Miller, J. G. Railsback, and S. A. Barnett, "A perspective on low-temperature solid oxide fuel cells," *Energy and Environmental Science*, vol. 9, no. 5, pp. 1602–1644, 2016.

[10] N. Mahato, A. Banerjee, A. Gupta, S. Omar, and K. Balani, "Progress in material selection for solid oxide fuel cell technology: a review," *Progress in Materials Science*, vol. 72, pp. 141–337, 2015.

[11] M. Trini, A. Hauch, S. De Angelis, X. Tong, P. V. Hendriksen, and M. Chen, "Comparison of microstructural evolution of fuel electrodes in solid oxide fuel cells and electrolysis cells," *Journal of Power Sources*, vol. 450, p. 227599, 2 2020.

[12] M. A. Laguna-Bercero, "Recent advances in high temperature electrolysis using solid oxide fuel cells: a review," *Journal of Power Sources*, vol. 203, pp. 4–16, 4 2012.

[13] Y. Zheng, J. Wang, B. Yu, W. Zhang, J. Chen, J. Qiao, and J. Zhang, "A review of high temperature co-electrolysis of H_2O and CO_2 to produce sustainable fuels using solid oxide electrolysis cells (SOECs): advanced materials and technology," *Chemical Society Reviews*, vol. 46, pp. 1427–1463, 2017.

[14] M. Gandiglio, A. Lanzini, and M. Santarelli, *Large Stationary Solid Oxide Fuel Cell (SOFC) Power Plants BT - Modeling, Design, Construction, and Operation of Power Generators with Solid Oxide Fuel Cells: From Single Cell to Complete Power System*. Springer International Publishing AG, 2018.

[15] E. D. Wachsman and K. T. Lee, "Lowering the temperature of solid oxide fuel cells," *Science*, vol. 334, no. 6058, pp. 935–939, 2011.

[16] A. B. Stambouli and E. Traversa, "Solid oxide fuel cells (SOFCs): A review of an environmentally clean and efficient source of energy," *Renewable and Sustainable Energy Reviews*, vol. 6, no. 5, pp. 433–455, 2002.

[17] B. C. H. Steele and A. Heinzel, "Materials for fuel-cell technologies," *Nature*, vol. 414, no. November, pp. 345–352, 2001.

[18] D. J. Brett, A. Atkinson, N. P. Brandon, and S. J. Skinner, "Intermediate temperature solid oxide fuel cells," *Chemical Society Reviews*, vol. 37, no. 8, pp. 1568–1578, 2008.

[19] B. Shri Prakash, R. Pavitra, S. Senthil Kumar, and S. T. Aruna, "Electrolyte bi-layering strategy to improve the performance of an intermediate temperature solid oxide fuel cell: a review," *Journal of Power Sources*, vol. 381, no. September 2017, pp. 136–155, 2018.

[20] A. Pesaran, A. Jaiswal, and E. D. Wachsman, *Bilayer electrolytes for low temperature and intermediate temperature solid oxide fuel cells–a review*. Royal Society of Chemistry, 2019.

[21] D. W. Joh, J. H. Park, D. Kim, E. D. Wachsman, and K. T. Lee, "Functionally graded bismuth oxide/zirconia bilayer electrolytes for high-performance intermediate-temperature solid oxide fuel cells (IT-SOFCs)," *ACS Applied Materials and Interfaces*, vol. 9, no. 10, pp. 8443–8449, 2017.

[22] K. T. Lee, D. W. Jung, M. A. Camaratta, H. S. Yoon, J. S. Ahn, and E. D. Wachsman, "$Gd_{0.1}Ce_{0.9}O_{1.95}/Er_{0.4}Bi_{1.6}O_3$ bilayered electrolytes fabricated by a simple colloidal route using nano-sized $Er_{0.4}Bi_{1.6}O_3$ powders for high performance low temperature solid oxide fuel cells," *Journal of Power Sources*, vol. 205, pp. 122–128, 2012.

[23] L. Zhang, C. Xia, F. Zhao, and F. Chen, "Thin film ceria-bismuth bilayer electrolytes for intermediate temperature solid oxide fuel cells with $La_{0.85}Sr_0.15MnO_3Y_{0.25}Bi_{0.75}O_{1.5}$ cathodes," *Materials Research Bulletin*, vol. 45, no. 5, pp. 603–608, 2010.

[24] M. Feng, J. B. Goodenough, K. Huang, and C. Milliken, "Fuel cells with doped lanthanum gallate electrolyte," *Journal of Power Sources*, vol. 63, no. 1, pp. 47–51, 1996.

[25] Z. Shao and M. O. Tadé, *Green Chemistry and Sustainable Technology Intermediate- Temperature Solid Oxide Fuel Cells Materials and Applications*. 2016.

[26] S. Nakayama, T. Kageyama, and Y. Sadaokac, "Ionic conductivity of lanthanoid silicates, $Ln_{10}(SiO_4)_6O_3$ (Ln = La, Nb, Sm, Gd, Dy, Y, Ho, Er and YB)," *Journal of Materials Chemistry*, vol. 5, pp. 1801–1805, 1995.

[27] S. Nakayama, M. Sakamoto, M. Higuchi, K. Kodaira, M. Sato, S. Kakita, T. Suzuki, and K. Itoh, "Oxide ionic conductivity of apatite type $Nd_{9.33}(SiO_4)_6O_2$ single crystal," *Journal of the European Ceramic Society*, vol. 19, no. 4, pp. 507–510, 1999.

[28] S. Nakayama, H. Aono, and Y. Sadaoka, " Ionic conductivity of $Ln_{10}(SiO_4)_6O_3$ (Ln = La, Nd, Sm, Gd and Dy) ," *Chemistry Letters*, vol. 24, no. 6, pp. 431–432, 1995.

[29] J. E. Auckett, A. J. Studer, E. Pellegrini, J. Ollivier, M. R. Johnson, H. Schober, W. Miiller, and C. D. Ling, "Combined experimental and computational study of oxide ion conduction dynamics in $Sr_2Fe_2O_5$ brownmillerite," *Chemistry of Materials*, vol. 25, no. 15, pp. 3080–3087, 2013.

[30] C. A. Fuller, Q. Berrod, B. Frick, M. R. Johnson, S. J. Clark, J. S. Evans, and I. R. Evans, "Brownmillerite-type Sr_2ScGaO_5 oxide ion conductor: Local structure, phase transition, and dynamics," *Chemistry of Materials*, vol. 31, pp. 7395–7404, 9 2019.

[31] G. B. Zhang and D. M. Smyth, "Defects and transport of the brownmillerite oxides with high oxygen ion conductivity $Ba_2In_2O_5$," *Solid State Ionics*, vol. 82, pp. 161–172, 12 1995.

[32] K. Kakinuma, H. Yamamura, H. Haneda, and T. Atake, "Oxide-ion conductivity of $(Ba_{1x}La_x)_2In_2O_{5+x}$ system based on brownmillerite structure," *Solid State Ionics*, vol. 140, pp. 301–306, 4 2001.

[33] Y. Li, H. Yi, J. Xu, and X. Kuang, "High oxide ion conductivity in the Bi^{3+} doped melilite $LaSrGa_3O_7$," *Journal of Alloys and Compounds*, vol. 740, pp. 143–147, 2018.

[34] X. Kuang, M. A. Green, H. Niu, P. Zajdel, C. Dickinson, J. B. Claridge, L. Jantsky, and M. J. Rosseinsky, "Interstitial oxide ion conductivity in the layered tetrahedral network melilite structure," *Nature Materials*, vol. 7, no. 6, pp. 498–504, 2008.

[35] J. Xu, X. Li, F. Lu, H. Fu, C. M. Brown, and X. Kuang, "Oxygen interstitials and vacancies in $LaSrGa_3O_7$-based melilites," *Journal of Solid State Chemistry*, vol. 230, pp. 309–317, 7 2015.

[36] J. W. Fergus, "Electrolytes for solid oxide fuel cells," *Journal of Power Sources*, vol. 162, no. 1, pp. 30–40, 2006.

[37] H. Shi, C. Su, R. Ran, J. Cao, and Z. Shao, "Electrolyte materials for intermediate-temperature solid oxide fuel cells," *Progress in Natural Science: Materials International*, vol. 30, pp. 764–774, 12 2020.

[38] J. B. Goodenough, "Oxide-ion electrolytes," *Annual Review of Materials Research*, vol. 33, no. 1, pp. 91–128, 2003.

[39] V. V. Kharton, F. M. Marques, and A. Atkinson, "Transport properties of solid oxide electrolyte ceramics: a brief review," *Solid State Ionics*, vol. 174, pp. 135–149, 2004.

[40] K. Huang, R. Tichy, J. B. Goodenough, and C. Milliken, "Superior perovskite oxide-ion conductor; strontium-and magnesium-doped lagao$_3$: Iii, performance tests of single ceramic fuel cells," *Journal of the American ceramic society*, vol. 81, no. 10, pp. 2581–2585, 1998.

[41] W. Lee, H. J. Jung, M. H. Lee, Y.-B. Kim, J. S. Park, R. Sinclair, and F. B. Prinz, "Oxygen surface exchange at grain boundaries of oxide ion conductors," *Advanced Functional Materials*, vol. 22, no. 5, pp. 965–971, 2012.

[42] C. Lenser and N. H. Menzler, "Impedance characterization of supported oxygen ion conducting electrolytes," *Solid State Ionics*, vol. 334, pp. 70–81, 2019.

[43] J. Zhang, C. Lenser, N. H. Menzler, and O. Guillon, "Comparison of solid oxide fuel cell (sofc) electrolyte materials for operation at 500 c," *Solid State Ionics*, vol. 344, p. 115138, 2020.

[44] Q.-A. Huang, R. Hui, B. Wang, and J. Zhang, "A review of ac impedance modeling and validation in sofc diagnosis," *Electrochimica Acta*, vol. 52, no. 28, pp. 8144–8164, 2007.

[45] D. Vladikova, Z. Stoynov, A. Barbucci, M. Viviani, P. Carpanese, J. Kilner, S. Skinner, and R. Rudkin, "Impedance studies of cathode/electrolyte behaviour in sofc," *Electrochimica Acta*, vol. 53, no. 25, pp. 7491–7499, 2008.

[46] A. R. Bredar, A. L. Chown, A. R. Burton, and B. H. Farnum, "Electrochemical impedance spectroscopy of metal oxide electrodes for energy applications," *ACS Applied Energy Materials*, vol. 3, no. 1, pp. 66–98, 2020.

[47] J. Hjelm, M. Sogaard, M. Wandel, M. Menon, M. Mogensen, and A. Hagen, "Electrochemical impedance studies of sofc cathodes," *ECS Transactions*, vol. 7, no. 1, p. 1261, 2007.

[48] J. Nielsen and J. Hjelm, "Impedance of sofc electrodes: A review and a comprehensive case study on the impedance of lsm: Ysz cathodes," *Electrochimica Acta*, vol. 115, pp. 31–45, 2014.

[49] A. Nechache, M. Cassir, and A. Ringuedé, "Solid oxide electrolysis cell analysis by means of electrochemical impedance spectroscopy: A review," *Journal of Power Sources*, vol. 258, pp. 164–181, 2014.

[50] M. L. Tate, D. A. Blom, M. Avdeev, H. E. Brand, G. J. McIntyre, T. Vogt, and I. R. Evans, "New apatite-type oxide ion conductor, $Bi_2La_8[(GeO_4)_6]O_3$: Structure, properties, and direct imaging of low-level interstitial oxygen atoms using aberration-corrected scanning transmission electron microscopy," *Advanced Functional Materials*, vol. 27, p. 1605625, 2017.

[51] M. S. Chambers, P. A. Chater, I. R. Evans, and J. S. Evans, "Average and local structure of apatite-type germanates and implications for oxide ion conductivity," *Inorganic Chemistry*, vol. 58, no. 21, pp. 14853–14862, 2019.

[52] J. Xiang, Z. G. Liu, J. H. Ouyang, and F. Y. Yan, "Ionic conductivity of oxy-apatite $La_{10}Si_{6-x}In_xO_{27-\delta}$ solid electrolyte ceramics," *Journal of Power Sources*, vol. 251, pp. 305–310, 2014.

[53] A. Chroneos, R. V. Vovk, and I. L. Goulatis, "Oxygen self-diffusion in apatites," *Monatshefte für Chemie*, vol. 143, no. 3, pp. 345–353, 2012.

[54] A. Kushima, D. Parfitt, A. Chroneos, B. Yildiz, J. A. Kilner, and R. W. Grimes, "Interstitialcy diffusion of oxygen in tetragonal $La_2CoO_{4+\delta}$," *Physical Chemistry Chemical Physics*, vol. 13, no. 6, pp. 2242–2249, 2011.

[55] D. Parfitt, A. Chroneos, J. A. Kilner, and R. W. Grimes, "Molecular dynamics study of oxygen diffusion in $Pr_2NiO_{4+\delta}$," *Physical Chemistry Chemical Physics*, vol. 12, no. 25, pp. 6834–6836, 2010.

[56] T. Murakami, T. Shibata, Y. Yasui, K. Fujii, J. R. Hester, and M. Yashima, "High oxide-ion conductivity in a hexagonal perovskite-related oxide $Ba_7Ta_{3.7}Mo_{1.3}O_{20.15}$ with cation site preference and interstitial oxide ions," *Small*, vol. 18, no. 10, p. 2106785, 2022.

[57] Y. Suzuki, T. Murakami, K. Fujii, J. R. Hester, Y. Yasui, and M. Yashima, "Simultaneous reduction of proton conductivity and enhancement of oxide-ion conductivity by aliovalent doping in $Ba_7Nb_4MoO_{20}$," *Inorganic Chemistry*, vol. 61, no. 19, pp. 7537–7545, 2022.

[58] G. Henkelman, B. P. Uberuaga, and H. Jónsson, "A climbing image nudged elastic band method for finding saddle points and minimum energy paths," *The Journal of Chemical Physics*, vol. 113, p. 9901, 11 2000.

[59] M. Nakayama and M. Martin, "First-principles study on defect chemistry and migration of oxide ions in ceria doped with rare-earth cations," *Physical Chemistry Chemical Physics*, vol. 11, pp. 3241–3249, 4 2009.

[60] G. Henkelman and H. Jónsson, "Improved tangent estimate in the nudged elastic band method for finding minimum energy paths and saddle points," *The Journal of Chemical Physics*, vol. 113, p. 9978, 11 2000.

[61] F. Shimojo and H. Okazaki, "Molecular dynamics studies of yttria stabilized zirconia. ii. microscopic mechanism of oxygen diffusion," *Journal of the Physical Society of Japan*, vol. 61, no. 11, pp. 4106–4118, 1992.

[62] M. Yashima, S. Kobayashi, and T. Yasui, "Positional disorder and diffusion path of oxide ions in the yttria-doped ceria $Ce_{0.93}Y_{0.07}O_{1.96}$," *Faraday discussions*, vol. 134, pp. 369–376, 2007.

[63] J. Lee, N. Ohba, and R. Asahi, "Oxygen conduction mechanism in $Ca_3Fe_2Ge_3O_{12}$ garnet-type oxide," *Scientific Reports 2019 9:1*, vol. 9, pp. 1–8, 2 2019.

[64] U. Matsumoto, T. Ogawa, C. A. J. Fisher, S. Kitaoka, and I. Tanaka, "Cooperative oxide-ion transport in pyrochlore $Y_2Ti_2O_7$: A first-principles molecular dynamics study," *The Journal of Physical Chemistry C*, vol. 125, p. 15, 2021.

[65] K. Toyoura, Y. Sakakibara, T. Yokoi, A. Nakamura, and K. Matsunaga, "Oxide-ion conduction via interstitials in scheelite-type $LaNbO_4$: a first-principles study," *Journal of Materials Chemistry A*, vol. 6, pp. 12004–12011, 6 2018.

[66] B. O. Grope, T. Zacherle, M. Nakayama, and M. Martin, "Oxygen ion conductivity of doped ceria: A kinetic monte carlo study," *Solid State Ionics*, vol. 225, pp. 476–483, 10 2012.

[67] A. F. Voter, "Introduction to the kinetic monete carlo method," *Radiation Effects in Solids*, pp. 1–23, 5 2007.

[68] C. C. Battaile, "The kinetic monte carlo method: Foundation, implementation, and application," *Computer Methods in Applied Mechanics and Engineering*, vol. 197, pp. 3386–3398, 7 2008.

[69] J. Koettgen, S. Grieshammer, P. Hein, B. O. H. Grope, M. Nakayama Cd, and M. Martin, "Understanding the ionic conductivity maximum in doped ceria: trapping and blocking," *Physical Chemistry Chemical Physics*, vol. 20, p. 14291, 2018.

[70] R. Pornprasertsuk, P. Ramanarayanan, C. B. Musgrave, and F. B. Prinz, "Predicting ionic conductivity of solid oxide fuel cell electrolyte from first principles," *Journal of Applied Physics*, vol. 98, no. 10, p. 103513, 2005.

[71] N. Yao, X. Chen, Z.-H. Fu, and Q. Zhang, "Applying classical, ab initio, and machine-learning molecular dynamics simulations to the liquid electrolyte for rechargeable batteries," *Chemical Reviews*, vol. 122, no. 12, pp. 10970–11021, 2022.

[72] O. T. Unke, S. Chmiela, H. E. Sauceda, M. Gastegger, I. Poltavsky, K. T. Schu, A. Tkatchenko, and K.-R. Mu, "Machine learning force fields," *Chemical Review*, vol. 121, pp. 10142–10186, 2021.

[73] R. Jinnouchi, F. Karsai, and G. Kresse, "On-the-fly machine learning force field generation: application to melting points," *Physical Review B*, vol. 100, p. 14105, 2019.

[74] R. Jinnouchi, J. Lahnsteiner, F. Karsai, G. Kresse, and M. Bokdam, "Phase transitions of hybrid perovskites simulated by machine-learning force fields trained on the fly with bayesian inference," *Physical Review Letters*, vol. 122, p. 225701, Jun 2019.

[75] G. Kresse and J. Furthmüller, "Efficiency of ab-initio total energy calculations for metals and semiconductors using a plane-wave basis set," *Computational Materials Science*, vol. 6, pp. 15–50, 7 1996.

[76] C. Ling, "A review of the recent progress in battery informatics," *npj Computational Materials*, vol. 8, no. 1, pp. 1–22, 2022.

[77] M. K. Gupta, J. Ding, N. C. Osti, D. L. Abernathy, W. Arnold, H. Wang, Z. Hood, and O. Delaire, "Fast Na diffusion and anharmonic phonon dynamics in superionic Na_3PS_4," *Energy & Environmental Science*, vol. 14, no. 12, pp. 6554–6563, 2021.

[78] A. Hajibabaei and K. S. Kim, "Universal machine learning interatomic potentials: surveying solid electrolytes," *The Journal of Physical Chemistry Letters*, vol. 12, no. 33, pp. 8115–8120, 2021.

[79] A. Hajibabaei, C. W. Myung, and K. S. Kim, "Sparse gaussian process potentials: Application to lithium diffusivity in superionic conducting solid electrolytes," *Physical Review B*, vol. 103, no. 21, p. 214102, 2021.

[80] K. Kim, A. Dive, A. Grieder, N. Adelstein, S. Kang, L. F. Wan, and B. C. Wood, "Flexible machine-learning interatomic potential for simulating structural disordering behavior of $Li_7La_3Zr_2O_{12}$ solid electrolytes," *The Journal of Chemical Physics*, vol. 156, no. 22, p. 221101, 2022.

[81] H. Niu, Y. Jing, Y. Sun, L. Guo, N. Aluru, W. Li, J. Yang, and X. Li, "On the anomalous diffusion of proton in Y-doped $BaZrO_3$ perovskite oxide," *Solid State Ionics*, vol. 376, p. 115859, 2022.

[82] M. A. González, "Force fields and molecular dynamics simulations," *Collection SFN*, vol. 12, pp. 169–200, 2011.

[83] A. Braun, S. Duval, P. Ried, J. Embs, F. Juranyi, T. Strässle, U. Stimming, R. Hempelmann, P. Holtappels, and T. Graule, "Proton diffusivity in the $BaZr_{0.9}Y_{0.1}O_{3-\delta}$ proton conductor," *Journal of Applied Electrochemistry*, vol. 39, pp. 471–475, 4 2009.

[84] R. Hempehnann, C. Karmonik, T. Matzke, M. Cappadonia, U. Stimming, T. Springer, and M. A. Adams, "Quasielastic neutron scattering study of proton diffusion in $SrCe_{0.95}Yb_{0.05}H_{0.02}O_{2.985}$," *Solid State Ionics*, vol. 77, pp. 152–156, 4 1995.

[85] M. Karlsson, "Proton dynamics in oxides: insight into the mechanics of proton conduction from quasielastic neutron scattering," *Physical Chemistry Chemical Physics*, vol. 17, pp. 26–38, 12 2014.

[86] N. Jalarvo, O. Gourdon, Z. Bi, D. Gout, M. Ohl, and M. P. Paranthaman, "Atomic-scale picture of the ion conduction mechanism in a tetrahedral network of lanthanum barium gallate," *Chemistry of Materials*, vol. 25, pp. 2741–2748, 7 2013.

[87] D. J. Buttrey, T. Vogt, G. P. Yap, and A. L. Rheingold, "The structure of $Bi_{26}Mo_{10}O_{69}$," *Materials Research Bulletin*, vol. 32, pp. 947–962, 7 1997.

[88] C. D. Ling, W. Miiller, M. R. Johnson, D. Richard, S. Rols, J. Madge, and I. R. Evans, "Local structure, dynamics, and the mechanisms of oxide ionic conduction in $Bi_{26}Mo_{10}O_{69}$," *Chemistry of Materials*, vol. 24, no. 23, pp. 4607–4614, 2012.

[89] E. Mashkina, A. Magerl, J. Ollivier, M. Göbbels, and F. Seifert, "Oxygen mobility in the perovskite $SrTi_{1-x}Fe_xO_{3-\delta}$ (x=0.8)," *Physical Review B - Condensed Matter and Materials Physics*, vol. 74, no. 21, pp. 1–7, 2006.

[90] W. Paulus, H. Schober, S. Eibl, M. Johnson, T. Berthier, O. Hernandez, M. Ceretti, M. Plazanet, K. Conder, and C. Lamberti, "Lattice dynamics to trigger low temperature oxygen mobility in solid oxide ion conductors," *Journal of the American Chemical Society*, vol. 130, no. 47, pp. 16080–16085, 2008.

[91] C. T. Chudley and R. J. Elliott, "Neutron scattering from a liquid on a jump diffusion model," *Proceedings of the Physical Society*, vol. 77, no. 2, pp. 353–361, 1961.

[92] E. Mamontov, "Fast oxygen diffusion in bismuth oxide probed by quasielastic neutron scattering," *Solid State Ionics*, vol. 296, pp. 158–162, 2016.

[93] P. D. Battle, C. R. Catlow, J. Drennan, and A. D. Murray, "The structural properties of the oxygen conducting δ phase of Bi_2O_3," *Journal of Physics C: Solid State Physics*, vol. 16, no. 17, pp. L561–L566, 1983.

[94] C. E. Mohn, S. Stølen, S. T. Norberg, and S. Hull, "Ab initio molecular dynamics simulations of oxide-ion disorder in the δ-Bi_2O_3," *Physical Review B*, vol. 80, no. 2, p. 024205, 2009.

[95] J. Wind, R. A. Mole, D. Yu, and C. D. Ling, "Liquid-like ionic diffusion in solid bismuth oxide revealed by coherent quasielastic neutron scattering," *Chemistry of Materials*, vol. 29, pp. 7408–7415, 9 2017.

[96] H. A. Harwig and A. G. Gerards, "Electrical properties of the α, β, γ, and δ phases of bismuth sesquioxide," *Journal of Solid State Chemistry*, vol. 26, no. 3, pp. 265–274, 1978.

[97] J. Wind, R. A. Mole, and C. D. Ling, "Oxygen dynamics in transition metal-doped bismuth oxides," *The Journal of Physical Chemistry C*, vol. 123, pp. 15877–15884, 2019.

[98] P. Goel, M. K. Gupta, R. Mittal, S. J. Skinner, S. Mukhopadhyay, S. Rols, and S. L. Chaplot, "Phonons and oxygen diffusion in Bi_2O_3 and $(Bi_{0.7}Y_{0.3})_2O_3$," *Journal of Physics: Condensed Matter*, vol. 32, p. 334002, 2020.

[99] J. R. Peet, C. A. Fuller, B. Frick, M. Zbiri, A. Piovano, M. R. Johnson, and I. R. Evans, "Direct observation of oxide ion dynamics in $La_2Mo_2O_9$ on the nanosecond timescale," *Chemistry of Materials*, vol. 29, no. 7, pp. 3020–3028, 2017.

[100] P. Lacorre, F. Goutenoire, O. Bohnke, R. Retoux, and Y. Laligant, "Designing fast oxide-ion conductors," *Nature*, vol. 404, no. April, pp. 9–11, 2000.

[101] S. Georges, F. Goutenoire, F. Altorfer, D. Sheptyakov, F. Fauth, E. Suard, and P. Lacorre, "Thermal, structural and transport properties of the fast oxide-ion conductors $La_{2-x}R_xMo_2O_9$ (R= Nd, Gd, Y)," *Solid State Ionics*, vol. 161, pp. 231–241, 2003.

[102] J. Liu, R. J. Chater, B. Hagenhoff, R. J. Morris, and S. J. Skinner, "Surface enhancement of oxygen exchange and diffusion in the ionic conductor $La_2Mo_2O_9$," *Solid State Ionics*, vol. 181, pp. 812–818, 6 2010.

[103] N. Kim, C. H. Hsieh, H. Huang, F. B. Prinz, and J. F. Stebbins, "High temperature ^{17}O MAS NMR study of calcia, magnesia, scandia and yttria stabilized zirconia," *Solid State Ionics*, vol. 178, pp. 1499–1506, 11 2007.

[104] K. Fuda, K. Kishio, S. Yamauchi, K. Fueki, and Y. Onoda, "^{17}O NMR study of Y_2O_3-doped CeO_2," *Journal of Physics and Chemistry of Solids*, vol. 45, no. 11-12, pp. 1253–1257, 1984.

[105] A. B. Santibanez-Mendieta, C. Didier, K. K. Inglis, A. J. Corkett, M. J. Pitcher, M. Zanella, J. F. Shin, L. M. Daniels, A. Rakhmatullin, M. Li, M. S. Dyer, J. B. Claridge, F. Frede, F. Blanc, and M. J. Rosseinsky, "$La_3Li_3W_2O_{12}$: Ionic diffusion in a perovskite with lithium on both A-and B-Sites," *Chemistry of Materials*, vol. 28, pp. 7833–7851, 2016.

[106] B. T. Leube, K. K. Inglis, E. J. Carrington, P. M. Sharp, J. F. Shin, A. R. Neale, T. D. Manning, M. J. Pitcher, L. J. Hardwick, M. S. Dyer, *et al.*, "Lithium transport in $Li_{4.4}M_{0.4}M_{0.6}S_4$ (M = Al^{3+}, Ga^{3+}, and M= Ge^{4+}, Sn^{4+}): Combined crystallographic, conductivity, solid state NMR, and computational studies," *Chemistry of Materials*, vol. 30, no. 20, pp. 7183–7200, 2018.

[107] C. J. Hou, Y. D. Li, P. J. Wang, C. S. Liu, X. P. Wang, Q. F. Fang, and D. Y. Sun, "Oxygen-ion arrangements and concerted motion in β- $La_2Mo_2O_9$," *Physical Review B - Condensed Matter and Materials Physics*, vol. 76, p. 014104, 7 2007.

[108] J. R. Peet, C. A. Fuller, B. Frick, M. M. Koza, M. R. Johnson, A. Piovano, and I. R. Evans, "Insight into design of improved oxide ion conductors: Dynamics and conduction mechanisms in the $Bi_{0.913}V_{0.087}O_{1.587}$ solid electrolyte," *Journal of the American Chemical Society*, vol. 141, no. 25, pp. 9989–9997, 2019.

[109] X. Kuang, J. L. Payne, M. R. Johnson, and I. R. Evans, "Remarkably high oxide ion conductivity at low temperature in an ordered fluorite-type superstructure," *Angewandte Chemie - International Edition*, vol. 51, no. 3, pp. 690–694, 2012.

[110] C. A. Fuller, Q. Berrod, B. Frick, M. R. Johnson, M. Avdeev, J. S. Evans, and I. R. Evans, "Oxide ion and proton conductivity in highly oxygen-deficient cubic perovskite $SrSc_{0.3}Zn_{0.2}Ga_{0.5}O_{2.4}$," *Chemistry of Materials*, vol. 32, pp. 4347–4357, 5 2020.

[111] L. E. Smart and E. A. Moore, *Solid state chemistry: an introduction*. CRC press, 2012.

[112] R. Ropp, *Chapter 4. Mechanism and Reactions in the Solid State*. 2003.

[113] J. S. Evans and I. R. Evans, "Beyond classical applications of powder diffraction," *Chemical Society Reviews*, vol. 33, no. 8, pp. 539–547, 2004.

[114] G. W. Stinton and J. S. Evans, "Parametric Rietveld refinement," *Journal of Applied Crystallography*, vol. 40, no. 1, pp. 87–95, 2007.

[115] S. Kerman, B. J. Campbell, K. K. Satyavarapu, H. T. Stokes, F. Perselli, and J. S. Evans, "The superstructure determination of displacive distortions via symmetry-mode analysis," *Acta Crystallographica Section A: Foundations of Crystallography*, vol. 68, no. 2, pp. 222–234, 2012.

[116] J. W. Lewis, J. L. Payne, I. R. Evans, H. T. Stokes, B. J. Campbell, and J. S. Evans, "An exhaustive symmetry approach to structure determination: phase transitions in $Bi_2Sn_2O_7$," *Journal of the American Chemical Society*, vol. 138, no. 25, pp. 8031–8042, 2016.

[117] P. Atkins and J. DePaula, *Physical Chemistry*, vol. 9. OUP Oxford, 2010.

[118] P. Atkins, T. Overton, J. Rourke, M. Weller, F. Armstrong, and M. Hagerman, *Inorganic Chemistry*, vol. 5. OUP Oxford, 2010.

[119] H. M. Rietveld, "A profile refinement method for nuclear and magnetic structures," *Journal of Applied Crystallography*, vol. 2, pp. 65–71, 6 1969.

[120] G. Pawley, "Unit-cell refinement from powder diffraction scans," *Journal of Applied Crystallography*, vol. 14, pp. 357–361, 1981.

[121] A. A. Coelho, J. Evans, I. Evans, A. Kern, and S. Parsons, "The TOPAS symbolic computation system," *Powder Diffraction*, vol. 26, pp. S22–S25, 12 2011.

[122] G. Bergerhoff, I. Brown, F. Allen, *et al.*, "Crystallographic databases," *International Union of Crystallography, Chester*, vol. 360, pp. 77–95, 1987.

[123] G. L. Squires, *Introduction to the theory of thermal neutron scattering*. Courier Corporation, 1996.

[124] S. W. Lovesey, *Theory of neutron scattering from condensed matter*. Clarendon Press, 1984.

[125] R. Pynn, *Neutron Applications in Earth, Energy and Environmental Sciences*. Boston, MA: Springer US, 2009.

[126] B. Carlile, C.J; Willis, *Experimental neutron scattering*. Oxford University Press, 1 ed., 2013.

[127] Institut Laue-Langevin, *Technical characteristics of the high-flux reactor*. Available: https://www.ill.eu/reactor-and-safety/high-flux-reactor/technical-characteristics, 3 2023.

[128] G. E. Bacon, *Neutron diffraction*. Clarendon Press, 1975.

[129] J. S. Gardner, G. Ehlers, A. Faraone, and V. García Sakai, "High-resolution neutron spectroscopy using backscattering and neutron spin-echo spectrometers in soft and hard condensed matter," *Nature Reviews Physics*, vol. 2, no. 2, pp. 103–116, 2020.

[130] A. T. Boothroyd, *Principles of Neutron Scattering from Condensed Matter*. Oxford University Press, 2020.

[131] L. Van Hove, "Correlations in space and time and born approximation scattering in systems of interacting particles," *Physical Review*, vol. 95, no. 1, pp. 249–262, 1954.

[132] R. Hempelmann, *Quasielastic Neutron Scattering and Solid State Diffusion*. Oxford University Press, 2000.

[133] P. Damay and F. Leclercq, "Diffusion quasiélastique de neutrons; étude des mouvements localisés," *Le Journal de Physique IV*, vol. 10, pp. Pr1–105, 2000.

[134] P. G. De Gennes, "Liquid dynamics and inelastic scattering of neutrons," *Physica*, vol. 25, no. 7-12, pp. 825–839, 1959.

[135] S. Varley F, "Neutron scattering lengths and cross sections," *Neutron News*, vol. 3, no. 3, pp. 26–37, 1992.

[136] O. Arnold, J. C. Bilheux, J. M. Borreguero, A. Buts, S. I. Campbell, L. Chapon, M. Doucet, N. Draper, R. Ferraz Leal, M. A. Gigg, V. E. Lynch, A. Markvardsen, D. J. Mikkelson, R. L. Mikkelson, R. Miller, K. Palmen, P. Parker, G. Passos, T. G. Perring, P. F. Peterson, S. Ren, M. A. Reuter, A. T. Savici, J. W. Taylor, R. J. Taylor, R. Tolchenov, W. Zhou, and J. Zikovsky, "Mantid - Data analysis and visualization package for neutron scattering and μSR experiments," *Nuclear Instruments and Methods in Physics Research, Section A: Accelerators, Spectrometers, Detectors and Associated Equipment*, vol. 764, pp. 156–166, 11 2014.

[137] B. Frick, E. Mamontov, L. van Eijck, and T. Seydel, "Recent backscattering instrument developments at the ILL and SNS," *Zeitschrift für Physikalische Chemie*, vol. 224, no. 1-2, pp. 33–60, 2010.

[138] Institut Laue-Langevin, "IN16b", Available: "https://www.ill.eu/users /instruments/instruments-list/in16b/description/instrument-layout," 3 2020.

[139] Institut Laue-Langevin, "IN5", Available: "https://www.ill.eu/users /instruments/instruments-list/in5/description/instrument-layout," 3 2020.

[140] J. R. Copley and T. J. Udovic, "Neutron time-of-flight spectroscopy," *Journal of research of the National Institute of Standards and Technology*, vol. 98, no. 1, p. 71, 1993.

[141] A. West, J. Irvine, and D. Sinclair, "Electroceramics : Characterization by impedance spectroscopy," *Advanced Materials*, vol. 2, no. 3, pp. 132–138, 1990.

[142] E. Barsoukov and J. R. Macdonald, *Impedance Spectroscopy: Theory, Experiment, and Applications*, vol. 125. Wiley, 2005.

[143] C. K. Alexander, M. N. Sadiku, and M. Sadiku, *Fundamentals of electric circuits*. McGraw-Hill Higher Education Boston, 2007.

[144] S. Wang, J. Zhang, O. Gharbi, V. Vivier, M. Gao, and M. E. Orazem, "Electrochemical impedance spectroscopy," *Nature Reviews Methods Primers*, vol. 1, no. 1, p. 41, 2021.

[145] S. P. Jiang, J. G. Love, and S. P. Badwal, "Electrochemical techniques in studies of solid ionic conductors," *Key Engineering Materials*, vol. 126, no. 125-126, pp. 81–132, 1996.

[146] A. Tarancón, T. Norby, G. Dezanneau, A. Morata, F. Peiró, and J. R. Morante, "Conductivity dependence on oxygen partial pressure and oxide-ion transport numbers determination for $La_2Mo_2O_9$," *Electrochemical and Solid-State Letters*, vol. 7, no. 10, pp. 373–375, 2004.

[147] T. Miruszewski, J. Karczewski, B. Bochentyn, P. Jasinski, M. Gazda, and B. Kusz, "Determination of the ionic conductivity of Sr-doped lanthanum manganite by modified Hebb-Wagner technique," *Journal of Physics and Chemistry of Solids*, vol. 91, pp. 163–169, 2016.

[148] R. W. Hockney, "The potential calculation and some applications," *Methods in Computational Physics*, vol. 9, p. 136, 1970.

[149] L. Verlet, "Computer "experiments" on classical fluids. I. thermodynamical properties of Lennard-Jones molecules," *Physical Review*, vol. 159, p. 98, 7 1967.

[150] W. Koch and M. C. Holthausen, *A Chemist's Guide to Density Functional Theory Second Edition A Chemist's Guide to Density Functional Theory. Second Edition.* Wiley VCH, 2 ed., 2001.

[151] D. S. Sholl and J. A. Steckel, "What is density functional theory?," *Density Functional Theory*, pp. 1–33, 2009.

[152] P. Hohenberg and W. Kohn, "Density functional theory (DFT)," *Physical Review*, vol. 136, p. B864, 1964.

[153] W. Kohn and L. J. Sham, "Self-consistent equations including exchange and correlation effects," *Physical Review*, vol. 140, p. A1133, 11 1965.

[154] G. Kresse and D. Joubert, "From ultrasoft pseudopotentials to the projector augmented-wave method," *Physical Review B*, vol. 59, pp. 1758–1775, 1 1999.

[155] J. P. Perdew, K. Burke, and M. Ernzerhof, "Generalized gradient approximation made simple," *Physical Review Letters*, vol. 77, pp. 3865–3868, 10 1996.

[156] G. Goret, B. Aoun, and E. Pellegrini, "MDANSE: An interactive analysis environment for molecular dynamics simulations," *Journal of chemical information and modeling*, vol. 57, pp. 1–5, 1 2017.

[157] D. Richard, M. Ferrand, and G. J. Kearley, "Analysis and visualisation of neutron-scattering data," *Journal of Neutron Research*, vol. 4, no. 1-4, pp. 33–39, 1996.

[158] T. Takahashi and H. Iwahara, "Oxide ion conductors based on bismuth-sesquioxide," *Materials Research Bulletin*, vol. 13, pp. 1447–1453, 1978.

[159] T. Takahashi, T. Esaka, and H. Iwahara, "Conduction in Bi_2O_3-based oxide ion conductor under low oxygen pressure. II. Determination of the partial electronic conductivity," *Journal of Applied Electrochemistry*, vol. 7, no. 4, pp. 303–308, 1977.

[160] P. Shuk, H. D. Wiemhöfer, U. Guth, W. Göpel, and M. Greenblatt, "Oxide ion conducting solid electrolytes based on Bi_2O_3," *Solid State Ionics*, vol. 89, no. 3-4, pp. 179–196, 1996.

[161] J. L. Payne, J. D. Farrell, A. M. Linsell, M. R. Johnson, and I. R. Evans, "The mechanism of oxide ion conductivity in bismuth rhenium oxide, $Bi_{28}Re_2O_{49}$," *Solid State Ionics*, vol. 244, pp. 35–39, 2013.

[162] M. L. Tate, J. Hack, X. Kuang, G. J. McIntyre, R. L. Withers, M. R. Johnson, and I. R. Evans, "$Bi_{1-x}Nb_xO_{1.5+x}$ (x=0.0625, 0.12) fast ion conductors: structures, stability and oxide ion migration pathways," *Journal of Solid State Chemistry*, vol. 225, pp. 383–390, 2015.

[163] N. Jiang, E. D. Wachsman, and S. H. Jung, "A higher conductivity Bi_2O_3-based electrolyte," *Solid State Ionics*, vol. 150, no. 3-4, pp. 347–353, 2002.

[164] J. Y. Park and E. D. Wachsman, "Stable and high conductivity ceria/bismuth oxide bilayer electrolytes for lower temperature solid oxide fuel cells," *Ionics*, vol. 12, no. 1, pp. 15–20, 2006.

[165] R. Punn, A. M. Feteira, D. C. Sinclair, and C. Greaves, "Enhanced oxide ion conductivity in stabilized δ-Bi_2O_3," *Journal of the American Chemical Society*, vol. 128, no. 48, pp. 15386–15387, 2006.

[166] A. Dapčević, D. Poleti, J. Rogan, A. Radojković, M. Radović, and G. Branković, "A new electrolyte based on Tm^{3+}-doped δ-Bi_2O_3-type phase with enhanced conductivity," *Solid State Ionics*, vol. 280, pp. 18–23, 2015.

[167] C. H. Hervoches and C. Greaves, "Crystal structure and oxide ion conductivity in cubic (disordered) and tetragonal (ordered) phases of $Bi_{25}Ln_3Re_2O_{49}$ (Ln = La, Pr)," *Journal of Materials Chemistry*, vol. 20, no. 32, pp. 6759–6763, 2010.

[168] Z. Luo, H. Wang, Y. Ma, G. Zhang, D. Yan, X. Bai, D. Wang, and R. Liu, "High ionic conductivity of Lu_2O_3-TiO_2 co-doped Bi_2O_3 ceramics," *Materials Research Express*, vol. 8, no. 2, p. 025001, 2021.

[169] X. Kuang, J. L. Payne, J. D. Farrell, M. R. Johnson, and I. R. Evans, "Polymorphism and oxide ion migration pathways in fluorite-type bismuth vanadate, $Bi_{46}V_8O_{89}$," *Chemistry of Materials*, vol. 24, no. 11, pp. 2162–2167, 2012.

[170] A. Watanabe, "$Bi_{23}M_4O_{44.5}$ (M = P and V): new oxide-ion conductors with triclinic structure based on a pseudo-fcc subcell," *Solid State Ionics*, vol. 96, no. 1-2, pp. 75–81, 1997.

[171] J. Darriet, J. C. Launay, and F. J. Zúniga, "Crystal structures of the ionic conductors $Bi_{46}M_8O_{89}$ (M=P, V) related to the fluorite-type structure," *Journal of Solid State Chemistry*, vol. 178, no. 6, pp. 1753–1764, 2005.

[172] M. T. Dunstan, D. M. Halat, M. L. Tate, I. R. Evans, and C. P. Grey, "Variable-temperature multinuclear solid-state NMR study of oxide ion dynamics in fluorite-type bismuth vanadate and phosphate solid electrolytes," *Chemistry of Materials*, vol. 31, no. 5, pp. 1704–1714, 2019.

[173] H. J. Jakobsen, H. Bildsøe, M. Brorson, Z. Gan, and I. Hung, "Quantitative dynamics and structure for crystalline Cs_2WO_4 and $KMnO_4$ determined from high-field ^{17}O variable-temperature MAS NMR experiments," *Journal of Physical Chemistry C*, vol. 118, pp. 20639–20646, 9 2014.

[174] D. Wilmer, H. Feldmann, and R. E. Lechner, "Ion dynamics in solid solutions of sodium phosphate and sodium sulfate," *Physical Chemistry Chemical Physics*, vol. 4, pp. 3260–3265, 7 2002.

[175] B. Schwaighofer, M. A. Gonzalez, M. Appel, M. M. Koza, and I. R. Evans, "Oxide ion mobility in V-and P-doped Bi_2O_3-based solid electrolytes: Combining quasielastic neutron scattering with ab initio molecular dynamics," *Chemistry of Materials*, vol. 35, pp. 1125–1133, 2023.

[176] I. Evans, M. Appel, M. A. Gonzalez, M. Koza Michael, A. Piovano, and B. Schwaighofer, "Fluorite-type solid electrolytes with complex oxide ion diffusion mechanisms. Institut Laue-Langevin (ILL), doi: 10.5291/ILL-DATA.7-03-184," 2020.

[177] C. Goodway, P. McIntyre, A. Sears, N. Belkhier, G. Burgess, O. Kirichek, E. Lelièvre-Berna, F. Marchal, S. Turc, and S. Wakefield, "A fast-cooling mode for blue series furnaces," *Journal of Neutron Research*, vol. 21, no. 3-4, pp. 137–142, 2020.

[178] B. Frick, J. Combet, and L. Van Eijck, "New possibilities with inelastic fixed window scans and linear motor Doppler drives on high resolution neutron backscattering spectrometers," *Nuclear Instruments and Methods in Physics Research, Section A: Accelerators, Spectrometers, Detectors and Associated Equipment*, vol. 669, pp. 7–13, 2012.

[179] X. Yang, A. J. Fernández-Carrión, J. Wang, F. Porcher, F. Fayon, M. Allix, and X. Kuang, "Cooperative mechanisms of oxygen vacancy stabilization and migration in the isolated tetrahedral anion scheelite structure," *Nature Communications*, vol. 9, no. 1, p. 4484, 2018.

[180] R. D. Shannon, "Revised effective ionic radii and systematic studies of interatomie distances in halides and chaleogenides," *Acta Crystallographica Section A*, vol. 32, pp. 751–767, 1976.

[181] J. R. Peet, C. M. Widdifield, D. C. Apperley, P. Hodgkinson, M. R. Johnson, and I. R. Evans, "Na^+ mobility in sodium strontium silicate fast ion conductors," *Chemical Communications*, vol. 51, no. 96, pp. 17163–17165, 2015.

[182] T. Esaka, T. Mina-ai, and H. Iwahara, "Oxide ion conduction in the solid solution based on the scheelite-type oxide $PbWO_4$," *Solid State Ionics*, vol. 57, no. 3-4, pp. 319–325, 1992.

[183] M. Nikl, P. Bohacek, E. Mihokova, M. Kobayashi, M. Ishii, Y. Usuki, V. Babin, A. Stolovich, S. Zazubovich, and M. Bacci, "Excitonic emission of scheelite tungstates AWO (A = Pb, Ca, Ba, Sr)," *Journal of Luminescence*, pp. 1136–1139, 2000.

[184] Z. Wang, H. Liang, M. Gong, and Q. Su, "Luminescence investigation of Eu^{3+} activated double molybdates red phosphors with scheelite structure," *Journal of Alloys and Compounds*, vol. 432, no. 1-2, pp. 308–312, 2007.

[185] J. Bin, H. Liu, L. Mei, L. Liang, H. Gao, H. Li, and L. Liao, "Multicolor luminescence evolution and efficient energy transfer of scheelite-type $LiCaGd(WO_4)_3$: Ln^{3+} (Ln = Eu, Dy, Tb) phosphors," *Ceramics International*, vol. 45, no. 2, pp. 1837–1845, 2019.

[186] T. Saison, N. Chemin, C. Chaneac, O. Durupthy, L. Mariey, F. Mauge, V. Brezova, and J.-P. Jolivet, "New insights into $BiVO_4$ properties as visible light photocatalyst," *The Journal of Physical Chemistry C*, vol. 119, no. 23, pp. 12967–12977, 2015.

[187] H. S. Park, K. E. Kweon, H. Ye, E. Paek, G. S. Hwang, and A. J. Bard, "Factors in the metal doping of $BiVO_4$ for improved photoelectrocatalytic activity as studied by scanning electrochemical microscopy and first-principles density-functional calculation," *The Journal of Physical Chemistry C*, vol. 115, no. 36, pp. 17870–17879, 2011.

[188] S. Tokunaga, H. Kato, and A. Kudo, "Selective preparation of monoclinic and tetragonal $BiVO_4$ with scheelite structure and their photocatalytic properties," *Chemistry of Materials*, vol. 13, no. 12, pp. 4624–4628, 2001.

[189] J. K. Cooper, S. Gul, F. M. Toma, L. Chen, P. A. Glans, J. Guo, J. W. Ager, J. Yano, and I. D. Sharp, "Electronic structure of monoclinic $BiVO_4$," *Chemistry of Materials*, vol. 26, no. 18, pp. 5365–5373, 2014.

[190] K. Toyoura, Y. Sakakibara, T. Yokoi, A. Nakamura, and K. Matsunaga, "Oxide-ion conduction via interstitials in scheelite-type $LaNbO_4$: a first-principles study," *Journal of Materials Chemistry A*, vol. 6, no. 25, pp. 12004–12011, 2018.

[191] G. C. Mather, C. A. Fisher, and M. S. Islam, "Defects, dopants, and protons in $LaNbO_4$," *Chemistry of Materials*, vol. 22, no. 21, pp. 5912–5917, 2010.

[192] T. Esaka, "Ionic conduction in substituted scheelite-type oxides," *Solid State Ionics*, vol. 136-137, pp. 1–9, 2000.

[193] J. E. Auckett, L. Lopez-Odriozola, S. J. Clark, and I. R. Evans, "Exploring the nature of the fergusonite–scheelite phase transition and ionic conductivity enhancement by Mo^{6+} doping in $LaNbO_4$," *Journal of Materials Chemistry A*, vol. 9, no. 7, pp. 4091–4102, 2021.

[194] R. Kawaguchi, R. Akizawa, Y. J. Shan, K. Tezuka, and T. Katsumata, "Synthesis and examination of $GdNb_{1-x}W_xO_{4+\delta}$ new scheelite-type oxide-ion conductor," *Solid State Ionics*, vol. 355, p. 115415, 2020.

[195] S. S. Pramana, T. Baikie, T. An, M. G. Tucker, J. Wu, M. K. Schreyer, F. Wei, R. D. Bayliss, C. L. Kloc, T. J. White, A. P. Horsfield, and S. J. Skinner, "Correlation of local structure and diffusion pathways in the modulated anisotropic oxide ion conductor $CeNbO_{4.25}$," *Journal of the American Chemical Society*, vol. 138, no. 4, pp. 1273–1279, 2016.

[196] T. Lu and B. Steele, "Electrical conductivity of polycrystalline $BiVO_4$ samples having the scheelite structure," *Solid State Ionics*, vol. 21, pp. 339–342, 1986.

[197] J. Li, F. Pan, S. Geng, C. Lin, L. Palatinus, M. Allix, X. Kuang, J. Lin, and J. Sun, "Modulated structure determination and ion transport mechanism of oxide-ion conductor $CeNbO_{4+\delta}$," *Nature Communications*, vol. 11, no. 1, p. 4751, 2020.

[198] R. J. Packer, E. V. Tsipis, C. N. Munnings, V. V. Kharton, S. J. Skinner, and J. R. Frade, "Diffusion and conductivity properties of cerium niobate," *Solid State Ionics*, vol. 177, no. 19-25 SPEC. ISS., pp. 2059–2064, 2006.

[199] C. Li, S. S. Pramana, and S. J. Skinner, "Room temperature structure and transport properties of the incommensurate modulated $LaNb_{0.88}W_{0.12}O_{4.06}$," *Dalton Transactions*, vol. 48, no. 5, pp. 1633–1646, 2019.

[200] M. A. Laguna-Bercero, R. D. Bayliss, and S. J. Skinner, "$LaNb_{0.84}W_{0.16}O_{4.08}$ as a novel electrolyte for high temperature fuel cell and solid oxide electrolysis applications," *Solid State Ionics*, vol. 262, pp. 298–302, 2014.

[201] C. Li, S. S. Pramana, R. D. Bayliss, C. P. Grey, F. Frede, F. Blanc, and S. J. Skinner, "Evolution of structure in the incommensurate modulated $LaNb_{1-x}W_xO_{4+x/2}$(x = 0.040.16) oxide ion conductors," *Chemistry of Materials*, vol. 32, pp. 2292–2303, 2020.

[202] S. Uma, R. Bliesner, and A. W. Sleight, "Oxygen ion conductivity in new oxygen deficient phases with scheelite related structures," *Solid State Sciences*, vol. 4, no. 3, pp. 329–333, 2002.

[203] X. Yang, X. Zeng, X. Ming, L. Yang, A. J. Fernández-Carrión, S. Deng, L. He, and X. Kuang, "Oxide-ion conductivity optimization in $BiVO_4$ scheelite by an acceptor doping strategy," *Inorganic Chemistry Frontiers*, vol. 9, no. 11, pp. 2644–2658, 2022.

[204] A. W. Sleight and W. Jeitschko, "$Bi_3(FeO_4)(MoO_4)_2$ and $Bi_3(GaO_4)(MoO_4)_2$ - new compounds with scheelite related structures," *Materials Research Bulletin*, vol. 9, no. 2142, pp. 951–954, 1974.

[205] S. Jeitschko, A. Sleight, W. R. Mcclellan, and J. F. Weiher, "Comprehensive study of disordered and ordered scheelite-related $Bi_3(FeO_2)(MoO_4)_2$," *Acta Crystallographica Section B Structural Science*, vol. B32, 1976.

[206] M. Saura-Múzquiz, F. P. Marlton, B. G. Mullens, J. Liu, T. Vogt, H. E. Maynard-Casely, M. Avdeev, D. A. Blom, and B. J. Kennedy, "Cation and lone pair order–disorder in the polymorphic mixed metal bismuth scheelite $Bi_3FeMo_2O_{12}$," *Chemistry of Materials*, pp. 123–135, 2022.

[207] U. Kolitsch and E. Tillmanns, "$Bi_3ScMo_2O_{12}$: The difference from $Bi_3FeMo_2O_{12}$," *Acta Crystallographica Section E: Structure Reports Online*, vol. 59, no. 3, pp. 43–46, 2003.

[208] X. Nie, W. Wulayin, T. Song, T. Li, and X. Qiao, "A scheelite-type semiconductor $InBi_3(MoO_6)_2$ nanoparticles: preparation, structural and optical properties," *Journal of the Taiwan Institute of Chemical Engineers*, vol. 74, pp. 263–271, 2017.

[209] D. Zhou, L. X. Pang, D. W. Wang, H. H. Guo, F. Yang, Z. M. Qi, C. Li, B. B. Jin, and I. M. Reaney, "Crystal structure, impedance and broadband dielectric spectra of ordered scheelite-structured $Bi(Sc_{1/3}Mo_{2/3})O_4$ ceramic," *Journal of the European Ceramic Society*, vol. 38, no. 4, pp. 1556–1561, 2018.

[210] A. W. Sleight and W. J. Linn, "Olefin oxidation over oxide catalysts with the scheelite structure," *Annals of the New York Academy of Sciences*, vol. 272, no. 1, pp. 22–44, 1976.

[211] B. Schwaighofer, MChem Report, "Garnet- and scheelite-type solid oxide fuel cell (SOFC) materials," *Durham University*, 2019.

[212] P. J. Bereciartua, F. J. Zuñiga, J. M. Perez-Mato, V. Petříček, E. Vila, A. Castro, J. Rodríguez-Carvajal, and S. Doyle, "Structure refinement and superspace description of the system $Bi_{2(n+2)}MonO_{6(n+1)}$ (n = 3, 4, 5 and 6)," *Acta Crystallographica Section B: Structural Science*, vol. 68, no. 4, pp. 323–340, 2012.

[213] D. Waroquiers, X. Gonze, G.-M. Rignanese, C. Welker-Nieuwoudt, F. Rosowski, M. Gobel, S. Schenk, P. Degelmann, R. André, R. Glaum, *et al.*, "Statistical analysis of coordination environments in oxides," *Chemistry of Materials*, vol. 29, no. 19, pp. 8346–8360, 2017.

[214] N. E. Brese and M. O'Keeffe, "Bondvalence parameters for solids," *Acta Crystallographica Section B*, vol. 47, no. 2, pp. 192–197, 1991.

[215] L. Pauling, "The principles determining the structure of complex ionic crystals," *Journal of the American Chemical Society*, vol. 51, no. 4, pp. 1010–1026, 1929.

[216] I. D. Brown, "Recent developments in the methods and applications of the bond valence model," *Chemical Reviews*, vol. 109, no. 12, pp. 6858–6919, 2009.

[217] I. Brown and D. Altermatt, "Bond-valence parameters obtained from a systematic analysis of the inorganic crystal structure database," *Acta Crystallographica Section B Structural Science*, vol. 244, no. 2, pp. 244–247, 1985.

[218] J. Bisquert and A. Compte, "Theory of the electrochemical impedance of anomalous diffusion," *Journal of Electroanalytical Chemistry*, vol. 499, no. 1, pp. 112–120, 2001.

[219] A. D. Brand˜, I. Antunes, J. R. Frade, J. Torre, V. V. Kharton, and D. P. Fagg, "Enhanced low-temperature proton conduction in $Sr_{0.02}La_{0.98}$ $NbO_{4-\delta}$ by scheelite phase retention," *Chemistry of Materials*, vol. 22, p. 6673, 2010.

[220] X. Ding, G. Hua, D. Ding, W. Zhu, and H. Wang, "Enhanced ionic conductivity of apatite-type lanthanum silicate electrolyte for IT-SOFCs through copper doping," *Journal of Power Sources*, vol. 306, pp. 630–635, 2016.

[221] A. Bhalla, R. Guo, and R. Roy, "The perovskite structurea review of its role in ceramic science and technology," *Materials Research Innovations*, vol. 4, no. 1, pp. 3–26, 2000.

[222] E. A. R. Assirey, "Perovskite synthesis, properties and their related biochemical and industrial application," *Saudi Pharmaceutical Journal*, vol. 27, no. 6, pp. 817–829, 2019.

[223] J. Y. Kim, J.-W. Lee, H. S. Jung, H. Shin, and N.-G. Park, "High-efficiency perovskite solar cells," *Chemical Reviews*, vol. 120, no. 15, pp. 7867–7918, 2020.

[224] Y. Rong, Y. Hu, A. Mei, H. Tan, M. I. Saidaminov, S. I. Seok, M. D. McGehee, E. H. Sargent, and H. Han, "Challenges for commercializing perovskite solar cells," *Science*, vol. 361, no. 6408, p. eaat8235, 2018.

[225] M. Li, M. J. Pietrowski, R. A. De Souza, H. Zhang, I. M. Reaney, S. N. Cook, J. A. Kilner, and D. C. Sinclair, "A family of oxide ion conductors based on the ferroelectric perovskite $Na_{0.5}Bi_{0.5}TiO_3$," *Nature Materials*, vol. 13, no. 1, pp. 31–35, 2014.

[226] L. Shu, J. Sunarso, S. S. Hashim, J. Mao, W. Zhou, and F. Liang, "Advanced perovskite anodes for solid oxide fuel cells: a review," *International Journal of Hydrogen Energy*, vol. 44, no. 59, pp. 31275–31304, 2019.

[227] S. Tao and J. T. Irvine, "A redox-stable efficient anode for solid-oxide fuel cells," *Nature Materials*, vol. 2, no. 5, pp. 320–323, 2003.

[228] P. Kaur and K. Singh, "Review of perovskite-structure related cathode materials for solid oxide fuel cells," *Ceramics International*, vol. 46, no. 5, pp. 5521–5535, 2020.

[229] S. Paydar, M. H. Shariat, and S. Javadpour, "Investigation on electrical conductivity of LSM/YSZ8, LSM/$Ce_{0.84}Y_{0.16}O_{0.96}$ and LSM/$Ce_{0.42}Zr_{0.42}Y_{0.16}O_{0.96}$ composite cathodes of SOFCs," *International Journal of Hydrogen Energy*, vol. 41, no. 48, pp. 23145–23155, 2016.

[230] W. Fang, T. Yang, and K. Huang, "In situ synthesis of a high-performance bismuth oxide based composite cathode for low temperature solid oxide fuel cells," *Chemical Communications*, vol. 55, no. 19, pp. 2801–2804, 2019.

[231] P. Hjalmarsson, M. Søgaard, A. Hagen, and M. Mogensen, "Structural properties and electrochemical performance of strontium- and nickel-substituted lanthanum cobaltite," *Solid State Ionics*, vol. 179, no. 17-18, pp. 636–646, 2008.

[232] Y. Li, J. W. Cai, J. A. Alonso, H. Q. Lian, X. G. Cui, and J. B. Goodenough, "Evaluation of $LaNi_{0.6}M_{0.4O3}$ (M = Fe, Co) cathodes in LSGM-electrolyte-supported solid-oxide fuel cells," *International Journal of Hydrogen Energy*, vol. 42, no. 44, pp. 27334–27342, 2017.

[233] J. Y. Chen, J. Rebello, V. Vashook, D. M. Trots, S. R. Wang, T. L. Wen, J. Zosel, and U. Guth, "Thermal stability, oxygen non-stoichiometry and transport properties of $LaNi_{0.6}Fe_{0.4}O_3$," *Solid State Ionics*, vol. 192, no. 1, pp. 424–430, 2011.

[234] L. Katz and R. Ward, "Structure relations in mixed metal oxides," *Inorganic Chemistry*, vol. 3, no. 2, pp. 205–211, 1964.

[235] J. Darriet and M. A. Subramanian, "Structural relationships between compounds based on the stacking of mixed layers related to hexagonal perovskite-type structures," *Journal of Materials Chemistry*, vol. 5, no. 4, pp. 543–552, 1995.

[236] V. Goldschmidt, "Die Gesetze der Krystallochemie," *Naturwissenschaften*, vol. 14, pp. 477–485, 1926.

[237] S. Fop, K. S. McCombie, E. J. Wildman, J. M. Skakle, and A. C. Mclaughlin, "Hexagonal perovskite derivatives: a new direction in the design of oxide ion conducting materials," *Chemical Communications*, vol. 55, no. 15, pp. 2127–2137, 2019.

[238] X. Kuang, X. Jing, C. K. Loong, E. E. Lachowski, J. M. Skakle, and A. R. West, "A new hexagonal 12-layer perovskite-related structure: $Ba_6R_2Ti_4O_{17}$

(R = Nd and Y)," *Chemistry of Materials*, vol. 14, no. 10, pp. 4359–4363, 2002.

[239] X. Kuang, M. Allix, R. M. Ibberson, J. B. Claridge, H. Niu, and M. J. Rosseinsky, "Oxygen vacancy ordering phenomena in the mixed-conducting hexagonal perovskite $Ba_7Y_2Mn_3Ti_2O_{20}$," *Chemistry of Materials*, vol. 19, no. 11, pp. 2884–2893, 2007.

[240] C. D. Ling, M. Avdeev, V. V. Kharton, A. A. Yaremchenko, R. B. Macquart, and M. Hoelzel, "Structures, phase transitions, hydration, and ionic conductivity of $Ba_4Ta_2O_9$," *Chemistry of Materials*, vol. 22, no. 2, pp. 532–540, 2010.

[241] S. Fop, J. M. Skakle, A. C. McLaughlin, P. A. Connor, J. T. Irvine, R. I. Smith, and E. J. Wildman, "Oxide ion conductivity in the hexagonal perovskite derivative $Ba_3MoNbO_{8.5}$," *Journal of the American Chemical Society*, vol. 138, no. 51, pp. 16764–16769, 2016.

[242] S. Fop, K. S. McCombie, E. J. Wildman, J. M. S Skakle, J. T. S Irvine, P. A. Connor, C. Savaniu, C. Ritter, and A. C. Mclaughlin, "High oxide ion and proton conductivity in a disordered hexagonal perovskite," *Nature Materials*, vol. 19, no. 7, pp. 752–757, 2020.

[243] E. García-González, M. Parras, and J. M. González-Calbet, "Electron microscopy study of a new cation deficient perovskite-like oxide: $Ba_3MoNbO_{8.5}$," *Chemistry of Materials*, vol. 10, no. 6, pp. 1576–1581, 1998.

[244] M. S. Chambers, K. S. Mccombie, J. E. Auckett, A. C. Mclaughlin, J. T. S. Irvine, P. A. Chater, J. S. O. Evans, and I. R. Evans, "Hexagonal perovskite related oxide ion conductor $Ba_3NbMoO_{8.5}$: phase transition, temperature evolution of the local structure and properties," *Journal of Materials Chemistry A*, vol. 7, no. 44, pp. 25503–25510, 2019.

[245] J. E. Auckett, K. L. Milton, and I. R. Evans, "Cation distributions and anion disorder in $Ba_3NbMO_{8.5}$ (M = Mo, W) materials: Implications for oxide ion conductivity," *Chemistry of Materials*, vol. 31, p. 58, 2019.

[246] S. Fop, E. J. Wildman, J. T. S. Irvine, P. A. Connor, J. M. S. Skakle, C. Ritter, and A. C. Mclaughlin, "Investigation of the relationship between the structure and conductivity of the novel oxide ionic conductor $Ba_3MoNbO_{8.5}$," *Chemistry of Materials*, vol. 29, pp. 4146–4152, 2017.

[247] S. Fop, E. J. Wildman, J. M. S. Skakle, C. Ritter, and A. C. Mclaughlin, "Electrical and structural characterization of $Ba_3Mo_{1-x}Nb_{1+x}O_{8.5-x/2}$: The relationship between mixed coordination, polyhedral distortion and the ionic conductivity of $Ba_3MoNbO_{8.5}$," *Inorganic Chemistry*, vol. 56, pp. 10505–10512, 2017.

[248] K. S. McCombie, E. J. Wildman, C. Ritter, R. I. Smith, J. M. Skakle, and A. C. McLaughlin, "Relationship between the crystal structure and electrical

properties of oxide ion conducting $Ba_3W_{1.2}Nb_{0.8}O_{8.6}$," *Inorganic Chemistry*, vol. 57, no. 19, pp. 11942–11947, 2018.

[249] K. S. McCombie, E. J. Wildman, S. Fop, R. I. Smith, J. M. Skakle, and A. C. McLaughlin, "The crystal structure and electrical properties of the oxide ion conductor $Ba_3WNbO_{8.5}$," *Journal of Materials Chemistry A*, vol. 6, no. 13, pp. 5290–5295, 2018.

[250] S. Fop, K. McCombie, R. I. Smith, and A. C. Mclaughlin, "Enhanced oxygen ion conductivity and mechanistic understanding in $Ba_3Nb_{1-x}V_xMoO_{8.5}$," *Chemistry of Materials*, vol. 32, no. 11, pp. 4724–4733, 2020.

[251] A. Bernasconi, C. Tealdi, M. Mühlbauer, and L. Malavasi, "Synthesis, crystal structure and ionic conductivity of the $Ba_3Mo_{1-x}W_xNbO_{8.5}$ solid solution," *Journal of Solid State Chemistry*, vol. 258, no. December 2017, pp. 628–633, 2018.

[252] J. E. Auckett, M. J. Gutmann, and I. R. Evans, "Understanding the correlation between oxide ion mobility and site distributions in $Ba_3NbWO_{8.5}$," *Inorganic Chemistry*, vol. 59, no. 19, pp. 14245–14250, 2020.

[253] M. Yashima, T. Tsujiguchi, K. Fujii, E. Niwa, S. Nishioka, J. R. Hester, and K. Maeda, "Direct evidence for two-dimensional oxide-ion diffusion in the hexagonal perovskite-related oxide $Ba_3MoNbO_{8.5-\delta}$," *Journal of Materials Chemistry A*, vol. 7, no. 23, pp. 13910–13916, 2019.

[254] Y. Yasui, T. Tsujiguchi, Y. Sakuda, J. R. Hester, and M. Yashima, "Oxide-ion occupational disorder, diffusion path, and conductivity in hexagonal perovskite derivatives $Ba_3WNbO_{8.5}$ and $Ba_3MoNbO_{8.5}$," *The Journal of Physical Chemistry C*, vol. 126, no. 5, pp. 2383–2393, 2022.

[255] A. Gilane, S. Fop, F. Sher, R. I. Smith, and A. C. Mclaughlin, "The relationship between oxide-ion conductivity and cation vacancy order in the hybrid hexagonal perovskite $Ba_3VWO_{8.5}$," *Journal of Materials Chemistry A*, vol. 8, no. 32, pp. 16506–16514, 2020.

[256] M. Parras, E. Garcia-Gonzalez, and M. Gonzalez-Calbet, J, "Crystal structure of an unusual polytype : 7H-$Ba_7Nb_4MoO_{20}$," *Chemistry of Materials*, vol. 11, pp. 433–437, 1999.

[257] M. Yashima, T. Tsujiguchi, Y. Sakuda, Y. Yasui, Y. Zhou, K. Fujii, S. Torii, T. Kamiyama, and S. J. Skinner, "High oxide-ion conductivity through the interstitial oxygen site in $Ba_7Nb_4MoO_{20}$-based hexagonal perovskite related oxides," *Nature Communications*, vol. 12, 12 2021.

[258] Y. Sakuda, J. R. Hester, and M. Yashima, "Improved oxide-ion and lower proton conduction of hexagonal perovskite-related oxides based on $Ba_7Nb_4MoO_{20}$ by Cr^{6+} doping," *Journal of the Ceramic Society of Japan*, vol. 130, no. 7, pp. 442–447, 2022.

[259] S. Fop, J. A. Dawson, A. D. Fortes, C. Ritter, and A. C. McLaughlin, "Hydration and ionic conduction mechanisms of hexagonal perovskite derivatives," *Chemistry of Materials*, vol. 33, no. 12, pp. 4651–4660, 2021.

[260] M. Yashima, T. Tsujiguchi, Y. Sakuda, Y. Yasui, Y. Zhou, K. Fujii, S. Torii, T. Kamiyama, and S. J. Skinner, "High oxide-ion conductivity through the interstitial oxygen site in $Ba_7Nb_4MoO_{20}$-based hexagonal perovskite related oxides," *Nature Communications*, vol. 12, no. 1, p. 556, 2021.

[261] R. Mittal, S. Kumar, M. K. Gupta, S. K. Mishra, S. Mukhopadhyay, M. D. Le, R. Shukla, S. N. Achary, A. K. Tyagi Bd, and S. L. Chaplot, "Sodium diffusion and dynamics in $Na_2Ti_3O_7$: neutron scattering and ab initio simulations," *Materials Advances*, vol. 3, pp. 2104–2116, 2022.

[262] Y. Mo, S. P. Ong, and G. Ceder, "First principles study of the $Li_{10}GeP_2S_{12}$ lithium super ionic conductor material," *Chemistry of Materials*, vol. 24, no. 1, pp. 15–17, 2012.

[263] X. He, Y. Zhu, A. Epstein, and Y. Mo, "Statistical variances of diffusional properties from ab initio molecular dynamics simulations," *npj Computational Materials*, vol. 4, no. 1, p. 18, 2018.

[264] Z. Deng, B. Radhakrishnan, and S. P. Ong, "Rational composition optimization of the lithium-rich $Li_3OCl_{1-x}Br_x$ anti-perovskite superionic conductors," *Chemistry of Materials*, vol. 27, no. 10, pp. 3749–3755, 2015.

[265] I. R. Evans, J. A. K. Howard, and J. S. O. Evans, "The crystal structure of α-$La_2Mo_2O_9$ and the structural origin of the oxide ion migration pathway," *Chemistry of Materials*, vol. 17, pp. 4074–4077, 2005.

[266] E. Ruiz-Agudo, C. V. Putnis, and C. Rodriguez-Navarro, "Interaction between epsomite crystals and organic additives," *Crystal Growth and Design*, vol. 8, no. 8, pp. 2665–2673, 2008.

[267] O. B. Lapina, D. F. Khabibulin, K. V. Romanenko, Z. Gan, M. G. Zuev, V. N. Krasilnikov, and V. E. Fedorov, "^{93}Nb NMR chemical shift scale for niobia systems," *Solid State Nuclear Magnetic Resonance*, vol. 28, no. 2-4, pp. 204–224, 2005.

[268] O. Lapina, D. Khabibulin, A. Shubin, and V. Terskikh, "Practical aspects of ^{51}V and ^{93}Nb solid-state NMR spectroscopy and applications to oxide materials," *Progress in Nuclear Magnetic Resonance Spectroscopy*, vol. 3, no. 53, pp. 128–191, 2008.

[269] C. A. Fuller, Q. Berrod, B. Frick, M. R. Johnson, S. J. Clark, J. S. Evans, and I. R. Evans, "Brownmillerite-type Sr_2ScGaO_5 oxide ion conductor: local structure, phase transition, and dynamics," *Chemistry of Materials*, vol. 31, no. 18, pp. 7395–7404, 2019.

[270] V. Kharton, I. Marozau, N. Vyshatko, A. Shaula, A. Viskup, E. Naumovich, and F. Marques, "Oxygen ionic conduction in brownmillerite $CaAl_{0.5}Fe_{0.5}O_{2.5+\delta}$," *Materials Research Bulletin*, vol. 38, no. 5, pp. 773–782, 2003.

[271] J. Goodenough, J. Ruiz-Diaz, and Y. Zhen, "Oxide-ion conduction in $Ba_2In_2O_5$ and $Ba_3In_2MO_8$(M= Ce, Hf, or Zr)," *Solid State Ionics;(Netherlands)*, vol. 44, no. 1-2, pp. 21–31, 1990.

[272] G. Amow and S. Skinner, "Recent developments in ruddlesden–popper nickelate systems for solid oxide fuel cell cathodes," *Journal of Solid State Electrochemistry*, vol. 10, pp. 538–546, 2006.

[273] M. Patrakeev, I. Leonidov, V. Kozhevnikov, and V. Kharton, "Ion–electron transport in strontium ferrites: relationships with structural features and stability," *Solid State Sciences*, vol. 6, no. 9, pp. 907–913, 2004.

[274] H. Yaguchi, K. Fujii, Y. Tsuchiya, H. Ogino, Y. Tsujimoto, and M. Yashima, "Ruddlesden–popper oxychlorides $Ba_3Y_2O_5Cl_2$, $Sr_3Sc_2O_5Cl_2$, and Sr_2ScO_3Cl: First examples of oxide-ion-conducting oxychlorides," *ACS Applied Energy Materials*, vol. 5, no. 1, pp. 295–304, 2021.

[275] D. Lee and H. N. Lee, "Controlling oxygen mobility in ruddlesden–popper oxides," *Materials*, vol. 10, no. 4, p. 368, 2017.

[276] W. Zhang, K. Fujii, E. Niwa, M. Hagihala, T. Kamiyama, and M. Yashima, "Oxide-ion conduction in the dion–jacobson phase $CsBi_2Ti_2NbO_{10-\delta}$," *Nature Communications*, vol. 11, no. 1, p. 1224, 2020.

[277] A. Jacobson, J. W. Johnson, and J. Lewandowski, "Interlayer chemistry between thick transition-metal oxide layers: synthesis and intercalation reactions of $K[Ca_2Na_{n-3}Nb_nO_{3n+1}]$," *Inorganic chemistry*, vol. 24, no. 23, pp. 3727–3729, 1985.

[278] M. Dion, M. Ganne, and M. Tournoux, "The new phase families $M^IM^{II}_2Nb_3O_{10}$ with perovskite sheets," *Materials Research Bulletin*, vol. 16, no. 11, pp. 1429–1435, 1981.

[279] E. E. McCabe, E. Bousquet, C. P. Stockdale, C. A. Deacon, T. T. Tran, P. S. Halasyamani, M. C. Stennett, and N. C. Hyatt, "Proper ferroelectricity in the dion–jacobson material $CsBi_2Ti_2NbO_{10}$: experiment and theory," *Chemistry of Materials*, vol. 27, no. 24, pp. 8298–8309, 2015.

[280] W. Zhang, K. Fujii, T. Ishiyama, H. Kandabashi, and M. Yashima, "Dion–jacobson-type oxide-ion conductor $CsLa_2Ti_2NbO_{10-\delta}$ without phase transitions," *Journal of Materials Chemistry A*, vol. 8, no. 47, pp. 25085–25093, 2020.

[281] W. Zhang and M. Yashima, "Improved oxide-ion conductivity by substitution of sr for bi in dion–jacobson phase $CsBi_2Ti_2NbO_{10}$," *Ceramics International*, vol. 48, no. 12, pp. 16522–16528, 2022.

[282] W. Zhang and M. Yashima, "Recent developments in oxide ion conductors: focusing on dion–jacobson phases," *Chemical Communications*, vol. 59, pp. 134–152, 2023.

[283] M. Shishkin and G. Kresse, "Implementation and performance of the frequency-dependent *GW* method within the PAW framework," *Physical Review B*, vol. 74, p. 035101, Jul 2006.

[284] K. Andersen and C. Carlile, "A proposal for a next generation european neutron source," *Journal of Physics: Conference Series*, vol. 746, no. 1, p. 012030, 2016.

[285] K. H. Andersen, D. N. Argyriou, A. J. Jackson, J. Houston, P. F. Henry, P. P. Deen, R. Toft-Petersen, P. Beran, M. Strobl, T. Arnold, *et al.*, "The instrument suite of the european spallation source," *Nuclear Instruments and Methods in Physics Research Section A: Accelerators, Spectrometers, Detectors and Associated Equipment*, vol. 957, p. 163402, 2020.

APPENDIX A

Publications

Expanded Chemistry and Proton Conductivity in Vanadium-Substituted Variants of γ-$Ba_4Nb_2O_9$

A. J. Brown, B. Schwaighofer, M. Avdeev, B. Johannessen, I. R. Evans, and C. D. Ling

(This collaborative work is unrelated to this thesis)

Chemistry of Materials, 2021, 33, 18, 74757483

Oxide Ion Mobility in V- and P-doped Bi_2O_3-Based Solid Electrolytes: Combining Quasielastic Neutron Scattering with Ab Initio Molecular Dynamics

B. Schwaighofer, M. A. Gonzalez, M. Appel, M. M. Koza, and I. R. Evans

Chemistry of Materials, 2023, 35, 3, 11251133

Oxide Ion Dynamics in the Hexagonal Perovskite $Ba_7Nb_4MoO_{20}$

B. Schwaighofer, M. A. Gonzalez, M. Appel, and I. R. Evans

In Preparation